Enhanced magnetoelectric effects in electrolyte-gated nanoporous metallic alloy and dense metal oxide films

Alberto Quintana Puebla

Tesi Doctoral

Programa de Doctorat en Ciència de Materials

Enric Menéndez Dalmau (Director)

Eva Pellicer Vilà (Directora i Tutora)

Jordi Sort Viñas (Director)

Departament de Física

Facultat de Ciències

2018

II

UAB

Universitat Autònoma de Barcelona

Memòria presentada per aspirar al Grau de Doctor per
Alberto Quintana Puebla

Vist i plau

Dra. Eva Pellicer Vilà

(Directora i Tutora)

Prof. Jordi Sort Viñas   Dr. Enric Menéndez Dalmau

(Director)   (Director)

Bellaterra, 22 de Maig de 2018

La **Dra. Eva Pellicer Vilà**, investigadora Ramón y Cajal del Departament de Física de la Universitat Autònoma de Barcelona,

el **Dr. Jordi Sort Viñas**, professor ICREA del Departament de Física de la Universitat Autònoma de Barcelona,

i el **Dr. Enric Menéndez Dalmau**, investigador Post-Doctoral del Departament de Física de la Universitat Autònoma de Barcelona,

CERTIFIQUEN:

Que **Alberto Quintana Puebla** ha realitzat sota la seva direcció el treball d'investigació que s'exposa a la memòria titulada "Enhanced magnetoelectric effects in electrolyte-gated nanoporous metallic alloy and dense metal oxide films" per optar al grau de **Doctor per la Universitat Autònoma de Barcelona**.

Que el disseny dels experiments, síntesi de mostres, llur caracterització, l'anàlisi dels resultats, la redacció dels articles i d'aquesta memòria són fruit del treball d'investigació realitzat per **Alberto Quintana Puebla**.

I perquè així consti, signen el present certificat,

Dra. Eva Pellicer Vilà   Dr. Jordi Sort Viñas

Dr. Enric Menéndez Dalmau

Bellaterra, 22 de Maig de 2018

v

Acknowledgments

Ahora que se acercan las despedidas y después de unos cuantos años rondando por la facultad, son muchas las personas que me vienen a la mente, siendo cada una de ellas importantes de algún u otro modo.

Me viene a la memoria mis inicios en este mundillo, mi paso por Cetemmsa. Siempre recordaré el primer día que fui a trabajar y tú, Eugenia, me preguntaste: *¿Tú eres físico, no? ¿Y qué sabes hacer?*. Tras mi largo silencio me dijiste *Tranquilo, que yo te enseño*. Gracias Eugenia, Marco, Oscar, Edu, Irene, Eli, Paul... y a muchos más. Gracias por enseñarme y por acogerme como uno más. ¡Qué buenos recuerdos tengo!

Luego vino un ya lejano proyecto final de carrera aquí ya en FMII. ¡Cuánto ha llovido desde entonces! Siempre os estaré agradecidos Jordi, Eva, Dolors y Santi por darme la oportunidad de iniciarme en este mundillo, el cual me encandiló inmediatamente. Gracias Aïda por tu inestimable dedicación y cariño durante aquellos meses, simplemente ¡gracias!

Después de una época de máster intensa pero agradecida y llena de gente 10, vino la época de la tesis. Gracias Jordi por confiar en mí, y darme la oportunidad de realizar este reto bajo tu ERC Consolidator Grant. I would like to acknowledge the European Research Council for the provided funding (SPIN-PORICS 2014-Consolidator Grant, Agreement No. 648454) which allowed me to develop my PhD research. Gracias Enric, Eva y Jordi por vuestra ayuda y tutelaje durante estos años. Gracias a la confianza depositada en mi persona, siento haber crecido tanto personal como laboralmente.

Gracias también a toda la gente con la que he tenido el placer de colaborar y que tanto me ha ayudado estos años. Es un placer seguir aprendiendo de vosotros. Gracias a los "Serveis Cientificotècnics de la UB" y a los "Serveis d'Anàlisi Química, de Microscòpia i de Difracció de Raig X de la UAB" por el soporte técnico durante estos años.

Aterrizar por estas tierras, no solo me ha beneficiado laboralmente, sino que también me ha aportado mucho a nivel personal. ¡Aïda, Patxi, Pablo, Pau, Jordina, Irati y Alex, gracias por acogerme tan bien. ¡Es un placer haber y seguir compartiendo momentos con vosotros! ¡Larga vida a las paellas, barbacoas, sardinadas, teatros, vermutadas,...!

Agradecer los buenos momentos con mis compañeros de FMII (Anna H., Veronica, Jin, Fan, Patrick, Huiyan, Cristina, Dani, Miguel, Shauna, Evangelia, Doga). Los interminables cafés con Isarain y Enric, arreglando el mundo e ideando más de lo que una persona podría abarcar en una vida. ¡Los echaré de menos!

Mención especial se merecen los que siempre están. Esos amigos incondicionales que entienden tu obsesión, la respetan y te animan a tirarla adelante, aunque no se enteren de una mierda ;-). La familia que con sus sacrificios e incondicionalidad me han permitido llegar hasta aquí. Y por último y no por ello menos importante, a mi mujer. *Gràcies per tot, ets la millor!*

Resumen

Esta tesis abarca el estudio de propiedades magnetoeléctricas en aleaciones magnéticas y metálicas nanoporosas, y en capas densas de óxidos de metales de transición.

La naturaleza interfacial de los procesos magnetoeléctricos ha hecho que históricamente el estudio de estos fenómenos se abordara en sistemas de elevada relación superficie/volumen, limitándose muchas veces a capas ultradelgadas (1-2 nm). En esta tesis, se postula una nueva forma de afrontar el estudio de estos procesos, basada en el uso de materiales nanoporosos los cuales se caracterizan por tener una relación superficie/volumen muy elevada y una pared de poro o ligamento de pocos nanómetros. De esta forma, se han obtenido efectos magnetoeléctricos en materiales cuyo grosor global supera el centenar de nanometros.

La síntesis de los materiales de interés se ha llevado a cabo por métodos de deposición electroquímica. Específicamente, se ha sacado partido de la formación de micelas al disolver copolímeros bloque en soluciones acuosas por encima de la concentración micelar crítica. Estas micelas quedan atrapadas durante el proceso de electrodeposición, actuando como agente moldeador. Usando este enfoque, se han podido sintetizar diferentes muestras de distintas morfologías y composiciones de la aleación cobre-níquel.

La aplicación de voltaje se ha realizado haciendo uso de electrolitos, aprovechando la formación de una doble capa eléctrica. Con la intención de obtener efectos magnetoeléctricos puros (acumulación de carga) y evitar procesos oxidativos simultáneos, se ha utilizado un electrolito orgánico aprótico. Con este método, se pueden obtener campos eléctricos del orden de centenares de MV/cm. Gracias a este elevado campo eléctrico, junto con la enrome relación superficie/volumen de los materiales nanoporosos, se ha obtenido una disminución de la coercitividad de una muestra nanoporosa de $Cu_{25}Ni_{75}$ en un 32 %. Simulaciones *ab-initio* atribuyen estos cambios a modificaciones en la energía de anisotropía magnética adscritos a la acumulación de cargas electrostáticas en la aleación.

En una segunda aproximación, se han realizado estudios de procesos de oxidación-reducción en medios acuosos (1M NaOH) controlados por voltaje, en este tipo de aleaciones. Después de aplicar potenciales positivos, se ha visto una modificación de un 33 % en la magnetización, debido a la oxidación selectiva del cobre en una muestra

nanoporosa de $Cu_{20}Ni_{80}$. La oxidación resulta en una aleación enriquecida en níquel y, por ende, en una aleación con mayor momento magnético.

En esta tesis, también se ha demostrado la idoneidad de la técnica de deposición por capas atómicas para producir recubrimientos conformales en materiales nanoporosos. Se ha visto que esta técnica permite preservar la integridad morfológica y estructural de la capa activa, asentando así las bases para aplicaciones en estado sólido.

En la última parte de esta tesis, se ha demostrado la posibilidad de inducir ferromagnetismo mediante la aplicación de voltaje eléctrico en capas densas de Co_3O_4. El campo eléctrico aplicado da lugar a una migración iónica controlada, resultando en regiones ricas en oxígeno y otras en cobalto, estas últimas originando el ferromagnetismo. Este experimento es una de las primeras evidencias de movimiento iónico inducido por voltaje a temperatura ambiente y sin la necesidad de utilizar capas donadoras/aceptores de oxígeno (en otras palabras, sin fuentes o sumideros de oxígeno).

Abstract

This Thesis covers the study of the magnetoelectric response in nanoporous metallic alloy and transition metal oxide dense films.

The interfacial nature of magnetoelectric processes, independently of its origin, has limited its study to ultrathin film configurations (usually 1-2 nm). Here we propose a novel approach to overcome this thickness limitation, thus achieving magnetoelectric response in materials whose overall thickness is larger than 100 nm. To accomplish this, we have employed nanoporous materials, with pore walls and ligands of very few nanometers, which are characterized by a large surface to volume ratio.

These materials have been synthesized by micelle assisted electrodeposition. Micelles get trapped during the electrodeposition process thus acting as a soft templating agent, allowing us to synthesize nanoporous copper-nickel alloy films with tunable composition and morphology.

Voltage application has been performed through electrolyte-gating, taking advantage of the generation of an electrical double layer in aprotic organic electrolytes which helps to avoid spurious oxidation processes. This method allows for the application of electric fields as high as hundreds of MV/cm. Thanks to the high electric field achieved, together with the ultrahigh surface area of nanoporous materials, a 32 % reduction in the coercivity of a $Cu_{25}Ni_{75}$ nanoporous film has been achieved. Ab-initio simulations attribute this large effect to changes in the magnetic anisotropy energy due to charge accumulation in the sample|electrolyte interface.

In a second approach, the voltage control of redox processes has been studied in aqueous electrolytes (1M NaOH). After positive bias application up to a 33 % reduction in the magnetization has been achieved in a $Cu_{20}Ni_{80}$ nanoporous sample thanks to the selective Cu oxidation. The controlled oxidation process resulted in an enriched Ni alloy which possesses a larger magnetic moment.

Moreover, we have demonstrated the suitability of atomic layer deposition to conformally coat the nanoporous alloys, preserving the morphology and structure, thus setting the basis for future solid state applications.

In the last part of this Thesis, it has been demonstrated that, upon electric field application, a ferromagnetic response arises in a paramagnetic single Co_3O_4 layer, at room

temperature. The applied voltage promotes the ionic diffusion, resulting in oxygen rich and cobalt rich regions, being the latter the responsible of the induced magnetic signal. This experiment is one of the first evidences of ionic motion at room temperature without the assistance of oxygen buffer layers such as Gd_2O_3 or HfO_2.

Glossary

- 1-Ethyl-3-methylimidazolium bis(trifluoromethylsulfonyl)imide (EMIM-TFSI)
- Antiferromagnetic (AFM)
- Applied Magnetic Field ($\mathbf{H_{applied}}$)
- Atomic Layer Deposition (ALD)
- Atomic Superposition (ATSUP)
- $BaTiO_3$ (BTO)
- Bohr Magneton (μ_B)
- Centimeter-Gram-Second (CGS)
- Coercivity (H_C)
- Coincidence Doppler Broadening Positron Annihilation Spectroscopy (cDB-PAS)
- Composite Multiferroics (c-MFs)
- Converse Magnetoelectric Coefficient (α_{-1})
- Critical Micellar Concentration (cmc)
- Curie Temperature (T_C)
- Demagnetizing Field ($\mathbf{H_d}$)
- Density Functional Theory (DFT)
- Diethylmethyl(2-methoxyethyl) ammonium bis(trifluoromethylsulfonyl)imide (DEME-TFSI)
- Diluted Magnetic Semiconductors (DMS)
- Electric Field (E-field)
- Electrical Double Layer (EDL)
- Electrical Polarization (P)
- Electron Energy Loss Spectroscopy (EELS)
- Energy Dispersive X-Ray Analyses (EDX)
- Energy Filtered Transmission Electron Microscopy (EFTEM)
- Evaporation Induced Self-Assembly (EISA)
- Exchange Constant (J)
- Exchange Energy ($E_{EXCHANGE}$)
- Face Centered Cubic (FCC)
- Fast Fourier Transform (FFT)
- Ferrimagnetism (FiM)
- Ferromagnetic (FM)
- Field-Effect Transistor (FET)
- First-Order Reversal Curve (FORC)
- Focused Ion Beam (FIB)
- Free Space Permeability (μ_0)
- Giant Magnetoresistance (GMR)
- Hexagonal Close-Packed (HCP)
- High Resolution Transmission Electron Microscopy (HRTEM)
- High-Angle Annular Dark-Field Scanning Transmission Electron Microscopy (HAADF-STEM)
- Hydrogen Evolution Reaction (HER)
- Inductively Coupled Plasma Mass Spectrometry (ICPMS)
- Internal Magnetic Field (H)
- International System (IS)
- International Union of Pure and Applied Chemistry (IUPAC)
- Kelvin Degree (K)
- Lyotropyc Liquid Crystal (LLC)
- Magnetic Anisotropy Energy (MAE)
- Magnetic Induction ($\mathbf{B}$)
- Magnetic Moment ($\mathbf{m}$)

- Magnetic Random-Access Memory (MRAM)
- Magnetic Susceptibility (χ)
- Magnetization (**M**)
- Magnetocrystalline Energy (E_{MC})
- Magnetoelectric (ME)
- Magnetoelectric Coefficient (α_E)
- Magneto-Optic Kerr Effect (MOKE)
- Magnetostatic Energy (E_{MS})
- Material Permeability (μ)
- Molar (M)
- Multiferroics (MFs)
- Néel Temperature (T_N)
- Open Circuit Potential (OCP)
- Orbital Angular Momentum (**l**)
- Perpendicular Magnetic Anisotropy (PMA)
- Plasma-Enhanced Atomic Layer Deposition (PE-ALD)
- Polarized Neutron Reflectivity (PNR)
- Poly(ethylene glycol)-block-poly(propylene glycol)-block-poly(ethylene glycol) (Pluronic P123®)
- Poly(ethylene oxide) (PEO)
- Poly(propylene oxide) (PPO)
- Poly(ω-hydroxypoly(ethyleneco-butylene)-co poly(ethyleneoxide)) (KLE)
- Polyimide (PI)
- Polyvinil difluoride (PVDF)
- Positron Annihilation Lifetime Spectroscopy (PALS)
- Positron Annihilation Spectroscopy (PAS)
- Reduced Plank Constant ($\hbar$)
- Relative Permeability (μ_r)
- Remnant Magnetization (M_R)
- Saturation Magnetization (M_S)
- Scanning Electron Microscopy (SEM)
- Scanning Transmission Electron Microscopy (STEM)
- Selected Area Electron Diffraction (SAED)
- Single-Phase Multiferroics (s-MFs)
- Spin (**s**)
- Squareness Ratio (M_R/M_S)
- Transmission Electron Microscopy (TEM)
- Tunneling Magnetoresistance (TMR)
- Variable Energy Positron Annihilation Spectroscopy (VE-PAS)
- Vibrating Sample Magnetometer (VSM)
- X-Ray Absorption (XAS)
- X-Ray Diffraction (XRD)
- X-Ray Magnetic Circular Dichroism (XMCD)
- X-Ray Photoelectron Spectroscopy (XPS)
- Yttria-Stabilized Zirconia (YSZ)
- Zeeman Energy ($E_{Happlied}$)

Preface

The contents of this Thesis have been organized in different chapters as follows:

- **Chapter 1**: The introduction presents the theoretical basis of the main concepts on magnetism and magnetic materials, paying attention to recording media and spintronics fields. The state-of-the-art of the different approaches to control magnetism by means of electric field is shown. A brief section on the electrodeposition of porous materials is included. Finally, the main goals and a schedule of the whole Thesis work are presented.

- **Chapter 2** presents the obtained results on this Thesis as a compilation of articles. A brief summary of the work is included prior to each article.

- **Chapter 3** describes the magneto-ionic driven *ON-OFF* ferromagnetism in a dense Co_3O_4 film. Despite not being formally included in the compilation of articles, the work presented herein complements the results obtained in chapter 2 and thus, it is equally relevant.

- **Chapter 4** includes an overall discussion of the results obtained throughout this Thesis.

- **Chapter 5** points out the main conclusions of the Thesis.

- **Chapter 6** briefly outlines some future perspectives.

- **Chapter 7**: the *Curriculum Vitae* is enclosed at the end of this dissertation.

Please note that a specific chapter devoted to an "Experimental Section" is not listed in the UAB Guidelines for the presentation of a PhD dissertation as a compilation of peer-reviewed articles. Nonetheless, I would like to point out that the experimental details for each work are given in the corresponding papers (see Chapters 2 and 3). Although the fundamentals of each technique are not described in the Thesis, we consider that they can be found in advanced textbooks.

Table of Contents

Chapter 2: Compilation of articles

Chapter 3: Further insights

Chapter 4: Discussion

Chapter 5: Conclusions

Chapter 6: Future Perspectives

Chapter 7: Curriculum Vitae

01

Introduction

1.1 Magnetic materials

All materials, in the presence of an **applied magnetic field** ($\mathbf{H_{applied}}$), respond to it in one way or another, with more or less intensity. The magnetic moment, **m**, of an isolated atom originates from the intrinsic spin of the electrons and the orbital movement of the electrons around the nucleus. For an individual electron, its magnetic moment is:

$$\mathbf{m} = -\frac{\mu_B}{\hbar}(\mathbf{l} + 2\mathbf{s}) \ \ (\text{eq. } 1)$$

Where **s** is the intrinsic spin, **l** the orbital angular momentum, μ_B the Bohr magneton (μ_B = 9.27×10^{-24} JT^{-1}) and $\hbar$ is the reduced Plank constant ($\hbar$ = 1.055×10^{-34} Js). In an atom within a solid, the net magnetic moment depends on the configuration of and the interaction between the electrons. The net magnetic moment per unit of volume is the so-called **magnetization** (**M**). Specifically, in the presence of an external field $\mathbf{H_{applied}}$, materials can suffer from a reorganization/reorientation of spins, generating an induced magnetic field termed "**magnetic induction**" (**B**). In free space, both fields are related each other as follows:

$$\mathbf{B} = \mu_0\mathbf{H_{applied}} \ \ (\text{eq. } 2)$$

where μ_0 is the free space permeability (μ_0 = 4π x 10^{-7} N·A^{-2} in units of the international system (IS) or μ_0 = 1 in the Centimeter-Gram-Second (CGS) system). The permeability (μ) can be understood as the ability a material has to arrange its spins in the presence of an $\mathbf{H_{applied}}$. Thus, eq. 2 slightly changes when dealing with materials[1]:

$$\mathbf{B} = \mu_0(\mathbf{H} + \mathbf{M}) \ \ (\text{eq. } 3)$$

Note that now **B** is a function of **H** (not of $\mathbf{H_{applied}}$), which is often called internal magnetic field, and **M**. Moreover, Eq. 3 turns to be:

$$\mathbf{B} = \mu_0(\mathbf{H} + 4\pi\mathbf{M}) \ \ (\text{eq. } 4)$$

in the CGS system of units. Applying the relationship[2]:

$$\mathbf{M} = \chi\mathbf{H} \ \ (\text{eq. } 5)$$

Eq. 4, results in:

$$\mathbf{B} = \mu_0(\mathbf{H} + \mathbf{M}) = \mu_0\mathbf{H} + \mu_0\chi\mathbf{H} = \mu_0(1 + \chi)\mathbf{H} = \mu_0\mu_r\mathbf{H} = \mu\mathbf{H} \ \ (\text{eq. } 6)$$

Where μ_r is the relative permeability, μ is the material permeability and χ is the magnetic susceptibility.

It is important to highlight that when dealing with materials, **H** is no longer equal to **H**$_{applied}$. Namely:

$$H = H_{applied} + H_d \ \text{(eq. 7)}$$

Its origin resides in the magnetic redistribution in the material, generating an internal magnetic field, which is strongly dependent on the sample shape, called demagnetizing field (**H**$_d$).

Depending on the type of response, magnetic materials can be classified in (**Figure 1**):

- **Diamagnetic** (χ<0 and $\chi\downarrow\downarrow$)
- **Paramagnetic** (χ>0 and $\chi\downarrow\downarrow$)
- **Ferromagnetic** (χ>0, $\chi\uparrow\uparrow$ and χ(**H**), μ(**H**))
- **Ferrimagnetic** (χ>0, $\chi\uparrow\uparrow$ and χ(**H**), μ(**H**))
- **Antiferromagnetic** (χ>0 and $\chi\downarrow\downarrow$)

Diamagnetism arises from the bounded electrons in an atom, which under an external magnetic field undergo Larmor precession, and as a result, a small negative magnetic moment is generated. This induced magnetic field tends to oppose to the external magnetic field ($\chi < 0$). As diamagnetism arises from bounded electrons, all materials present a diamagnetic response to an external magnetic field. However, in some cases, other contributions can overcome the weak diamagnetic signal. Hence, diamagnetic substances are usually composed of elements with orbital shells completed with no unpaired electrons. As it depends on the external magnetic field, diamagnetism vanishes after **H**$_{applied}$ is removed. Contrarily, the magnetic moments in paramagnetic and **ferromagnetic (FM)** materials align with **H**$_{applied}$. In the latter case, the interaction between spins (exchange interaction) is very strong and positive and thus, in the absence of these fields, ferromagnetic materials retain the alignment (exhibit spontaneous magnetization). The exchange energy is defined as follows:

$$E_{exchange} = -2J\mu^2\cos\theta \ \text{(eq. 8)}$$

Where J is the exchange constant (J > 0 in ferromagnetic materials)[3]. Note that if J > 0, the exchange energy minimizes for parallel configurations (θ = 0 degrees).
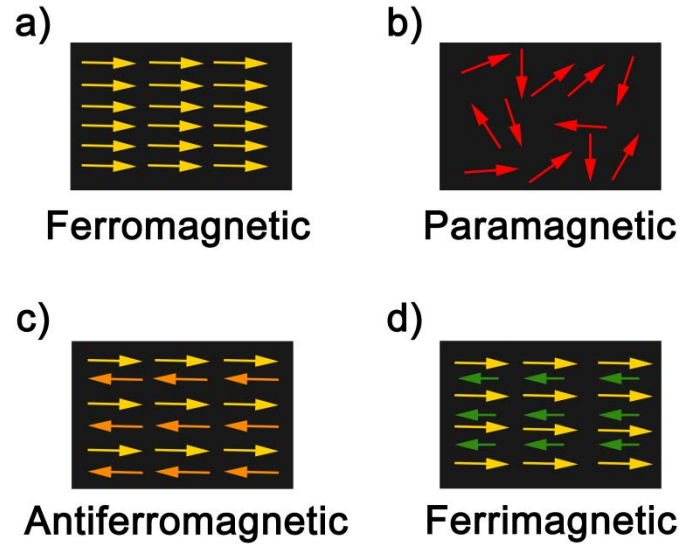
Figure 1: (a-d) Schematic illustration of the spin arrangement in different magnetic materials.

In the case of **paramagnetic** materials, spins tend to align with the external magnetic field generating a small attractive response but, contrary to ferromagnetic materials, the exchange interactions are overcome by thermal fluctuations, so that spins become misaligned in the absence of $H_{applied}$. Thus, no retention of net magnetic moment is found after removal of the applied magnetic field in paramagnetic materials. **Ferrimagnetic** (**FiM**) materials (compounds) behave like ferromagnets with the difference that they are made of two spin sublattices with antiparallel alignment (negative exchange interactions ($J < 0$)) but of dissimilar strength. Upon application of a magnetic field, even if some spins tend to oppose $H_{applied}$, the overall response is not vanished and, therefore, ferrimagnets have a positive net magnetic moment. Finally, like ferrimagnets, **antiferromagnetic** (**AFM**) materials have oppositely aligned spin sublattices ($J < 0$) but in this case providing a total zero macroscopic magnetic moment. The dependence of the magnetization on the applied field is linear, as for paramagnetic materials.

1.1.1 Characterizing magnetic materials: M vs $H_{applied}$ curves or hysteresis loops

By plotting the dependence of the magnetization (**M**) with respect to the external applied magnetic field ($H_{applied}$), some characteristic fingerprints of the magnetic materials arise, determining their potential applications.

A simplified picture to understand the dependence is the one that describes a magnetic material as a collection of small regions called magnetic domains. These domains are strongly dependent on several parameters such as the exchange energy, magnetocrystalline anisotropy (E_{MC}), magnetostatic energy (E_{MS}) and, also, an energy term which depends on the external applied field ($E_{H_{applied}}$ or Zeeman energy). Magnetocrystalline anisotropy arises from the spin-orbit and electrostatic crystal field. In systems with uniaxial symmetry, magnetocrystalline energy can be expressed as a series expansion[3]:

$$E_{MC} = K_1 \sin^2 \theta + K_2 \sin^4 \theta + \cdots \ \ (eq. 9)$$

where K_1, K_2... are the anisotropy constants and θ is the angle between the magnetization and the crystal axis. The magnetostatic energy stands for the self-induced energy, which is expressed as follows:

$$E_{MS} = \int_V \ \mathbf{M} \cdot \mathbf{H_d} \ dV \ \ (eq. 10)$$

This term is the responsible of the shape anisotropy, since the demagnetizing field is strongly dependent on sample's shape. Finally, the external magnetic field provides an energy to the system[2] described by eq. 11:

$$E_{H_{applied}} = -\mu_0 \int_V \ \mathbf{M} \cdot \mathbf{H_{applied}} \ dV \ \ (eq. 11)$$

Sweeping the external magnetic field from one value to another will make the energy balance among all these contributions to be different, giving rise to the hysteretic character of ferromagnetic and ferrimagnetic materials (**Figure 2a**). In the case of diamagnetic, antiferromagnetic and paramagnetic materials, they all present a linear **M** vs. **H$_{applied}$** behavior with different slopes. Some important parameters that can be extracted from a hysteresis loop are: saturation magnetization (M_S), remnant magnetization or remanence (M_R), the so-called squareness ratio (M_R/M_S) and coercivity (H_C). The first term accounts for the magnetization achieved by a material when all the moments are aligned with the direction of the applied field. Remnant magnetization is the magnetization that is kept after saturation when **H$_{applied}$** is brought back to zero. H_C accounts for the magnetic field necessary to suppress the net remaining magnetization in the material (**Figure 2b**). Another important parameter parameter is the **Curie temperature** (T_C) that is the temperature at which a ferromagnetic or ferrimagnetic material becomes paramagnetic, or the **Néel temperature** (T_N) which is the same concept for the case of antiferromagnetic materials.
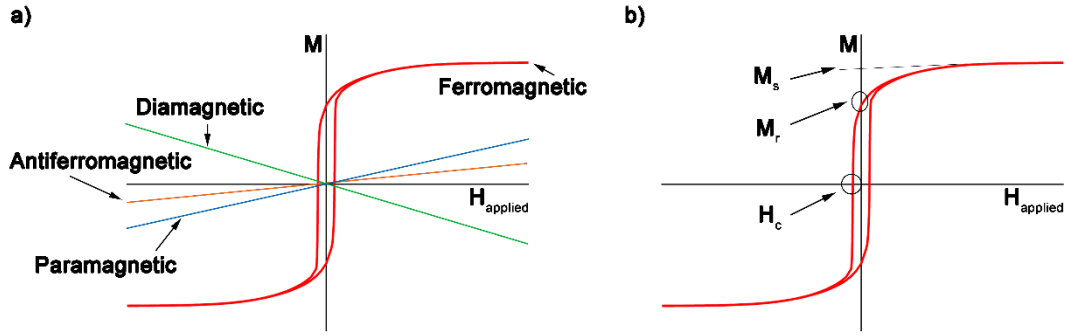
Figure 2: M vs H$_{applied}$ dependence for different magnetic materials. Slopes in diamagnetic, antiferromagnetic and paramagnetic materials have been magnified with the aim to exemplify their response, since ferromagnetic magnetization is several orders of magnitude larger.

1.2 Applications: Magnetic recording and spintronics

Magnetic materials are essential in our daily life. They are broadly employed in a wide range of devices and applications. In fact, one can get surprised from the extent of processes and applications where they are used. Just summarizing, we can find them in home devices (TV, phone, speakers, fridge, microwave…), in medicine treatments and diagnosis (magnetic resonance imaging, drug delivery, hyperthermia…), in data storage devices (computers) or in power generation plants, among others (**Figure 3**). In most previous examples, the magnetic materials properties remain invariantly. In other words, the magnetic properties of each magnetic element are not modified during the desired application process. However, in magnetic storage data devices, magnetization direction and sometimes other magnetic parameters such as coercivity (like in thermally-assisted switching), have a dynamic function i.e change during its operation.

Traditionally, digital information has been stored in magnetic tapes. These tapes, which have a 2D configuration are normally produced by embedding magnetic nanoparticles in a polymeric matrix. Initially, the media is in a demagnetized state, i.e., all the magnetizations of the individual magnetic domains are randomly distributed. As long as the demagnetized tape passes through the proximity of a recording head, magnetic recording is achieved by an external local magnetic field (**Figure 4a**). The written bits are stored in-plane, which makes them strongly dependent on microstructure, grain size, dispersion and chemical environment. As it is strongly important to minimize noise sources arising from, for example, dipolar interactions between domains, the achieved density of information is

limited. This configuration was widely employed in the field of Audio and Video recording technology although the density of information achievable is not so high.

Figure 3: Examples of daily objects that contain and employ magnetic materials. Icons designed by Freepik and Vectors Market on www.flaticon.com under 3.0 creative commons license.

Fortunately, with the span of new synthesis technologies, higher and higher densities have been achieved and novel approaches have been implemented like the production of perpendicular aligned bits. Conventional hard drive massive data storage devices are currently composed of many magnetic single units where information is stored. These bits are made of high magnetic anisotropy and high coercive field materials with the aim to provide stability to the stored data. Each of these bits can have the dipole moment up or down, generating the information bits (e.g., 1=Up or 0=Down) (**Figure 4b**).

However, information is not stored permanently, it is dynamically changed. In these devices, magnetic switching is conventionally achieved by locally applying an external magnetic field. With the span of new lithographic processes, denser and denser arrays of bits have been obtained. However, if a bit is too small, it becomes more sensitive to thermal fluctuations ($\approx K_B T$), thus boosting the need for materials with higher and higher magnetic anisotropy. At the same time, if the magnetic anisotropy is exceedingly high, the local magnetic field needed to flip the bit is also increased significantly, thus making its technological application difficult and energetically more costly. Instead of applying higher external fields, magnetic switching is sometimes assisted by locally heating the magnetic

bit with a laser, which drastically reduces the magnetic anisotropy energy and the coercivity (thermally-assisted writing). Hence, in such a case, the properties of the magnetic material are not invariant but purposely made to vary, in order to achieve an optimized performance.

With the aim to improve magnetically-actuated devices' performance, an intense research on magnetic manipulation has been carried out during the last decades. In the late 80's, it was discovered that different resistances values were obtained by currents passing through multilayers composed of alternating ferromagnetic and non-magnetic conductive layers depending on their relative magnetic orientation (giant magnetoresistance (GMR))[4]. With this discovery, spin was introduced as a new degree of freedom in the world of electronics, opening a new field called spin electronics or spintronics. This discovery boosted the performance of devices like hard drives and magnetic random-access memories (MRAMs) introducing components like spin-valves.

The working principle of MRAMs is a bit more complex but with the improvement of lithographic processes, they also have benefited from denser arrays of bits. MRAMs are composed of tunneling junctions which at the same time are built of a free ferromagnetic layer, a spacer layer (in this case an oxide, not a metal), a pinned ferromagnetic layer, a pinning layer (antiferromagnetic) and sandwiched between the word lines (bottom) and bit lines (above) which are used to provide the effective magnetic fields to tailor the orientation of the free and pinned layers (**Figure 4c**). Its working principle is also based on magnetoresistive effects: by analogy to GMR (as described above but for the case of metallic spacers), there exists the tunneling magnetoresistance (TMR) when the spacer is an insulating layer. The magnetoresistance effects arise from the spin nature of magnetism. When the free layer and the pinned layer are both parallel, the electrons crossing the tunneling junction encounter less resistance (0-bit) than when both layers are antiparallel, which promotes a high resistance state (1-bit). The free layer can be flipped externally by assistance of an external magnetic field. However, magnetic fields cannot be applied in a simple manner to a single tunneling junction without affecting the neighboring memory units. This represents a limiting factor of conventional magnetic actuation procedures. Remarkably, in the 2000's, scientists realized that when a spin-polarized current pass through a thin ferromagnet whose magnetization presents some tilt with respect to the spin direction of the electrons, a torque is transferred from the current to the magnetization itself and thus, magnetization switching can be achieved without the need of external magnetic fields (spin-torque effect). This phenomenon

increased the selectivity in the bit's flip while reducing the overall electric power consumption during the magnetization reversal process[5].

This helped to produce more efficient read-heads in data storage devices. However, both writing and reading processes are again current-mediated and, thus, the dissipation of energy in the form of heat (Joule heating effect) is still present, thus conditioning the efficiency of devices.
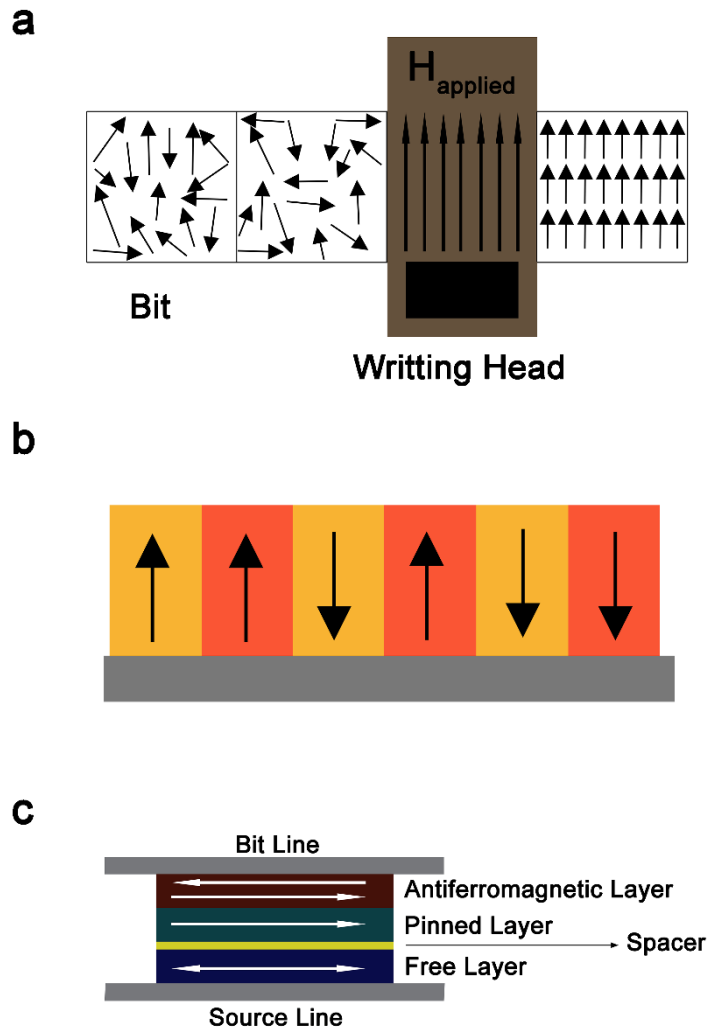

Figure 4: Scheme of a) magnetic tape, b) hard-disk memory and c) a tunneling junction of a MRAM.

1.3 Electric-field control of magnetism

Even though device performance has improved over the years, electric currents are still the main way to manipulate magnetic elements in memory devices, with the unavoidable energy loses by heat dissipation (Joule Effect, eq. 12):

$$P = VI = RI^2 \quad \text{(eq. 12)}$$

In parallel to the development of current-based magnetic manipulation strategies, alternative procedures have been envisaged to produce even more efficient devices. One of these approaches is the **electric-field (E-field) control of magnetism** (i.e., manipulation of magnetism using voltage). Recently, some works predicted a reduction in the energy consumption by a factor 500 by replacing current-based by electric field magnetic actuation[6]. For that, a tunable, strong and non-volatile magnetoelectric (ME) coupling is required.

Under E-field application, some magnetic materials can suffer a modification of their magnetic response. Generally speaking, it is possible to classify the ME phenomenology in: *strain-mediated*, *charge accumulation* and *redox processes.* The origin of these phenomena is complex and, usually, two or more effects may occur simultaneously[7].

The most promising magnetic materials to be modified by means of E-fields are the so-called **multiferroics** (MFs). Basically, there are two kinds of multiferroic materials: single-phase or 'intrinsic' (s-MFs) and composite multiferroics (c-MFs). In general, s-MFs are materials which possess two or more ferroic orders (i.e. (anti)ferromagnetic, ferroelectric and/or ferroelastic) which are mutually and intrinsically coupled. This means that under magnetic field application, a ferromagnetic + ferroelectric material (from now on, simply multiferroic, even being a more general concept) will suffer an internal electric polarization change (direct magnetoelectric effect) while, by application of an electric field, its magnetic response will be altered (converse ME effect).

$$\Delta P = \alpha \Delta H_{applied} \text{ or } \Delta E = \alpha_E \Delta H_{applied} \quad \text{(eq. 13)}$$

$$\Delta H_{applied} = \alpha_{-1} \Delta E \quad \text{(eq. 14)}$$

Where P is the electrical polarization, E-field is the electric field, **$H_{applied}$** is the applied magnetic field, α_E is the direct magnetoelectric coefficient and α_{-1} is the converse magnetoelectric coefficient.

In spite of the pioneering studies about one century ago, it was not until the last years that s-MFs materials have been deeply studied by scientists, prompted by the development of novel syntheses and technologies[8,9].

Although it could be thought that single phase multiferroics are the ideal candidates to be implemented in voltage-controlled devices (due to its intrinsic ferroelectric and ferromagnetic coupling[10]), s-MFs are scarce[11], with weak magnetoelectric coupling, and most of them present Curie temperatures far below room temperature.

In the case of composite multiferroics, none of the counterparts present an intrinsic magnetoelectric coupling but each of them possesses one of the ferroic orders. Contrary to s-MF[10], the coupling is usually mediated by elastic interactions in most of the c-MF:

$$\text{Direct ME} = \frac{\text{Magnetic}}{\text{Elastic}} \cdot \frac{\text{Elastic}}{\text{Electric}} \text{ (eq. 15)}$$

$$\text{Converse ME} = \frac{\text{Electric}}{\text{Elastic}} \cdot \frac{\text{Elastic}}{\text{Magnetic}} \text{ (eq. 16)}$$

In other words, in c-MFs, when voltage is applied to the piezoelectric counterpart, it subsequently deforms and such induced strain is transmitted to the ferromagnetic counterpart in which magnetic changes can occur due to the inverse magnetostriction effect. In this case, although the coupling is achieved extrinsically via strain, strong ME couplings at room temperature can be readily achieved. However, the obtained magnetic changes are volatile since they disappear upon strain removal.

1.3.1 Strain-mediated magnetoelectric coupling

Strain-mediated composite multiferroics opened the door for successful voltage control of magnetic parameters, such as magnetic anisotropy, coercivity or even phase transitions[12]. Pioneering studies stating magnetoelectric coupling between $BaTiO_3$ and $CoFe_2O_4$ were reported back in the seventies[13]. Since then, huge efforts have been made in the study of magnetoelectric effects in bulk composites[14]. It was with the development of new synthesis methods that much control has achieved. Note that the coupling is strongly dependent on the amount of structural defects, residual strain, and clamping effects. More recently, Sahoo and co-workers[15] demonstrated the intrinsic dependence of the magnetic properties of a 10 nm thick BCC Fe film grown on a (100) $BaTiO_3$ (BTO) substrate on the strain transferred from the substrate to the thin film under thermal phase transitions. BTO

is a ferroelectric material which presents several structural transitions: from cubic to tetragonal at 393 K, tetragonal to orthorhombic at 278 K and an orthorhombic to rhombohedral structural transition at 190 K. Due to these crystallographic changes in the substrate, it is easy to understand that under cooling/heating, different strain configurations can be transferred to the BCC Fe layer. As demonstrated in the work, changes up to 120 % in the in-plane coercive field and 33 % in the $\Delta M_r/M_s$ were obtained during the orthorhombic to rhombohedral transition. The authors also demonstrated that, thanks to the piezoelectric properties of the BTO, it was possible to tune coercivity up to 20 % for electric field above the ferroelectric coercive field [max applied E-Field of ±10 kV/cm] in the tetragonal phase. Another example of strain-mediated voltage control of magnetism is that presented in reference 16 which involves the metallic equiatomic FeRh alloy. Here, one can take advantage of the lattice parameter dependence of the AFM-FM first-order transition in FeRh. A 25 K shift is achieved in the transition due to the strain transmitted from the $BaTiO_3$ substrate upon voltage application. The symmetry presented with the E-field confirms the strain nature of the phenomenon. However, some density-functional simulations demonstrate that upon electron injection, the FM phase of FeRh tends to stabilize at the expense of the AFM phase, thus demonstrating that even if the strain-effects are high, pure electric field effects cannot be neglected.

In spite of the satisfactory results summarized above, strain-mediated ME effects are ultimately governed by the interface between both constituents, determining the strength of the coupling. Not only lattice mismatch plays a detrimental role on the coupling but also the nature of the ferroelectric counterpart. Since most of the ferroelectric substrates are oxide-based, a partial oxidation of the interface is unavoidable when depositing metals on top[17]. This worsens the quality of the interfaces and, hence, the ME coupling[18,19]. Moreover, long operation times can lead to fatigue-induced failure at the interfaces. An additional problem is that if the c-MFs are grown onto a substrate in the form of thin films, the mechanical clamping with the substrate limits the amount of achievable strain, hence the strength of the induced magnetoelectric effect. Conversely, if the substrate itself is used as piezoelectric material, then due its relatively large thickness, large voltages need to be applied in order to attain reasonable electric fields (since the electric field is inversely proportional to the thickness of the insulator).

Finally, even though many studies exploit the magneto-elastic coupling, many of the employed substrates, besides being piezoelectric, are also ferroelectric. Remarkably, in the interface between an insulator and a metallic ferromagnet, charge accumulation can occur, giving rise to the so-called charge-mediated ME effect. However, since all ferroelectric

materials are piezoelectric as well, combined effects are likely to occur, entangling each contribution[7,20-22].

1.3.2 Charge-mediated magnetoelectric coupling

Ferromagnetism in diluted magnetic semiconductors (DMS) like (In, Mn)As is known to be hole-mediated. Specifically, Mn substituting In provides localized magnetic moments. Additionally, due to its acceptor nature, Mn also provides holes which bridge ferromagnetic interactions. Density functional theory (DFT) calculations have demonstrated that Mn exhibits an AFM order in first neighbor interactions, i.e., in absence of holes, hence the whole system behaves antiferromagnetically. Thus, it seems logical to think that, by injecting electrostatic charges, a long-range FM order might be achieved, opening the possibility of an electric control of ferromagnetism. This was first demonstrated by H. Ohno, who in 2000[23] was able to isothermally tune the Curie temperature of (In, Mn)As thin films with voltage. A few years later, in 2003, people from the same group were successfully able to electrically switch and demagnetize thin films of similar composition in the presence of a small external field[24]. By taking advantage of the ± 1.5 K change in T_C after ∓ 1.5 MV/cm application, (**Figure 5a**), the authors are able to switch the magnetization using combined electric and magnetic fields. To do this, the authors first saturated the sample (point 1 in **Figure 5b**). Afterwards, a negative field smaller than the coercive field of the sample at 0 V but higher than that of the biased sample (point 2) was applied. After, the application of the electric field reduces the coercive field, reversing the magnetization (point 3).
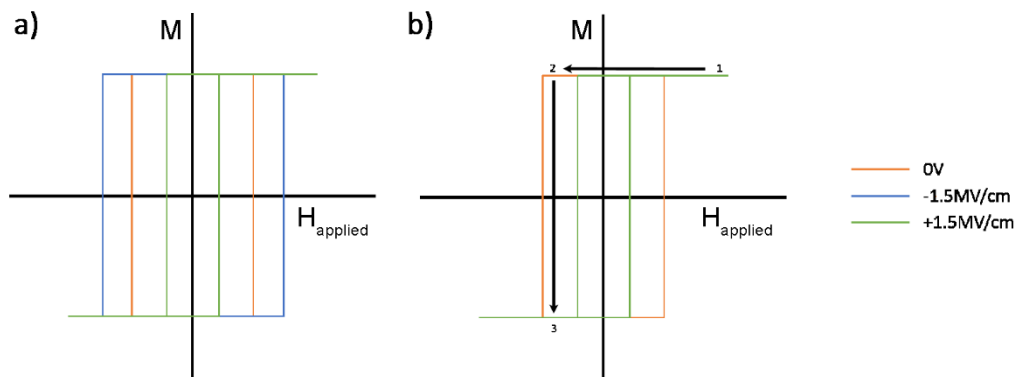

Figure 5: a) Hysteresis loop of (In,Mn)As at 40 K upon different electric fields, b) switching steps scheme. Adapted from reference 23.

Other systems, such as the Mn_xGe_{1-x}, which also show hole-mediated ferromagnetism were also studied. Interestingly, in this system, T_C increases up to 116 K for a 3.5 % Mn content, which is a 130 % higher than in the case of (In, Mn)As. Here, the authors were able to achieve on-off magnetization switching with only ±0.5 V. Boukari *et al.* predicted and successfully demonstrated a higher tuning in carrier mediated II-V group DMS, such as (Cd, Mn)Te, with a small bias of ± 0.7 V. However, the measurements were carried out at much lower temperatures[25]. Not only H_C and T_C parameters have been successfully controlled by voltage but also magnetic anisotropy[26,27]. Other semiconductor systems with higher T_C were also successfully manipulated under voltage application[28].

Importantly, in 2011, Yamada and colleagues successfully modified by means of voltage application the paramagnetic properties of a DMS with a T_C close to room temperature, and, therefore, induced a ferromagnetic moment at room temperature[29]. The authors were able to control the magnetic properties of Co-doped TiO_2 epitaxially grown on top of $LaAlO_3$. In this system, the magnetoelectric mechanism is also the mediation of carriers. However, contrary to (In, Mn)As, magnetic properties of this DMS instead of being hole- are electron-mediated.

An important milestone was achieved in 2007 when Weisheit and co-workers[30] found that, upon voltage application, the coercivity of ultrathin metallic ferromagnets could be tuned with voltage. Specifically, changes in coercivity up to –4.5 % and +1 % were obtained in 2 nm thick FePt and FePd $L1_0$ films, respectively. The authors explained the effect in terms of charge accumulation, which causes changes in the magnetic anisotropy energy (MAE). As the ferromagnetism arises from unpaired 3d electrons with energies close to Fermi energy and assuming that the MAE change depends in first approximation on the excess of electrons, changes in the MAE up to –200 % in FePt and +70 % in FePd were theoretically predicted. These values are in agreement with the reported experimental values. Further experiments carried out by the authors demonstrated a reduction on the response in thicker films (only changes of –1 % and no effect was observed for samples of 4 nm in thickness), evidencing the thickness-dependence of the effect, which can be understood bearing in mind that electric field in metals is confined at the surface of the material, within the so-called Thomas-Fermi screening length, which is < 1 nm). Importantly, the work by Weisheit and co-workers was the first result showing charge-mediated magnetoelectric effects in metals, not only in semiconductors, as in previous studies. The interfacial nature of this phenomenon in metallic films is related to the electric screening length of metals, typically of a few unit cells[31]. For this reason, the studied materials are typically in the form of ultrathin films, to enlarge the surface-to-

volume ratio. Changes in the coercive field have also been reported in FePt[32] and Fe[33], as well as in CoFeB in CoFeB|MgO tunnel junctions. Changes in the MAE have been also reported for CoSi[34], while voltage-driven variations in T_C have been observed in Co[35,36].

For applications, perpendicular magnetic anisotropy (PMA) is often requested since, among other advantages, it allows for a larger magnetic density packing (i.e., enhanced areal density of information). Maruyama *et al.*[37] prepared Fe deposits on top of Au in a layer-by-layer growth with PMA. Within this geometry, upon ±200 V application a maximum change in the PMA of 40 % was achieved. The authors attribute this change to the influence an electric field has on the Fe electron occupancy, taking advantage of the strong out-of-plane hybridization (spin-orbit coupling) between Au and Fe. These experimental results were in agreement with the theoretical predictions of Nakamura and co-workers[38]. Another system of interest is the CoFeB|MgO|CoFeB in which a much larger magnetoresistance has been reported when compared to the Fe|MgO|Fe. Wang *et al.*[39] found that PMA is achieved for a MgO barrier thicker than 1 nm. In that case, as in the previous work of Maruyama, a modification in the PMA was expected during voltage application. In the as-prepared sample, the magnetic switching occurs at 20 Oe and 125 Oe for the top and bottom layer, respectively. Upon application of –1.1 V, the upper/bottom layer shows a reduced/increased switching field. When +1.1 V are applied to the system, the behavior of the system inverts, i.e. the switching field of the upper layer increases whereas that of the bottom layer reduces. This opposite behavior with the sign of voltage is reasonable since charge is accumulated at both interfaces.

E-field control of PMA in other systems such as Fe, FeCo, CoFeB, FePd, FePt, Co|Pd multilayers has also been explored[40-46].

Domain wall motion has also been studied systematically under E-field actuation[47]. For example, Liu and co-workers demonstrated that under voltage application domain wall propagation velocity could be either increased or reduced[48]. Not only they were able to tune the propagation velocity but also they showed that nucleation and propagation of domains became altered. Specifically, under positive bias more nucleation centers appeared, in agreement with a previous work from Herrera *et al.*[49].

Very recently, magnetic properties of a 3 nm thick $La_{0.74}Sr_{0.26}MO_3$ film were modified exploiting its capacitive and pseudocapacitive behavior[50]. The film exhibits a T_C around 246 K, which can be shifted by 14 K under electric field application ($|\Delta V| = 1.7$ V). Thus, in measurements carried out at 235 K, a transition from ferromagnetic to paramagnetic behavior was achieved. Even further changes could be obtained measuring at 220 K (T_C

shift of 26 K). Interestingly, by increasing the electric field range ($|\Delta V| = 3$ V), not only the paramagnetic state could be recovered but an intermediate change in the magnetoelectric coefficient sign was also observed. Similar results have been obtained for $La_{1-x}Ca_xMnO_3$ (LCMO) samples[51].

1.3.3 Magnetoelectric coupling caused by electrochemical processes

Instead of taking advantage of the strain or charge accumulation, it is also possible to take profit of changes in the oxidation state of a ferromagnetic material induced with an externally applied voltage. These systems have gained huge interest recently due to the non-volatility of the achieved effect. Electrochemical processes also overcome one of the main drawbacks of charge accumulation effects in metallic films (i.e., the limited range of the phenomenon due to the electric field screening length). One of the drawbacks of electrochemical processes is, nevertheless, that the induced magnetoelectric effects are not instantaneous.

Broadly, voltage control of magnetism due to electrochemical processes can be classified in two main effects: *magneto-ionics*, in which the diffusion of mobile charged ions plays a major role (this includes lithiation)*, and redox reactions*. Since lithiation (Li^+ ion migration) has gained importance in the last years and has established as a domain field itself, it is discussed separately.

1.3.3.1 Magneto-ionics

Magneto-ionics has mostly relied in exploiting migration of oxygen species in a candidate material. Specifically, it is the effect in which oxygen diffuses back and forth from an oxygen source towards/backwards the magnetic material, especially when high O^{2-} mobility materials are used (i.e. HfO_2 or Gd_2O_3).

For example, in the work by Bi *et al.*[52], the magnetic anisotropy was controlled by the reversible oxidation of a 0.7 nm thick Co film adjacent to an 80 nm thick Gd_2O_3 layer. In this paper, the authors took advantage of the PMA arising from the Co 3d – O 2d orbital hybridization. In the as-prepared sample, the system presented a strong PMA which

vanished after the application of –5 V during 6 min. Not only the PMA was suppressed but also the in-plane magnetization, suggesting that under E-Field application O^{2-} diffused towards the Co turning the continuous films into a matrix of CoO_x with superparamagnetic cobalt. Interestingly, the initial state was recovered upon positive bias application (+ 5V for 13 min). If the positive bias was extended over time, the system turned from out-of-plane towards in-plane anisotropy suggesting oxidation at the interface. These results were further supported by X-ray absorption (XAS) measurements. In the as-prepared XAS spectra, a main contribution of metallic cobalt was obtained together with a small shoulder, corresponding to CoO. Upon negative bias, the CoO shoulder increased until it became a predominant peak while, at the same time, Co almost vanished. This was further corroborated by the X-ray magnetic circular dichroism (XMCD) signal suppression. In measurements in which positive voltage application was left for longer times, almost a metallic signal was obtained. In the work of Uwe Bauer and coworkers[53], electron energy loss spectroscopy (EELS) signal of oxygen was successfully monitored in-situ after biasing, confirming the oxygen source/sink behavior of Gd_2O_3. Moreover, they also demonstrated that, at RT, diffusion of oxygen is limited and non-uniform in contrast to a more homogeneous diffusion after biasing at 100 °C. Over time, the authors were able to suppress the PMA evidencing cobalt oxidation. These features were exploited to employ the magneto-optic Kerr effect (MOKE) microscope laser to locally heat assist and thus locally tune the PMA. By only increasing temperature by 20 °C (power increase of MOKE laser from 1 to 10 mW), successful voltage control was achieved. A deeper knowledge on the underlying mechanism was provided by Gilbert and coauthors[54] who studied, by polarized neutron reflectivity (PNR), first order reversal curves (FORC) and XAS, the magneto-ionic effects induced in a 15 nm Co film grown over 2 nm of GdO_x and 1 μm of Al_2O_3. Upon an electrothermal treatment (+40 V/230°C/15 min), PNR results showed a broadening of the GdO_x|Co interface which expanded over more than 10 nm (over the 15 nm of the total thickness). It also showed some changes in the Al region suggesting O transport from the alumina and gadolinium oxide layers towards Co. PNR results also evidenced a decrease in the magnetization close to the surface (up to 80 %) which lowered towards the bulk (decrease of 38 %), in agreement with magnetometry results, which showed a decrease in M_R and H_C of 68 % and 55 %. FORC and XAS measurements revealed the formation of a secondary phase (when comparing to the as-prepared FORC distribution), in line with the appearance of 2 peaks in the XAS spectra located at 779.2 and 776.8 eV, characteristic of CoO. The reversibility of the process was also studied, and some interesting conclusions were given. PNR results showed that upon negative bias, magnetization could be recovered up to 90 %. PNR also provided evidence for the

metallization of the interface between cobalt and gadolinium oxide. This metallic underlayer screens the electric field deeper in the Co film, thus representing a practical limit. The magneto-ionic control of magnetism has also been exploited to tune H_C, PMA, domain wall motion, M_S and T_C[55-58].

In spite of the successful voltage control of the magnetic properties, the above strategies and measurements have been performed above RT in order to promote oxygen diffusion, hence limiting potential use in actual devices and decreasing the energy efficiency of the process.

1.3.3.2 Redox reactions

Another approach which has been lately exploited to tune magnetism is through redox reactions. Using this concept Di and co-authors were able to controllably tune the anisotropy of an ultrathin layer of Co grown on top of Au/Si substrate[59]. With application of –1.16 V with respect to a mercury/mercury sulfate electrode, oxidation occurs. As mentioned above, the anisotropy of cobalt strongly depends on the degree of hybridization with oxygen and, thus, an in-plane/out-of-plane transition can be achieved. A more negative bias (–1.34 V) was necessary to reverse the process until its initial state. Redox effects in Fe thin film have been also studied employing different KOH and NaOH electrolytes[60,61].

Huge changes of around 200 % have been achieved under bias application in 0.1 M $LiClO_4$|dimethyl carbonate and ethylene carbonate to a CoPt sample. Authors ruled out the origin of the effects to be a direct consequence of electrochemical charging but to a pronounced oxidation/dissolution process[62]. Leistner *et al.* found similar results by employing 1M $LiPF_6$ in the same mixture of solvents in a sample of FePt. In a posterior work, they took advantage of controlled oxidation process to tune the magnetic anisotropy up to a 25 %[63,64].
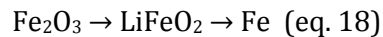
1.3.3.3 Lithiation

Many transition metal oxides have been postulated as excellent materials in Li-ion batteries, due to their large ability to incorporate charge into their lattice. Specifically, Co_3O_4 and Fe_3O_4 are able to incorporate up to 6 Li atoms[65]. Zhang *et al.* took advantage of

lithiation process to induce, in a reversible fashion, ferromagnetism in an electrode composed of nanoparticles of α-Fe_2O_3. Upon lithiation, the following reaction takes place:

$$Fe_2O_3 + 6Li^+ + 6e^- \rightleftarrows 3\ Li_2O + 2Fe \quad (eq.\ 17)$$
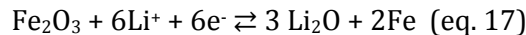
resulting in a sample enriched in iron, which enhanced the ferromagnetic response of the electrode. The magnetic response was followed by structural changes where an intermediate $LiFeO_2$ phase appeared on increasing the applied electric field.

$$Fe_2O_3 \rightarrow LiFeO_2 \rightarrow Fe \quad (eq.\ 18)$$

The authors demonstrated the reversibility and stability of the process upon voltage cycling. In another work, the authors studied two spinel ferrites systems, $CuFe_2O_4$ and $ZnFe_2O_4$[66]. Upon lithiation magnetization decreases up to 50 % and 70 % respectively. In the first system, it was believed that Li reduced Cu from Cu^{2+} to Cu^0, supressing the magnetic interaction between Cu^{2+}-O-Fe^{3+}. In the second system, additional pure charge effects needed to be taken into consideration, according to the authors. $MnFe_2O_4$[67], Fe_3O_4[68], α-$LiFe_5O_8$[69] have also been recently explored for lithiation purposes. Notice that lithiation also involves a transfer of electrons (i.e., a 'pure' redox reaction), but the major effect on the magnetic properties of the material is caused by the migration of lithium. This is way lithiation is typically classed into magneto-ionic phenomena.

1.4 Magnetoelectric characterization: How to apply an electric field while measuring the magnetic properties?

Magnetoelectric effects by means of charge accumulation or redox processes have been successfully achieved through two main geometries. The first one is the field effect transistor (FET) structure, composed of a source electrode, a drain electrode and a gate electrode. This geometry is mostly used to evaluate measurements through resistive Hall Effect. Here the gate voltage is the one that alters the magnetic properties of the ferromagnetic layer, and the current flowing from the source to the drain is the one which is used to track the changes in magnetization. The gate electrode and the ferromagnetic layer are isolated by an insulating layer (dielectric) (**Figure 6a**). Another employed geometry is the condenser-like structure (**Figure 6b**). This is commonly achieved through growing a ferromagnetic material on top of an insulating material. Here the voltage is

applied between the ferromagnetic material and a back electrode grown on the other side of the dielectric part.

The production of solid state devices is strongly hampered by the production of high quality insulating materials as any structural defect will result in pinholes where charge accumulated will leak. As it is still challenging to grow high quality insulating materials, some approaches have appeared to circumvent the drawbacks. The first one is the utilization of insulating polymers such as polyimide (PI) or polyvinyl difluoride (PVDF). The second approach is the employment of organic solvents such as ethylene carbonate, propylene carbonate (**Figure 7**), ionic liquids such as Diethylmethyl(2-methoxyethyl)ammonium bis(trifluoromethylsulfonyl)imide (DEME-TFSI), 1-Ethyl-3-methylimidazolium bis(trifluoromethylsulfonyl)imide (EMIM-TFSI) or the utilization of electrolytes such as $LiPF_6$-ethylene carbonate or $KClO_4$-polytethylene oxide.
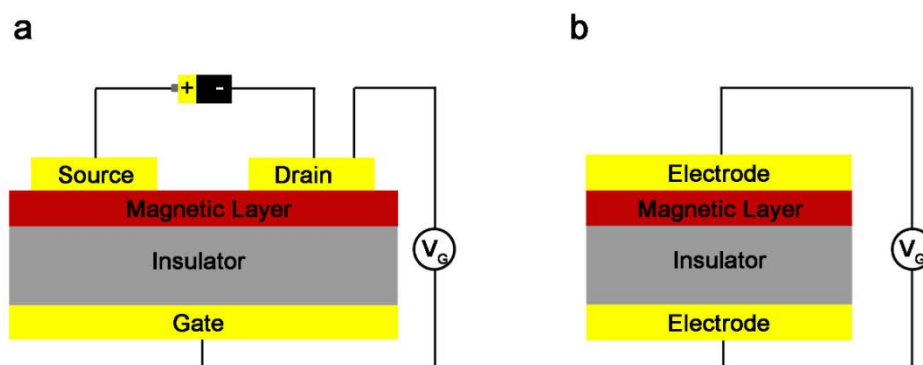

Figure 6: Scheme of the a) field-effect transistor and b) condenser-like geometry employed to evaluate the electric field effect on magnetic materials.

This last approach exploits the occurrence of the so-called electrical double layer (EDL) (**Figure 8**). In the interface between an electrolyte and an electrode, molecules tend to arrange according to the electrode polarization. If the electrode is positively (negatively) polarized, anionic (cationic) species will arrange along the electrode surface. The occurrence of the EDL can be spontaneous since the natural chemical reaction equilibrium between the electrode and the electrolyte leads to a potential difference (open-circuit potential (OCP)). Moreover, this configuration can be rearranged by an external polarization of the electrode. It is important to highlight that the spacing between the electrode and the ions close to the surface is at most of 1 nm and, therefore, the electric fields generated are much higher than those achieved in solid state dielectrics (whose thickness is typically larger).

21
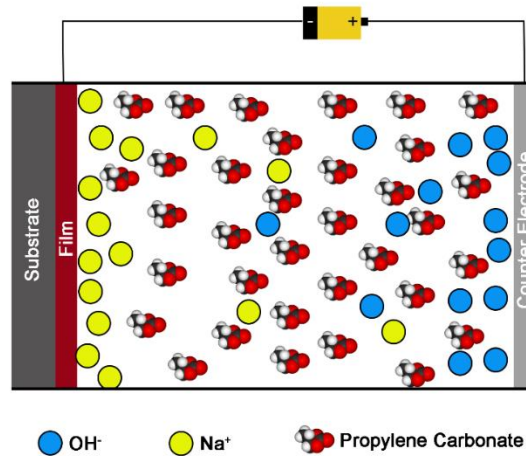
Figure 7: Set-up scheme employed by Weisheit *et al.* to apply electric field. In this configuration, the electric field is applied by forming an electrical double layer of solvated sodium ions in propylene carbonate. Scheme adapted from ref. 30.
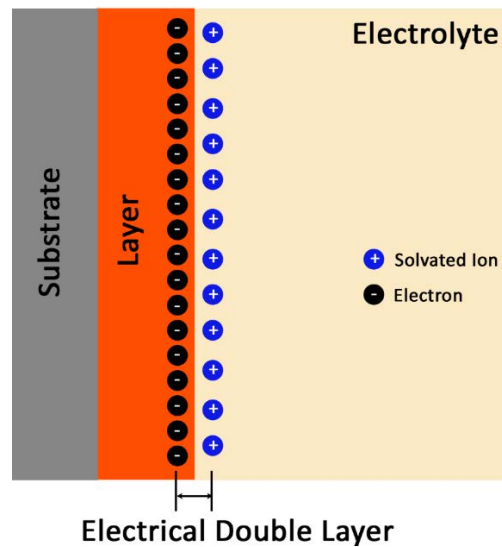
Figure 8: Scheme of the electrical double layer formed at the electrolyte | layer interface

1.5 Interfacial nature of magnetoelectric effects

As it has been demonstrated in the previous sections, all magnetoelectric effects are of interfacial nature. In the case of the multiferroic composites, the response of the heterostructure is governed by the quality of the interface between the ferroelectric and the ferromagnetic layer. In the case of pure magnetoelectric effects, i.e. those governed by modifying the carrier density through charge injection, the effect is limited by the Thomas-Fermi screening length which is smaller than 1 nm in metals and, thus, ultrathin films (few

monolayers) are needed[70]. Furthermore, it is also determined by the quality of the dielectric layer, since charges are accumulated at the interface of the heterostructure. In the case of magneto-ionics, the thickness of the layer does not play an important role, or at least not as important as in pure magnetoelectric effects, but the proper diffusion of oxygen from the adjacent oxygen reservoir determines its effectiveness. Finally, lithiation and 'pure' redox processes overcome thickness limitation of other methods. However, both lithiation and redox reactions are governed by the interface with the electrolyte and thus the effects are supposed to be enhanced in materials with large surface area.

From the abovementioned reasons, it is clear that large surface-to-volume ratio materials are expected to maximize the magnetoelectric response. Thus, suitable candidates to maximize ME effects are porous materials characterized by a huge surface area.

Surprisingly, so far, the study of magnetoelectric effects in porous structures has been widely overlooked, and only few works have tackled this point. One of them is the work by S. Ghosh who studied the charging effect in the magnetic response of a nanoporous electrode[71]. According to the author, the magnetization changes were related to strain induced by the charge accumulated in the surface, and thus due to the magneto-elastic response of the material. Similar studies carried out in 1M KOH electrolytes reported a 4.2% change in M_S in a nanoporous γ-Fe_2O_3-Pt electrode[72]. One plausible hypothesis was that electrochemical reactions in the γ-Fe_2O_3 counterpart could explain the magnetization changes, however further contributions (magneto-elastic or charge) cannot be discarded. Subkow and Fähnle[73] also suggested that the magnetoelectric response in nanoporous materials could induce changes in the MAE in the exposed surfaces.

1.5.1 Porosity: A boost towards energy-efficient magnetoelectric effects

Many materials' properties are interface-governed[74-77]. With the development of nanotechnology, novel nanostructures have led to improved or even new properties, which can be exploited in a myriad of applications such as photonic devices, catalysis, separation membranes, flexible nanoelectronics, sensing, hydrophobic surfaces, batteries, supercapacitors, fuel cells or thermal and acoustic insulators. Among the several novel morphologies, (nano)porosity is one of the most promising features in materials subject to applications where surface governs over the bulk[74,78-80].

Porous materials, according to the International Union of Pure and Applied Chemistry (IUPAC), can be classified into three categories depending on the pore size: macroporous materials are those whose pore size exceeds 50 nm, microporous if the pore size is below 2 nm and mesoporous when pore size lays between 2 and 50 nm. Sometimes the term 'nanoporous' is used instead to broadly refer to materials with pore sizes below 100 nm.

There are several approaches to synthesize porous materials showing either ordered or disordered pore arrangements[81]. For example, nanocasting, like classical casting techniques, takes advantage of a preexisting scaffold to mold the desired material (hard-templating). In the late 90's, Göltner and co-workers mimicked the casting approach to synthesize materials in the mesoporous regime. Specifically, the authors were able to produce mesoporous polymer networks using porous silica as a template[82]. Since then, a lot of work has been done to develop mesoporous organic and inorganic materials in powder form with tunable morphologies (porosity degree, interconnection, arrangement…) through nanocasting[83,84].

Similarly, evaporation-induced self-assembly (EISA) techniques use a soft-template to induce porosity[85]. The addition of a controlled amount, above the so-called critical micellar concentration (cmc), of surfactant into a polar solvent generates supramolecular aggregates (micelles) whose morphology and arrangement can be controlled. When those surfactants are introduced into a solution with the desired precursors, micelles generate voids in the resulting film and therefore, porosity is induced. This procedure is compatible with several deposition techniques such as spin-coating, dip-coating, doctor blading, inkjet printing or spray coating.

In spite of the potential of nanocasting and EISA to synthesize nanoporous materials with controlled morphology (**Figure 9a**), pore size, pore interconnection and composition, typical products are transition metal oxides and when metallic compounds are desired, costly post-synthesis H_2 reduction processes are involved[86]. Moreover, most of the time, several steps are involved (synthesis of the template, impregnation, calcination, selective etching of the template…). Alternative techniques, such as electrodeposition, allows to take advantage of both hard and soft- templating approaches in a more cost-effective way.

1.5.1.1 Electrodeposition of porous materials

Electrodeposition is a functional technique to grow a broad spectrum of materials like metals, oxides, hydroxides and other compounds on a substrate and, therefore, coatings or films of these materials are typically obtained[87-90]. Its cost-effectiveness relies on the fact that no vacuum systems are needed, a wide variety of substrate shapes and varied sizes can be coated, provided that they are conductive, and it can work at room temperature.

Electrodeposition is a chemical growth technique in which the deposition of the material of interest is produced by the reduction of parent ions presents in an electrolyte when electrons are provided to the system (eq. 19):

$$M^{2+} + 2e^- \rightarrow M^0 \text{ (eq. 19)}$$
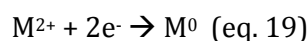
Apart from the working electrode, where the target material is to be deposited, the system is composed of a counter and, eventually a reference electrode (two or three electrode configuration), the latter for a more accurate control of the potential on the working electrode. The sum of the two or three electrodes plus the electrolyte is named as the electrolytic cell.

Interestingly, electrodeposition allows tuning materials' properties by simply modifying the electrodeposition parameters such as potential, pH, temperature, concentration of electroactive species in solution or addition of additives (grain refiners, stress relievers...)[91-93].

There exist several procedures to grow nanostructures by electrodeposition, to name a few: from the synthesis itself, where the growth mechanism can be exploited, such in the case of leave-shaped hydroxides[94]; by taking advantage of the influence of the substrate on the electrodeposition process[95], and by electrodepositing into patterned substrates like e-beam lithographed substrates or templates like anodic alumina or polycarbonate membranes[96]. Furthermore, electrodeposition has also been proved as a powerful technique in the production of porous materials with dissimilar pore sizes.

The Faraday law states that the amount of mass electrodeposited is directly proportional to the charge transferred to the system:

$$m \propto Q \text{ (eq. 20)}$$

However, this relationship takes into account 100 % efficiency in the process. Generally speaking, this law assumes that only the reaction of interest is taking place. However, side reactions can take place, reducing the efficiency of the system. One important side reaction is the hydrogen evolution reaction (HER). In acidic media, HER consists in the reduction of solvated protons to hydrogen gas:

$$4 \ H_3O^+ + 4 \ e^- \rightarrow 4 \ H_2O + 2H_2 \quad \text{(eq. 21)}$$
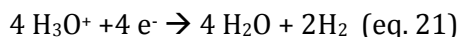
while in alkaline media, the water molecule reduces to molecular hydrogen:

$$2H_2O + 2e^- \rightarrow 2OH^- + H_2 \quad \text{(eq. 22)}$$

HER reaction and the concomitant decrease in the efficiency of the process has been long considered a drawback since it decreased the density of the metallic films and introduced fragility[97]. However, the hydrogen bubbles generated can be used as a soft-templating agent and this concept has been indeed exploited on purpose to produce metallic porous structures[98] (**Figure 9b**). In our Group, by taking advantage of hydrogen co-evolution during cations discharge and by simultaneously playing with different electrodeposition parameters, several morphologies and compositions of macroporous CuNi films were obtained[99]. Several other systems like Pt[100], Au[101], Ag[102], Cu[103,104], Ni[105], Pb[106] or Cu-Sn[108] have also been grown by the hydrogen bubble template deposition approach, giving rise to metallic frameworks with pore sizes in the micrometer range. However, in order to obtain magnetoelectric effects in porous materials, the pore wall must be reduced to a few nanometers and thus overcoming the Thomas-Fermi screening length.
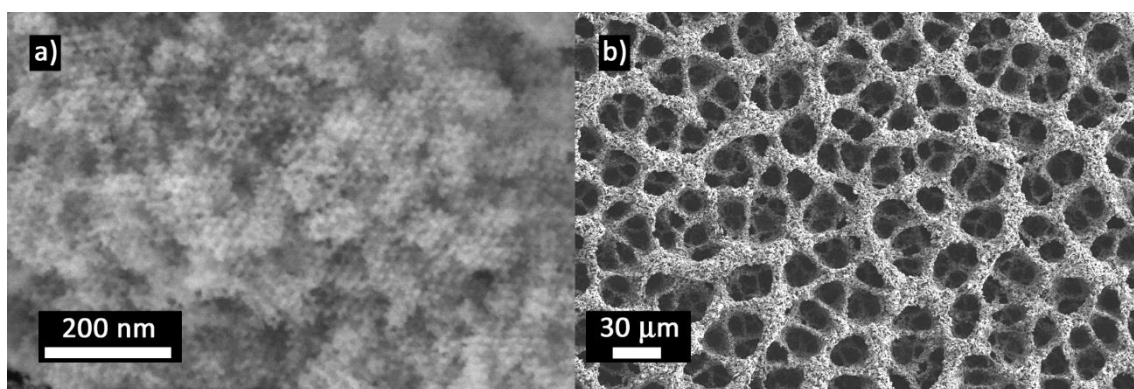

Figure 9: SEM images of a) Nanoporous SnO_2 powder prepared by nanocasting (courtesy of Dr. Junpeng Fan) and, b) macroporous CuNi film synthesized by hydrogen evolution templating electrodeposition (courtesy of Dr. Jin Zhang).

In order to reduce the pore size to the mesoporous regime, hydrogen co-evolution does not work. Alternatively, surfactants can be added to the electrolyte to act as soft-templating agents. This approach tries to mimic the aforementioned soft-templating phenomena exerted by the H_2 bubbles but these are replaced by surfactant micelles. When an amphiphilic surfactant is dissolved in a solvent (typically water) above a certain concentration referred to as the cmc, molecules tend to arrange forming supramolecular assemblies called micelles. These micelles form because of the amphiphilic character of these substances, which contain polar water-soluble groups and water-insoluble hydrocarbon chains in the same structure. At low concentrations, these entities are dispersed within the solvent and lack long range order. However, when the concentration of some surfactants such as amphiphilic block copolymers keeps rising, micelles start to form long-range order structures in solution known as lyotropic liquid crystal (LLC) phases and different metallic mesostructures can be achieved[108]. Examples of amphiphilic block polymers are Poly(ethylene glycol)-block-poly(propylene glycol)-block-poly(ethylene glycol) (Pluronic P123®), or poly(ω-hydroxypoly(ethyleneco-butylene)-co-poly(ethyleneoxide)) (KLE).

In the last few years, several systems have been studied combining electrodeposition and LLC, putting emphasis in the synthesis of mesoporous noble metals such as Pt[109,110], Pd[111], Rh[112] due to its powerful catalytic properties. Several other systems like Co[113], Ni[114,115], Sn[116], Se[117], Te[118], and many others[119] have also been studied. The synthesis of oxides and hydroxides following similar procedures remains less explored and only few works tackle it[93,120-122].

LLC based electrolytes are characterized by having a large viscosity which precludes an efficient stirring of the solution and by presenting complex phase diagrams. Therefore, co-deposition of alloys in LLC media is challenging and thus, scarcely reported[123]. As an alternative, electrodeposition from solutions containing block copolymers whose concentration is above de cmc but below the concentration threshold to LLC phases has been recently reported as a promising approach to synthesize nanoporous alloys. The micelles formed in solution adsorb onto the substrate and the cations coordinated at the outer shell of the micelles get reduced. Thus the micelles act as structure-directing agents[124,125]. Generally speaking, films with higher amount of noble metals like Pt or Au exhibit a better defined mesoporosity. The interaction between the cations and the surfactant has to be sufficiently strong so as to ensure the formation of extended networks at the solid/liquid interface but not too much in order to prevent pore collapse after surfactant removal or displacement. Whilst the affinity between block copolymer micelles

and noble metals is optimum, that between the polymeric micelles and non-noble metals like Cu or Ni may be too weak to form extended frameworks. Therefore, the synthesis of high-quality mesoporous films made of non-noble metals is rather challenging.

1.6 Objectives of this Thesis

This Thesis is mostly aimed at enhancing the magnetoelectric coupling in metallic alloys containing one ferromagnetic element by exploiting sample configurations with maximized surface-to-volume ratios, such as nanoporous samples. By means of introducing porosity, it is also expected to overcome the ultra-thin film regime (1 -2 nm) in which charge-mediated magnetoelectric effects are limited and, thus, induce magnetoelectric effects in samples with thicknesses beyond 1 -2 nm.

To achieve this, we aim to investigate new synthesis routes and thus modify current methods for the preparation of nanoporous materials, which have so far focused on noble-metal based alloys i.e., micelle-assisted electrodeposition.

Moreover, with the aim to obtain magnetoelectric effects in solid state configurations and thus replace electrolyte gating strategies to apply electric field, the prepared nanoporous materials are coated with dielectric materials to obtain condenser-like systems at the nanoscale. Finally, in the framework of magneto-ionics, we will try to exploit structural defects of materials in metal oxide films, such as vacancies and grain boundaries, to enhance ion mobility and allow for room temperature voltage-induced ionic motion. This would overcomes the current need of heat-assistance and the necessity of oxygen sources, such as Al_2O_3, HfO_2 or Gd_2O_3.

See below schematically the different objectives of this Thesis:

- Enhancement of the magnetoelectric coupling in metallic alloys by exploiting sample configurations with maximized surface-to-volume ratios, such as nanoporous samples.

- Overcome by nanoporosity the ultra-thin film regime (1 -2 nm) in which charge-mediated magnetoelectric effects are typically limited.

- Search for new synthesis routes to prepare nanoporous materials with tailored pore architectures and ultra-thin pore walls.

- Investigate routes to conformally coat metallic nanoporous materials with dielectrics to be able to apply electric fields in solid state and, thus, replace electrolyte gating strategies with solid-state configurations.

- Make magneto-ionics feasible at room temperature and without the need of external oxygen sources by engineering structural defects in metal oxide films.

1.7 Schedule

A schedule of the work carried out, including attendance to congresses and publications, is chronologically shown in the following table. The total length of the Thesis corresponds to 2 years and 6 months. Purple lines indicate the beginning of each academic year.
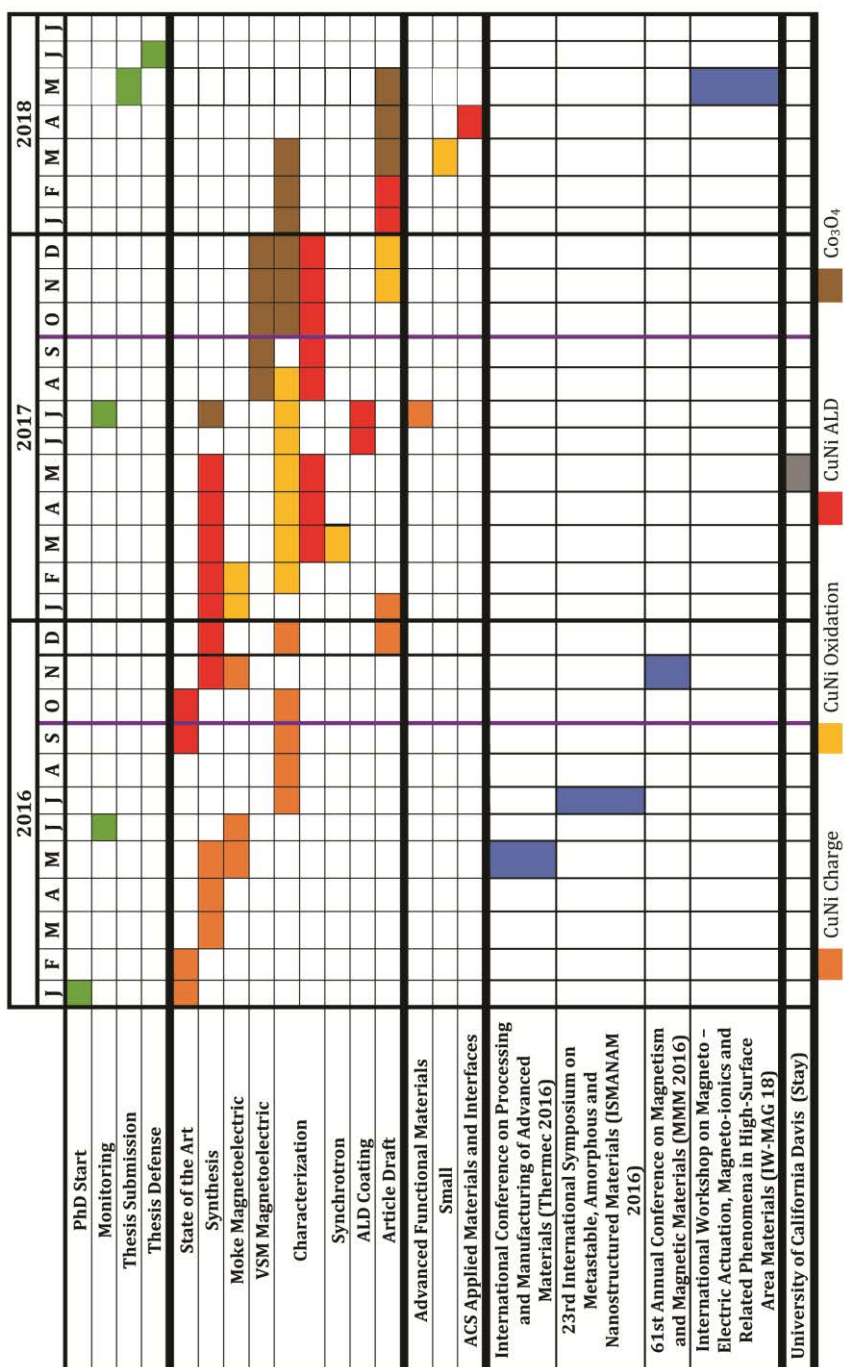
1.8 Bibliography

1. Cullity, B. D. & Graham, C. D. *Introduction to magnetic materials* (IEEE/Wiley, New Jersey, 2009).

2. Chikazumi, S. & Graham, C. D. *Physics of ferromagnetism* (Oxford University Press, New York, 1997).

3. Coey, J. M. D. *Magnetism and magnetic materials* (Cambridge University Press, New York, 2014).

4. Baibich, M. N. *et al.* Giant magnetoresistance of (001)Fe|(001)Cr magnetic superlattices. *Phys. Rev. Lett.* **61**, 2472–2475 (1988).

5. Bhatti, S. *et al.* Spintronics based random access memory: a review. *Mater. Today* **20**, 530–548 (2017).

6. Dieny, B. *et al.* Spin-transfer effect and its use in spintronic components. *Int. J. Nanotechnol.* **7**, 591 (2010).

7. Heidler, J. *et al.* Magnetoelectroelastic control of magnetism in an artificial multiferroic. *Phys. Rev. B* **94**, 014401 (2016).

8. Martin, L. W. *et al.* Multiferroics and magnetoelectrics: thin films and nanostructures. *J. Phys. Condens. Matter* **20**, 434220 (2008).

9. Chambers, S. A. Molecular beam epitaxial growth of doped oxide semiconductors. *J. Phys. Condens. Matter* **20**, 264004 (2008).

10. Vaz, C. A. F., Hoffman, J., Ahn, C. H. & Ramesh, R. Magnetoelectric coupling effects in multiferroic complex oxide composite structures. *Adv. Mater.* **22**, 2900–2918 (2010).

11. Hill, N. A. Why are there so few magnetic ferroelectrics? *J. Phys. Chem. B* **104**, 6694–6709 (2000).

12. Velev, J. P., Jaswal, S. S. & Tsymbal, E. Y. Multi-ferroic and magnetoelectric materials and interfaces. *Phil. Trans. R. Soc. A* **369**, 3069–3097 (2011).

13. Suchtelen, J. Product properties: a new application of composite materials. *Philips Res. Repts.* **27**, 28–37 (1972).

14. Ma, J., Hu, J., Li, Z. & Nan, C.-W. Recent progress in multiferroic magnetoelectric composites: from bulk to thin films. *Adv. Mater.* **23**, 1062–1087 (2011).

15. Sahoo, S. *et al.* Ferroelectric control of magnetism in $BaTiO_3$|Fe heterostructures via interface strain coupling. *Phys. Rev. B* **76**, 092108 (2007).

16. Cherifi, R. O. *et al.* Electric-field control of magnetic order above room temperature. *Nat. Mater.* **13**, 345–351 (2014).

17. Regan, T. J. *et al.* Chemical effects at metal/oxide interfaces studied by x-ray-absorption spectroscopy. *Phys. Rev. B* **64**, 214422 (2001).

18. Couet, S. *et al.* Electric field-induced oxidation of ferromagnetic/ferroelectric interfaces. *Adv. Funct. Mater.* **24**, 71–76 (2013).

19. Bisht, M. *et al.* Electric polarity-dependent modification of the Fe|BaTiO$_3$ interface. *Adv. Mater. Interfaces* **3**, 1500433 (2015).

20. Nan, T. *et al.* Quantification of strain and charge co-mediated magnetoelectric coupling on ultra-thin Permalloy/PMN-PT interface. *Sci. Rep.* **4**, 3688 (2014).

21. Shu, L. *et al.* Thickness-dependent voltage-modulated magnetism in multiferroic heterostructures. *Appl. Phys. Lett.* **100**, 022405 (2012).

22. Hu, J.-M., Nan, C.-W. & Chen, L.-Q. Size-dependent electric voltage controlled magnetic anisotropy in multiferroic heterostructures: interface-charge and strain co-mediated magnetoelectric coupling. *Phys. Rev. B* **83**, 134408 (2011).

23. Ohno, H. *et al.* Electric-field control of ferromagnetism. *Nature* **408**, 944–946 (2000).

24. Chiba, D., Yamanouchi, M., Matsukura, F. & Ohno, H. Electrical manipulation of magnetization reversal in a ferromagnetic semiconductor. *Science* **301**, 943–945 (2003).

25. Boukari, H. *et al.* Light and Electric field control of ferromagnetism in magnetic quantum structures. *Phys. Rev. Lett.* **88**, 207204 (2002).

26. Chiba, D. *et al.* Magnetization vector manipulation by electric fields. *Nature* **455**, 515–518 (2008).

27. Liu, X. *et al.* Perpendicular magnetization reversal, magnetic anisotropy, multistep spin switching, and domain nucleation and expansion in Ga$_{1-x}$Mn$_x$As films. *J. Appl. Phys.* **98**, 063904 (2005).

28. Tu, N. T., Hai, P. N., Anh, L. D. & Tanaka, M. Electrical control of ferromagnetism in the n-type ferromagnetic semiconductor (In,Fe)Sb with high Curie temperature. *Appl. Phys. Lett.* **112**, 122409 (2018).

29. Yamada, Y. *et al.* Electrically induced ferromagnetism at room temperature in cobalt-doped titanium dioxide. *Science* **332**, 1065–1067 (2011).

30. Weisheit, M. *et al.* Electric field-induced modification of magnetism in thin-film ferromagnets. *Science* **315**, 349–351 (2007).

31. Duan, C.-G. *et al.* Surface magnetoelectric effect in ferromagnetic metal films. *Phys. Rev. Lett.* **101**, 137201 (2008).

32. Seki, T., Kohda, M., Nitta, J. & Takanashi, K. Coercivity change in an FePt thin layer in a Hall device by voltage application. *Appl. Phys. Lett.* **98**, 212505 (2011).

33. Bauer, U., Przybylski, M., Kirschner, J. & Beach, G. S. D. Magnetoelectric charge trap memory. *Nano Lett.* **12**, 1437–1442 (2012).

34. Zhang, S., Zou, X., Zhu, Q. & Pang, H. Electric field induced modification of magnetic properties in Co_2Si_2 multilayers. *J. Appl. Phys.* **115**, 014301 (2014).

35. Chiba, D. *et al.* Electrical control of the ferromagnetic phase transition in cobalt at room temperature. *Nat. Mater.* **10**, 853–856 (2011).

36. Shimamura, K. *et al.* Electrical control of curie temperature in cobalt using an ionic liquid film. *Appl. Phys. Lett.* **100**, 122402 (2012).

37. Maruyama, T. *et al.* Large voltage-induced magnetic anisotropy change in a few atomic layers of iron. *Nat. Nanotechnol.* **4**, 158–161 (2009).

38. Nakamura, K. *et al.* Giant modification of the magnetocrystalline anisotropy in transition-metal monolayers by an external electric field. *Phys. Rev. Lett.* **102**, 187201 (2009).

39. Wang, W.-G., Li, M., Hageman, S. & Chien, C. L. Electric-field-assisted switching in magnetic tunnel junctions. *Nat. Mater.* **11**, 64–68 (2011).

40. Rajanikanth, A., Hauet, T., Montaigne, F., Mangin, S. & Andrieu, S. Magnetic anisotropy modified by electric field in V|Fe|MgO(001)|Fe epitaxial magnetic tunnel junction. *Appl. Phys. Lett.* **103**, 062402 (2013).

41. Ha, S.-S. *et al.* Voltage induced magnetic anisotropy change in ultrathin $Fe_{80}Co_{20}$/MgO junctions with Brillouin light scattering. *Appl. Phys. Lett.* **96**, 142512 (2010).

42. Endo, M., Kanai, S., Ikeda, S., Matsukura, F. & Ohno, H. Electric-field effects on thickness dependent magnetic anisotropy of sputtered $MgO|Co_{40}Fe_{40}B_{20}|Ta$ structures. *Appl. Phys. Lett.* **96**, 212503 (2010).

43. Bonell, F. *et al.* Large change in perpendicular magnetic anisotropy induced by an electric field in FePd ultrathin films. *Appl. Phys. Lett.* **98**, 232510 (2011).

44. Nozaki, T., Shiota, Y., Shiraishi, M., Shinjo, T. & Suzuki, Y. Voltage-induced perpendicular magnetic anisotropy change in magnetic tunnel junctions. *Appl. Phys. Lett.* **96**, 022506 (2010).

45. Kikuchi, Y., Seki, T., Kohda, M., Nitta, J. & Takanashi, K. Voltage-induced coercivity change in FePt|MgO stacks with different FePt thicknesses. *J. Phys. D Appl. Phys.* **46**, 285002 (2013).

46. Hibino, Y. *et al.* Peculiar temperature dependence of electric-field effect on magnetic anisotropy in Co|Pd|MgO system. *Appl. Phys. Lett.* **109**, 082403 (2016).

47. Bernand-Mantel, A. *et al.* Electric-field control of domain wall nucleation and pinning in a metallic ferromagnet. *Appl. Phys. Lett.* **102**, 122406 (2013).

48. Liu, Y. T. *et al.* Ionic-liquid gating of perpendicularly magnetized CoFeB|MgO thin films. *J. Appl. Phys.* **120**, 023901 (2016).

49. Diez, L. H. *et al.* Electric-field assisted depinning and nucleation of magnetic domain walls in FePt|Al$_2$O$_3$|liquid gate structures. *Appl. Phys. Lett.* **104**, 082413 (2014).

50. Molinari, A., Hahn, H. & Kruk, R. Voltage-controlled On|Off Switching of Ferromagnetism in Manganite Supercapacitors. *Adv. Mater.* **30**, 1703908 (2017).

51. Reitz, C., Leufke, P. M., Schneider, R., Hahn, H. & Brezesinski, T. Large magnetoresistance and electrostatic control of magnetism in ordered mesoporous La$_{1-x}$Ca$_x$MnO$_3$ thin films. *Chem. Mater.* **26**, 5745–5751 (2014).

52. Bi, C. *et al.* Reversible control of Co magnetism by voltage-induced oxidation. *Phys. Rev. Lett.* **113**, 267202 (2014).

53. Bauer, U. *et al.* Magneto-ionic control of interfacial magnetism. *Nat. Mater.* **14**, 174–181 (2015).

54. Gilbert, D. A. *et al.* Structural and magnetic depth profiles of magneto-ionic heterostructures beyond the interface limit. *Nat. Commun.* **7**, 12264 (2016).

55. Bauer, U., Emori, S. & Beach, G. S. D. Voltage-controlled domain wall traps in ferromagnetic nanowires. *Nat. Nanotechnol.* **8**, 411–416 (2013).

56. Bauer, U., Emori, S. & Beach, G. S. D. Electric field control of domain wall propagation in Pt|Co|GdO$_x$ films. *Appl. Phys. Lett.* **100**, 192408 (2012).

57. Yan, Y. N. *et al.* Electrical control of Co/Ni magnetism adjacent to gate oxides with low oxygen ion mobility. *Appl. Phys. Lett.* **107**, 122407 (2015).

58. Zhou, X. *et al.* Role of oxygen ion migration in the electrical control of magnetism in Pt|Co|Ni|HfO$_2$ films. *J. Phys. Chem. C* **120**, 1633–1639 (2016).

59. Di, N. *et al.* Influence of controlled surface oxidation on the magnetic anisotropy of Co ultrathin films. *Appl. Phys. Lett.* **106**, 122405 (2015).

60. Duschek, K., Uhlemann, M., Schlörb, H., Nielsch, K. & Leistner, K. Electrochemical and in situ magnetic study of iron|iron oxide films oxidized and reduced in KOH solution for magneto-ionic switching. *Electrochem. Commun.* **72**, 153–156 (2016).

61. Monteiro, J., Ivanova, Y. A., Kovalevsky, A., Ivanou, D. & Frade, J. Reduction of magnetite to metallic iron in strong alkaline medium. *Electrochim. Acta* **193**, 284–292 (2016).

62. Reichel, L., Oswald, S., Fähler, S., Schultz, L. & Leistner, K. Electrochemically driven variation of magnetic properties in ultrathin CoPt films. *J. Appl. Phys.* **113**, 143904 (2013).

63. Duschek, K., Pohl, D., Fähler, S., Nielsch, K. & Leistner, K. Research update: magnetoionic control of magnetization and anisotropy in layered oxide|metal heterostructures. *APL Mater.* **4**, 032301 (2016).

64. Leistner, K. *et al.* Electrode processes and in situ magnetic measurements of FePt films in a LiPF$_6$ based electrolyte. *Electrochim. Acta* **81**, 330–337 (2012).

65. Zhang, Q. *et al.* Lithium-ion battery cycling for magnetism control. *Nano Lett.* **16**, 583–587 (2016).

66. Dasgupta, S. *et al.* Toward on-and-off magnetism: reversible electrochemistry to control magnetic phase transitions in spinel ferrites. *Adv. Funct. Mater.* **26**, 7507–7515 (2016).

67. Wei, G. *et al.* Reversible control of the magnetization of spinel ferrites based electrodes by lithium-ion migration. *Sci. Rep.* **7**, 12554 (2017).

68. Wei, G. *et al.* Reversible control of magnetization of Fe$_3$O$_4$ by a solid-state film lithium battery. *Appl. Phys. Lett.* **110**, 062404 (2017).

69. Reitz, C., Suchomski, C., Wang, D., Hahn, H. & Brezesinski, T. In situ tuning of magnetization via topotactic lithium insertion in ordered mesoporous lithium ferrite thin films. *J. Mater. Chem. C* **4**, 8889–8896 (2016).

70. Kittel, C. *Introduction to solid state physics.* (Wiley, New Jersey, 2005).

71. Ghosh, S. Charge-response of magnetization in nanoporous Pd–Ni alloys. *J. Magn. Magn. Mater.* **323**, 552–556 (2011).

72. Topolovec, S., Jerabek, P., Szabó, D. V., Krenn, H. & Würschum, R. SQUID magnetometry combined with in situ cyclic voltammetry: A case study of tunable magnetism of γ-Fe$_2$O$_3$ nanoparticles. *J. Magn. Magn. Mater.* **329**, 43–48 (2013).

73. Subkow, S. & Fähnle, M. Potential explanation of charge response of magnetization in nanoporous systems. *Phys. Rev. B* **84**, 220409(R) (2011).

74. Yang, Y. *et al.* Morphology- and porosity-tunable synthesis of 3D nanoporous SiGe alloy as a high-performance lithium-ion battery anode. *ACS Nano* **12**, 2900–2908 (2018).

75. Chen, L.-M., Xu, Z., Hong, Z. & Yang, Y. Interface investigation and engineering – achieving high performance polymer photovoltaic devices. *J. Mater. Chem.* **20**, 2575–2598 (2010).

76. Sawa, A. Resistive switching in transition metal oxides. *Mater. Today* **11**, 28–36 (2008).

77. Qu, Y. & Duan, X. Progress, challenge and perspective of heterogeneous photocatalysts. *Chem. Soc. Rev.* **42**, 2568–2580 (2013).

78. Parlett, C. M. A., Wilson, K. & Lee, A. F. Hierarchical porous materials: catalytic applications. *Chem. Soc. Rev.* **42**, 3876–3893 (2013).

79. Adebajo, M., Frost, R., Kloprogge, J., Carmody, O. & Kokot, S. *J. Porous Mat.* **10**, 159–170 (2003).

80. Li, W. *et al.* Tailoring porous silicon for biomedical applications: from drug delivery to cancer immunotherapy. *Adv. Mater.,* 1703740 (2018).

81. Fattakhova-Rohlfing, D., Zaleska, A. & Bein, T. Three-dimensional titanium dioxide nanomaterials. *Chem. Rev.* **114**, 9487–9558 (2014).

82. Göltner, C. & Weißenberger, M. Mesoporous organic polymers obtained by "twostep nanocasting". *Acta Polym.* **49**, 704-709 (1998).

83. Deng, X., Chen, K. & Tüysüz, H. Protocol for the nanocasting method: preparation of ordered mesoporous metal oxides. *Chem. Mater.* **29**, 40–52 (2016).

84. Suib, S. L. A review of recent developments of mesoporous materials. *Chem. Rec.* **17**, 1169–1183 (2017).

85. Fan, J. *et al.* Evaporation-induced self-assembly synthesis of Ni-doped mesoporous SnO_2 thin films with tunable room temperature magnetic properties. *J. Mater. Chem. C* **5**, 5517–5527 (2017).

86. Yin, A., Wen, C., Dai, W.-L. & Fan, K. Nanocasting of CuAu alloy nanoparticles for methyl glycolate synthesis. *J. Mater. Chem.* **21**, 8997-8999 (2011).

87. Gomes, A. & Pereira, M. D. S. Pulsed electrodeposition of Zn in the presence of surfactants. *Electrochim. Acta* **51**, 1342–1350 (2006).

88. Yoshida, T., Komatsu, D., Shimokawa, N. & Minoura, H. Mechanism of cathodic electrodeposition of zinc oxide thin films from aqueous zinc nitrate baths. *Thin Solid Films* **451-452**, 166–169 (2004).

89. Zarębska, K., Kwiatkowski, M., Gniadek, M. & Skompska, M. Electrodeposition of $Zn(OH)_2$, ZnO thin films and nanosheet-like Zn seed layers and influence of their morphology on the growth of ZnO nanorods. *Electrochim. Acta* **98**, 255–262 (2013).

90. Jiang, N. *et al.* Electrodeposited nickel-sulfide films as competent hydrogen evolution catalysts in neutral water. *J. Mater. Chem. A* **2**, 19407–19414 (2014).

91. Azzaroni, O., Schilardi, P. L., Salvarezza, R. C. & Arvia, A. J. Smoothening mechanism of thiourea on silver electrodeposition. Real time imaging of the growth front evolution. *Langmuir* **15**, 1508–1514 (1999).

92. Natter, H. & Hempelmann, R. Nanocrystalline copper by pulsed electrodeposition: the effects of organic additives, bath temperature, and pH. *J. Phys. Chem.* **100**, 19525–19532 (1996).

93. Zhou, W.-J., Zhao, D.-D., Xu, M.-W., Xu, C.-L. & Li, H.-L. Effects of the electrodeposition potential and temperature on the electrochemical capacitance behavior of ordered mesoporous cobalt hydroxide films. *Electrochim. Acta* **53**, 7210–7219 (2008).

94. Kong, L.-B. *et al.* Porous cobalt hydroxide film electrodeposited on nickel foam with excellent electrochemical capacitive behavior. *J. Solid State Electrochem.* **15**, 571–577 (2010).

95. Elias, J., Tena-Zaera, R. & Lévy-Clément, C. Electrodeposition of ZnO nanowires with controlled dimensions for photovoltaic applications: role of buffer layer. *Thin Solid Films* **515**, 8553–8557 (2007).

96. Manzano, C. V., Bürki, G., Pethö, L., Michler, J. & Philippe, L. Determining the diffusion mechanism for high aspect ratio ZnO nanowires electrodeposited into anodic aluminum oxide. *J. Mater. Chem. C* **5**, 1706–1713 (2017).

97. Wu, X., Gao, Q. & Li, Z. Effects of additives on morphology and hydrogen evolution activities of nickel films prepared by electrodepositing *Int. J. Electrochem. Sci.*, **10**, 8823–8833 (2015).

98. Plowman, B. J., Jones, L. A. & Bhargava, S. K. Building with bubbles: the formation of high surface area honeycomb-like films via hydrogen bubble templated electrodeposition. *Chem. Commun.* **51**, 4331–4346 (2015).

99. Zhang, J., Baró, M. D., Pellicer, E. & Sort, J. Electrodeposition of magnetic, superhydrophobic, non-stick, two-phase Cu–Ni foam films and their enhanced performance for hydrogen evolution reaction in alkaline water media. *Nanoscale* **6**, 12490–12499 (2014).

100. Ott, A., Jones, L. A. & Bhargava, S. K. Direct electrodeposition of porous platinum honeycomb structures. *Electrochem. Commun.* **13,** 1248–1251 (2011).

101. Li, Y., Song, Y.-Y., Yang, C. & Xia, X.-H. Hydrogen bubble dynamic template synthesis of porous gold for nonenzymatic electrochemical detection of glucose. *Electrochem. Commun.* **9**, 981–988 (2007).

102. Cherevko, S. & Chung, C.-H. Impact of key deposition parameters on the morphology of silver foams prepared by dynamic hydrogen template deposition. *Electrochim. Acta* **55**, 6383–6390 (2010).

103. Shin, H.-C. & Liu, M. Copper foam structures with highly porous nanostructured walls. *Chem. Mater.* **16**, 5460–5464 (2004).

104. Li, Y., Jia, W.-Z., Song, Y.-Y. & Xia, X.-H. Superhydrophobicity of 3D porous copper films prepared using the hydrogen bubble dynamic template. *Chem. Mater.* **19**, 5758–5764 (2007).

105. Herraiz-Cardona, I., Ortega, E., Vázquez-Gómez, L. & Pérez-Herranz, V. Double-template fabrication of three-dimensional porous nickel electrodes for hydrogen evolution reaction. *Int. J. Hydrog. Energy* **37**, 2147–2156 (2012).

106. Cherevko, S., Xing, X. & Chung, C.-H. Hydrogen template assisted electrodeposition of sub-micrometer wires composing honeycomb-like porous Pb films. *Appl. Surf. Sci.* **257**, 8054–8061 (2011).

107. Shin, H.-C. & Liu, M. Three-dimensional porous copper-tin alloy electrodes for rechargeable lithium batteries. *Adv. Funct. Mater.* **15**, 582–586 (2005).

108. Collings, P. J. *Liquid crystals: natures delicate phase of matter*. (Princeton University Press, Princeton, 1990).

109. Attard, G. S. Mesoporous platinum films from lyotropic liquid crystalline phases. *Science* **278**, 838–840 (1997).

110. Attard, G. S., Corker, J. M., Göltner, C. G., Henke, S. & Templer, R. H. Liquid-crystal templates for nanostructured metals. *Angew. Chem. Int. Ed.* **36**, 1315–1317 (1997).

111. Bartlett, P. N., Gollas, B., Guerin, S. & Marwan, J. The preparation and characterisation of H_1-e palladium films with a regular hexagonal nanostructure formed by electrochemical deposition from lyotropic liquid crystalline phases. *Phys. Chem. Chem. Phys.* **4**, 3835–3842 (2002).

112. Bartlett, P. N. & Marwan, J. Preparation and characterization of H_1–e rhodium films. *Microporous Mesoporous Mater* **62**, 73–79 (2003).

113. Bartlett, P. N., Birkin, P. N., Ghanem, M. A., Groot, P. D. & Sawicki, M. The electrochemical deposition of nanostructured cobalt films from lyotropic liquid crystalline media*. J. Electrochem. Soc.* **148**, 119–123 (2001).

114. Ganesh, V. & Lakshminarayanan, V. Preparation of high surface area nickel electrodeposit using a liquid crystal template technique. *Electrochim. Acta* **49**, 3561–3572 (2004).

115. Nelson, P. A., Elliott, J. M., Attard, G. S. & Owen, J. R. Mesoporous nickel/nickel oxide - a nanoarchitectured electrode. *Chem. Mater.* **14**, 524–529 (2002).

116. Whitehead, A. H., Elliott, J. M., Owen, J. R. & Attard, G. S. Electrodeposition of mesoporous tin films. *Chem. Commun.* **0**, 331–332 (1999).

117. Nandhakumar, I., Elliott, J. M. & Attard, G. S. Electrodeposition of nanostructured mesoporous selenium films (H_1-eSe). *Chem. Mater.* **13**, 3840–3842 (2001).

118. Gabriel, T., Nandhakumar, I. S. & Attard, G. S. Electrochemical synthesis of nanostructured tellurium films. *Electrochem. Commun.* **4**, 610–612 (2002).

119. Bender, F., Mankelow, R., Hibbert, D. & Gooding, J. Lyotropic liquid crystal templating of groups 11 and 12 metal films. *Electroanalysis* **18,** 1558–1563 (2006).

120. Zhao, D.-D., Xu, M. W., Zhou, W.-J., Zhang, J. & Li, H. L. Preparation of ordered mesoporous nickel oxide film electrodes via lyotropic liquid crystal templated electrodeposition route. *Electrochim. Acta* **53**, 2699–2705 (2008).

121. Huang, L. *et al.* Cuprite Nanowires by Electrodeposition from lyotropic reverse hexagonal liquid crystalline phase. *Chem. Mater.* **14**, 876–880 (2002).

122. Luo, H., Zhang, J. & Yan, Y. Electrochemical deposition of mesoporous crystalline oxide semiconductor films from lyotropic liquid crystalline phases. *Chem. Mater.* **15**, 3769–3773 (2003).

123. Yamauchi, Y., *et al.* Ferromagnetic mesostructured alloys: design of ordered mesostructured alloys with multicomponent metals from lyotropic liquid crystals. *Angew. Chem. Int. Ed.* **48,** 7792–7797 (2009).

124. Isarain-Chávez, E., Baró, M. D., Pellicer, E. & Sort, J. Micelle-assisted electrodeposition of highly mesoporous Fe–Pt nodular films with soft magnetic and electrocatalytic properties. *Nanoscale* **9**, 18081–18093 (2017).

125. Isarain-Chávez, E. *et al.* Micelle-assisted electrodeposition of mesoporous Fe-Pt smooth thin films and their electrocatalytic activity towards the hydrogen evolution reaction. *ChemSusChem* **11**, 367–375 (2017).

Compilation of Articles

2.1 Charge-mediated magnetoelectric effects in nanoporous CuNi alloys

In this article, we show that the coercivity of nanoporous CuNi can be drastically reduced by subjecting this type of materials to the action of an electric field (i.e., electric voltage). Such electric control of the magnetic properties is very appealing for energy-efficient magnetic actuation. In our case, a reduction in coercivity implies that lower currents are needed to switch the magnetization of the system (either when using an electromagnet or in spin-torque devices), thus reducing the energy loss in the form of heat dissipation (Joule effect).

Nanoporous CuNi samples were electrodeposited potentiostatically from an electrolyte containing 0.2 M $Ni(CH_3COO)_2 \cdot 4H_2O$, 0.02 M $CuSO_4 \cdot 5H_2O$, and 8 mg mL^{-1} (0.8 wt. %) of poly(ethylene oxide)-block-poly(propylene oxide)-block-poly(ethylene oxide) (PEO-PPO-PEO) triblock copolymer (Pluronic P-123). The concentration of P123 was chosen to be above the cmc but below the concentration of LLC formation, with the aim to induce porosity but with a reduced electrolyte viscosity so as to enhance the CuNi codeposition. Structural, compositional and morphological characterization techniques (X-Ray diffraction (XRD), energy dispersive X-Ray analyses (EDX) and selected area electron diffraction (SAED)) confirmed the formation of a face centered cubic (FCC) CuNi solid solution ($Cu_{25}Ni_{75}$), highly textured along the (111) direction. Transmission electron microscopy (TEM) and scanning TEM (STEM) revealed the formation of a nanoporous structure with a pore size of 5 nm and interpore distance between 4-5 nm. Porosity was preserved along the whole thickness of the sample (600 nm).

Due to the difficulties to produce large area defect-free dielectric layers, the electric field was applied to the nanoporous film through the formation of an EDL in an anhydrous organic solvent (propylene carbonate) which contains solvated Na$^+$ and OH$^-$ ions. The EDL allows for the generation of high intense electric fields up to hundreds of MV/cm. The magnetoelectric measurements were all carried by electrolyte-gating in a home-made cell developed specifically to be able to apply voltage while performing MOKE measurements. Upon positive voltage, a reduction of coercivity down to 32 % of the initial value was achieved, while almost no change was observed for negative voltages. This is ultimately ascribed to the large surface-area-to-volume ratio and the ultra-narrow pore walls of the system, which allow for much larger accumulation of electrostatic charges compared to fully-dense films. That is, the whole nanoporous structure is affected by the electric field

and not only the outer topmost surface, thus resulting in a pronounced voltage-induced reduction of coercivity. *Ab-initio* calculations support that this voltage modulation of coercivity arises from changes in the magnetic anisotropy energy, which stem from electric field-induced spin-dependent modifications of the magnetic density of states in the alloy.

Finally, voltammetric studies and magnetoelectric measurements in oxidative media ruled out oxidation-reduction processes as the origin of the observed effect.

ADVANCED FUNCTIONAL MATERIALS

Voltage-Induced Coercivity Reduction in Nanoporous Alloy Films: A Boost toward Energy-Efficient Magnetic Actuation

Alberto Quintana,[1] Jin Zhang,[1] Eloy Isarain-Chávez,[1] Enric Menéndez,[1] Ramón Cuadrado,[2] Roberto Robles,[2,*] Maria Dolors Baró,[1] Miguel Guerrero,[1] Salvador Pané,[3] Bradley J. Nelson,[3] Carlos Maria Müller,[4] Pablo Ordejón,[2] Josep Nogués,[2,5,*] Eva Pellicer,[1,*] and Jordi Sort[1,5,*]

1.- Departament de Física, Universitat Autònoma de Barcelona, E-08193 Cerdanyola del Vallès, Spain.

2.- Catalan Institute of Nanoscience and Nanotechnology (ICN2), CSIC and The Barcelona Institute of Science and Technology. Campus UAB, Cerdanyola del Valles, E-08193 Barcelona, Spain.

3.- Institute of Robotics and Intelligent Systems (IRIS), ETH Zürich, CH-8092 Zürich, Switzerland.

4.- Departament de Ciència de Materials i Química Física, Universitat de Barcelona. Martí i Franquès 1, E-08028 Barcelona, Spain.
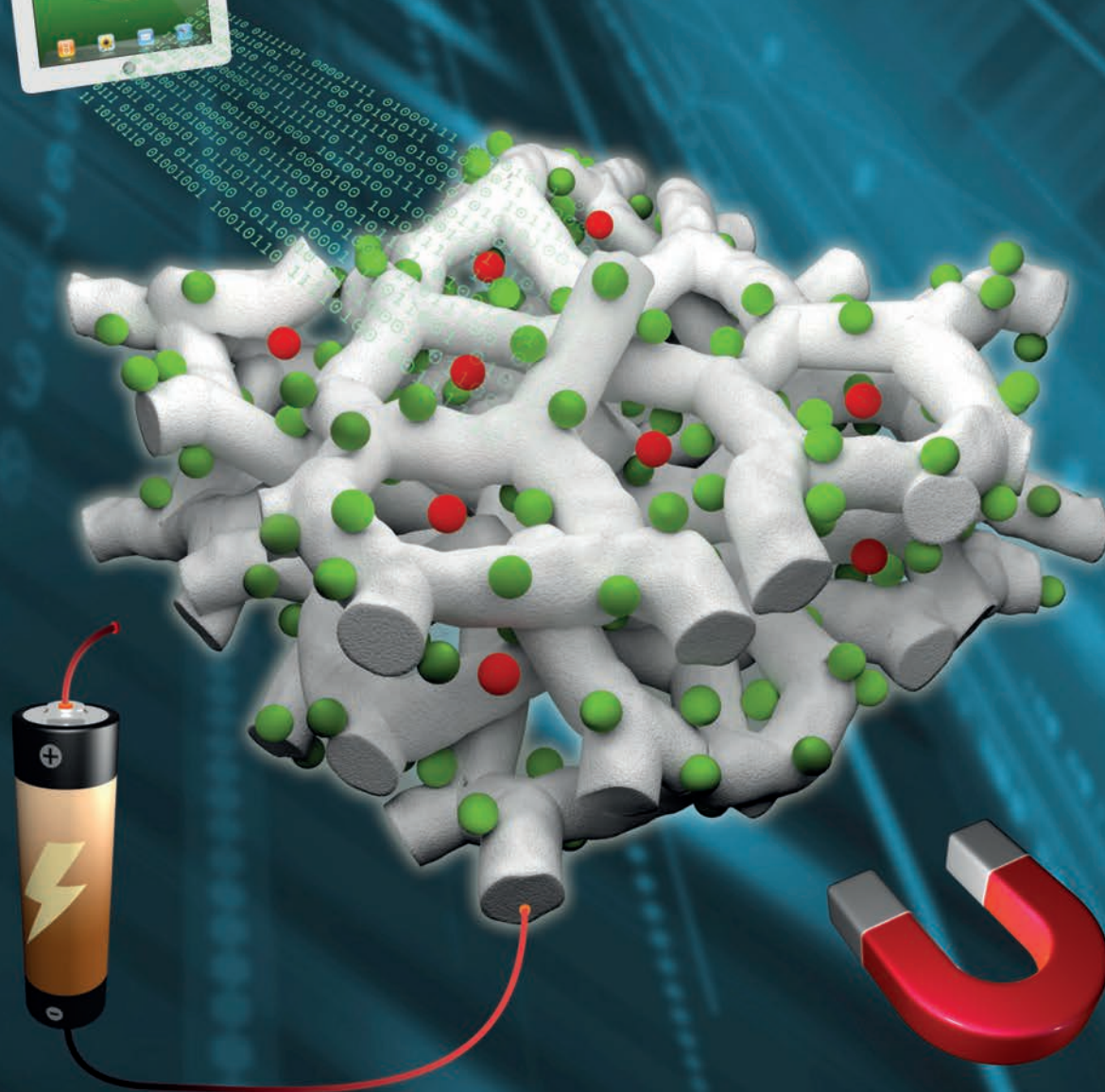
5.- ICREA. Pg. Lluís Companys 23, E-08010 Barcelona, Spain.

Correspondence should be addressed to: eva.pellicer@uab.cat; jordi.sort@uab.cat, roberto.robles@icn2.cat; josep.nogues@icn2.cat

ADVANCED FUNCTIONAL MATERIALS

FULL PAPER

Magnetic Actuation

**ADVANCED
FUNCTIONAL
MATERIALS**

www.afm-journal.de

Voltage-Induced Coercivity Reduction in Nanoporous Alloy Films: A Boost toward Energy-Efficient Magnetic Actuation

Alberto Quintana, Jin Zhang, Eloy Isarain-Chávez, Enric Menéndez, Ramón Cuadrado, Roberto Robles,* Maria Dolors Baró, Miguel Guerrero, Salvador Pané, Bradley J. Nelson, Carlos Maria Müller, Pablo Ordejón, Josep Nogués,* Eva Pellicer,* and Jordi Sort*

Magnetic data storage and magnetically actuated devices are conventionally controlled by magnetic fields generated using electric currents. This involves significant power dissipation by Joule heating effect. To optimize energy efficiency, manipulation of magnetic information with lower magnetic fields (i.e., lower electric currents) is desirable. This can be accomplished by reducing the coercivity of the actuated material. Here, a drastic reduction of coercivity is observed at room temperature in thick ($\approx$600 nm), nanoporous, electrodeposited Cu–Ni films by simply subjecting them to the action of an electric field. The effect is due to voltage-induced changes in the magnetic anisotropy. The large surface-area-to-volume ratio and the ultranarrow pore walls of the system allow the whole film, and not only the topmost surface, to effectively contribute to the observed magnetoelectric effect. This waives the stringent "ultrathin-film requirement" from previous studies, where small voltage-driven coercivity variations were reported. This observation expands the already wide range of applications of nanoporous materials (hitherto in areas like energy storage or catalysis) and it opens new paradigms in the fields of spintronics, computation, and magnetic actuation in general.

1. Introduction

The continuous progress in information and communication technologies critically depends on an optimized utilization of electric power. Magnetism and spintronics have largely contributed to the digital revolution by dramatically enhancing the hard disk capacity and the data processing speed.[1,2] Magnetic actuation is also at the heart of many micro-/nano-electromechanical systems and other engineering applications. However, power consumption in magnetoelectronic devices continues to be a constraining issue.[3] Magnetization switching in devices

is conventionally done by localized magnetic fields (generated via electromagnetic induction) or by spin-polarized electric currents (spin-transfer torque).[2,4] Both principles require of relatively high electric currents and therefore involve significant loss of energy in the form of heat dissipation (Joule effect). For example, the currents needed to operate conventional magnetic random-access memories (MRAMs) are of the order of 10 mA, whereas spin-transfer torque MRAMs require currents of at least 0.5 mA. This is still a factor five times larger than the output currents delivered by highly miniaturized metal-oxide-semiconductor field-effect transistors.[5] Replacement of electric currents by electric fields would drastically contribute to reduce the overall power consumption in these and other devices.

Several approaches to tailor magnetism by means of an electric field have been proposed so far: (i) strain-mediated magnetoelectric coupling in piezoelectric–magnetostrictive composite materials,[6,7] (ii) multiferroic materials in which the ferroelectric and ferromagnetic order parameters are coupled to each other,[8] and (iii) electric-field induced oxidation-reduction transitions (magnetoionics).[9,10] However, each of these approaches faces some drawbacks, e.g., (i) clamping effects with the substrate, need of epitaxial interfaces, and risk of fatigue-induced mechanical failure; (ii) the dearth of available multiferroic materials and the reduced strength of magnetoelectric coupling, even at low temperatures; and (iii) precise control of the chemical

A. Quintana, Dr. J. Zhang, Dr. E. Isarain-Chávez, Dr. E. Menéndez, Prof. M. D. Baró, Dr. M. Guerrero, Dr. E. Pellicer, Prof. J. Sort
Departament de Física
Universitat Autònoma de Barcelona
E-08193 Cerdanyola del Vallès, Spain
E-mail: eva.pellicer@uab.cat; jordi.sort@uab.cat

Dr. R. Cuadrado, Dr. R. Robles, Prof. P. Ordejón, Prof. J. Nogués
Catalan Institute of Nanoscience and Nanotechnology (ICN2)
CSIC and The Barcelona Institute of Science and Technology
Campus UAB, Bellaterra, E-08193 Barcelona, Spain
E-mail: roberto.robles@icn2.cat; josep.nogues@icn2.cat

Dr. S. Pané, Prof. B. J. Nelson
Institute of Robotics and Intelligent Systems (IRIS)
ETH Zürich, CH-8092 Zürich, Switzerland

Prof. C. M. Müller
Departament de Ciència de Materials i Química Física
Universitat de Barcelona
Martí i Franquès 1, E-08028 Barcelona, Catalonia, Spain

Prof. J. Nogués, Prof. J. Sort
ICREA
Pg. Lluís Companys 23, E-08010 Barcelona, Spain

The ORCID identification number(s) for the author(s) of this article can be found under https://doi.org/10.1002/adfm.201701904.

**ADVANCED
SCIENCE NEWS**
www.advancedsciencenews.com

**ADVANCED
FUNCTIONAL
MATERIALS**
www.afm-journal.de

reactions, their kinetics, and the reversibility of the process. Thus, there is clearly a technological demand for alternative approaches to manipulate magnetism with an electric field at room temperature.

Interestingly, a number of exciting experiments performed in recent years have shown the possibility to modify the magnetic properties of diluted magnetic semiconductors[11,12] and some metallic elements and alloys[13–16] directly with an applied electric field, via accumulation of electrostatic charges at their surface. This is very promising for the development of low-power magnetic actuators and spintronic devices. Among the magnetic effects caused by electric field one can mention: change of Curie temperature in diluted magnetic semiconductors such as (Ga,Mn)As or (In,Mn)As[11]; changes of coercivity[11,17] and, in some cases, reorientation of the magnetic easy axis in thin films.[12,18] In semiconductors these effects are mostly observed at low temperatures and are due to electric-field induced modification of the charge carriers' concentration. In metals, magnetoelectric phenomena are related to spin-dependent screening (i.e., electrons with different spin characters respond differently to the applied electric field[16]) and, therefore, only occur within a few nm from the surface.[19] This restricts the effect to ultrathin films (consisting of a few monolayers),[13–15,17,18] which can be difficult to be integrated in real devices.

Given the surface origin of voltage-induced magnetic changes in metals, it is envisaged that an increase of the surface area-to-volume (S/V) ratio in nanoporous materials could trigger a significant enhancement of magnetoelectric effects, provided that the pore walls are kept sufficiently narrow.[20,21] During the last few years, the advances in the synthetic pathways to produce nanoporous materials with controllable pore size and composition have boosted a wealth of applications in diverse fields such as catalysis, bioimplants, dampers, gas sensing or energy storage, where materials with a high surface area are essential.[22–24] However, although many of the cutting-edge technological applications in spintronics and magnetic actuators also rely on surface or interface magnetic phenomena, the use of nanoporous materials in these technologically relevant fields has been largely overlooked,[25,26] particularly for pure magnetoelectric effects, i.e., neither mediated by strain nor resulting from oxidation/reduction reactions.

In this work, we explore intrinsic magnetoelectric effects in nanoporous Cu–Ni films grown by micelle-assisted electrodeposition (**Figure 1**a). We demonstrate that a drastic reduction of coercivity can be obtained in the nanoporous metallic alloy (with very narrow pore walls) under the application of voltage across an electrical double layer using a nonaqueous liquid electrolyte. The nanoporous morphology of the investigated material allows for much larger accumulation of surface electric charges compared to fully dense films. Since the whole porous structure is affected by the electric field, this results in a much more pronounced voltage-induced reduction of coercivity compared to previous studies.[13] The purely magnetoelectric effects in Cu–Ni are ascribed by ab initio calculations to changes in the magnetic anisotropy energy stemming from electric field-induced spin-dependent modifications of the magnetic density of states at the surface.

2. Results and Discussion

2.1. Morphology and Structure of the Electrodeposited Films

The typical morphology of the cross-section of the electrodeposited Cu–Ni films, observed by scanning transmission electron microscopy (STEM), is shown in Figure 1b. STEM observations demonstrate the occurrence of open-cell porosity, with highly interconnected ligaments whose lateral size is typically around 5–7 nm. The overall film's thickness is around 600 nm. Further structural analysis, performed by high-resolution transmission electron microscopy (HRTEM), reveals the occurrence of crystalline planes within the pore walls (Figure 1c). The corresponding selected area electron diffraction (SAED) patterns (Figure 1d) indicate the formation of a face-centered cubic (FCC) solid solution, similar to electrodeposited Cu–Ni dense films.[27] X-ray diffraction (XRD) measurements (Figure 1e) corroborate that the films grow forming a FCC solid solution and they are actually textured along the (111) direction, i.e., the (200) FCC peak, expected at around $2\theta = 51°–52°$, is not detected.[27] Moreover, even if the Gibbs free energy of mixing between Cu and Ni is slightly positive,[28] no phase separation into Cu-rich and Ni-rich regions takes place during electrodeposition. Compositional analyses, carried out by energy-dispersive X-ray (EDX) spectroscopy, reveal that the composition of the films is $Cu_{25}Ni_{75}$ (at%). The nanoporous character of the Cu–Ni films brings about a drastic increase of the S/V ratio. Indeed, simple geometrical reasoning can be used to show, for example, that the S/V ratio of a 600 nm thick porous film covering an area of 1×1 mm^2 and being made of an array of vertically oriented pores, with 5 nm pore diameter and 5 nm interpore distance would be about 120 times larger than the S/V ratio of a fully dense layer of 600 nm covering the same area. Interestingly, the total volume of "active material" (i.e., influenced by the action of an electric field) in the nanoporous layer case would be around 250 times larger than that of an ultrathin (2 nm thick) film.

2.2. Control of Coercivity Using Voltage

Figure 2a illustrates the experimental setup used for the magnetoelectric measurements. The formation of the electrical double layer surrounding the pore walls is depicted in Figure 2b. The sample was mounted in a home-made electrolytic cell filled with anhydrous propylene carbonate with Na$^+$ solvated species, and the magnetic properties were measured along the film plane by magneto-optic Kerr effect (MOKE), while applying different constant voltages between the sample and the counter-electrode. The use of a liquid electrolyte is very convenient to generate high electric fields. Namely, the large dielectric constant ($\varepsilon_r = 64$ for propylene carbonate) and the formation of the so-called electrical double-layer (with thickness ≈1 nm)[29] promote significant charging effects when applying moderate voltages. Representative hysteresis loops, measured at different positive voltages, from 0 to 14 V, are shown in Figure 2c. A progressive narrowing of the hysteresis loop is clearly observed as the voltage is increased. The coercivity, H_C, decreases from ≈97 to 66 Oe, which represents a relative variation close to 32%

**ADVANCED
SCIENCE NEWS**
www.advancedsciencenews.com

**ADVANCED
FUNCTIONAL
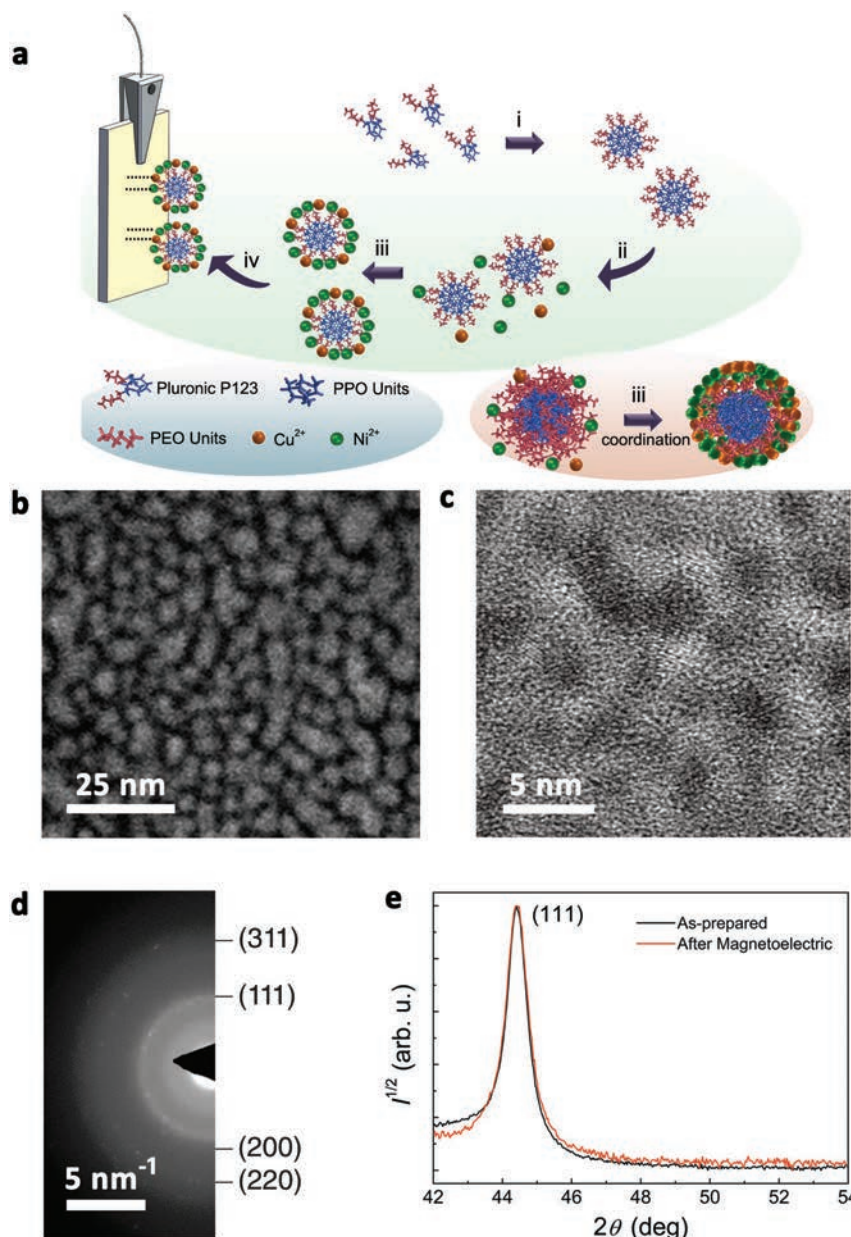MATERIALS**
www.afm-journal.de

Figure 1. a) Illustration of the micelle-assisted electrodeposition procedure, where PPO and PEO denote, respectively, the poly(ethylene oxide) and poly(propylene oxide) blocks of the PluronicP-123 triblock copolymer and (i–iv) denote the different synthetic steps: (i) stirring for clear solution, (ii) addition of metal salt, (iii) coordination of dissolved metal species with the hydrophilic shell domains of the micelles, (iv) electrodeposition. b) Cross-section image of the electrodeposited nanoporous Cu–Ni films (which are about 600 nm thick), observed by scanning transmission electron microscopy (STEM)—image taken after making a slice of the film and observing it along the perpendicular to film direction (cross-section), at a depth of about 300 nm from the outer film surface. c) High-resolution transmission electron microscopy (HRTEM) image of the nanoporous Cu–Ni alloy. d) Corresponding selected area diffraction (SAED) pattern. e) X-ray diffraction (XRD) patterns of the nanoporous films before and after the magneto-electric measurements.

(see **Figure 3**a). This is a remarkably larger change compared to previous works from the literature on ultrathin metallic films, reporting variations of only up to 4.5%.[13] The loops

also tend to become progressively more square-shaped as the applied voltage is increased. The corresponding variation of the remanence-to-saturation magnetization ratio, M_R/M_S,
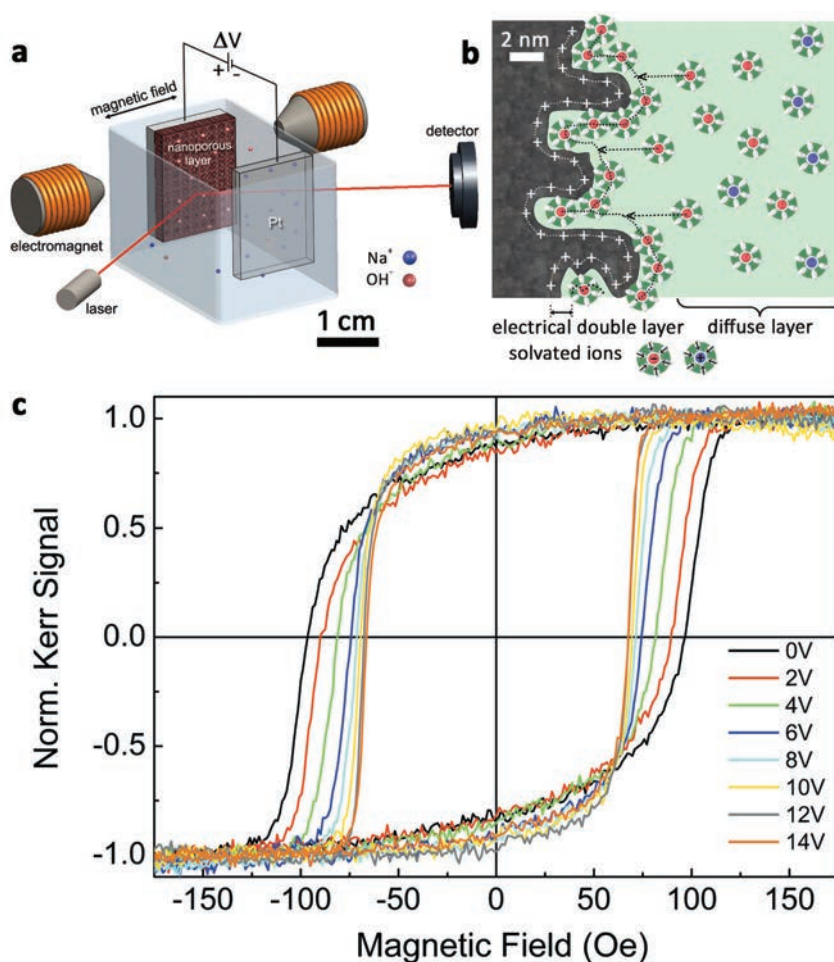
**ADVANCED
SCIENCE NEWS**
www.advancedsciencenews.com

**ADVANCED
FUNCTIONAL
MATERIALS**
www.afm-journal.de

Figure 2. a) Schematic illustration of the experimental setup used for the magnetoelectric measurements. As an example, this panel depicts the case where the sample is subject to positive polarity (that means that anions would accumulate at the surface of the nanoporous Cu–Ni alloy by Coulombic attraction). b) Representation of the formation of the electrical double layer around the pore walls during the magnetoelectric measurements. c) Representative hysteresis loops of the nanoporous Cu–Ni films acquired under application of different voltage values.

and the normalized differential magnetic susceptibility around the coercivity, $\chi = (dm/dH)_{H = HC}$ (where m denotes here the normalized Kerr amplitude signal) are shown in Figure 3b. The effects on H_C, M_R/M_S, and χ for negative voltages are significantly smaller and opposite to those observed with positive voltage (see Figure S1 in the Supporting Information). No significant variations in the Kerr signal amplitude were observed for either positive or negative applied voltages. To corroborate the crucial role played by the porosity on the observed magnetoelectric effects, the same experiments were performed on fully dense Cu–Ni films with the same composition and thickness, prepared by electrodeposition. As shown in Figure S2 (Supporting Information), the variations of H_C in that case are negligible, both for positive and negative applied voltages.

In order to rule out that oxidation/reduction reactions might govern the observed variations of H_C, cyclic electrochemical voltammetry experiments were performed, both for the

nanoporous and the fully dense Cu–Ni films, using the same nonaqueous electrolyte as for the magnetoelectric measurements. The results, shown in Figure S3 (Supporting Information), indicate absence of clear oxidation/reduction peaks, with current densities of the order of µA cm^{-2}, varying smoothly with potential. This suggests that capacitive processes (i.e., charge accumulation), rather than faradaic ones (involving charge transfer -electrons- across the electrode–electrolyte interface), dominate during in situ magnetoelectric measurements. This is in agreement with the XRD results since no diffraction peaks corresponding to metal oxides/hydroxides were observed after the magnetoelectric measurements (see Figure 1e). Also no evidence for phase separation (i.e., occurrence of peaks from Ni-rich and Cu-rich FCC solid solutions) was encountered after the magnetoelectric measurements. Additionally, the Cu/Ni ratio of the films did not vary after the measurements, confirming that selective dissolution of either Cu or
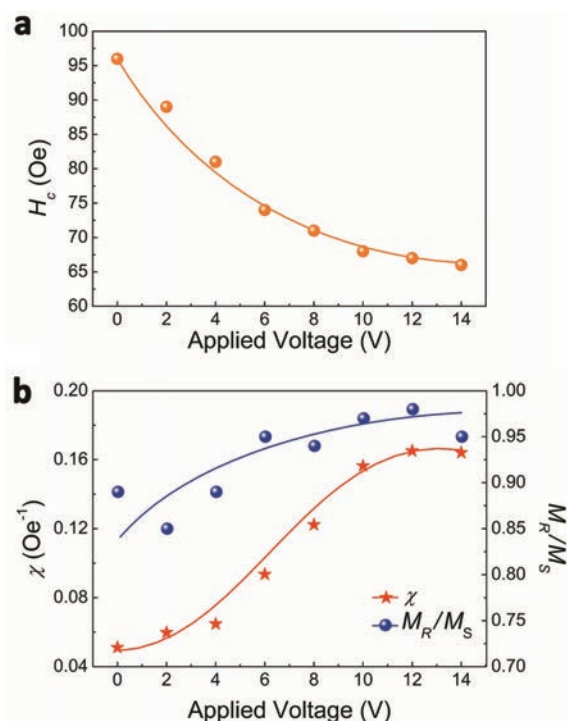
**ADVANCED
SCIENCE NEWS**
www.advancedsciencenews.com

**ADVANCED
FUNCTIONAL
MATERIALS**
www.afm-journal.de

Figure 3. a) Dependence of the coercivity, H_C, on the applied positive voltage. b) Dependence of the susceptibility around the coercivity (see definition in the text), χ, and the remanence-to-saturation magnetization ratio, M_R/M_S, as a function of voltage. Note that the lines are guides to the eye.

Ni does not take place during the voltage application (i.e., the observed magnetic changes are not due to variations in the film composition).

To further confirm that oxidation/reduction processes are not responsible for the observed trends in magnetic properties, hysteresis loops were also acquired while applying voltage using an aqueous electrolyte (0.1 M NaOH solution). In this case, oxidation indeed takes place upon application of a positive potential, as evidenced by cyclic voltammetry (Figure S4a, Supporting Information), where relatively high current densities ($\approx$mA cm^{-2}) are attained for $V > \pm1$ V. However, in spite of the oxidation, the changes in H_C were always <6% and actually H_C slightly increased (not decreased) after partial oxidation (Figure S4b, Supporting Information).

2.3. Ab Initio Calculations

The fundamental physical origin of intrinsic magnetoelectric effects in metallic alloys remains still not fully understood. However, in metals, electric fields are screened very effectively and such screening is known to be spin-dependent due to exchange interactions.[16] Hence, the electrostatic charges that are accumulated at the surface (within the so-called Thomas–Fermi screening length, $\lambda_{TF} \approx 0.5$ nm) can induce modifications

in the electronic band structure (i.e., in the charge density of unpaired d electrons with energy close to the Fermi level[13,16]) and, consequently, cause changes in the surface magnetization and the magnetic anisotropy energy (MAE).[16,30,31] Magnetic effects can propagate a few nm toward the interior of the alloy, within the spin–spin correlation length, which exceeds 20 nm in many metallic systems.[32] Given the 3D nanoporous morphology of the films, the electric field affects the nanopore walls from "all directions" (see Figure 2b). Interestingly, since the pore walls are very narrow and fully interconnected, the overall porous structure (i.e., the entire porous film) contributes to the observed voltage-induced large reduction of coercivity.

Although magnetoelectric phenomena in ultrathin $Cu_{1-x}Ni_x$ films have been predicted theoretically (in particular, changes in the Curie temperature),[32] this is the first experimental demonstration of such effects for this type of alloys. To get a deeper understanding of the fundamental origin of magnetoelectric effects in Cu–Ni we carried out ab initio calculations,[33,34] including spin–orbit interactions, on (111) slabs of $Cu_{25}Ni_{75}$ (**Figure** 4a,b). Different configurations of randomly arranged Cu and Ni atoms were averaged in order to simulate an alloy (three examples are depicted in Figure 4a). The results show an almost linear dependence of the surface magnetic moment with the applied electric field (Figure 4c), which can be quantified as

$$\mu_0 \Delta M = \alpha_S E \tag{1}$$

where ΔM is the surface magnetization, E is the applied electric field, and α_S is the so-called surface magnetoelectric coefficient. Note that E of the order of 1 V Å^{-1} indeed corresponds to the values obtained from voltages around 10 V (as in our experiments), assuming that the electrical double layer is $\approx$1 nm thick.[29] Fitting the data in Figure 4c, we obtain that $\alpha_S \approx 3.6 \times 10^{-14}$ G cm^2 V^{-1} when the magnetic moment is in-plane, and $\alpha_S \approx 3.0 \times 10^{-14}$ G cm^2 V^{-1} when the magnetic moment is pointing out-of-plane. These values are of the same order of magnitude as the ones calculated for a pure Fe(001) film.[30] Similar trends are obtained considering the (001) plane (see Figure S5 in the Supporting Information). The applied electric field also induces changes in the density of states (Figure S6, Supporting Information) and an increase of the change of the surface orbital moment m_L (Figure 4d), which can be related to an increase of the MAE using Bruno's relation[35]

$$MAE \propto \Delta m_L \tag{2}$$

The changes in total and orbital magnetic moments shown in Figure 4 are confined to the surface atoms. Overall, the effect would be negligible, as shown in Figure S2 (Supporting Information) for a fully dense film. The use of a nanoporous material allows enhancing the effect to make it measurable. Changes in MAE are generally correlated with variations in H_C, M_R/M_S, and χ (i.e., the overall shape and width of the loop).[13,16] However, in our case, due to the complex morphology of mesoporous Cu–Ni films, the correlation between MAE, H_C, and χ is not straightforward. An increase of positive MAE indicates an enhancement of perpendicular magnetocrystalline anisotropy per Ni atom. Magnetocrystalline anisotropy
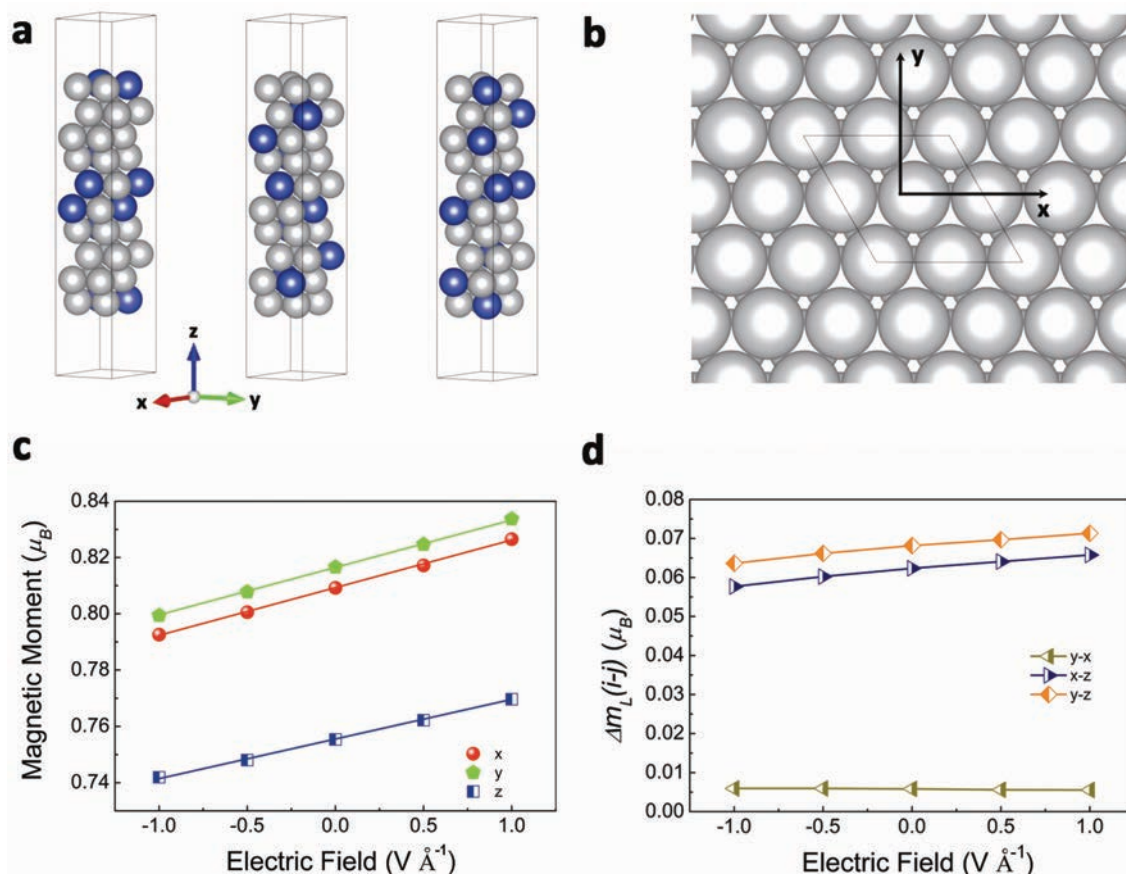
**ADVANCED
SCIENCE NEWS**
www.advancedsciencenews.com

**ADVANCED
FUNCTIONAL
MATERIALS**
www.afm-journal.de

Figure 4. a) Representative configurations, corresponding to the (111) orientation with different positions for Cu and Ni atoms within the lattice, which were considered for the ab initio calculations. Blue (gray) spheres represent Cu (Ni) atoms. b) In-plane directions considered for the (111) surface. The z direction is perpendicular to the plane. c) Dependence with the applied electric field of the magnetic moment oriented along the given directions for the Ni surface atoms. The lines are guides to the eye. d) Orbital moment differences Δm_L between the indicated directions for the surface Ni atoms. The lines are guides to the eye. According to Bruno's relation higher orbital moments correspond to lower energies in the corresponding magnetization direction.

competes with the shape anisotropy (which promotes magnetic easy axis along the nanopores ligaments directions, which are randomly distributed). Such competing anisotropies make the correlation between H_C and MAE rather complex. Nonetheless, the variation of H_C and χ with the electric field can be considered consistent with changes in the calculated MAE of the system.

3. Conclusions

In conclusion, our work demonstrates that the coercivity of nanoporous Cu–Ni thick films can be drastically decreased by simply applying an electric field. The large surface-area-to-volume ratio and the ultranarrow pore walls of the system play a crucial role in the discovered effect. Such electrically driven modification of magnetic properties is very appealing for energy-efficient magnetic actuation. Indeed, a reduction in coercivity implies that lower currents are needed to switch the magnetization of the

system (either when using an electromagnet or in spin-torque devices), hence considerably reducing energy loss in the form of heat dissipation (Joule effect). The voltage-induced decrease of coercivity could also be used as an alternative to thermally assisted magnetic writing in magnetic recording applications, since the latter is less energetically effective. Thus, the results from this work will likely expand the already wide range of applications of nanoporous materials (so far, mainly in chemistry), to areas like magnetically actuated micro-electromechanical systems, magnetic recording or spintronics, where their potential has been hitherto largely overlooked.

4. Experimental Section

Nanoporous Cu–Ni Film Growth: The electrodeposition of nanoporous Cu–Ni films was performed in a thermostatized three-electrode cell using a PGSTAT302N Autolab potentiostat/galvanostat (Ecochemie). Contrary to other more sophisticated methods, here the nanoporosity is induced during single-step micelle-assisted electrodeposition (see Figure 1a), a

procedure which has been used in recent years for the growth of only very few types of nanoporous layers, i.e., Pt-based alloys[36–38] and Cu,[39] but not magnetic alloys. Together with the lyotropic liquid crystals, this synthetic approach can be categorized as a soft templating method. Above the "critical micellar concentration" (c.m.c.) (e.g., 0.004 wt% for P123 at room temperature[40]), the micelles start to spontaneously form in the aqueous solution, get progressively in contact and tend to self-assemble at the solid–liquid interface, interfering and guiding the electrodeposition process, leading to the growth of mesoporous metallic films (see Figure 1a). Si/SiO$_2$ chips coated with Ti (10 nm)/Au (90 nm) adhesion/seed layers were used as cathodes (0.25 cm^2 working area), a platinum spiral served as counter electrode and a double junction Ag|AgCl (E = +0.210 V/SHE) with 3 M KCl inner solution and 1 M NaSO$_4$ outer solution was employed as the reference electrode (Metrohm AG). Prior to deposition, the substrates were degreased with acetone and ethanol, and rinsed in Milli-Q water. The electrolyte contained 0.2 M Ni(CH$_3$COO)$_2$·4H$_2$O, 0.02 M CuSO$_4$·5H$_2$O, and 8 mg mL^{-1} (0.8 wt%) of poly(ethylene oxide)-block-poly(propylene oxide)-block-poly(ethylene oxide) (PEO-PPO-PEO) triblock copolymer (PluronicP-123). The pH was left as-prepared (pH = 6.0). Electrodeposition was carried out galvanostatically at 25 °C, at a current density (j) of −80 mA cm^{-2}, during 120 s, under mild agitation (200 rpm) to favor mass transport of the electroactive species toward the cathode. N$_2$ was bubbled through the solution to get rid of oxygen before each deposition. The electrodeposited films (600 nm thick) were rinsed with Milli-Q water and ultrasonicated in ethanol for 5 min to remove remaining micelles from the growth process.

Fully Dense Cu–Ni Film Growth: The electrodeposition of fully dense Cu–Ni films is described elsewhere.[27]

Magnetoelectric Measurements: Hysteresis loops at different DC voltage values were measured at room temperature, along the film plane, in a MOKE setup from Durham Magneto-Optics (see Figure 2a). An external Agilent B2902A power supply was employed to generate voltage. The sample was mounted vertically in a quartz SUPRASIL cell filled with anhydrous propylene carbonate containing Na$^+$ ions. The anhydricity of the electrolyte avoided oxidation of the Cu–Ni during magnetoelectric measurements. Metallic sodium ions played a twofold role: (i) to react with any trace amounts of water that could enter the electrochemical system during experimental manipulation, forming Na$^+$OH$^-$; (ii) to promote the creation of the electrical double layer from the solvated Na$^+$ and OH$^-$ ions. A waiting time of 300 s was introduced between each voltage change and the hysteresis loop measurement in order to allow the diffusion of the electrolyte toward the interior of the pores of the Cu–Ni film and the formation of the electrical double layer. For the sake of comparison, magnetoelectric experiments were also carried out using a 0.1 M NaOH solution that forced sample oxidation during voltage application. The oxidation potentials were selected in agreement with cyclic voltammetry results.

Morphology and Structural Characterization: The morphology of the nanoporous films was assessed by HRTEM (FEI Tecnai G2 F20 operated at 200 kV) and scanning transmission electron microscopy (STEM, model FEI Tecnai F20) and compositional analyses were performed using EDX analysis in a field emission scanning electron microscope (Zeiss Merlin, at 2kV and 100pA). The crystal structure was investigated by XRD on a Philips X'Pert diffractometer (Panalytical) using Cu-Kα radiation, in the 42°–54° 2θ range.

Electrochemical Characterization: Cyclic voltammetries were carried out in a PGSTAT 302 N Autolab potentiostat/galvanostat (Ecochemie) and a VSP potentiostat with low-current option from BIOLOGIC.

Ab Initio Calculations: First principle calculations were performed by means of density functional theory using the SIESTA code.[33,34] Norm–conserving Troulliers–Martins pseudopotentials[41] including pseudocore corrections were used to describe the core electrons, and double-zeta polarized strictly localized numerical atomic orbitals were used as basis set. An additional shell of diffuse orbitals was used in the surface atoms, as described in ref. [42], to improve the accuracy of the description of the surface properties. The generalized gradient approximation in the Perdew–Burke–Ernzerhof version was used for the exchange

correlation potential.[43] Spin–orbit interactions were included in the on-site approximation.[44,45] An electric field was applied perpendicular to the film. Exhaustive convergence tests were performed to guarantee a tolerance below 10^{-5} eV in the total energies and below 10^{-3} μ$_B$ in the spin and orbital moments. To achieve that level of convergence a 25 × 25 × 1 k-grid was used, together with a temperature of 1 K in the Fermi–Dirac distribution and a mesh grid of 600 Ry.

A FCC Cu$_{25}$Ni$_{75}$ alloy was simulated using a (2 × 2) 10 layer slab with randomly arranged Cu and Ni atoms. The lattice constant of 3.542 Å was obtained from experimental data at this concentration.[27] Symmetry was applied, so up and down surfaces were equivalent. In this way results for positive and negative electric fields were extracted from a single calculation. Several atomic configurations were considered for the (111) orientation and the results were averaged among them. A single configuration was considered for the (001) orientation to show that the results are qualitatively similar for both orientations (see Figure S5 in the Supporting Information).

The magnetic density of states (Figure S6, Supporting Information) was calculated as the density of states for spin up minus the density of states for spin down projected in the direction of the magnetization.

Supporting Information

Supporting Information is available from the Wiley Online Library or from the author.

Conflict of Interest

The authors declare no conflict of interest.

Keywords

coercivity, energy efficiency, magnetic actuation, magnetoelectric effects, nanoporous alloys

[1] I. Žutić, J. Fabian, S. D. Sarma, *Rev. Mod. Phys.* **2004**, *76*, 323.
[2] C. Chappert, A. Fert, F. N. Van Dau, *Nat. Mater.* **2007**, *6*, 813.
[3] J.-M. Hu, Z. Li, L.-Q. Chen, C.-W. Nan, *Nat. Commun.* **2011**, *2*, 553.

**ADVANCED
SCIENCE NEWS**
www.advancedsciencenews.com

**ADVANCED
FUNCTIONAL
MATERIALS**
www.afm-journal.de

[4] S. Urazhdin, V. E. Demidov, H. Ulrichs, T. Kendziorczyk, T. Kuhn, J. Leuthold, G. Wilde, S. O. Demokritov, *Nat. Nanotechnol.* **2014**, *9*, 509.

[5] B. Dieny, R. C. Sousa, J. Hérault, C. Papusoi, G. Prenat, U. Ebels, D. Houssameddine, B. Rodmacq, S. Auffret, L. D. Buda-Prejbeanu, *Int. J. Nanotechnol.* **2010**, *7*, 591.

[6] Y. Wang, J. Hu, Y. Lin, C.-W. Nan, *NPG Asia Mater.* **2010**, *2*, 61.

[7] H. K. D. Kim, L. T. Schelhas, S. Keller, J. L. Hockel, S. H. Tolbert, G. P. Carman, *Nano Lett.* **2013**, *13*, 884.

[8] R. Ramesh, N. A. Spaldin, *Nat. Mater.* **2007**, *6*, 21.

[9] U. Bauer, L. Yao, A. J. Tan, P. Agrawal, S. Emori, H. L. Tuller, S. van Dijken, G. S. D. Beach, *Nat. Mater.* **2015**, *14*, 174.

[10] D. A. Gilbert, A. J. Grutter, E. Arenholz, K. Liu, B. J. Kirby, J. A. Borchers, B. B. Maranville, *Nat. Commun.* **2016**, *7*, 12264.

[11] H. Ohno, D. Chiba, F. Matsukura, T. Omiya, E. Abe, T. Dietl, Y. Ohno, K. Ohtani, *Nature* **2000**, *408*, 944.

[12] D. Chiba, M. Sawicki, Y. Nishitani, Y. Nakatani, F. Matsukura, H. Ohno, *Nature* **2008**, *455*, 515.

[13] M. Weisheit, S. Fähler, A. Marty, Y. Souche, C. Poinsignon, D. Givord, *Science* **2007**, *315*, 349.

[14] T. Maruyama, Y. Shiota, T. Nozaki, K. Ohta, N. Toda, M. Mizuguchi, A. A. Tulapurkar, T. Shinjo, M. Shiraishi, S. Mizukami, Y. Ando, Y. Suzuki, *Nat. Nanotechnol.* **2009**, *4*, 158.

[15] D. Chiba, S. Fukami, K. Shimamura, N. Ishiwata, K. Kobayashi, T. Ono, *Nat. Mater.* **2011**, *10*, 853.

[16] O. O. Brovko, P. Ruiz-Díaz, T. R. Dasa, V. S. Stepanyuk, *J. Phys.: Condens. Matter* **2014**, *26*, 093001.

[17] W.-G. Wang, M. Li, S. Hageman, C. L. Chien, *Nat. Mater.* **2012**, *11*, 64.

[18] F. Bonell, S. Murakami, Y. Shiota, T. Nozaki, T. Shinjo, Y. Suzuki, *Appl. Phys. Lett.* **2011**, *98*, 232510.

[19] F. Matsukura, Y. Tokura, H. Ohno, *Nat. Nanotechnol.* **2015**, *10*, 209.

[20] B. Jiang, C. Li, V. Malgras, M. Imura, S. Tominaka, Y. Yamauchi, *Chem. Sci.* **2016**, *7*, 1575.

[21] L. Wang, Y. Yamauchi, *J. Am. Chem. Soc.* **2013**, *135*, 16792.

[22] D. Gu, F. Schüth, *Chem. Soc. Rev.* **2014**, *43*, 313.

[23] T. Wagner, S. Haffer, C. Weinberger, D. Klaus, M. Tiemann, *Chem. Soc. Rev.* **2013**, *42*, 4036.

[24] J. Zhang, C. M. Li, *Chem. Soc. Rev.* **2012**, *41*, 7016.

[25] T. E. Quickel, L. T. Schelhas, R. A. Farrell, N. Petkov, V. H. Le, S. H. Tolbert, *Nat. Commun.* **2015**, *6*, 6562.

[26] S. Gosh, *J. Magn. Magn. Mater.* **2011**, *323*, 552.

[27] E. Pellicer, A. Varea, S. Pané, B. J. Nelson, E. Menéndez, M. Estrader, S. Suriñach, M. D. Baró, J. Nogués, J. Sort, *Adv. Funct. Mater.* **2010**, *20*, 983.

[28] E. Pellicer, A. Varea, K. M. Sivaraman, S. Pané, S. Suriñach, M. D. Baró, J. Nogués, B. J. Nelson, J. Sort, *ACS Appl. Mater. Interfaces* **2011**, *3*, 2265.

[29] K. Bohinc, V. Kralj-lglic, A. Iglic, *Electrochim. Acta* **2001**, *46*, 3033.

[30] K. Nakamura, R. Shimabukuro, Y. Fujiwara, T. Akiyama, T. Ito, *Phys. Rev. Lett.* **2009**, *102*, 187201.

[31] C.-G. Duan, J. P. Velev, R. F. Sabirianov, Z. Zhu, J. Chu, S. S. Jaswal, E. Y. Tsymbal, *Phys. Rev. Lett.* **2008**, *101*, 137201.

[32] I. V. Ovchinnikov, K. L. Wang, *Phys. Rev. B* **2009**, *79*, 020402.

[33] J. M. Soler, E. Artacho, J. D. Gale, A. García, J. Junquera, P. Ordejón, D. Sánchez-Portal, *J. Phys.: Condens. Matter* **2002**, *14*, 2745.

[34] E. Artacho, E. Anglada, O. Diéguez, J. D. Gale, A. García, J. Junquera, R. M. Martin, P. Ordejón, J. M. Pruneda, D. Sánchez-Portal, J. M. Soler, *J. Phys.: Condens. Matter* **2008**, *20*, 064208.

[35] P. Bruno, *Phys. Rev. B* **1989**, *39*, 865.

[36] H. Wang, L. Wang, T. Sato, Y. Sakamoto, S. Tominaka, K. Miyasaka, N. Miyamoto, Y. Nemoto, O. Terasaki, Y. Yamauchi, *Chem. Mater.* **2012**, *24*, 1591.

[37] H. Wang, S. Ishihara, K. Ariga, Y. Yamauchi, *J. Am. Chem. Soc.* **2012**, *134*, 10819.

[38] V. Malgras, H. Ataee-Esfahani, H. Wang, B. Jiang, C. Li, K. C.-W. Wu, J. H. Kim, Y. Yamauchi, *Adv. Mater.* **2016**, *28*, 993.

[39] C. Li, B. Jiang, Z. Wang, Y. Li, Md. S. A. Hossain, J. H. Kim, T. Takei, J. Henzie, O. Dag, Y. Bando, Y. Yamauchi, *Angew. Chem. Int. Ed.* **2016**, *55*, 12746.

[40] G. Wanka, H. Hoffmann, W. Ulbricht, *Macromolecules* **1994**, *27*, 4145.

[41] N. Troullier, J. L. Martins, *Phys. Rev. B* **1991**, *43*, 1993.

[42] S. García-Gil, A. García, N. Lorente, P. Ordejón, *Phys. Rev. B* **2009**, *79*, 075441.

[43] J. P. Perdew, K. Burke, M. Ernzerhof, *Phys. Rev. Lett.* **1996**, *77*, 3865.

[44] L. Fernández-Seivane, M. A. Oliveira, S. Sanvito, J. Ferrer, *J. Phys.: Condens. Matter* **2006**, *18*, 7999.

[45] L. Fernández-Seivane, J. Ferrer, *Phys. Rev. Lett.* **2007**, *99*, 183401.

1701904 (8 of 8)

**ADVANCED
FUNCTIONAL
MATERIALS**

Supporting Information

Voltage-Induced Coercivity Reduction in Nanoporous Alloy Films: A Boost toward Energy-Efficient Magnetic Actuation

Alberto Quintana, Jin Zhang, Eloy Isarain-Chávez, Enric Menéndez, Ramón Cuadrado, Roberto Robles,* Maria Dolors Baró, Miguel Guerrero, Salvador Pané, Bradley J. Nelson, Carlos Maria Müller, Pablo Ordejón, Josep Nogués,* Eva Pellicer,* and Jordi Sort*

Supporting Information

Voltage-induced coercivity reduction in nanoporous alloy films: a boost towards energy-efficient magnetic actuation

Alberto Quintana, Jin Zhang, Eloy Isarain-Chávez, Enric Menéndez, Ramon Cuadrado, Roberto Robles[*], Maria Dolors Baró, Miguel Guerrero, Salvador Pané, Bradley J. Nelson, Carlos M. Müller, Pablo Ordejón, Josep Nogués[*], Eva Pellicer[*], Jordi Sort[*]
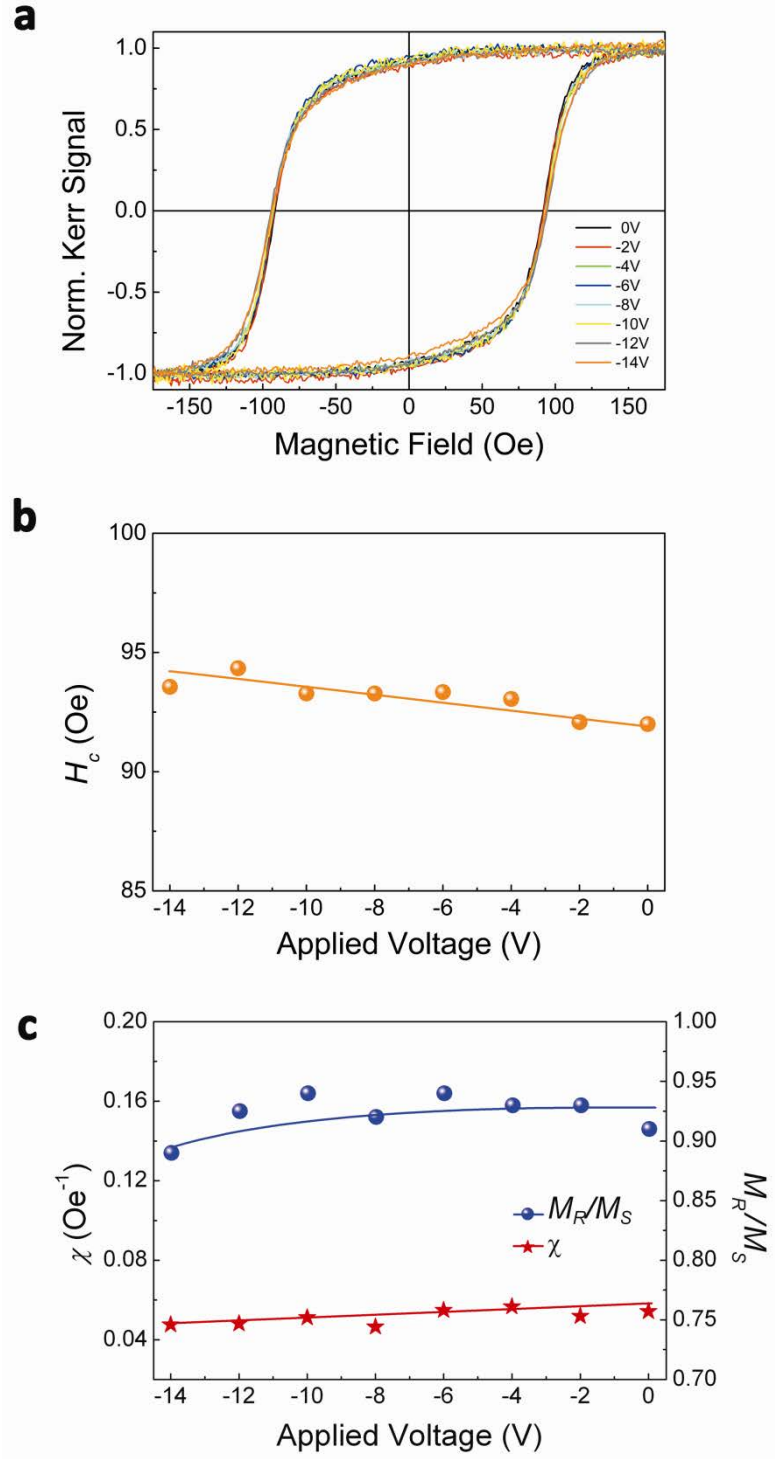
Figure S1. (a) Representative hysteresis loops of the nanoporous Cu-Ni films acquired under application of different negative voltage values. (b) Dependence of the coercivity, H_C, on the negative applied voltage. (c) Dependence of the susceptibility around coercivity (see definition in the text), χ, and the remanence-to-saturation magnetization ratio, M_R/M_S, as a function of negative voltage. Note that the lines in (b) and (c) are guides to the eye.

57

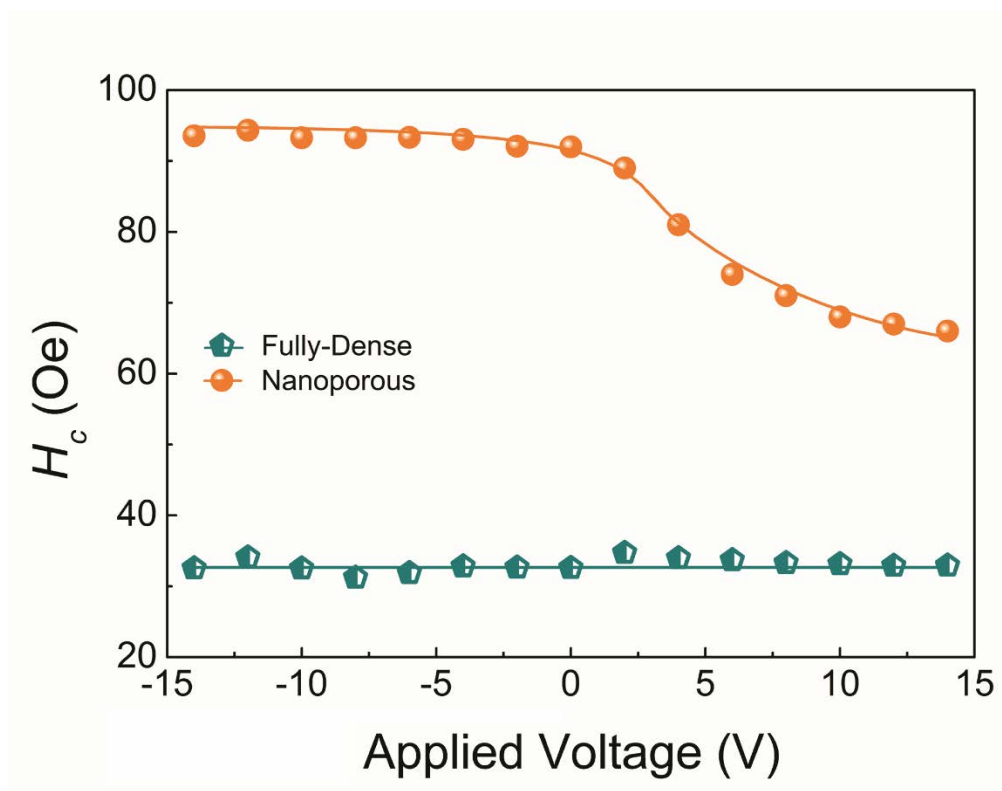**Figure S2**. Dependence of the coervivity, H_C, on the applied voltage (both for negative and positive values), for the fully-dense and nanoporous Cu-Ni electrodeposited films with the same composition ($Cu_{25}Ni_{75}$ at.%) and thickness (600 nm).
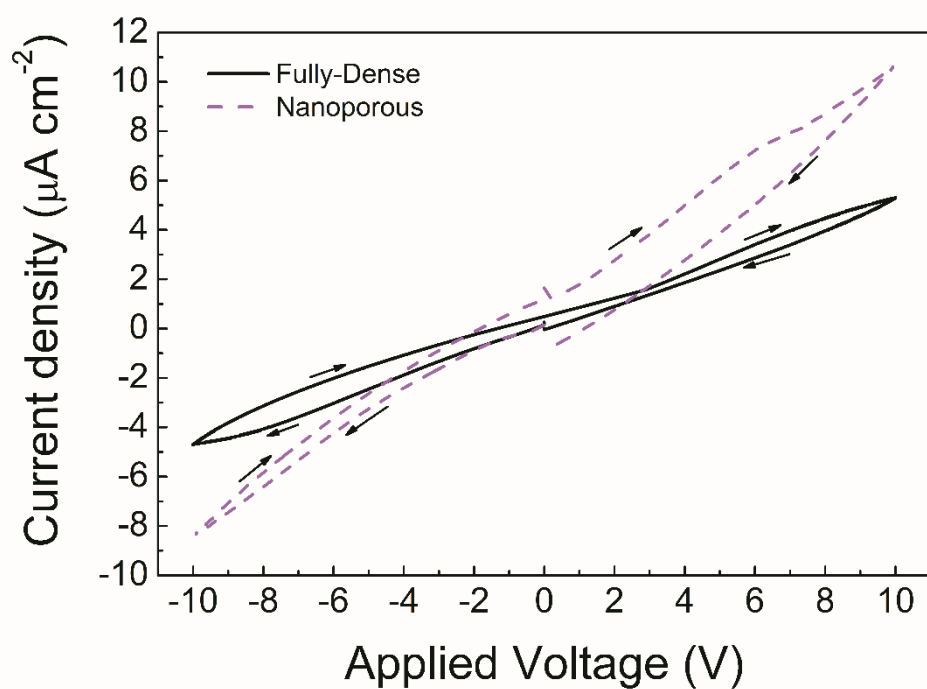
Figure S3. Cyclic voltammetry curves, measured while immersing the Cu-Ni films in the anhydrous electrolyte (propylene carbonate), for both nanoporous and fully-dense films.
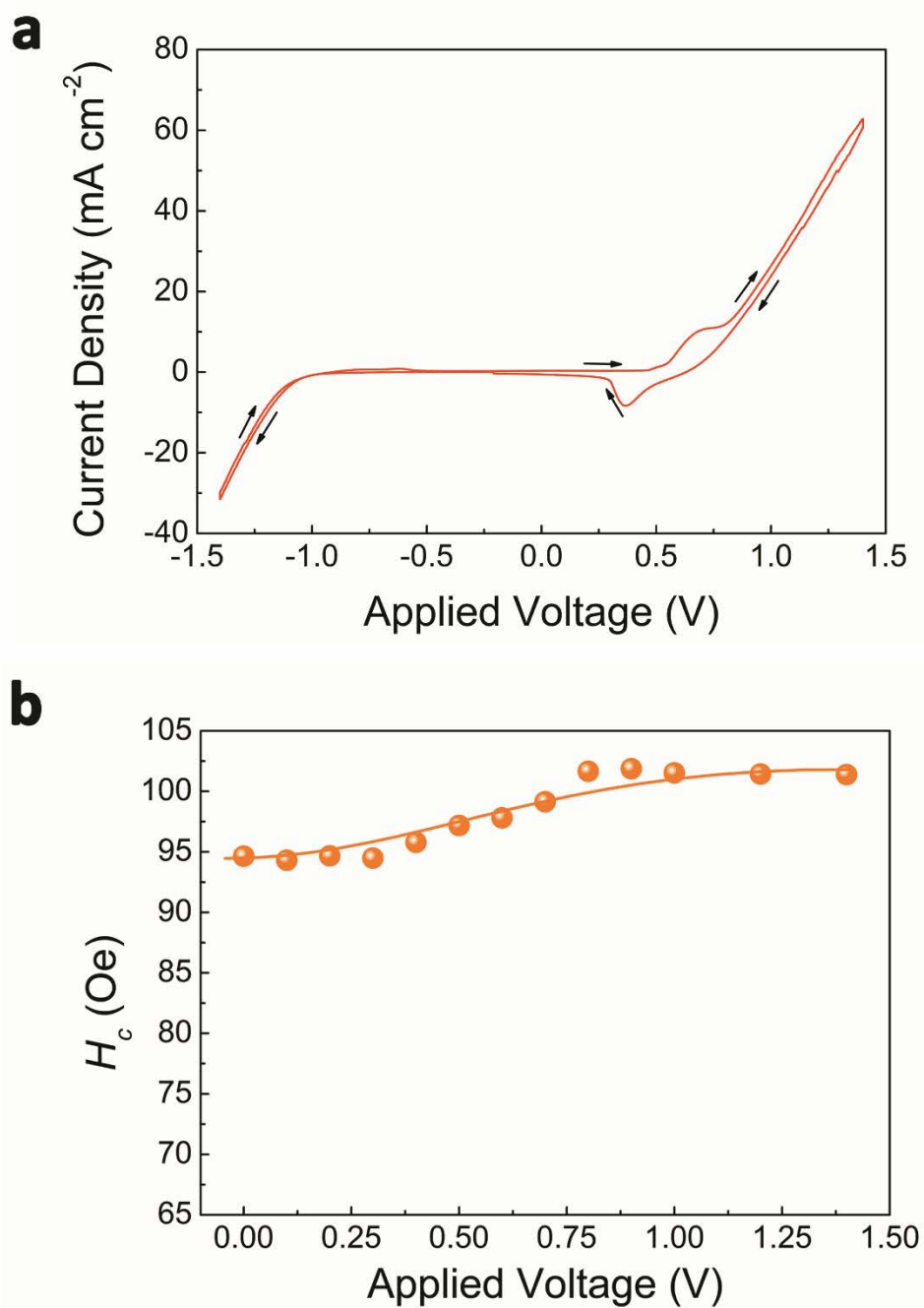
Figure S4. (a) Cyclic voltammetry curves from the nanoporous Cu-Ni films acquired while immersing the films in the aqueous electrolyte (0.1M NaOH). (b) Dependence of the coercivity, H_C, on the applied voltage when using the aqueous electrolyte. The line in (b) is a guide to the eye.
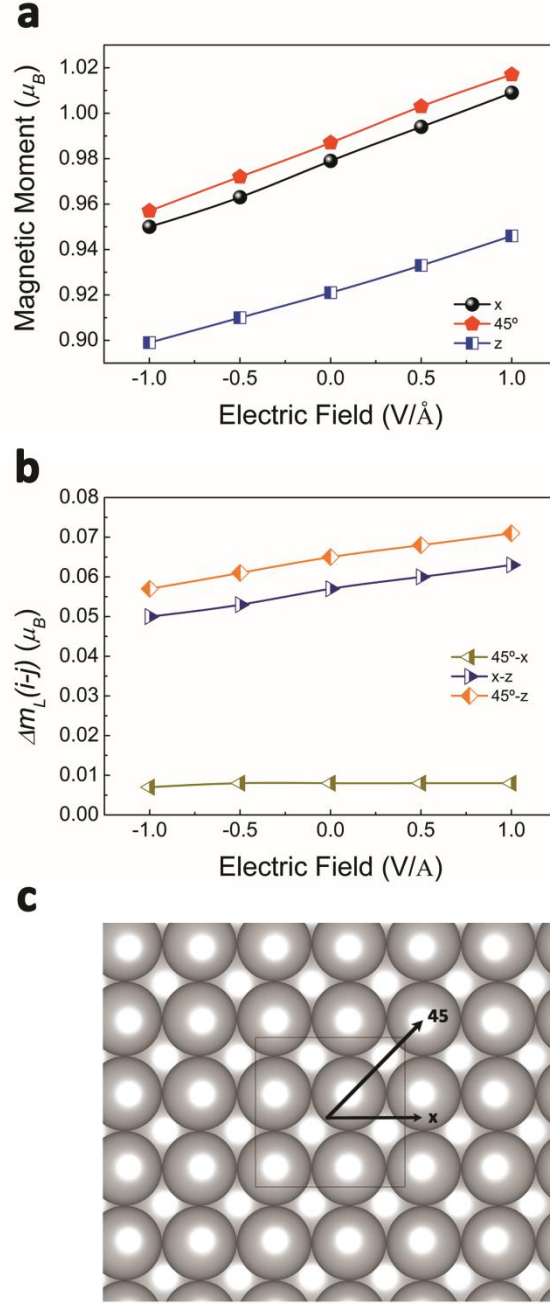
Figure S5. (a) Dependence of the magnetic moment oriented along the given directions of the (001) surface with the applied electric field. Only the surface Ni atoms are considered. The calculated surface magnetoelectric coefficients are $\alpha_S \approx 5.5 \times 10^{-14}$ G cm$^2 \cdot$V^{-1} in-plane and $\alpha_S \approx 4.3 \times 10^{-14}$ G cm$^2 \cdot$V^{-1} out-of-plane. (b) Orbital moment differences Δm_L between the indicated directions of the (001) surface for the surface Ni atoms. (c) In-plane directions considered for the (001) surface. The lines in (a) and (b) are guides to the eye.

Figure S6. Magnetic density of states (MDOS) for the surface Ni atoms of one considered (111) configuration. MDOS is defined as the DOS for spin up minus DOS for spin down. Changes of the MDOS with the applied electric field illustrate the origin of the magnetoelectric effect.

2.2 Redox control of magnetization in nanoporous CuNi alloys

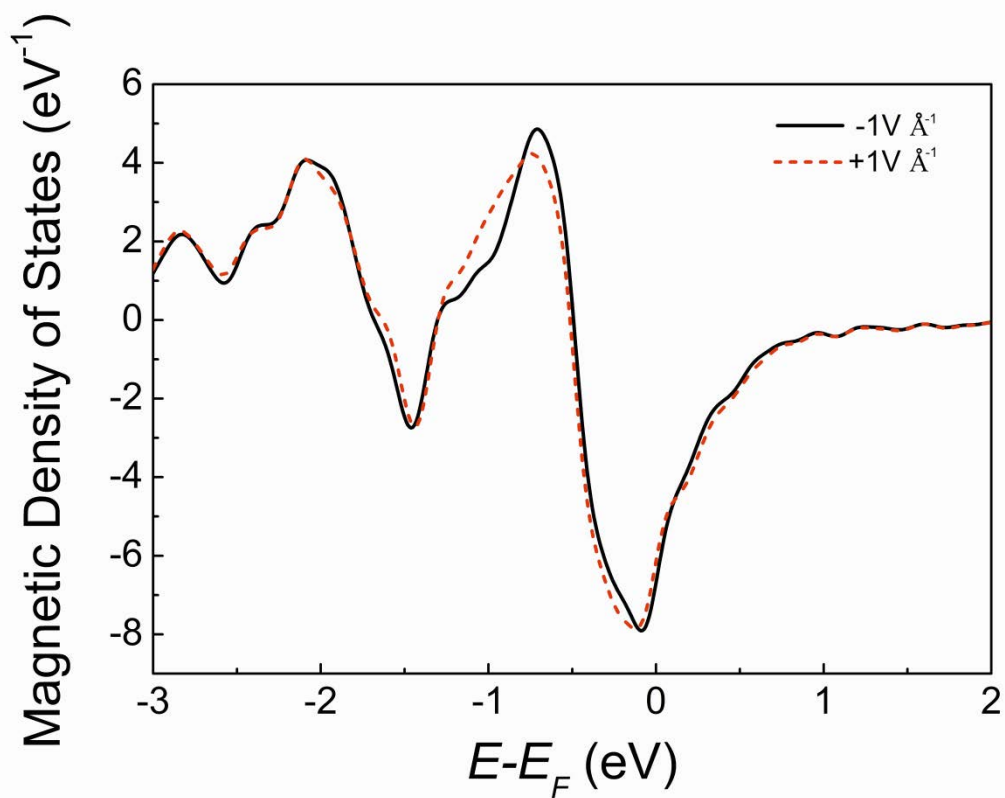In this article, we demonstrate that the magnetization of a nanoporous $Cu_{20}Ni_{80}$ (at. %) film can be tailored by voltage-controlled redox processes in a protic liquid medium (1M NaOH).

The sample was prepared by surfactant-assisted electrodeposition and consists of a FCC CuNi solid solution. Morphological cross-section characterization carried out by scanning electron microscopy (SEM) showed that the film consists of a stack of elongated nanoparticles. TEM and STEM confirmed that the nanoporosity is preserved along the sample thickness.

In contrast to the previous article, a protic aqueous solution (i.e., oxidative medium) was employed to induce electro-oxidation processes in a controlled manner. Upon positive bias, magnetic moment at saturation enhancements up to 33 % can be achieved by tailoring the magnitude of the applied voltage. This is ascribed to the selective electrochemical oxidation of the Cu counterpart, as confirmed by synchrotron XRD and X-Ray photoelectron spectroscopy (XPS). Specifically, synchrotron XRD revealed a shift towards higher 2θ angles of the CuNi peaks which is consistent with the occurrence of a Ni-enriched alloy.

This process can be fully reversed by negative biasing. This reversibility takes place by the electrochemical reduction of Cu oxides and hydroxides back towards metallic Cu which, in spite of the miscibility gap known for the CuNi system, gets dissolved again in the CuNi solid solution. This is consistent with theoretical studies which demonstrate the shift in the miscibility gap to temperatures below room temperature in nanostructured systems, such as ours, allowing for Cu and Ni miscibility at room temperature.

The use of nanoporous morphologies, with an increased surface-area-to-volume ratio, enhance these redox effects which are of interfacial nature and, moreover, allow for the propagation of the effect all along the sample.

NANO MICRO
small

Tunable Magnetism in Nanoporous CuNi Alloys by Reversible Voltage-Driven Element-Selective Redox Processes

Alberto Quintana,[1,*] Enric Menéndez,[1,*] Eloy Isarain-Chávez,[1] Jordina Fornell,[1] Pau Solsona,[1]

François Fauth,[2] Maria Dolors Baró,[1] Josep Nogués,[3,4] Eva Pellicer,[1] and Jordi Sort[1,4,*]

1.- Departament de Física, Universitat Autònoma de Barcelona, E-08193 Cerdanyola del Vallès, Spain.

2.- CELLS-ALBA. BP1413, Cerdanyola del Vallès, 08290 Barcelona, Spain.

3.- Catalan Institute of Nanoscience and Nanotechnology (ICN2), CSIC and The Barcelona Institute of Science and Technology. Campus UAB, Cerdanyola del Valles, E-08193 Barcelona, Spain.

4.- ICREA. Pg. Lluís Companys 23, E-08010 Barcelona, Spain.

Correspondence should be addressed to: alberto.quintana@uab.cat; enric.menendez@uab.cat; jordi.sort@uab.cat.

Tunable Magnetism in Nanoporous CuNi Alloys by Reversible Voltage-Driven Element-Selective Redox Processes

Alberto Quintana,* Enric Menéndez,* Eloy Isarain-Chávez, Jordina Fornell, Pau Solsona, François Fauth, Maria Dolors Baró, Josep Nogués, Eva Pellicer, and Jordi Sort*

Voltage-driven manipulation of magnetism in electrodeposited 200 nm thick nanoporous single-phase solid solution $Cu_{20}Ni_{80}$ (at%) alloy films (with sub 10 nm pore size) is accomplished by controlled reduction-oxidation (i.e., redox) processes in a protic solvent, namely 1 M NaOH aqueous solution. Owing to the selectivity of the electrochemical processes, the oxidation of the CuNi film mainly occurs on the Cu counterpart of the solid solution, resulting in a Ni-enriched alloy. As a consequence, the magnetic moment at saturation significantly increases (up to 33% enhancement with respect to the as-prepared sample), while only slight changes in coercivity are observed. Conversely, the reduction process brings Cu back to its metallic state and, remarkably, it becomes alloyed to Ni again. The reported phenomenon is fully reversible, thus allowing for the precise adjustment of the magnetic properties of this system through the sign and amplitude of the applied voltage.

1. Introduction

Since the pioneering studies on magnetoelectric effects in the 50's and 60's, a flurry of research has been undertaken on the electric control of magnetism.[1] Conventional magnetoelectric studies focused on strain-mediated systems, in which the magnetic properties were modified by the interfacial coupling between piezoelectric and magnetostrictive counterparts.[2] However, the strain caused by the voltage in these heterostructured systems limits the applications of this phenomenon

in technological devices due to fatigue-induced mechanical failure. Controlling magnetism with electric fields without involving strain is an emerging field of research and might boost current magnetic technologies. Novel applications such as low power or multilevel voltage controlled magnetic memories are envisaged.[3]

Due to the intrinsic coupling between ferroic orders, single-phase multiferroics are the most promising candidates for magnetoelectric applications not mediated by strain. However, so far, the observed magnetoelectric coupling is weak, thus hindering its use in real devices.[4] Moreover, the amount of intrinsic multiferroic materials is rather limited since the underlying physical mechanisms of ferroelectricity and magnetism are different and tend to exclude each other.[5] To overcome these drawbacks, several approaches to electrically tailor magnetism are being proposed. For example, another route consists in the injection of electrostatic charges to a ferromagnetic material in order to modify its electronic band structure and, consequently, its magnetic anisotropy and magnetization.[6] This is commonly accomplished by preparing a condenser-like configuration in which a dielectric material is sandwiched between the ferromagnetic material of interest and a metallic electrode. Materials with a high dielectric constant are preferred, with the aim of being able to accumulate large amounts of electrostatic charges. However, some of these dielectrics also exhibit high ion mobility, e.g., HfO_2 or Gd_2O_3. In this case, oxygen diffusion (and the concomitant oxidation–reduction processes) may play a predominant role, even overcoming charge accumulation effects during voltage actuation and, thus, becoming the main factor determining the overall magnetic properties of the system. Similar phenomena have been reported in ferromagnetic/ferroelectric interfaces prior and after voltage application.[7] Actually, controlled plasma oxygen has been utilized to externally promote oxygen migration and tailor perpendicular magnetic anisotropy in Pt/Co/AlO_x systems via Co–O hybridization at the interface between Co and Al.[8] A reversible change of the perpendicular magnetic anisotropy by voltage actuation has been reported in Pt/Co/GdO_x layers due to the diffusion of O^{2-} from the oxide to the cobalt layer.[9] The voltage control of oxygen migration (i.e., controlled oxidation and reduction) with the aim of modifying magnetism in both solid state[9,10] and liquid[11] ferromagnetic/insulating interfaces has evidenced very satisfactory results

A. Quintana, Dr. E. Menéndez, Dr. E. Isarain-Chávez, Dr. J. Fornell,
Dr. P. Solsona, Prof. M. D. Baró, Dr. E. Pellicer, Prof. J. Sort
Departament de Física
Universitat Autònoma de Barcelona
Cerdanyola del Vallès, E-08193 Barcelona, Spain
E-mail: Alberto.quintana@uab.cat; Enric.menendez@uab.cat;
Jordi.sort@uab.cat
Dr. F. Fauth
CELLS-ALBA
BP1413, Cerdanyola del Vallès, 08290 Barcelona, Spain
Prof. J. Nogués
Catalan Institute of Nanoscience and Nanotechnology (ICN2)
CSIC and The Barcelona Institute of Science and Technology
Campus UAB, Cerdanyola del Vallès, E-08193 Barcelona, Spain
Prof. J. Nogués, Prof. J. Sort
Institució Catalana de Recerca i Estudis Avançats (ICREA)
Pg. Lluís Companys 23, E-08010 Barcelona, Spain

(iD) The ORCID identification number(s) for the author(s) of this article can be found under https://doi.org/10.1002/smll.201704396.

and has led to the emergence of magneto-ionics as a means to induce magnetoelectric effects.

In general, when a material is subjected to an electric field, charge accumulation, redox processes, and magnetostriction (the latter only in case piezoelectric materials are involved) may simultaneously occur. Disentangling these contributions is essential to further control magnetism by voltage actuation. All these phenomena are interface-driven and, consequently, are expected to be maximized in materials with a high surface area-to-volume ratio, a parameter which is largely exploited in a widespread range of applications.[12] Although this is typically achieved in ultrathin films, nanoporous magnetic alloys, with extremely large surface area-to-volume ratios, may be an appealing alternative.[13] However, so far, the magnetoelectric effects in nanoporous materials have been rather overlooked.

In a previous study, we showed that the coercivity of the CuNi nanoporous alloys can be drastically reduced by voltage actuation using an organic aprotic (and water-free) electrolyte, essentially due to purely electrically induced changes in the magnetic anisotropy. This effect could be utilized to significantly reduce energy consumption in magnetically actuated devices. In this article, we present a voltage-driven electrochemical approach to tailor not the coercivity but the overall magnetization of the ferromagnetic nanoporous $Cu_{20}Ni_{80}$ films using an aqueous electrolyte (i.e., via controlled electrochemical redox processes). The strong element selectivity of the oxidation process allows for an enhancement of the magnetic moment at saturation up to 33%. This effect turns out to be fully reversible by changing the sign of the applied voltage. Besides the interest of these results in the field of magnetic devices and spintronics, our work also contributes to extend the potential applications of the porous materials, so far mainly employed in fields such as catalysis,[14] water cleaning,[15] self-cleaning and superhydrophobic surfaces,[16] and energy storage and conversion.[17]

2. Results and Discussion

Figure 1a shows a representative SEM image of an as-prepared nanoporous $Cu_{20}Ni_{80}$ film. A homogeneous granular morphology is observed at the surface of the film. The size of these granules typically ranges between 50 and 200 nm. A magnified image (Figure 1b) reveals that these clusters are, in fact, nanoporous, i.e., they consist of agglomerated sub 10 nm nanoparticles. The morphology along sample thickness was characterized by scanning transmission electron microscopy (STEM) and TEM (Figure 1c,d, respectively). STEM reveals that the porosity spans the whole thickness of the film, where the bottom bright layer in the STEM image corresponds to the Au surface. The nanoporous morphology is further confirmed by high-resolution TEM (Figure 1d), from which the average pore size can be estimated to be between 5 and 7 nm. Compositional analyses performed by energy dispersive X-ray analysis (EDX) give Cu and Ni contents of 20 and 80 at%, respectively.

The as-prepared samples were characterized from a structural viewpoint by synchrotron grazing incidence X-ray diffraction (GIXRD) at the ALBA light source facility. As can be seen in **Figure 2**, the GIXRD pattern of an as-prepared sample exhibits several X-ray diffraction (XRD) peaks arising from face
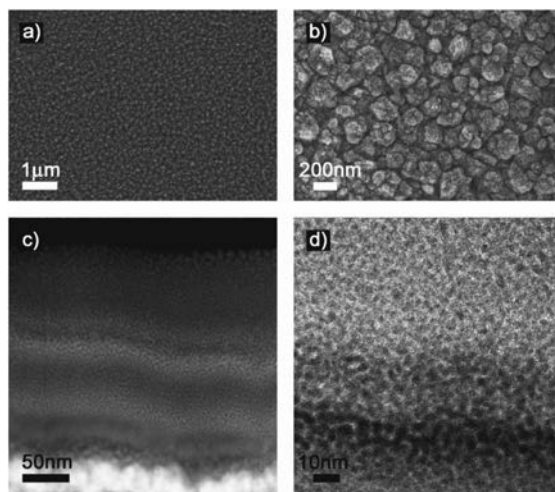

Figure 1. a) Low-magnification and b) high-magnification SEM images of the top surface of a nanoporous $Cu_{20}Ni_{80}$ film. c) STEM and d) TEM images of the cross-section of the same film.

centered cubic $Cu_{20}Ni_{80}$, indicating the polycrystalline nature of the film. No additional peaks from pure Cu or Ni are observed, ruling out phase separation and, thus, indicating that the Cu and Ni grow forming a solid solution.

In order to investigate the voltage-driven redox processes, in situ magneto-optic Kerr effect measurements at selected oxidation/reduction voltages were carried out in liquid medium. Prior to the first measurement (i.e., 0 V), the sample was submerged in the electrolyte during 30 min in order to allow the solution (1 M NaOH) to wet the nanopores by capillary action. Subsequently, hysteresis loops were acquired at increasingly applied voltages in steps of 0.1 V, up to a maximum applied voltage $V = +1.2$ V. The as-prepared sample exhibits a rather square-shaped loop with a coercivity around 100 Oe, indicating an in-plane easy axis. As can be seen in **Figure 3**a, while the coercivity
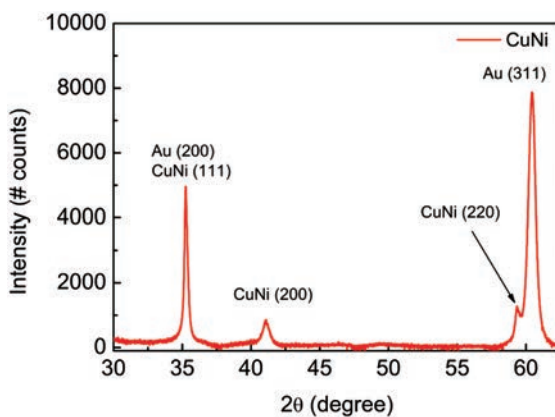

Figure 2. Synchrotron grazing incidence XRD pattern corresponding to the nanoporous $Cu_{20}Ni_{80}$ film.
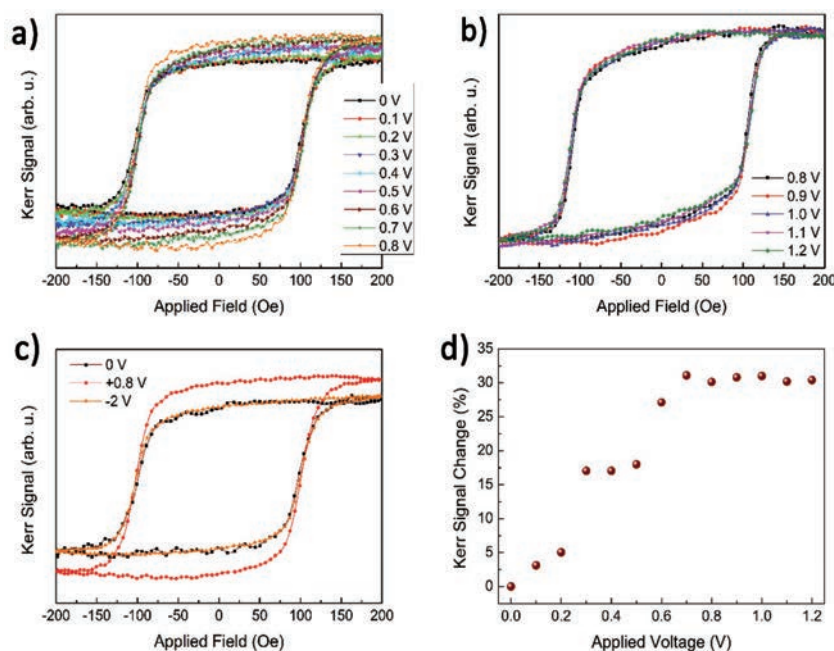
Figure 3. a) MOKE hysteresis loops taken under the application of increasing positive voltages, up to $V = 0.8$ V. b) MOKE hysteresis loops for applied voltages larger than 0.8 V. c) MOKE hysteresis loops corresponding to the pristine (0 V), oxidized (+0.8 V), and reduced (−2 V) states. d) Dependence of the Kerr signal change (in %) on the applied voltage. Note that, for all hysteresis loops, the Kerr signal was normalized by the signal measured in absence of the magnetic field, so that the differences are indeed representative of variations in the magnetic moment, not simply due to the changes in the optical reflection.

remains rather unaltered with the applied voltage (relative changes are below 5%), the Kerr signal (i.e., the amplitude of the magneto-optic Kerr effect (MOKE) signal) monotonously increases with the applied voltage up to $V = +0.8$ V. Figure 3b shows that no significant changes are observed beyond +0.8 V, confirming that the Kerr signal tends to saturate at +0.8 V. Remarkably, the pristine magnetic state (i.e., same coercivity and Kerr signal) can be recovered by applying negative voltages. Full recovery is achieved after applying −2 V for 10 min (Figure 3c). Since, in a first approximation, the Kerr signal can be considered to be proportional to the magnetic moment,[18] the increase in Kerr signal with positive voltages can be understood as an increase of the magnetic moment in the film volume probed by MOKE. This change in Kerr signal can be quantified as follows (see scheme in Figure S1, Supporting Information)

$$\% \text{ change} = \left(\left(A_k(V) - A_k(0) \right) / A_k(0) \right) \times 100 \qquad (1)$$

where $A_k(V)$ is the difference in Kerr signal between positive and negative saturation and $A_k(0)$ is the Kerr signal amplitude at 0 V. Figure 3d represents the change in Kerr signal as a function of the positive applied voltage. The maximum relative increase in the Kerr signal amplitude is 33%, for an applied voltage $V = +0.8$ V. It is worth noting that the coercivity remains rather unaltered upon voltage application, evidencing that the intrinsic porous microstructure dominates over other parameters, such as composition or crystallite size.[16]

In order to elucidate if any structural change is responsible for the observed magneto-electric effect, synchrotron XRD measurements were carried out ex situ in grazing incidence (2° as angle of incidence) mode for the as-prepared sample, after subjected to oxidation at +0.8 V and the sample reduced using −2 V.

As can be seen in **Figure 4**, upon oxidation, the (220) $Cu_{20}Ni_{80}$ GIXRD peak significantly shifts toward higher 2θ
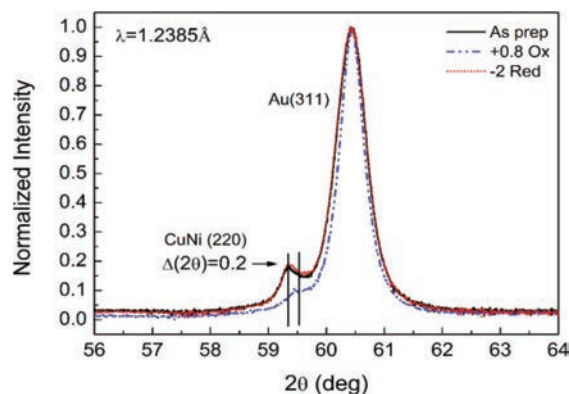

Figure 4. Detail of the synchrotron grazing incidence XRD peaks corresponding to the CuNi (220) and Au (311) of an as-prepared sample, a sample subjected to +0.8 V (oxidized) and a sample subjected to −2 V (reduced). The normalization of the intensity has been done by dividing the chosen 2θ window by the intensity of the (311) Au peak.

ADVANCED
SCIENCE NEWS
www.advancedsciencenews.com

NANO · MICRO
small
www.small-journal.com

angles (0.2° difference), indicating a decrease of the lattice cell parameter which could be ascribed to a change in composition in the Cu–Ni solid solution, more specifically, to an increase in the Ni content.[19] This is consistent with the obtained magnetic results since an increase in the Ni content would explain the enhancement of Kerr signal (i.e., magnetic moment) upon the application of positive voltages. Such an increase of Ni content would indicate that Cu preferentially oxidizes during the application of a positive voltage.[20] Negem and Nady studied the oxidation of nanocrystalline Cu–Ni alloys in 1.0 M KOH solution and found that the oxidation peaks recorded in the cyclic voltammetry studies were related to the formation of oxidized Cu species ($Cu(OH)^{ads-} \rightarrow Cu_2O \rightarrow Cu(OH)_2$). Parallel cyclic voltammetry studies with electrodeposited pure Ni counterpart showed the absence of oxidation peaks in the anodic scan.[21] Interestingly, when negative voltages are applied, the (220) Cu–Ni GIXRD peak shifts back to the initial position, suggesting that the negative voltage not only induces reduction of the previously oxidized atoms but also the metallic Cu reincorporates into the Cu–Ni solid solution. In other words, the original composition ($Cu_{20}Ni_{80}$) is recovered. As a result, the magnetic properties of the as-deposited pristine films are also recovered (Figure 3c).

We have further analyzed the patterns by Rietveld refinement (Figure S2, Supporting Information) using the MAUD software[22] to extract structural information on the crystallite size (average coherently diffracting domain) of the nanoporous CuNi film before and upon voltage actuation. As can be seen in Table S1 (Supporting Information), the oxidation process (i.e., +0.8 V) results in a decrease of crystallite size from 22 nm (crystallite size of the as-prepared sample) down to 16 nm. Interestingly, the crystallite size fully recovers the pristine value after applying a voltage of –2 V (reduction), suggesting that the redox processes are grain boundary mediated and evidencing the high reversibility of the process. It is worth mentioning that, in all samples, the crystallite size is larger than the interpore distance which is around 4 nm. This evidences that the crystallinity is preserved independently of the porosity over the extension of the crystallite size which is roughly five times larger than the interpore distance.[23] As can be seen in Table S2 (Supporting Information), the crystallite size in the Au of the different samples does not change, indicating that the buffer Au layer does not play any role in the redox processes.

Further insight from a structural point of view have been obtained by the TEM characterization of the sample cross-section (Figure S2, Supporting Information), which reveals that the oxidation process is accompanied by the formation of Cu oxides and Cu and Ni hydroxides. This is also confirmed by Fourier transform infrared spectroscopy (FT-IR) measurements (Figure S4, Supporting Information). Indeed, the as-prepared sample shows an almost featureless pattern whereas, upon oxidation, a broad band appears around 3600 cm^{-1}, which corresponds to O–H stretching modes. Moreover, a new band appears around 690 cm^{-1} which is characteristic of Cu and Ni oxides or Ni hydroxides,[24] in agreement with the TEM analyses. Further characterization was carried out by ex situ (i.e., not in the solution) X-ray photoelectron spectroscopy (XPS) on an as-prepared sample, a sample oxidized at +0.8 V

and a sample first subjected to +0.8 V and then subsequently reduced at –2 V. The voltage protocols to treat the samples were performed in the same cell setup used to apply voltage in the MOKE apparatus and immediately measured. **Figure 5** shows the deconvoluted core-level XPS spectra of the Cu 2p and Ni 2p peaks. All the spectra were fitted assuming a linear background and employing Gaussian functions. Deconvolution was performed according to the work by Biesinger et al.[25] Several parameters resulting from the multiplet peak fitting (binding energy, area, half-width half-maximum, and the fraction of the spectra corresponding to each compound) are summarized in Tables S3 and S4 (Supporting Information) for Cu 2p and Ni 2p, respectively. Figure 5 shows that the spectra can be described assuming the existence of up to 4 counterparts. Specifically, metallic Cu, Cu_2O, CuO, and $Cu(OH)_2$ need to be considered for the deconvolution of the Cu $2p_{3/2}$ spectra while metallic Ni, NiO, $Ni(OH)_2$, and NiOOH contribute to the Ni $2p_{3/2}$.

Already for the as-prepared sample, NiO, CuO, and Cu_2O species are present in the outmost surface, which may arise from the natural tendency toward passivation of Cu and Ni.[26] Cu and Ni are susceptible to oxidation in air even at room temperature and the occurrence of a nanostructured porous architecture would likely enhance surface oxidation. $Ni(OH)_2$, NiOOH, and $Cu(OH)_2$ could also form during the rinsing step in water aimed to remove electrolyte residues after electroplating[27] or as a side reaction product during electrodeposition, due to local pH alkalinization, especially when plating at high overpotentials.[28]

Two clear trends are identified upon careful analysis of the XPS (**Table 1**). For the Cu $2p_{3/2}$ transition, the contribution of metallic Cu and Cu_2O species is drastically reduced when the $V = +0.8$ V is applied. Instead, the $Cu(OH)_2$ signal is remarkably enhanced. When $V = -2$ V is applied, metallic Cu and Cu_2O contributions increase notably, particularly that of metallic Cu. Indeed, the metallic Cu signal is even clearer than in the as-prepared state. The increase in the relative amount of Cu_2O and the concomitant decrease of CuO and $Cu(OH)_2$ amounts are understandable taking into account that all the reduction processes from CuO and $Cu(OH)_2$ to Cu involve Cu_2O as an intermediate step.[20] For the Ni $2p_{3/2}$ transition, during the oxidation process NiOOH is favored at the expense of $Ni(OH)_2$ and NiO, but not by oxidizing metallic Ni. Following an inverse tendency, when the reduction process is carried out, NiOOH is transformed into $Ni(OH)_2$. This means that the Cu-based species are prone to significantly change upon voltage application, whereas the Ni-based compounds remain rather unaltered, in agreement with the fact that the oxidation and reduction is driven by the Cu counterpart in the alloy. Indeed, it has been claimed that NiO and $Ni(OH)_2$ constitute highly stable passive layers, being thus less susceptible to undergo changes upon the application of negative/positive potentials.[21]

Remarkably, our results reveal that, contrary to common wisdom, oxidation of the Cu–Ni alloy leads to an increase of magnetic moment (rather than a decrease, as it would be the case in most magnetic metals and metallic alloys upon oxidation). Such counterintuitive behavior can be explained as being due to the selective oxidation of Cu during the application of positive voltages on the Cu–Ni solid solution. It is also worth mentioning that voltage actuation does not result in phase
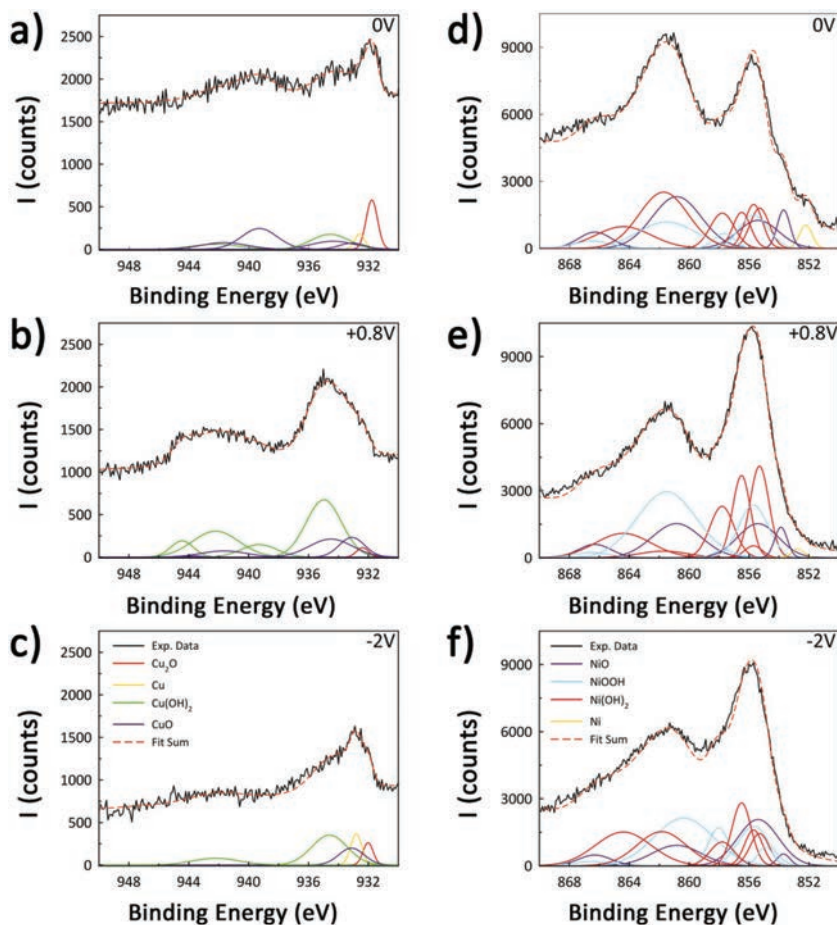
**ADVANCED
SCIENCE NEWS**
www.advancedsciencenews.com

NANO · MICRO
small
www.small-journal.com

Figure 5. Deconvoluted XPS spectra for the pristine (0 V), oxidized (+0.8 V), and reduced state (–2 V) for a–c) Cu, and d–f) Ni.

separation (i.e., Ni-rich and Cu-rich regions). Therefore, voltage can be used to reversibly modify the composition of the Cu–Ni solid solution. Moreover, in spite of the positive enthalpy of mixing of the Cu–Ni system, during the reduction process Cu gets incorporated to the solid solution. It is known that the Cu–Ni bulk alloys present a miscibility gap for temperatures below 600 K.[29] However, in recent works, it is suggested that in nanoparticles with sizes below 10 nm, the driving forces dominating segregation are much weaker, thus eventually lowering the miscibility gap to below room temperature.[30] Hence, it is a plausible hypothesis that the metallic Cu obtained for negative voltages gets dissolved again in the Cu–Ni solid solution at

room temperature owing to the narrow pore walls and the high surface area-to-volume ratio of the investigated material.

3. Conclusions

Voltage control of magnetism in a nanoporous Cu–Ni solid solution thin film (with atomic composition $Cu_{20}Ni_{80}$) has been successfully achieved in a reversible manner by selectively oxidizing/reducing the copper from the nanoporous CuNi alloy in a 1 M NaOH electrolyte. A maximum change in the Kerr signal amplitude of 33% is reached after application of + 0.8 V.

Table 1. Summary of the area (in %) for each metallic element or compound calculated from the deconvoluted XPS spectra.

	Cu	Cu_2O	CuO	$Cu(OH)_2$	Ni	NiO	NiOOH	$Ni(OH)_2$
0 V	5%	18%	26%	50%	2%	28%	27%	43%
+0.8 V	1%	1%	27%	71%	1%	22%	42%	35%
–2 V	15%	10%	18%	58%	0%	22%	34%	43%

**ADVANCED
SCIENCE NEWS**
www.advancedsciencenews.com

**NANO · MICRO
small**
www.small-journal.com

The voltage-driven compositional changes in the nanoporous alloy are confirmed by synchrotron X-ray diffraction. Specifically, the Cu-mediated redox processes result in a reversible shift of the $Cu_{20}Ni_{80}$ peaks toward higher/lower 2θ values when oxidizing/reducing, respectively. This is consistent with an increase/decrease of the Ni content in the solid solution. X-ray photoelectron spectroscopy further corroborates the oxidation of Cu by means of the formation of $Cu(OH)_2$ under positive voltages, whereas Ni oxidation states at the surface remain rather unaffected by voltage. Full reduction of the copper hydroxide is achieved when applying –2 V. Remarkably, upon application of negative voltages, Cu is reincorporated into the Cu–Ni solid solution and does not form any secondary phase, hence allowing for the full reversibility of the process.

4. Experimental Section

200 nm thick $Cu_{20}Ni_{80}$ films were electrodeposited onto Au (100 nm)/Ti (10 nm)/Si substrates using a thermostatized three-electrode cell in a PGSTAT302N Autolab potentiostat/galvanostat (Ecochemie). A platinum spiral served as a counter electrode and a double junction Ag|AgCl (E = +0.210 V/standard hydrogen electrode) with 3 M KCl inner solution and 1 M Na_2SO_4 outer solution was employed as a reference electrode. Substrates were cleaned with acetone, isopropanol, and Milli-Q water. An electrolyte (100 mL) consisting of 0.2 M $Ni(CH_3COO)_2\cdot 4H_2O$, 0.02 M $CuSO_4.5H_2O$, and 8 g L^{-1} of poly(ethylene oxide)-block-poly(propylene oxide)-block-poly(ethylene oxide) (PEO-PPO-PEO) tri-block copolymer was employed. The bath temperature was set at 30 °C and the pH was kept at 6. The deposition was galvanostatically performed at a constant current density of –80 mA cm^{-2} during 120 s under mild agitation (200 rpm). The concentration of PEO-PPO-PEO tri-block copolymer was chosen to be above the critical micellar concentration (cmc), which at 30 °C lays between 1×10^{-3} and 4×10^{-3} wt%.[31] During the electrodeposition process, the micelles adsorb on the cathode acting as a structure directing agent and hence inducing nanometric porosity (templating). Mild agitation favors the mass transport of electroactive species toward the cathode. The bath was deaerated before each deposition with N_2 to get rid of oxygen.

In order to perform in situ magnetic measurements, a home-made cell setup was employed.[13] Voltage was applied between the nanoporous CuNi film and a platinum wire. A 1 M NaOH solution was used to promote the occurrence of oxidation–reduction events on the CuNi film. The in situ in-plane magnetic properties were characterized at room temperature by MOKE (Durham Magneto-Optics setup) while applying a ramp voltage. The voltage was externally applied with an Agilent B2902A power supply.

The as-prepared samples and the samples subjected to different voltages were ex situ characterized from morphological and structural viewpoints by scanning and transmission electron microscopies (SEM and TEM, respectively), EDX and XRD using Cu Kα radiation, including synchrotron XRD using a wavelength of 1.2385 Å. FT-IR measurements have been performed in a Hyperion 2000 FT-IR microscope in reflection mode with a 15× IR Schwarzschild objective. SEM observations were carried out in a Zeiss Merlin microscope operated at 7 keV, whereas TEM characterization was performed on the cross section of the nanoporous films using a FEI Tecnai G2 F20 microscope operated at 200 kV. The composition was evaluated by EDX at 15 kV and 1 nA. GIXRD using synchrotron radiation was performed at the BL04-MSPD beamline of the ALBA synchrotron light facility. The angle of incidence was chosen to be 2° in order to fully probe the porous layer while minimizing the contribution from substrate. Data were collected in reflection mode using the position sensitive detector MYTHEN.[32]

XPS analyses were performed in a PHI 5500 Multitechnique System (from Physical Electronics) spectrometer, equipped with a monochromatic X-ray source (Al Kα line with and energy of 1486.6 eV

and 350 W), placed perpendicular to the analyzer axis and calibrated using the $3d_{5/2}$ line of Ag with a full-width at half-maximum of 0.8 eV. The analyzed area was a 0.6 mm^2 for each sample. Charging effects were corrected by referencing the binding energies to that of the adventitious C1s line at 284.8 eV.

Conflict of Interest

The authors declare no conflict of interest.

[1] a) W. Eerenstein, N. D. Mathur, J. F. Scott, *Nature* **2006**, *442*, 759; b) F. Matsukura, Y. Tokura, H. Ohno, *Nat. Nanotechnol.* **2015**, *10*, 209.

[2] R. O. Cherifi, V. Ivanovskaya, L. C. Phillips, A. Zobelli, I. C. Infante, E. Jacquet, V. Garcia, S. Fusil, P. R. Briddon, N. Guiblin, A. Mougin, A. A. Ünal, F. Kronast, S. Valencia, B. Dkhil, A. Barthélémy, M. Bibes, *Nat. Mater.* **2014**, *13*, 345.

[3] a) M. Bibes, A. Barthélémy, *Nat. Mater.* **2008**, *7*, 425; b) J.-M. Hu, Z. Li, L.-Q. Chen, C.-W. Nan, *Nat. Commun.* **2011**, *2*, 553.

[4] N. A. Hill, *J. Phys. Chem. B* **2000**, *104*, 6694.

[5] N. Izyumskaya, Y. Alivov, H. Morkoç, *Crit. Rev. Solid State Mater. Sci.* **2009**, *34*, 89.

[6] M. Weisheit, S. Fahler, A. Marty, Y. Souche, C. Poinsignon, D. Givord, *Science* **2007**, *315*, 349.

[7] a) G. Radaelli, D. Petti, E. Plekhanov, I. Fina, P. Torelli, B. R. Salles, M. Cantoni, C. Rinaldi, D. Gutiérrez, G. Panaccione, M. Varela, S. Picozzi, J. Fontcuberta, R. Bertacco, *Nat. Commun.* **2014**, *5*, 3404;

b) C. Zhang, F. Wang, C. Dong, C. Gao, C. Jia, C. Jiang, D. Xue, *Nanoscale* **2015**, *7*, 4187.

[8] A. Manchon, C. Ducruet, L. Lombard, S. Auffret, B. Rodmacq, B. Dieny, S. Pizzini, J. Vogel, V. Uhlí, M. Hochstrasser, G. Panaccione, *J. Appl. Phys.* **2008**, *104*, 043914.

[9] U. Bauer, L. Yao, A. J. Tan, P. Agrawal, S. Emori, H. L. Tuller, S. van Dijken, G. S. D. Beach, *Nat. Mater.* **2015**, *14*, 174.

[10] a) S. Emori, U. Bauer, S. Woo, G. S. D. Beach, *Appl. Phys. Lett.* **2014**, *105*, 222401; b) C. Bi, Y. Liu, T. Newhouse-Illige, M. Xu, M. Rosales, J. W. Freeland, O. Mryasov, S. Zhang, S. G. E. te Velthuis, W. G. Wang, *Phys. Rev. Lett.* **2014**, *113*, 267202; c) D. A. Gilbert, J. Olamit, R. K. Dumas, B. J. Kirby, A. J. Grutter, B. B. Maranville, E. Arenholz, J. A. Borchers, K. Liu, *Nat. Commun.* **2016**, *7*, 1; d) A. J. Grutter, D. A. Gilbert, U. S. Alaan, E. Arenholz, B. B. Maranville, J. A. Borchers, Y. Suzuki, K. Liu, *Appl. Phys. Lett.* **2016**, *108*, 082405.

[11] K. Leistner, J. Wunderwald, N. Lange, S. Oswald, M. Richter, H. Zhang, L. Schultz, S. Fähler, *Phys. Rev. B* **2013**, *87*, 224411.

[12] a) V. Malgras, H. Ataee-Esfahani, H. Wang, B. Jiang, C. Li, K. C.-W. Wu, J. H. Kim, Y. Yamauchi, *Adv. Mater.* **2016**, *28*, 993; b) B. Jiang, C. Li, Ö. Dag, H. Abe, T. Takei, T. Imai, Md. Shahriar, A. Hossain, Md. T. Islam, K. Wood, J. Henzie, T. Yamauchi, *Nat. Commun.* **2017**, *8*, 15581; c) Y. Li, B. P. Bastakoti, V. Malgras, C. Li, J. Tang, J. H. Kim, Y. Yamauchi, *Angew. Chem., Int. Ed.* **2015**, *54*, 11073.

[13] A. Quintana, J. Zhang, E. Isarain-Chávez, E. Menéndez, R. Cuadrado, R. Robles, M. D. Baró, M. Guerrero, S. Pané, B. J. Nelson, C. M. Müller, P. Ordejón, J. Nogués, E. Pellicer, J. Sort, *Adv. Funct. Mater.* **2017**, *27*, 1701904.

[14] S. Sen, D. Liu, G. T. R. Palmore, *ACS Catal.* **2014**, *4*, 3091.

[15] N. Chen, Q. Pan, *ACS Nano* **2013**, *7*, 6875.

[16] J. Zhang, M. D. Baró, E. Pellicer, J. Sort, *Nanoscale* **2014**, *6*, 12490.

[17] S. Kondrat, C. R. Pérez, V. Presser, Y. Gogotsi, A. A. Kornyshev, *Energy Environ. Sci.* **2012**, *5*, 6474.

[18] Z. Q. Qiu, S. D. Bader, *J. Magn. Magn. Mater.* **1999**, *200*, 664.

[19] E. Pellicer, A. Varea, S. Pané, B. J. Nelson, E. Menéndez, M. Estrader, S. Suriñach, M. D. Baró, J. Nogués, J. Sort, *Adv. Funct. Mater.* **2010**, *20*, 983.

[20] A. M. Zaky, F. H. Assaf, *Br. Corros. J.* **2002**, *37*, 48.

[21] M. Negem, H. Nady, *Int. J. Hydrogen Energy* **2017**, *42*, 28386.

[22] MAUD (Materials Analysis Using Diffraction), http://maud.radiographema.com/ (accessed: December 2017).

[23] E. J. W. Crossland, N. Noel, V. Sivaram, T. Leijtens, J. A. Alexander-Webber, H. J. Snaith, *Nature* **2013**, *495*, 215.

[24] a) B. Lefez, R. Souchet, K. Kartouni, M. Lenglet, *Thin Solid Films* **1995**, *268*, 45; b) X. Wang, L. Andrews, *Inorg. Chem.* **2005**, *44*, 9076; c) D. S. Hall, D. J. Lockwood, C. Bock, B. R. MacDougall, *Proc. R. Soc. A* **2015**, *471*, 20140792.

[25] a) M. C. Biesinger, L. W. M. Lau, A. R. Gerson, R. S. C. Smart, *Appl. Surf. Sci.* **2010**, *257*, 887; b) M. C. Biesinger, B. P. Payne, A. P. Grosvenor, L. W. M. Lau, A. R. Gerson, R. S. C. Smart, *Appl. Surf. Sci.* **2011**, *257*, 2717.

[26] T. L. Barr, *J. Phys. Chem.* **1978**, *82*, 1801.

[27] E. Apen, B. R. Rogers, J. A. Sellers, *J. Vac. Sci. Technol., A* **1998**, *16*, 1227.

[28] S. Gadad, T. M. Harris, *J. Electrochem. Soc.* **1998**, *145*, 3699.

[29] J. Teeriniemi, P. Taskinen, K. Laasonen, *Intermetallics* **2015**, *57*, 41.

[30] E. Panizon, J. A. Olmos-Asar, M. Peressi, R. Ferrando, *Phys. Chem. Chem. Phys.* **2015**, *17*, 28068.

[31] G. Wanka, H. Hoffmann, W. Ulbricht, *Macromolecules* **1994**, *27*, 4145.

[32] F. Fauth, R. Boer, F. Gil-Ortiz, C. Popescu, O. Vallcorba, I. Peral, D. Fulla, J. Benach, J. Juanhuix, *Eur. Phys. J. Plus* **2015**, *130*, 1.

NANO   MICRO

small

Supporting Information

Tunable Magnetism in Nanoporous CuNi Alloys by Reversible Voltage-Driven Element-Selective Redox Processes

Alberto Quintana,* Enric Menéndez,* Eloy Isarain-Chávez, Jordina Fornell, Pau Solsona, François Fauth, Maria Dolors Baró, Josep Nogués, Eva Pellicer, and Jordi Sort*

WILEY-VCH

Supporting Information

Tunable magnetism in nanoporous CuNi alloys by reversible voltage-driven element-selective redox processes

Alberto Quintana,* Enric Menéndez,* Eloy Isarain-Chávez, Jordina Fornell, Pau Solsona, François Fauth, Maria Dolors Baró, Josep Nogués, Eva Pellicer, Jordi Sort*

Figure S1: Scheme for the calculation of the Kerr amplitude employed in the determination of the % of change.

1
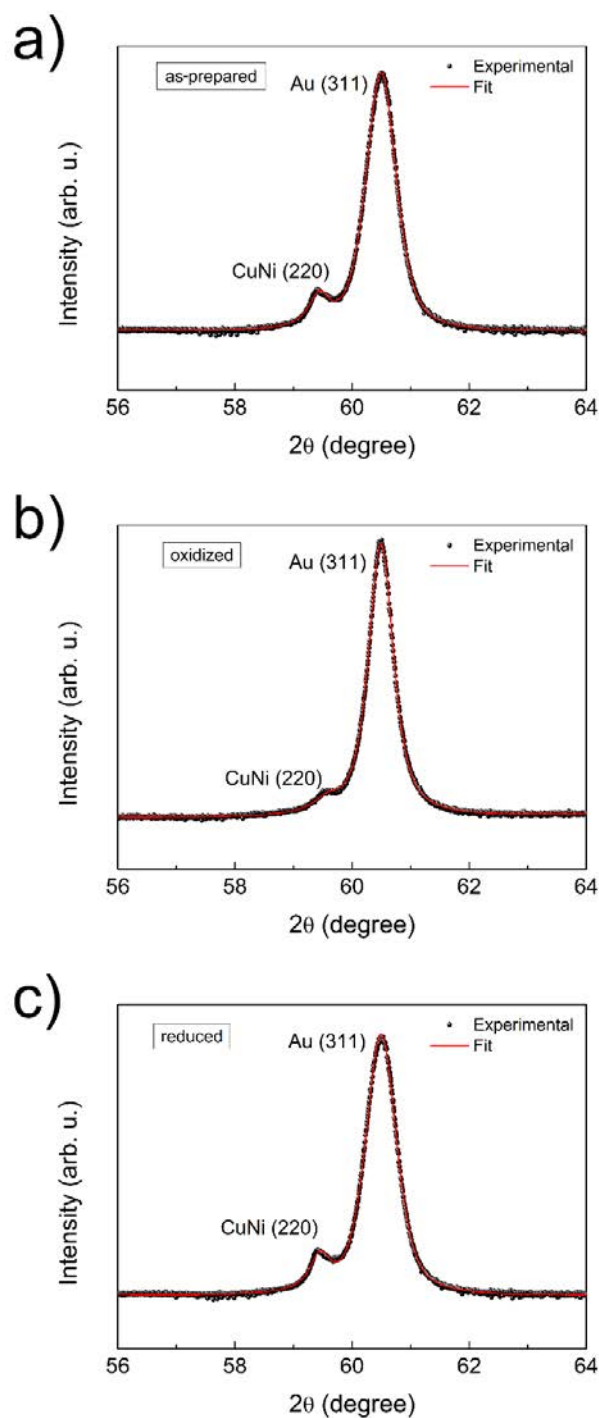
Figure S2: 56-64° 2θ region of the synchrotron GIXRD patterns and the corresponding Rietveld refinement fits of the as-prepared, oxidized and reduced samples.

2
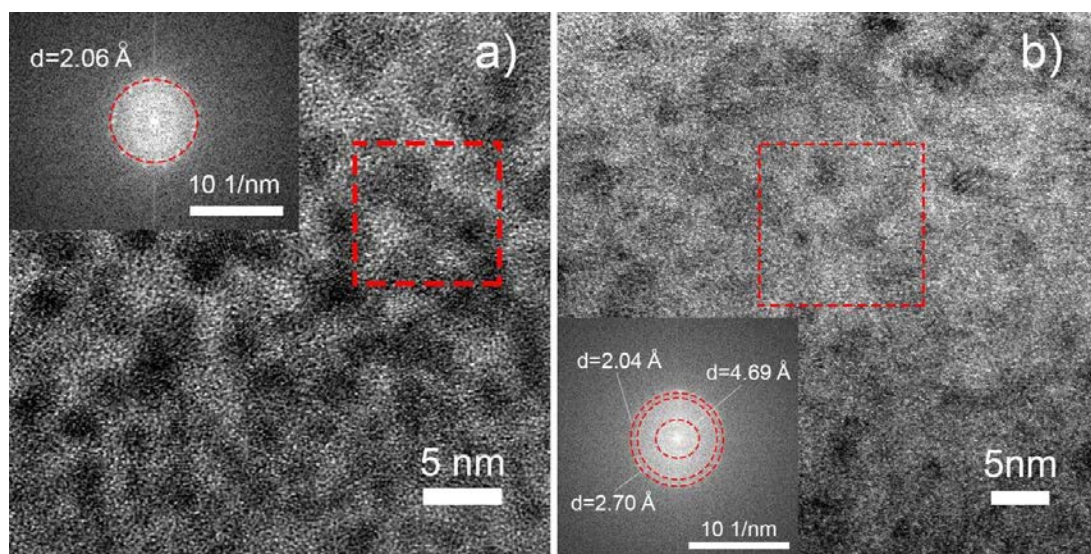
Figure S3: TEM image and corresponding fast Fourier transform (FFT) of the as-prepared (a) and oxidized sample at +0.8 V (b).

3
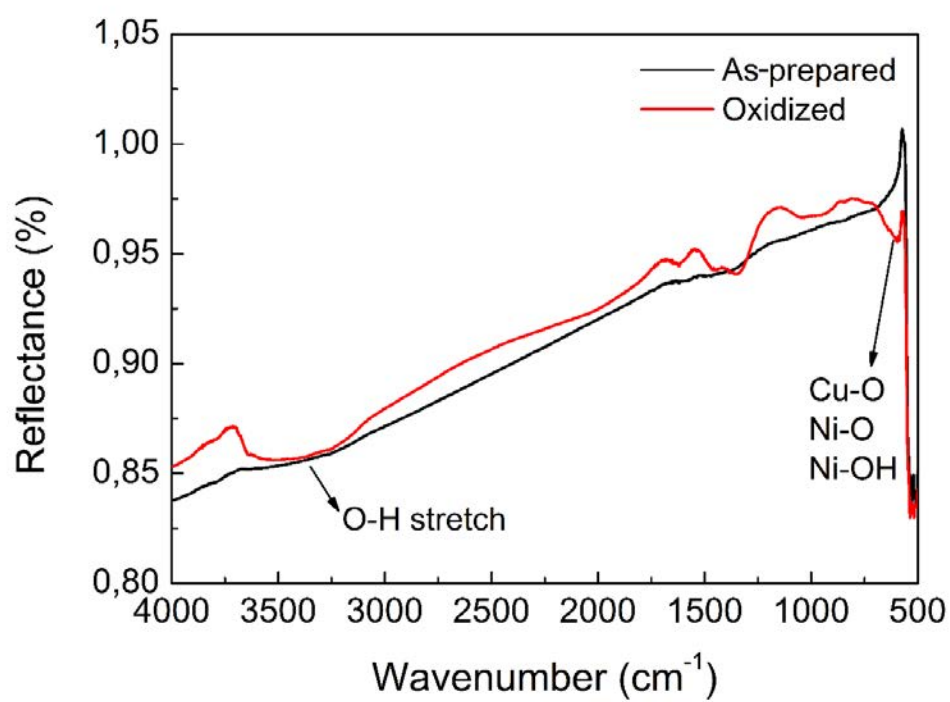
Figure S4: FT-IR spectra in reflectance mode of the as-prepared and oxidized samples.

CuNi	*As-prepared*	*Oxidized (+0.8 V)*	*Reduced (–2 V, "Recovered")*
<D> ± δ<D> (nm)	22 ± 1	16 ± 2	22 ± 1

Table S1: Table 1: Crystallite size <D> of the CuNi phase obtained by Rietveld refinement of the synchrotron GIXRD patterns in the 56-64° 2θ range corresponding to the as-prepared, oxidized and reduced samples.

Au	*As-prepared*	*Oxidized (+0.8 V)*	*Reduced (–2 V, "Recovered")*
<D> ± δ<D> (nm)	22 ± 1	22 ± 1	22 ± 1

Table S2: Crystallite size <D> of the Au phase obtained by Rietveld refinement of the GIXRD patterns in the 56-64° 2θ range corresponding to the as-prepared, the oxidized and reduced samples.

5

As Prep.	Cu₂O	Cu	CuO				Cu(OH)₂			
Binding Energy (eV)	931.8	932.6	933.1	934.4	941.7	-	934.6	939.3	942.2	-
Area (arb. u.)	554.6	153.3	153.9	342.3	294.1	-	554.6	727.7	231.7	-
FWHM	0.45	0.40	1.00	1.70	1.78	-	1.48	1.40	1.83	-
% Area	18 %	5 %	26 %				50 %			
+0.8V	Cu₂O	Cu	CuO				Cu(OH)₂			
Binding Energy (eV)	932.1	932.6	933.1	934.5	941.7	943.6	935.0	939.3	942.2	944.4
Area (arb. u.)	54.1	63.78	494.1	769.3	280.0	19.2	2007.27	455.3	1190.31	366.1
HWHM	0.42	0.40	1.00	1.70	1.80	0.60	1.40	1.40	1.83	0.90
% Area	1 %	1 %	27 %				71 %			
-2V	Cu₂O	Cu	CuO				Cu(OH)₂			
Binding Energy (eV)	932.0	932.8	933.1	-	-	-	934.6	942.2	-	-
Area (arb. u.)	223.7	343.6	423.3	-	-	-	1048.6	313.3	-	-
HWHM	0.40	0.44	1.00	-	-	-	1.40	1.83	-	-
% Area	10 %	15 %	18 %				58 %			

Table S3: Binding energy, area of the Gaussian curve, half-width at half maximum of all the fitting curves of each copper compound. % area is obtained for each compound from the calculated areas.

6

As Prep.	Ni		NiO			Ni(OH)₂					NiOOH					
Binding Energy (eV)	852.2	853.7	855.4	860.8	866.3	-	855.7	857.7	861.5	866.5	855.3	855.7	856.5	857.8	861.7	864.4
Area (arb. u.)	1104.4	1827.3	4278.6	9514.2	1281.7	-	3632.7	3502.7	8544.1	1033.9	2875.7	2929.2	2403.9	3190.1	10354.1	4565.7
FWHM	0.50	0.50	1.60	1.93	1.30	-	1.15	0.80	2.32	1.50	0.75	0.7	0.7	0.95	1.93	2.2
% Area	2 %		28 %			27 %					43 %					

+0.8V	Ni		NiO			Ni(OH)₂					NiOOH					
Binding Energy (eV)	852.7	853.9	855.4	860.8	866.3	-	855.7	857.7	861.5	866.5	855.3	855.7	856.5	857.8	861.7	864.4
Area (arb. u.)	409.2	1459.1	5205.3	6288.2	1661.0	-	5783.9	604.5	14572.7	7301.1	6550.6	801.1	5484.5	4556.3	1229.8	5120.6
HWHM	0.50	0.50	1.60	1.93	1.30	-	1.15	0.80	2.32	1.50	0.75	0.7	0.7	0.95	1.93	2.2
% Area	1 %		22 %			42 %					35 %					

-2V	Ni		NiO			Ni(OH)₂					NiOOH					
Binding Energy (eV)	-	853.7	855.4	860.8	866.3	854.9	855.7	857.7	861.5	866.5	855.3	855.7	856.5	857.8	861.7	864.4
Area (arb. u.)	-	563.7	7060.8	3769	1333.4	1087.4	4512.5	2892.6	10562.2	591.8	2308.4	2392.8	4495.8	2155.7	6282.6	7080.8
HWHM	-	0.50	1.60	1.93	1.30	0.60	1.20	0.80	2.32	1.50	0.75	0.7	0.7	0.95	1.93	
% Area	0 %		22 %			34 %					43 %					

Table S4: Binding energy, area of the Gaussian curve, half-width at half maximum of all the fitting curves of each Nickel compound. % area is obtained for each compound from the calculated areas.

79

2.3. Coating nanoporous Ni-based alloys by atomic layer deposition

This third work tackles the preparation of three-dimensional (3D) nanoengineered composite films with tunable composition and magnetic properties, having an strong potential for solid state magnetoelectric applications. These materials were synthesized by means of a two-step, 'all-chemical' deposition approach combining (i) surfactant assisted electrochemical deposition with (ii) atomic layer deposition (ALD), which is a subclass of chemical vapor deposition.

More specifically, this work demonstrates the possibility to grow Ni and Cu-Ni mesoporous metallic films, with highly tunable composition (pure Ni, $Cu_{20}Ni_{80}$ and $Cu_{45}Ni_{55}$ in at. %), pore architectures (continuous porous networks, corrugated mesophases or circular pore morphologies) and magnetic properties, that depend on the electrodeposition conditions. In all cases, as observed by SEM and TEM images, mesopores (with sizes ranging between 5 nm and 30 nm) are clearly observed both throughout the surface and in the interior of the films.

XRD and Rietveld refinement structural analyses revealed the occurrence of two phases in the electrodeposited CuNi films. This explains their dissimilar magnetic properties. While $Cu_{20}Ni_{80}$ presents a clear two-contribution loop arising from two ferromagnetic phases, $Cu_{45}Ni_{55}$, which should be non-ferromagnetic, exhibits a clear hysteresis loop, confirming the presence of a Ni-rich ferromagnetic phase.

Until this point, magnetoelectric measurements have been carried out employing liquid electrolytes. To further envisage real applications, it is desirable to replace liquid by solid state dielectrics. This problematic has been tackled in this work, by successfully coat the synthesized nanoporous layers with insulating layers.

Specifically, this is proven for the $Cu_{20}Ni_{80}$ film utilizing a 50 nm-thick amorphous alumina coating. Compared to other deposition methods, ALD allows for a conformal coverage of the CuNi matrix, precisely following the pore contours. Although some surface oxidation occurs during the ALD process since this is carried out at a temperature of around 100-200 °C, both the crystallographic structure and the magnetic properties of the parent metallic framework are largely preserved.

Although preliminary magnetoelectric studies revealed the occurrence of leakage currents (pinholes) and further work is in progress to improve the quality of the ALD coatings, this synthetic approach opens new paths for solid state magnetoelectric studies.

Electrodeposited Ni-Based Magnetic Mesoporous Films as Smart Surfaces for Atomic Layer Deposition: An "All-Chemical" Deposition Approach toward 3D Nanoengineered Composite Layers

Jin Zhang,[1,2,*] Alberto Quintana,[1] Enric Menéndez,[1] Mariona Coll,[3] Eva Pellicer,[1,*] and Jordi Sort[1,4,*]

1.- Departament de Física, Universitat Autònoma de Barcelona, E-08193 Cerdanyola del Vallès, Spain.

2.- State Key laboratory of Solidification Processing, Center of Advanced Lubrication and Seal Materials, Northwestern Polytechnical University, Xi'an, Shaanxi 710072, P. R. China.

3.- Institut de Ciència de Materials de Barcelona (ICMAB-CSIC) Campus UAB, E-08193 Cerdanyola del Vallès, Barcelona, Spain.

4.- ICREA. Pg. Lluís Companys 23, E-08010 Barcelona, Spain.

Correspondence should be addressed to: jinzhang@nwpu.edu.cn; eva.pellicer@uab.cat; jordi.sort@uab.cat.

Electrodeposited Ni-Based Magnetic Mesoporous Films as Smart Surfaces for Atomic Layer Deposition: An "All-Chemical" Deposition Approach toward 3D Nanoengineered Composite Layers

Jin Zhang,[*,†,‡] Alberto Quintana,[†] Enric Menéndez,[†] Mariona Coll,[§] Eva Pellicer[*,†] and Jordi Sort[*,†,∥]

[†]Departament de Física, Facultat de Ciències, Universitat Autònoma de Barcelona, E-08193 Bellaterra, Barcelona, Spain

[‡]State Key laboratory of Solidification Processing, Center of Advanced Lubrication and Seal Materials, Northwestern Polytechnical University, Xi'an, Shaanxi 710072, P. R. China

[§]Institut de Ciència de Materials de Barcelona (ICMAB-CSIC) Campus UAB, E-08193 Bellaterra, Barcelona, Spain

[∥]Institució Catalana de Recerca i Estudis Avançats (ICREA), Passeig Lluís Companys, 23, E-08010 Barcelona, Spain

S Supporting Information

ABSTRACT: Mesoporous Ni and Cu−Ni ($Cu_{20}Ni_{80}$ and $Cu_{45}Ni_{55}$ in at. %) films, showing a three-dimensional (3D) porous structure and tunable magnetic properties, are prepared by electrodeposition from aqueous surfactant solutions using micelles of P-123 triblock copolymer as structure-directing entities. Pores between 5 and 30 nm and dissimilar space arrangements (continuous interconnected networks, circular pores, corrugated mesophases) are obtained depending on the synthetic conditions. X-ray diffraction studies reveal that the Cu−Ni films have crystallized in the face-centered cubic structure, are textured, and exhibit certain degree of phase separation, particularly those with a higher Cu content. Atomic layer deposition (ALD) is used to conformally coat the mesopores of $Cu_{20}Ni_{80}$ film with amorphous Al_2O_3, rendering multiphase "nano-in-meso" metal-ceramic composites without compromising the ferromagnetic response of the metallic scaffold. From a technological viewpoint, these 3D nanoengineered composite films could be appealing for applications like magnetically actuated micro/nanoelectromechanical systems (MEMS/NEMS), voltage-driven magneto-electric devices, capacitors, or as protective coatings with superior strength and tribological performance.

KEYWORDS: *mesoporous films, nanoengineered composites, surfactant-assisted electrodeposition, atomic layer deposition, magnetic properties*
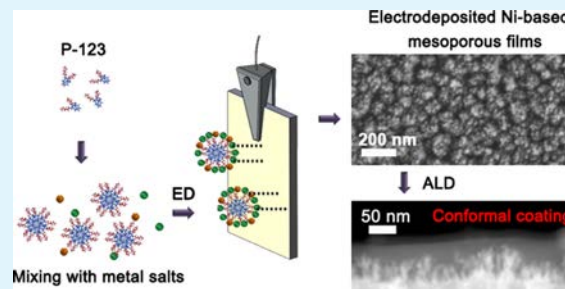
1. INTRODUCTION

Mesoporous metallic materials with high electroconductivity and surface area have sparked much attention during recent years owing to their wide range of applications in areas such as electronic devices, catalysis, energy technologies, or even recording media.[1] Their intrinsically porous structure has proven to be useful for the adsorption, selection, sensing, removal, storage, and release of second-phase materials.[2−7] Given their large potential, several techniques have been developed during the last decades in order to controllably create nanoporosity, by either selective etching from the fully dense counterparts (e.g., dealloying or foaming)[8,9] or spontaneous association of small building blocks while leaving empty spaces in between (bottom-up approach).[10−12] From the viewpoint of the material's architecture, control of the alloy composition often needs to be combined with precise tailoring of the mesoporous morphology, pore alignment, and orientation. This still remains a challenging issue. Most

approaches rely on relatively slow, multistep synthetic procedures, sometimes including costly clean room facilities. Ideally, such materials should be synthesized in a series of easy steps (preferably in a single- or two-step) allowing for a simple but precise control of the shape and morphology of the obtained structures.

During the past few years, mesoporous metals and alloys have been extensively prepared by means of sacrificial templates, using the replication method, from either soft or hard templates.[13−15] In the case of the templated deposition of metals, their growth from the substrate is guided by the template and the mesoporous structure often emerges after the template is removed. Very recently, the usage of spherical micelles of di- or triblock copolymers (e.g., polystyrene-*block-*

14877

Table 1. Optimized Electrodeposition Parameters for the Growth of Mesoporous Ni, $Cu_{20}Ni_{80}$, and $Cu_{45}Ni_{55}$ Films

mesoporous metallic film	Ni	$Cu_{20}Ni_{80}$ (at. %)	$Cu_{45}Ni_{55}$ (at. %)
Bath composition	0.08 g/mL P-123	0.008 g/mL P-123	0.008 g/mL P-123
	20 mL ethanol	0.2 M Ni(OCOCH$_3$)$_2$·4H$_2$O	0.2 M Ni(OCOCH$_3$)$_2$·4H$_2$O
	0.4 M NiSO$_4$	0.02 M CuSO$_4$·5H$_2$O	0.02 M CuSO$_4$·5H$_2$O
	0.5 M NaSO$_4$	0.5 M NaOCOCH$_3$	0.5 M NaOCOCH$_3$
	0.2 M boric acid	0.2 M boric acid	0.2 M boric acid
	0.5 mg/mL saccharine	0.4 mg/mL saccharine	0.4 mg/mL saccharine
Applied potential or current	$E = -1.8$ V	$j = -100$ mA cm^{-2}	$j = -100$ mA cm^{-2}
Deposition time/s	1200	150	150
pH	3.65	6.25	4.00
Bath temperature/°C		25	

poly(oxyethylene) (PS-*b*-PEO) known as KLE or poly-(ethylene glycol)-*block*-poly(propylene glycol)-*block*-poly-(ethylene glycol) (PEG–PPG–PEG) known as P-123) in water as soft-templates have been demonstrated for a number of metals (e.g., Au, Pt, Pd, Cu)[16−19] and alloys (Pt–Cu, Pt–Ru, Pt–Fe, and Cu–Ni).[20−24] Contrary to the evaporation-induced self-assembly approach, metal deposition and micelle assembly take place simultaneously in liquid phase without involving any solvent evaporation. Furthermore, because the concentration of the block copolymers is above the critical micelle concentration (cmc) but well below the threshold for the formation of lyotropic liquid crystal structures,[25] the viscosity of the electrolyte does not dramatically increase.

The advances in the synthetic pathways to produce magnetic materials with different nanoarchitectures has boosted the discovery of new magnetic phenomena and, in turn, expanded the range of applications of magnetic materials, since many magnetic properties of materials rely on surface or interface phenomena.[26] In this context, very recently, we demonstrated that magnetic mesoporous metallic materials, with an increased surface area-to-volume ratio, show enhanced magneto-electric phenomena compared to fully dense films with analogous compositions.[24] The system under study was Cu–Ni and mesoporous films of this alloy were successfully prepared by electrodeposition (ED) from "micelle assembly" of P-123 in water. The coercivity of the as-prepared mesoporous Cu–Ni films could be drastically decreased by simply applying an external electric field. In our previous work, however, only the general features concerning the mesoporous organization for a particular Cu/Ni ratio were introduced. Instead, emphasis was laid on the electrically driven modification of magnetic properties. The key experimental factors enabling the formation of the mesoporous structure were mostly overlooked.

Remarkably, besides the aforementioned magneto-electric effects, magnetic mesoporous metallic materials can also be successfully employed as supports to host other functional materials that could bring biocompatible, hydrophilic/hydrophobic properties, electrical insulation, or even enhanced mechanical or magnetic performance.[27] For example, 3D macroporous Ni films prepared by the hydrogen bubble templating approach can function as scaffolds to anchor electrodeposited Co(OH)$_2$ nanoflakes or sputtered Si to produce nanoporous composites with superior supercapacitor and electrochemical performance.[28,29] In the case of mesoporous materials of metallic nature, an appropriate technique should be carefully selected in order to conformally coat the mesopores with a second-phase material while avoiding or minimizing its oxidation and eventual pore collapse. Atomic layer deposition (ALD) turns out to be a powerful deposition technique that allows not only precise control over the composition of the deposited materials, but also these can continuously coat high-aspect-ratio substrates.[30−32] In fact, we proposed the combination of ED and ALD to prepare composite layers consisting of 3D macroporous magnetic metals coated with metal oxide nanolayers, i.e., Ni/Al$_2$O$_3$ and Ni/Co$_2$FeO$_4$.[33] It was demonstrated that both the porosity and the magnetic properties of the electrodeposited metallic matrix were maintained after the ALD step under optimized ALD conditions. However, the ALD deposition was only tested on metallic films exhibiting large pore sizes, on the order of 5−15 μm. It was then envisaged that such a synthetic approach could be well applied to out-of-sight surfaces of nanometric sizes (e.g., mesopores) grown by surfactant-assisted ED.

In this work, $Cu_{20}Ni_{80}$, $Cu_{45}Ni_{55}$, and Ni magnetic mesoporous films are electrodeposited in the presence of P-123 triblock copolymer dissolved in the aqueous electrolyte. The growth of mesoporous Ni coatings was carried out under potentiostatic mode, whereas Cu–Ni alloys were fabricated under galvanostatic means. Although all samples show mesoporosity, the resulting morphologies (e.g., pore alignment) are different depending on the electroplating conditions. Insulating Al$_2$O$_3$, with a high dielectric constant, is chosen to coat the $Cu_{20}Ni_{80}$ framework (which is taken as a model) by means of ALD. The structure and magnetic properties of the films, before and after the ALD process, are studied in detail.

2. EXPERIMENTAL SECTION

2.1. Synthesis of the $Cu_{20}Ni_{80}$, $Cu_{45}Ni_{55}$, and Ni Magnetic Mesoporous Films. All the chemicals were purchased from Sigma-Aldrich and used without further purification. Electrochemical fabrication of nanoporous Ni and Cu–Ni films was carried out in a PGSTAT120N Autolab potentionstat/galvamostat (Eco Chemie) with a standard three-electrode cell system. Si/Ti (25 nm)/Au (125 nm) substrates (working area 0.25 cm^2) were used as cathode. A platinum wire served as counter electrode. The cathode and anode were mounted parallel to each other at a distance of 2 cm. A double junction Ag|AgCl 3 M KCl electrode ($E = +0.210$ V versus standard hydrogen electrode (SHE)) was utilized as the reference electrode. The optimized growth parameters for the ED of nanoporous Ni, $Cu_{20}Ni_{80}$, and $Cu_{45}Ni_{55}$ are listed in Table 1. Note that due to the dissimilar deposition conditions (mainly the deposition time, which is different, but also other parameters like the bath formulation and deposition mode), the thickness of the mesoporous Ni film was measured to be around 7 μm, whereas those of $Cu_{20}Ni_{80}$ and $Cu_{45}Ni_{55}$ were approximately 600 nm and 1 μm, respectively. We anticipate that the thickness of the Cu richer film is probably a bit overestimated due to the influence of its higher roughness. Al$_2$O$_3$ nanolayers were deposited by ALD onto the previously electrodeposited porous metallic films in a Cambridge Nanotech Savannah 100 reactor in exposure mode. The Al$_2$O$_3$ coatings were produced by alternate
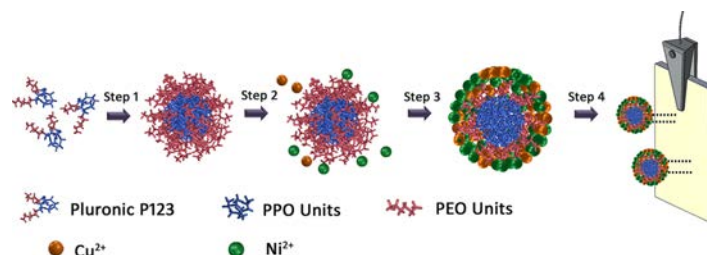
Figure 1. Schematic illustration of Pluronic P-123 micelle assembly strategy for the preparation of mesoporous magnetic films. Step 1: stirring to form the P-123 slurry; Step 2: addition of metal species to the aqueous solution; Step 3: the dissolved metal species coordinate to the PEO region of the micelles. Step 4: electrodeposition.

pulsing of trimethylaluminum (TMA) and ozone (O_3) at a deposition temperature of 100−200 °C.

2.2. Structural Characterization. Scanning electron microscopy (SEM) images and energy-dispersive X-ray spectroscopy (EDX) analyses were acquired using a Zeiss Merlin microscope operated at 3 kV and 15 kV, respectively. Transmission electron microscopy (TEM) and scanning transmission electron microscopy (STEM)-EDX analyses were performed on a Tecnai F20 HRTEM/STEM microscope operated at 200 kV. Cross sectional specimens were prepared by embedding the films in EPON epoxy resin. Subsequently, a very thin slide was cut using a microtome apparatus and placed onto a carbon-coated Cu TEM grid. $\theta/2\theta$ X-ray diffraction (XRD) patterns of the different samples were recorded on a Philips X'Pert diffractometer in the 42−54° 2θ range using Cu K_α radiation (λ = 0.1541 nm). The crystallographic structural parameters, such as crystallite sizes, microstrains, lattice parameter, and stacking fault probability were evaluated by fitting the full XRD patterns using the Materials Analysis Using Diffraction (MAUD) Rietveld refinement program.[34,35] Hysteresis loops were recorded at room temperature in a vibrating sample magnetometer (VSM) from Micro Sense (LOT-Quantum Design), with a maximum applied magnetic field of 4500 Oe. The loops were normalized to emu g^{-1} using the amount of material deposited as determined by coupled plasma optical emission spectroscopy (ICP-OES, model optima 4300DV). For this purpose, the films were digested in concentrated nitric acid solution at room temperature and further diluted to 1% HNO_3.

3. RESULTS AND DISCUSSION

Nanoporous Ni, $Cu_{20}Ni_{80}$ and $Cu_{45}Ni_{55}$ (at. %) films were electrodeposited from an aqueous solution containing the metal salts and the nonionic, amphiphilic poly(ethylene oxide)-*block*-poly(propylene oxide)-*block*-poly(ethylene oxide) (PEO−PPO−PEO) triblock copolymer (Pluronic P-123) (Table 1). In a typical preparation, the P-123 slurry was mixed manually using a glass rod upon addition of the aqueous solution containing the metal salts. Mixing time of 1 h was required to ensure the dissolved metal species were well incorporated at the outer shell of the hydrophilic domains of the micelles. Complete mixing was confirmed by the homogeneous color and transparency of the solution. An external potential or current density was applied to reduce the metallic cations, eventually forming a silvery slab of nanoporous magnetic films (Figure 1). Hence, the surface of the working electrode acted as a solid−liquid interface, where the metallic films were deposited and patterned by the surfactant-inorganic aggregates. During the ED, the metal species are thought to move toward the working electrode together with the P-123 micelles, which act as structure-directing agents. The essence of this method is thus to exploit the self-assembly of P-123 molecules into micelles which gather spontaneously at the solid−liquid interface during the synthesis of the mesoporous films.

First, the nanoporous $Cu_{20}Ni_{80}$ film was prepared, and its surface morphology was directly observed by SEM using secondary electrons. Shown in Figure 2a is the low-

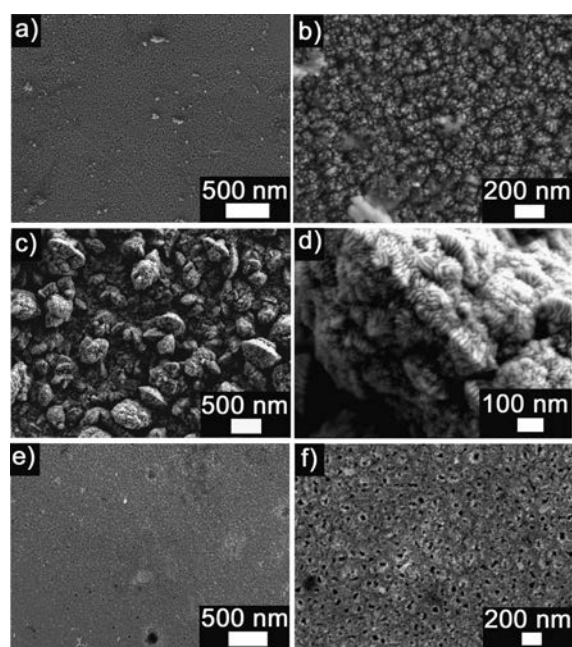**Figure 2.** Low and high magnification SEM images of mesoporous (a, b) $Cu_{20}Ni_{80}$; (c, d) $Cu_{45}Ni_{55}$; and (e, f) Ni films.

magnification top view image of the film, in which a rather homogeneous nanoporosity can be distinguished. The high-magnification SEM observations (Figure 2b) demonstrate the occurrence of a hierarchical porous architecture, consisting of aggregates of nanoparticles which leave in between a high density of nanopores, whose size ranges from 5 to 10 nm. In a dilute surfactant electrolyte, as in our case, the P-123 molecules assemble into spherical micelles. A long-range organized surfactant structure does not exist in solution, because the concentration of the block copolymer is not high enough to form a lyotropic liquid crystal phase.

The interaction (electrostatic, hydrogen bonding, etc.) between metal ions and surfactant assemblies is essential to tune the arrangement of the surfactant species. Therefore, using strongly acidic or basic conditions can modify the interactions and can influence the organization of inorganic polymerizing

species. Namely, the decrease of the pH of the electrolyte, from 6.25 to 4.00 (see Table 1 and Figure S1), has an impact on the morphology of the coatings. Film morphology changes from hierarchical nanoparticulated/nanoporous film to a striated patterned porous structure (Figure 2c,d). This process is probably driven by the enhanced interaction between metal ions and P-123 at a lower bath pH, which may cause alignment of the micelle spheres, ultimately resulting in the formation of a corrugated mesophase. In both cases, the concentration of surfactant was set at around 0.8 wt % which is above the cmc of P-123 at 25 °C[25] but lower than the threshold for lyotropic liquid phase formation. Besides modifications in the mesopore arrangement, the composition of the film fabricated at pH = 4.00 also changed to $Cu_{45}Ni_{55}$. In principle, one would expect the amount of Cu in the films to diminish with a decrease in the bath pH. A simple speciation analysis of the electrolyte proves that the relative fraction of free Ni^{2+} in solution increases much faster than that of free Cu^{2+} upon lowering the pH. However, it has been demonstrated for various electrolytes that there is not a linear relationship between the percentage of Cu in the films and the pH (in the range from 4 to 9) but a minimum in the Cu content is typically observed at pH ∼ 6.[36,37] An increase of the copper content has been observed in acetate-based electrolytes and for $C_{Ni2+} \gg C_{Cu2+}$ when the pH is decreased from near neutral pH to 4.[36]

Attempts to produce Ni films with mesoporous network from the same Cu−Ni bath were proven unsuccessful. Instead, the deposition was carried out in a more predictable way by using a ternary surfactant−cosolvent−water system. The introduction of ethanol as cosurfactant to the binary surfactant/water system enriches the aqueous P-123 phase diagram.[38] The mesopore size is largely determined by the hydrophobic core of the micelle spheres. The ethanol molecules are most likely anchored to the hydroxyl groups (−OH) located at the hydrophilic−hydrophobic interface, thus increasing the apparent volume of the hydrophobic blocks rather than that of the hydrophilic blocks. Thus, the ethanol cosurfactant, which acts as a swelling agent, allows for an additional degree of control over the pore size.[39,40]

As depicted in Figure 2e, the as-deposited Ni layer is homogeneous and rather free from defects such as perforations or bumps. The pore connectivity is relatively low and many isolated pores can be observed (Figure 2e,f). High magnification observations reveal the occurrence of pores with on-top circular morphology, whose sizes range from 10 to 30 nm. As mentioned earlier, this increase in the pore size probably stems from the addition of the ethanol cosurfactant and the concomitant increase in the carbon chain length. In all cases, the metal species were deposited uniformly on the substrates without any cracks or voids.

To further access the inner mesoporous architecture of the films, the $Cu_{20}Ni_{80}$ specimen was embedded in resin and sliced in order to study its cross section morphology. The sample was fairly robust and no obvious broken pieces were observed. The typical morphology of the cross section of this sample, observed by SEM, is shown in Figure 3a. It is worth noting that the mesoporous structure formed on the Au cathode developed from the very initial stages of the ED process. This observation is in accordance with our preceding observations regarding the growth of pure Ni mesoporous films.[39] Freshly formed crystallites serve as nucleiseeds for the subsequent metallic ions discharge, hence rendering truly nanoporous sizes. TEM images demonstrate the occurrence of open-cell porosity, with
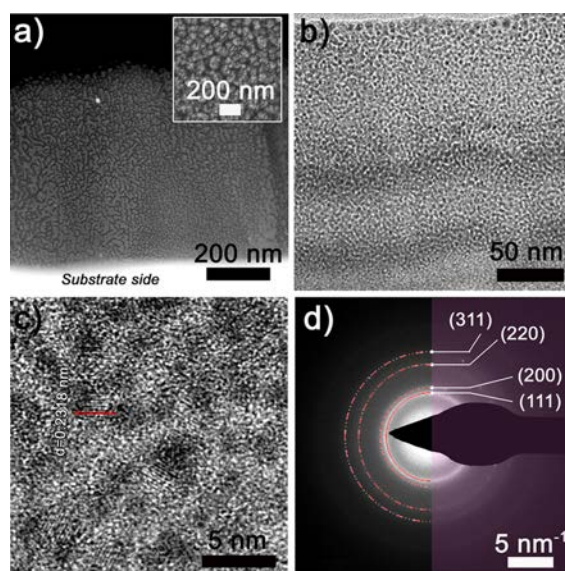

Figure 3. (a) SEM, (b) TEM, and (c) HRTEM images of the cross section of the mesoporous $Cu_{20}Ni_{80}$ film. The inset in (a) corresponds to the top SEM image, for the sake of comparison. (d) Corresponding SAED pattern with the Miller indices of the diffracting rings.

highly interconnected ligaments whose lateral size is typically around 5−7 nm (Figure 3b). The high-resolution TEM (HRTEM) image reveals that the $Cu_{20}Ni_{80}$ frameworks are highly crystalline and the lattice fringes are visible in the entire cross section (Figure 3c). The interplanar distance seen on the image (0.2318 nm) matches the (111) planes of the face-centered cubic (fcc) structure. Figure 3d shows the corresponding selected area electron diffraction (SAED) pattern, for which the continuous rings indicate the formation of a polycrystalline material.

The crystallographic structure and phase composition of the $Cu_{45}Ni_{55}$, $Cu_{20}Ni_{80}$, and Ni films were studied by XRD (Figure 4). The most intense peaks at 44−45° match the 2θ position expected for (111) fcc Ni and Cu−Ni solid solutions, suggesting that all the samples fully crystallize in the fcc structure (space group $Fm3m$, as for Cu and Ni). In the case of $Cu_{20}Ni_{80}$, the (200) fcc peak, which should appear at around 2θ = 51−52°, is not detected, suggesting a pronounced crystallographic texture along the (111) direction.

For both $Cu_{45}Ni_{55}$ and $Cu_{20}Ni_{80}$ samples, although there is no peak splitting detected, the (111) peak asymmetric broadening gives a clear indication of the coexistence of Cu-rich and Ni-rich phases (i.e., two fcc solid solutions with slightly different cell parameters). In order to validate this hypothesis, the Rietveld's refinement of the XRD pattern corresponding to $Cu_{45}Ni_{55}$ was performed in four different ways (Figure S2). First, the XRD pattern was fitted assuming only a single fcc solid solution without crystallographic texture (Figure S 2d). Such an approach did not provide a good fitting. Likewise, poor fittings were also obtained assuming a single fcc phase with (111) texture or two fcc solid solutions without texture (Figure S2b,c). Instead, a good agreement between the experimental pattern and the simulated curve was achieved upon assuming the coexistence of two fcc solutions and (111) texture (Figure S2a). In fact, phase-separation has been commonly observed for
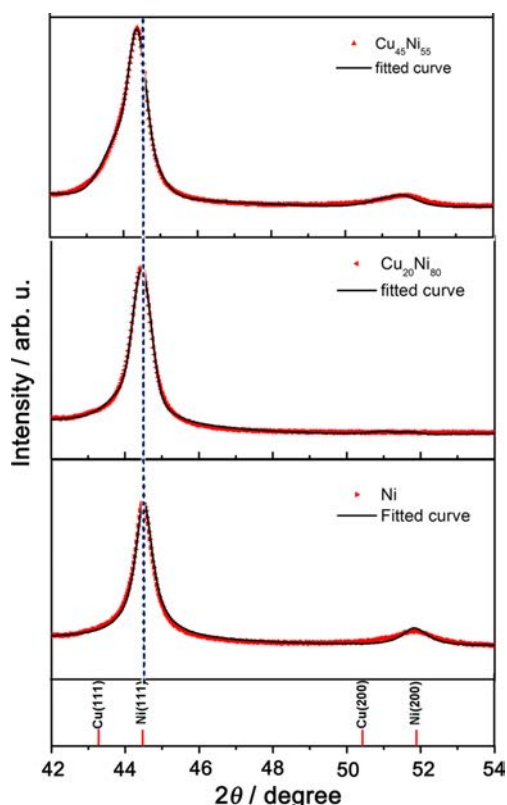
Figure 4. $\theta/2\theta$ XRD patterns in the 42−54° 2θ range for (rightward triangle, mesoporous Ni; leftward triangle, mesoporous $Cu_{20}Ni_{80}$; upward triangle, mesoporous $Cu_{45}Ni_{55}$). The computed profiles (black solid lines) obtained using the MAUD program are also shown. The bottom panel shows the theoretical lines for isotropic, pure fcc Cu and Ni.

the Cu−Ni system when electrodeposition events are confined inside small cavities, as is the case here. There are several examples in the literature (micropillars, nanowires, nanotubes) for which phase separation in Cu−Ni is observed, even in the presence of complexing agents in the electrolyte.[41,42] Actually, the enthalpy of mixing between Ni and Cu is slightly positive (with maximum values ranging between +0.5 and +1.5 kJ/mol).[43,44] Hence, there is a natural tendency for Cu and Ni to mutually segregate forming Cu-rich and Ni-rich solid solution regions when the system is brought to thermodynamical equilibrium.[45]

The values of cell parameters, crystallite sizes, microstrains, and stacking fault probabilities of the three samples, determined

by the MAUD software, are listed in Table 2. Note that the (111) fcc main reflection shifts toward higher angles as the Cu content is decreased, suggesting an overall reduction of the lattice cell parameter (which is expected, since the lattice constant of Ni is lower than that of Cu, and Cu−Ni alloys typically obey the Vegard's law[46]). Crystallite sizes for both Ni-rich and Cu-rich solid solution phases in the Cu−Ni films are kept below 100 nm, while a value greater than 150 nm is obtained for the pure Ni film which cannot be resolved by line profile analysis.[47] The addition of ethanol to the Ni electrolyte lowers the dielectric constant. The decrease of conductivity of the plating solution together with the overall different bath composition induces the observed changes in crystallite size. Interestingly, particularly for the Cu−Ni mesoporous films, the crystallite size is considerably larger than the width of the pore walls, suggesting that several nanopores are contained inside coherently diffracting domains (i.e., the films comprises truly nanoporous crystals rather than simply being an assembly of tiny nanoparticulate clusters). The microstrains were found to be rather low in all films, in the range of 10^{-3} and below. Saccharine is known to be an excellent tensile macrostress reducing agent and is thus responsible for the low microstrains (low density of dislocations in the crystals). The Rietveld refinement of the XRD patterns using MAUD also includes the Warren's formalism to evaluate the stacking fault (SF) probability, α_{SF}. According to the Warren's description of the SFs, $1/\alpha_{SF}$ designates the average number of planes between two consecutive SFs. Significant stacking fault probability was only found for pure Ni, and the value is around 0.0113 (Table 2); hence, there are ca. 88 planes between consecutive SFs.

The hysteresis loops of the nanoporous Cu−Ni and Ni films are shown in Figure 5. The highest value of saturation
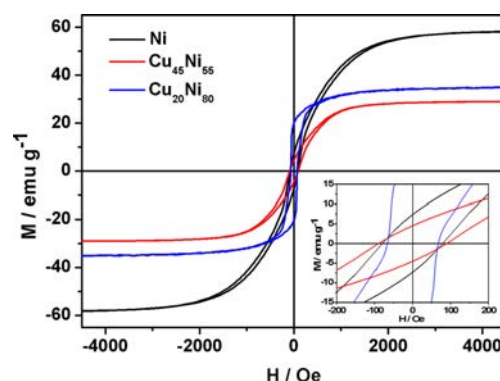

Figure 5. Room temperature hysteresis loops corresponding to Ni, $Cu_{45}Ni_{55}$, and $Cu_{20}Ni_{80}$ mesoporous films.

Table 2. Crystallographic Structural Parameters Obtained after Rietveld's Refinement of the XRD Patterns of $Cu_{45}Ni_{55}$, $Cu_{20}Ni_{80}$, and Ni Mesoporous Films

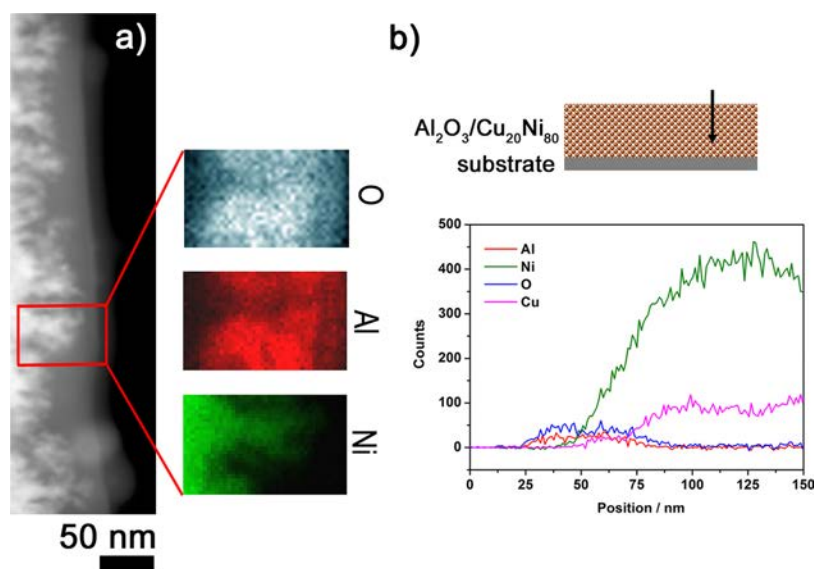|		lattice parameter/Å ($\pm$0.0005 Å)	crystallite size/nm ($\pm$2 nm)	microstrains ($\pm$1.0 × 10^{-4})	stacking fault probability ($\pm$0.0005)
$Cu_{45}Ni_{55}$	Ni-rich phase	3.5402	60	32 × 10^{-4}	0.0058
	Cu-rich phase	3.5720	16	2 × 10^{-4}	−
$Cu_{20}Ni_{80}$	Phase richer in Ni	3.5383	74	32 × 10^{-4}	0.0067
	Phase less rich in Ni	3.5574	14	1 × 10^{-4}	−
Ni		3.5298	>150	9 × 10^{-4}	0.0113

Figure 6. (a) STEM image and EDX elemental distribution of O, Al, and Ni in the interfacial area enclosed within the red rectangle for a cross-sectioned $Al_2O_3/Cu_{20}Ni_{80}$ film; (b) EDX line scan performed across the interface between $Cu_{20}Ni_{80}$ and Al_2O_3, as indicated by the arrow in the scheme shown above.

magnetization, M_S, corresponds to pure Ni while $Cu_{45}Ni_{55}$ and $Cu_{20}Ni_{80}$ films exhibit lower M_S. Interestingly, a constriction is observed in the central part of the $Cu_{20}Ni_{80}$ hysteresis loop, suggesting the presence of two magnetic phases in this sample. With the results from XRD taken into account, these two phases could be ascribed to the two fcc solid solutions indicated in Table 2. Actually, according to the Vegard's law, the two solid solutions for the $Cu_{20}Ni_{80}$ sample presumably contain about 85 at. % and 60 at. % Ni;[46] hence, both could show a ferromagnetic response (since the threshold for ferromagnetic behavior in Cu−Ni alloys at room temperature is indeed around 60 at. %[46]). The $Cu_{45}Ni_{55}$ film does not show such narrowing of the hysteresis, indicating the presence of a single magnetic phase. In this case, according to the Vegard's law, the Ni-rich solid solution would contain approximately 70 at. % Ni, whereas the Cu-rich phase would contain only 20 at. % Ni, hence being nonmagnetic. Note also that the loop corresponding to $Cu_{20}Ni_{80}$ shows a higher remanence-to-saturation magnetization ratio (i.e., a large squareness ratio, M_R/M_S). This is probably due to the in-plane shape anisotropy of this film, which is presumably fully magnetic (i.e., consisting mainly of exchange coupled ferromagnetic regions). The reduction of M_R/M_S for the $Cu_{45}Ni_{55}$ film is an indication of a lower magnetic shape anisotropy (see Figure 5). This reduction of shape anisotropy is consistent with the former assumption that this film is made of Ni-rich ferromagnetic clusters embedded in a nonmagnetic Cu-rich matrix (i.e., a "discontinuous" magnetic structure). This nonconnected magnetic structure yields to an overall decrease of exchange interactions between ferromagnetic counterparts, explaining the enhanced coercivity of the $Cu_{45}Ni_{55}$ sample with respect to the Ni film since exchange interactions are usually in detriment of the coercivity.[48] Finally, the M_R/M_S value for pure Ni is also relatively low, but this could be anticipated due to its much larger thickness (7 μm, as opposed to the 600 nm to 1 μm thickness of the Cu−Ni films) and consequently lower magnetic shape anisotropy.

Mesoporous materials provide well-controlled nanosized environments where other materials with dissimilar chemical and physical properties can be hosted, leading to "nano-in-meso" multiphase composites. In this work, Al_2O_3, which is the most widely studied material of those prepared by ALD, was chosen to coat and fill the pores of the $Cu_{20}Ni_{80}$ films. A $Cu_{20}Ni_{80}/Al_2O_3$ specimen was prepared for cross-sectional imaging to assess the quality of the oxide nanocoating. After the ALD process, as shown in the STEM image (Figure 6a), the $Cu_{20}Ni_{80}$ alloy, featuring a brighter contrast, is covered by a darker-contrast layer. The composition profile across the interface was determined by STEM-EDX elemental distribution mapping. The analysis reveals that the local distribution of Al (in red) and Ni (in green) elements is well-distinguished and that the irregular border between the two elemental maps follows the surface geometry, hence pointing to a conformal coating of Al_2O_3. However, there is not such a clear compositional distinction between the O and Ni signals, but instead, they coexist within a few nanometers interval. This was further proven by performing a STEM-EDX line scan analysis (Figure 6b). When the electron beam was swept from the outer surface of the film toward the inner part of the material (vertical arrow in the scheme), the Al and O signals first appear at 20 nm from the starting point and vanish at approximately 90 nm. The Cu and Ni signals monotonically increase from around 35 nm, suggesting that the thickness of the Al_2O_3 coating is about 50 nm. Hence, there is not an abrupt switch in composition, but rather the four elements are present within a distance of about 55 nm from the upper surface. Therefore, it is conjectured that the outermost surface of mesoporous Cu−Ni films got slightly oxidized during the ALD process, which is plausible bearing in mind that such treatments are performed under O_3 atmosphere. Hence, Ni-oxide, Cu-oxide, and some mixed $(Al,Cu,Ni)_xO_y$ phases may exist within this region.

XRD patterns were recorded to confirm the formation of oxidized Cu−Ni phases and to assess whether the ALD

87

treatments could have induced further phase separation, as previously reported in fully dense Cu–Ni films subject to annealing treatments.[45] As depicted in Figure 7a, a small peak
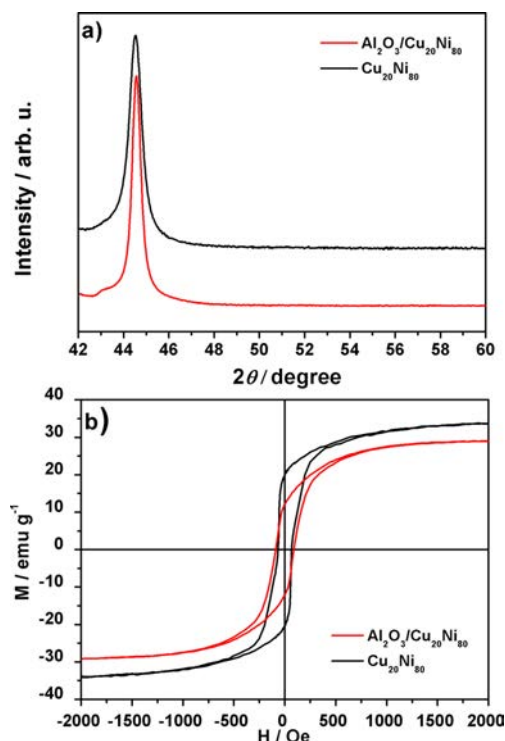

Figure 7. (a) XRD patterns and (b) room temperature hysteresis loops of mesoporous $Cu_{20}Ni_{80}$ and $Al_2O_3@Cu_{20}Ni_{80}$ composite films.

appears after ALD at around $2\theta = 43°$, which can be ascribed to Cu- or Ni-oxides. However, no obvious change of the (111) fcc reflections is observed (no peak splitting or further asymmetric shape), suggesting that the Cu–Ni mesoporous films can withstand the ALD process to a great extent from both morphological and crystallographic aspects. This could be anticipated since phase separation in electrodeposited Cu–Ni films was observed above 250 °C.[45] Only a narrowing of the (111) peak occurs, which is indicative of grain growth and reduction of residual stresses caused by the annealing process which accompanies the ALD process (crystallite size after the ALD treatment is larger than 150 nm and cannot be resolved by X-ray line profile analysis, as evaluated using MAUD).

No peaks corresponding to crystalline Al_2O_3 are observed in the measured 2θ range. This is in agreement with the formation of amorphous Al_2O_3 by ALD, as previously reported in the literature when similar ALD conditions are employed.[33] Finally, due to the slight oxidation that takes place during ALD, the saturation magnetization is found to decrease (Figure 7b) but only by 15%; hence, a clear ferromagnetic response is preserved.

4. CONCLUSIONS

This work demonstrates the possibility of growing Ni and Cu–Ni mesoporous metallic films, with highly tunable pore architectures, compositions, and magnetic properties, by ED in the presence of a triblock copolymer surfactant. Nanopores

well distributed both throughout the surface and within the films were observed. The mesoporous films can serve as scaffolds and be successfully coated with Al_2O_3 nanolayers by atomic layer deposition. This has been proven on the $Cu_{20}Ni_{80}$ film. Although some surface oxidation occurs during the ALD process, both the crystallographic structure and the parent magnetic properties of the metallic matrix are greatly preserved. Hence, the concept exploited here can render functional multiphase metal-ceramic nanocomposites which are entirely processed using a chemical-like route: electrochemical deposition followed by a subclass of chemical vapor deposition (ALD). These "nano-in-meso" composites could find applications in several fields like magnetic MEMS/NEMS or protective coatings.

■ ASSOCIATED CONTENT

Ⓢ Supporting Information

The Supporting Information is available free of charge on the ACS Publications website at DOI: 10.1021/acsami.8b01626.

Additional EDX spectra and Rietveld fitted XRD patterns (PDF)

■ AUTHOR INFORMATION

Corresponding Authors
*E-mail: jinzhang@nwpu.edu.cn.
*E-mail: eva.pellicer@uab.cat.
*E-mail: jordi.sort@uab.cat.

ORCID
Alberto Quintana: 0000-0002-9813-735X
Enric Menéndez: 0000-0003-3809-2863
Eva Pellicer: 0000-0002-8901-0998
Jordi Sort: 0000-0003-1213-3639

Author Contributions
The manuscript was written through contributions of all authors. All authors have given approval to the final version of the manuscript.

Notes
The authors declare no competing financial interest.

■ REFERENCES

(1) Yamauchi, Y.; Suzuki, N.; Radhakrishnan, L.; Wang, L. Breakthrough and Future: Nanoscale Control of Compositions, Morphologies, and Mesochannel Orientations toward Advanced Mesoporous Materials. *Chem. Rec.* **2009**, *9*, 321–339.
(2) Corma, A. From Microporous to Mesoporous Molecular Sieve Materials and Their Use in Catalysis. *Chem. Rev.* **1997**, *97*, 2373–2419.

(3) Ying, J. Y.; Mehnert, C. P.; Wong, M. S. Synthesis and Applications of Supramolecular-Templated Mesoporous Materials. *Angew. Chem., Int. Ed.* **1999**, *38*, 56−77.

(4) Davis, M. E. Ordered Porous Materials for Emerging Applications. *Nature* **2002**, *417*, 813−821.

(5) Soler-Illia, G. J. A. A.; Azzaroni, O. Multifunctional Hybrids by Combining Ordered Mesoporous Materials and Macromolecular Building Blocks. *Chem. Soc. Rev.* **2011**, *40*, 1107−1150.

(6) Boissiere, C.; Grosso, D.; Chaumonnot, A.; Nicole, L.; Sanchez, C. Aerosol Route to Functional Nanostructured Inorganic and Hybrid Porous Materials. *Adv. Mater.* **2011**, *23*, 599−623.

(7) Liu, J.; Qiao, S. Z.; Hu, Q. H.; Lu, G. Q. Magnetic Nanocomposites with Mesoporous Structures: Synthesis and Applications. *Small* **2011**, *7*, 425−443.

(8) Scaglione, F.; Rizzi, P.; Battezzati, L. De-alloying Kinetics of an Au-based Amorphous Alloys. *J. Alloys Compd.* **2012**, *536*, S60−S64.

(9) Bansal, V.; Jani, H.; Du Plessis, J.; Coloe, P. J.; Bhargava, S. K. Galvanic Replacement Reaction on Metal Films: A One-Step Approach to Create Nanoporous Surfaces for Catalysis. *Adv. Mater.* **2008**, *20*, 717−723.

(10) Attard, G. S.; Glyde, J. C.; Göltner, C. G. Liquid-crystalline Phases as Templates for the synthesis of Mesoporous Silica. *Nature* **1995**, *378*, 366−368.

(11) Attard, G. S.; Göltner, C. G.; Corker, J. M.; Henke, S.; Templer, R. H. Liquid-Crystal Templates for Nanostructured Metals. *Angew. Chem., Int. Ed. Engl.* **1997**, *36*, 1315−1317.

(12) Attard, G. S.; Bartlett, P. N.; Coleman, N. R. B.; Elliott, J. M.; Owen, J. R.; Wang, J. H. Mesoporous Platinum Films from Lyotropic Liquid Crystalline Phases. *Science* **1997**, *278*, 838−840.

(13) Wang, H.; Jeong, H. Y.; Imura, M.; Wang, L.; Radhakrishnan, L.; Fujita, N.; Castle, T.; Terasaki, O.; Yamauchi, Y. Shape- and Size-Controlled Synthesis in Hard Templates: Sophisticated Chemical Reduction for Mesoporous Monocrystalline Platinum Nanoparticles. *J. Am. Chem. Soc.* **2011**, *133*, 14526−14529.

(14) Choi, K. S.; McFarland, W.; Stucky, G. D. Electrocatalytic Properties of Thin Mesoporous Platinum Films Synthesized Utilizing Potential-Controlled Surfactant Assembly. *Adv. Mater.* **2003**, *15*, 2018−2021.

(15) Malgras, V.; Araee-Esfahani, H.; Wang, H.; Jiang, B.; Li, C.; Wu, K. C. W.; Kim, J. H.; Yamauchi, Y. Nanoarchitechtures for Mesoporous Metal. *Adv. Mater.* **2016**, *28*, 993−1010.

(16) Li, C.; Dag, O.; Dao, T. D.; Nagao, T.; Sakamoto, Y.; Kimura, T.; Terasaki, O.; Yamauchi, Y. Electrochemical Synthesis of Mesoporous Gold Films toward Mesospace-stimulated Optical Properties. *Nat. Commun.* **2015**, *6*, 6608.

(17) Iqbal, M.; Li, C.; Wood, K.; Jiang, B.; Takei, T.; Dag, O.; Baba, D.; Nugraha, A. S.; Asahi, T.; Whitten, A. E.; Hossain, Md. S. A.; Malgras, V.; Yamauchi, Y. Continuous Mesoporous Pd Films by Electrochemical Deposition in Nonionic Micellar Solution. *Chem. Mater.* **2017**, *29*, 6405−6413.

(18) Wang, H.; Wang, L.; Sato, T.; Sakamoto, Y.; Tominaka, S.; Miyasaka, K.; Miyamoto, N.; Nemoto, Y.; Terasaki, O.; Yamauchi, Y. Synthesis of Mesoporous Pt Films with Tunable Pore Sizes from Aqueous Surfactant Solutions. *Chem. Mater.* **2012**, *24*, 1591−1598.

(19) Li, C.; Jiang, B.; Wang, Z.; Li, Y.; Hossain, Md. S. A.; Kim, J. H.; Takei, T.; Henzie, J.; Dag, O.; Bando, Y.; Yamauchi, Y. First Synthesis of Continuous Mesoporous Copper Films with Uniformly Sized Pores by Electrochemical Soft Templating. *Angew. Chem.* **2016**, *128*, 12938−12942.

(20) Li, C.; Yamauchi, Y. Synthesis of Mesoporous Platinum−Copper Films by Electrochemical Micelle Assembly and Their Electrochemical Applications. *Chem. - Eur. J.* **2014**, *20*, 729−733.

(21) Isarain-Chavez, E.; Baró, M. D.; Pellicer, E.; Sort, J. Micelle-assisted Electrodeposition of Highly Mesoporous Fe−Pt Nodular Films with Soft Magnetic and Electrocatalytic Properties. *Nanoscale* **2017**, *9*, 18081−18093.

(22) Isarain-Chavez, E.; Baró, M. D.; Alcantara, C.; Pané, S.; Sort, J.; Pellicer, E. Micelle-Assisted Electrodeposition of Mesoporous Fe-Pt Smooth Thin Films and their Electrocatalytic Activity towards the Hydrogen Evolution Reaction. *ChemSusChem* **2018**, *11*, 367−375.

(23) Wang, H.; Imura, M.; Nemoto, Y.; Wang, L.; Jeong, H. Y.; Yokoshima, T.; Terasaki, O.; Yamauchi, Y. Electrochemical Design of Mesoporous Pt-Ru Alloy Films with Various Compositions toward Superior Electrocatalytic Performance. *Chem. - Eur. J.* **2012**, *18*, 13142−13148.

(24) Quintana, A.; Zhang, J.; Chavaz, E. I.; Menendez, E.; Cuadrado, R.; Robles, R.; Baró, M. D.; Guerrero, M.; Pané, S.; Nelson, B. J.; Muller, C. M.; Ordejon, P.; Nogués, J.; Pellicer, E.; Sort, J. Magnetic actuation: Voltage-induced Coercivity Reduction in Nanoporous Alloy Films: A Boost towards Energy Efficient Magnetic Actuation. *Adv. Funct. Mater.* **2017**, *27*, 1701904.

(25) Wanka, G.; Hoffmann, H.; Ulbricht, W. Phase Diagrams and Aggregation Behavior of Poly (ox yethy1ene)-Poly (oxypropylene)-Poly(oxyet hylene) Triblock Copolymers in Aqueous Solutions. *Macromolecules* **1994**, *27*, 4145−4159.

(26) Hellman, F.; Hoffmann, A.; Tserkovnyak, Y.; Beach, G. S. D.; Fullerton, E. E.; Leighton, C.; MacDonald, A. H.; Ralph, D. C.; Arena, D. A.; Dürr, H. A.; Fischer, P.; Grollier, J.; Heremans, J. P.; Jungwirth, T.; Kimel, A. V.; Koopmans, B.; Krivorotov, I. N.; May, S. J.; Petford-Long, A. K.; Rondinelli, J. M.; Samarth, N.; Schuller, I. K.; Slavin, A. N.; Stiles, M. D.; Tchernyshyov, O.; Thiaville, A.; Zink, B. L. Interface-induced Phenomena in Magnetism. *Rev. Mod. Phys.* **2017**, *89*, 025006.

(27) Liu, J.; Qiao, S. Z.; Hu, Q. H.; Lu, G. Q. Magnetic Nanocomposites with Mesoporous Structures: Synthesis and Applications. *Small* **2011**, *7*, 425−443.

(28) Xia, X. H.; Tu, J. P.; Zhang, Y. Q.; Mai, Y. J.; Wang, X. L.; Gu, C. D.; Zhao, X. B. Three-Dimentional Porous Nano-Ni/Co(OH)$_2$ Nanoflake Composite Film: A Pseudocapacitive Material with Superior Performance. *J. Phys. Chem. C* **2011**, *115*, 22662.

(29) Zhang, Y. Q.; Xia, X. H.; Wang, X. L.; Mai, Y. J.; Shi, S. J.; Tang, Y. Y.; Gu, C. G.; Tu, J. P. Three-dimensional Porous Nano-Ni Supported Silicon Composite Film for High-performance Lithium-ion Batteries. *J. Power Sources* **2012**, *213*, 106−111.

(30) Detavernier, C.; Dendooven, J.; Sree, S. P.; Ludwig, K. F.; Martens, J. A. Tailoring Nanoporous Materials by Atomic Layer Deposition. *Chem. Soc. Rev.* **2011**, *40*, 5242−5253.

(31) Elam, J. W.; Xiong, G.; Han, C. Y.; Wang, H. H.; Birrell, J. P.; Welp, U.; Hryn, J. N.; Pellin, M. J.; Baumann, T. F.; Poco, J. F.; Satcher, J. H. Atomic layer deposition for conformal coating of nanoporous materials. *J. Nanomater.* **2006**, *2006*, 1−5.

(32) Spende, A.; Sobel, N.; Lukas, M.; Zierold, R.; Riedl, J. C.; Gura, L.; Schubert, I.; Montero-Moreno, J. M.; Nielsch, K.; Stühn, B.; et al. TiO$_2$, SiO$_2$, and Al$_2$O$_3$ Coated Nanopores and Nanotubes Produced by ALD in Etched Ion-Track Membranes for Transport Measurements. *Nanotechnology* **2015**, *26*, 335301.

(33) Zhang, J.; Coll, M.; Puig, T.; Pellicer, E.; Sort, J. Conformal Oxide Nanocoatings on Electrodeposited 3D Porous Ni Films by Atomic Layer Deposition. *J. Mater. Chem. C* **2016**, *4*, 8655−8622.

(34) Lutterotti, L.; Scardi, P. Simultaneous Structure and Size-strain Refinement by the Rietveld Method. *J. Appl. Crystallogr.* **1990**, *23*, 246−252.

(35) MAUD (Materials Analysis Using Diffraction), http://maud.radiographema.com/.

(36) Silaimani, S. M.; Vivekanandan, G.; Veeramani, P. Nano-Nickel−Copper Alloy Deposit for Improved Corrosion Resistance in Marine Environment. *Int. J. Environ. Sci. Technol.* **2015**, *12*, 2299−2306.

(37) Sobha, J.; Krishna, N.; Sujatha, K. P.; Sriveeraraghavan, S.; Krishnan, R. M.; Natarajan, S. R. Electroplating of nickel-copper alloys. *Bull. Electrochem.* **1996**, *12*, 259−265.

(38) Soni, S. S.; Brotons, G.; Bellour, M.; Narayanan, T.; Gibaud, A. Quantitative SAXS Analysis of the P123/Water/Ethanol Ternary Phase Diagram. *J. Phys. Chem. B* **2006**, *110*, 15157−15165.

(39) Esque-de los Ojos, D.; Zhang, J.; Fornell, J.; Pellicer, E.; Sort, J. Nanomechanical Behaviour of Open-cell Nanoporous Metals: Homogeneous versus Thickness-dependent Porosity. *Mech. Mater.* **2016**, *100*, 167−174.

89

(40) Holmqvist, P.; Alexandridis, P.; Lindman, B. Phase Behavior and Structure of Ternary Amphiphilic Block Copolymer−Alkanol−Water Systems: Comparison of Poly(ethylene oxide)/Poly(propylene oxide) to Poly(ethylene oxide)/Poly(tetrahydrofuran) Copolymers. *Langmuir* **1997**, *13*, 2471−2479.

(41) Varea, A.; Pané, S.; Gerstl, S.; Zeeshan, M. A.; Özkale, B.; Nelson, B. J.; Suriñach, S.; Baró, M. D.; Nogués, J.; Sort, J.; Pellicer, E. Ordered Arrays of Ferromagnetic, Compositionally Graded $Cu_{1-x}Ni_x$ Alloy Nanopillars Prepared by Template-Assisted Electrodeposition. *J. Mater. Chem. C* **2013**, *1*, 7215−7221.

(42) Liu, Z.; Elbert, D.; Chien, C. L.; Searson, P. C. FIB/TEM Characterization of the Composition and Structure of Core/Shell Cu−Ni Nanowires. *Nano Lett.* **2008**, *8*, 2166−2170.

(43) Abrikosov, I. A.; Skriver, H. L. Self-Consistent Linear-Muffin-Tin-Orbitals Coherent-Potential Technique for Bulk and Surface Calculations: Cu-Ni, Ag-Pd, and Au-Pt Random Alloys. *Phys. Rev. B: Condens. Matter Mater. Phys.* **1993**, *47*, 16532−16541.

(44) Lee, B. J.; Shim, J. H. A Modified Embedded Atom Method Interatomic Potential for the Cu−Ni System. *CALPHAD: Comput. Coupling Phase Diagrams Thermochem.* **2004**, *28*, 125−132.

(45) Pellicer, E.; Varea, A.; Kartik, S.; Pané, S.; Suriñach, S.; Baró, M. D.; Nogués, J.; Nelson, B.; Sort, J. Grain Boundary Segregation and Interdiffusion Effects in Nickel−Copper Alloys: An Effective Means to Improve the Thermal Stability of Nanocrystalline Nickel. *ACS Appl. Mater. Interfaces* **2011**, *3*, 2265−2274.

(46) Pellicer, E.; Varea, A.; Pané, S.; Nelson, B. J.; Menéndez, E.; Estrader, M.; Suriñach, S.; Baró, M. D.; Nogués, J.; Sort, J. Nanocrystalline Electroplated Cu-Ni: Metallic Thin Films with Enhanced Mechanical Properties and Tunable Magnetic Behavior. *Adv. Funct. Mater.* **2010**, *20*, 983−991.

(47) Cullity, B. D. *Elements of X-ray Diffraction*; Addison-Wesley Publishing Company, Inc.: Reading, Massachusetts, USA, 1956; p 262.

(48) Chikazumi, S. *Physics of Magnetism*; John Wiley & Sons, Inc.: USA, 1964; p 254.

90

Supporting Information

Electrodeposited Ni-based magnetic mesoporous films as smart surfaces for atomic layer deposition: an 'all-chemical' deposition approach toward 3D nanoengineered composite layers

Jin Zhang[1,2,], Alberto Quintana[1], Enric Menéndez[1], Mariona Coll[3], Eva Pellicer[1,*], Jordi Sort[1,4,*]*

[1]Departament de Física, Facultat de Ciències, Universitat Autònoma de Barcelona, E-08193 Bellaterra, Cerdanyola del Vallès, Spain

[2]State Key laboratory of Solidification Processing, Center of Advanced Lubrication and Seal Materials, Northwestern Polytechnical University, Xi'an, Shaanxi, 710072, P. R. China

[3] Institut de Ciència de Materials de Barcelona (ICMAB-CSIC), Campus UAB 80193 Bellaterra, Barcelona Spain

[4]ICREA, Pg. Lluís Companys 23, E-08010 Barcelona, Spain

Corresponding Authors

* eva.pellicer@uab.cat

* jordi.sort@uab.cat

* jinzhang@nwpu.edu.cn
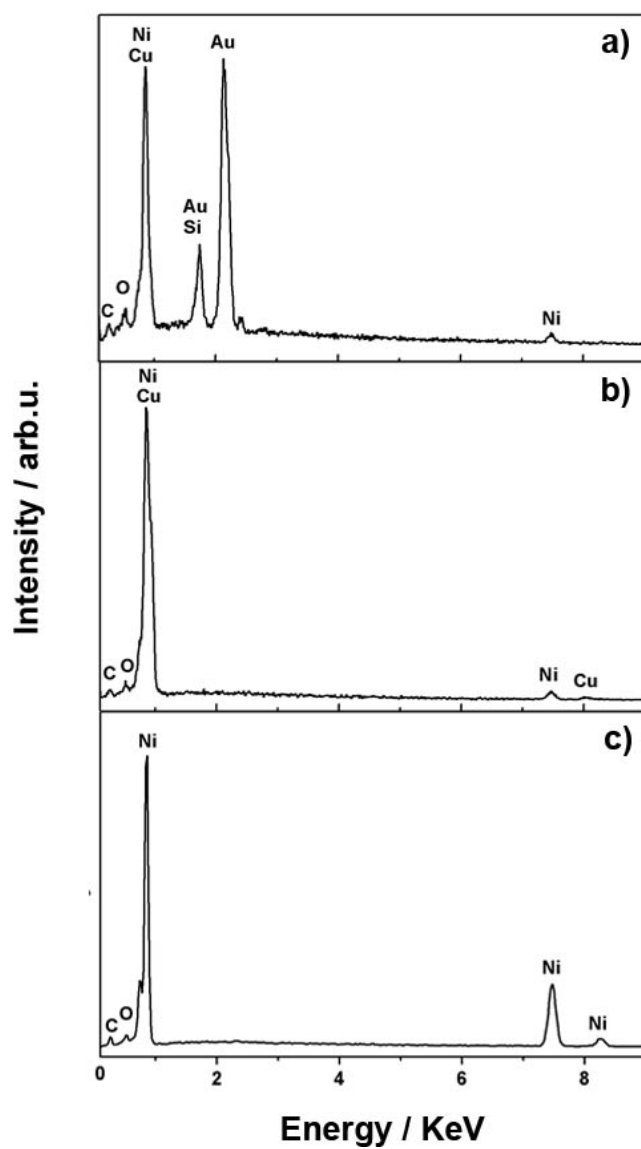
Figure S1. EDX spectra of nanoporous (a) $Cu_{20}Ni_{80}$, (b) $Cu_{45}Ni_{55}$ and (c) Ni layers.

S-2
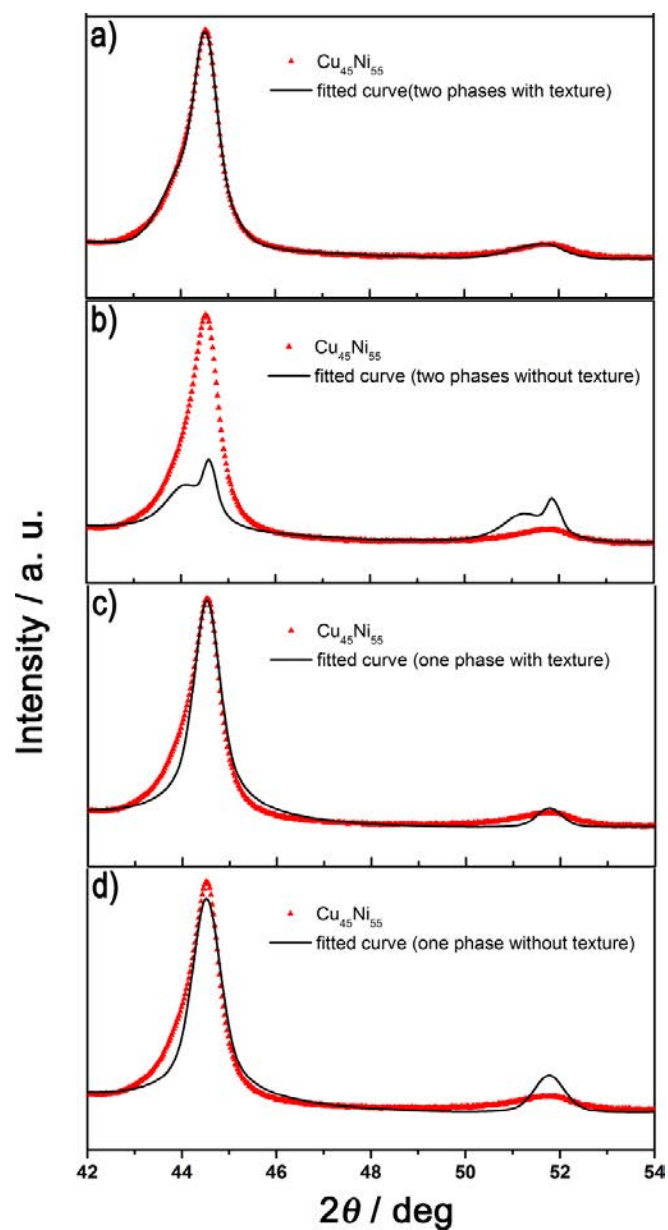
Figure S2. XRD experimental pattern and the fitted curves using the MAUD software, for the Cu$_{45}$Ni$_{55}$ sample. Different approaches are used for the Rietveld refinements: a) two fcc solid solutions with occurrence of crystallographic texture, b) two fcc phases but with no texture, c) one single fcc solid solution with texture, d) one single fcc solid solution without texture.

03

Further Insights

3. Magneto-ionics: An unprecedented magnetoelectric effect

In the previous chapter, the effectiveness to improve the charge-mediated magnetoelectric response of a CuNi alloy film by introducing nanoporosity by means of micelle assisted electrodeposition was demonstrated (1st article). In the second article, the selectiveness in the electrochemical oxidation, promoted by means of an oxidative electrolyte (1M NaOH solution), was exploited to tune the magnetization of a nanoporous CuNi alloy by selectively oxidizing/reducing Cu. In the last article of chapter 2, a novel dual approach to produce 3D metal-ceramic nanocomposites has been shown by conformally coating nanoporous CuNi alloy films with Al_2O_3 using ALD, establishing the basis to perform magnetoelectric experiments in solid state devices.

The above magnetoelectric measurements were all carried by electrolyte-gating in a home-made cell set-up which allows us to apply voltage while performing magneto-optic Kerr effect measurements. MOKE is a local and surface sensitive technique and does not allow for a quantitative determination of the magnetic moment. Therefore, in order to account for magnetization changes while performing magnetoelectric measurements, a similar experimental configuration was implemented in our vibrating sample magnetometer (VSM) setup.

In these previous works, magnetoelectric effects have been tackled in nanoporous metal alloys. Moreover, electrolyte gating has been employed to tune some physical properties, like conductivity, in oxide based superconductors. However, modification of other properties such as magnetic ones has been overlooked.

In order to further shed light on this effect, we investigated magnetoelectric effects via electrolyte-gating using a non-oxidative medium in 100 nm dense Co_3O_4 thin films. Upon electric field actuation, ionic diffusion occurs generating enriched Co and O regions, as demonstrated by EELS, and therefore a ferromagnetic arises. The magnetic signal scales with time and potential. A mechanism is proposed upon structural and defect characterization (TEM, EELS, energy filtered TEM (EFTEM), and positron annihilation spectroscopy (PAS)).

The importance of this work relies in the fact that it is one of the first evidences of room temperature ion migration, since other magneto-ionic approaches require from heat assistance. Moreover, the process is self-sustained, since no external oxygen sources (HfO_2, Gd_2O_3 or Al_2O_3) are needed.

Voltage-controlled ON-OFF ferromagnetism at room temperature in a single metal oxide film

<u>For consistency in the thesis structure, this chapter is structured like a research article.</u>

Abstract

Electric-field controlled magnetism can boost energy-efficiency in widespread applications. However, technologically, this effect is facing important challenges: mechanical failure in strain-mediated piezoelectric/magnetostrictive devices, dearth of room-temperature multiferroics or stringent thickness limitations in electrically-charged metallic films. Voltage-driven ion motion (magneto-ionics) circumvents most of these drawbacks while offering unprecedented magnetoelectric phenomena. Nevertheless, magneto-ionics typically requires heat-treatments and multi-component heterostructures. Here we report on the electrolyte-gated and defect-mediated O and Co transport in a Co_3O_4 *single layer* which allows for *room-temperature* voltage-controlled *ON-OFF ferromagnetism* (magnetic switch) via internal reduction/oxidation processes. Negative voltages partially reduce Co_3O_4 to Co (ferromagnetism: ON), resulting in graded films including Co- and O-rich areas. Positive bias oxidizes Co back to Co_3O_4 (paramagnetism: OFF). This electric-field-induced atomic-scale reconfiguration process is compositionally, structurally and magnetically reversible and self-sustained since no oxygen source other than the Co_3O_4 itself is required. This novel process could lead to new electric-field-controlled device concepts for spintronics.

The search for energy-efficient materials and processes has become central to increasing industrial competitiveness, as well as to fulfilling environmental, health and other societal expectations. A stable, strong, tuneable and non-volatile voltage-control of magnetism might allow for ultra-low-power magnetic storage and spintronic devices[1-4]. So far, magnetoelectric devices are controlled by electric currents, inherently involving a significant energy loss by Joule heating effect. The partial substitution of electric currents by electric fields to manipulate such devices (i.e., voltage-modulation of magnetism) would result in a remarkable energy saving with an important cost reduction[3]. Over the years, voltage control of magnetism has relied on several strategies, such as (i) development of single-phase multiferroic materials with intrinsic magnetoelectric coupling[5,6], (ii) inverse magnetostriction effects in epitaxial piezoelectric/ferromagnetic heterostructures[6-9] or (iii) electric charge accumulation in dielectric/ferromagnetic condenser-like structures[10-14]. Unfortunately, implementation of these materials in real devices is hampered by several factors. Single-phase multiferroics are scarce, usually operative only at low temperatures and still exhibit rather weak magnetoelectric coupling; artificial strain-mediated piezoelectric/magnetostrictive heterostructures are prone to mechanical fatigue and thus have a limited endurance; finally, due to the sub-nanometric electric-field screening length in metallic ferromagnetic materials, electric charge accumulation effects are typically observed only in ultrathin films (<2 nm) which are very sensitive to oxidation. Moreover, most of these approaches typically render volatile magnetic effects which disappear upon voltage removal.

Recently, voltage-induced ionic motion in magnetic materials [15-18] has attracted huge interest, since this phenomenon may allow for an electrical modulation of magnetism to an extent never attained by any other magnetoelectric means. Magneto-ionics opens a new paradigm since it is not limited to the electric-field screening length and it can therefore be relevant in relatively thick films. However, in most previous magneto-ionics studies, voltage needs to be applied at high temperature since ion migration is a thermally-activated process[15,16,18]. Furthermore, the material of interest typically needs to be in contact with Gd_2O_3 or HfO_2 layers, which act as ion reservoirs by accepting or donating oxygen ions depending on the voltage polarity[15,17,18]. So far, the reported magneto-ionic effects are mostly limited to changes in coercivity[16,17,18], anisotropy easy axis[15,17], or exchange bias[19].

Electrolyte gating (in particular, the use of EDL) allows for the generation of very large electric fields (due to the <1 nm EDL thickness) capable of inducing O^{2-} migration in some

oxides. This effect has been exploited to sensitively tune the electrical properties of a variety of materials, eventually suppressing/inducing insulator-to-conductive phase transitions[20-24]. However, to date, magneto-ionic control of ON-OFF ferromagnetism at room temperature has remained elusive.

A drastic voltage-induced ON-OFF ferromagnetism at room temperature has only been achieved by tuning the antiferromagnetic-to-ferromagnetic metamagnetic transition of FeRh[12] or the superparamagnetic blocking temperature of Ni nanoparticles[25], in both cases mediated by the coupling to underlying ferroelectric substrates. High-temperature voltage-assisted oxidation of ultrathin (0.7 nm) Co layers in contact with GdO_x underlayers has also been used to suppress magnetization[15]. In turn, ON-OFF ferromagnetism at low temperatures was achieved in $La_{0.74}Sr_{0.26}MnO_3$ films by electrochemical (pseudo-capacitance) doping[26]. A maximum of up to 70% change of the magnetization has been observed in $ZnFe_2O_4$ films at room temperature by electrochemistry-driven Li-ion exchange[27].

Herein, we report on the *room-temperature* voltage-induced ionic motion of oxygen and cobalt in a *single* 100 nm-thick polycrystalline paramagnetic Co_3O_4 film. Negative biasing tends to reduce Co_3O_4 to Co, resulting in ferromagnetism, whereas, upon positive voltages, the process can be completely reversed, oxidizing Co back to Co_3O_4. The amount of Co, and thus the induced ferromagnetism, scales with time and the applied bias. Part of the induced ferromagnetism is permanent, but can be fully erased by applying positive voltages. Non-stoichiometry, primarily determined by defects such as oxygen and cobalt vacancies and grain boundaries, circumvents the lack of heat assistance and allows for a significant voltage-driven ionic motion even at room temperature[28]. This approach opens up the possibility to take advantage of internal redox processes in single-phase thick layers, without the need of secondary oxides acting as donor/acceptor of oxygen.

To investigate the influence of electric field on the magnetic properties, the Co_3O_4 films, prepared by plasma-enhanced atomic layer deposition[29,30] (see Methods), were subjected to voltage for a given period of time using a home-made electrolytic cell, as sketched in Figure 1a (i.e., electrolyte-gating)[13,31]. The voltage was then switched off and, immediately after, in-plane VSM measurements were recorded *in-situ* inside the electrolyte. An anhydrous liquid media (propylene carbonate with Na+ solvated species) was used as electrolyte for two purposes: (i) to control the surroundings of the Co_3O_4 with a non-oxidizing medium, and (ii) to be able to maximize electric fields while applying low and

moderate voltages. In this configuration, the Co_3O_4 film is used as a working electrode. Voltage is applied between the film electrode and a Pt counter-electrode (see Figure S1).

As voltage is increased, ions in the electrolyte solution diffuse towards the surface of the electrode forming the EDL which leads to strong electric fields on the order of hundreds of MV/cm[13]. As can be seen in Figure 1b, the pristine Co_3O_4 sample shows no ferromagnetic behaviour in agreement with its paramagnetic nature at room temperature. Conversely, after subjecting the sample to –10 V for 60 min, the measurements show a clear hysteresis loop, evidencing ferromagnetism. This generated ferromagnetism can be fully removed (and, thus, the process reversed) by applying a positive voltage of 20 V for 60 min. It might be anticipated that this reversible phenomenon could be explained in a magneto-ionic framework through voltage-driven O^{2-} transport, giving rise to reduction and oxidation (i.e., redox) processes which are polarity dependent. For a given voltage (i.e., –10 V), Figure 1c shows the VSM measurements as a function of time. Further, Figure 1d shows the voltage-dependence of the hysteresis loops for a fixed biasing time (i.e., 60 min). The magnetic moment scales with time and, in a more pronounced manner, with voltage, indicating that the underlying atomic mechanisms probably rely on voltage-activated diffusion effects.

The measured magnetic signal after applying –50 V is equivalent to a metallic 6 nm–thick Co film. Treatments up to –200 V were also carried out to maximize the effects and to subsequently perform a detailed structural characterization of the samples. As shown in Figure S2, upon removal of the –200 V (applied for 30 min), the magnetic moment relaxes following an exponential decay but a clear ferromagnetic signal remains (even for several months). Note that the hysteresis loop recorded immediately after such a high negative applied voltage is open (Figure S2a) since the magnetic moment progressively decreases during the time needed to acquire the loop. However, once the film is relaxed, the loops close, as expected. Note that this relaxation effect is considerably weaker for lower applied electric fields. For example, the loops obtained after applying lower voltages for 60 min close completely at high applied magnetic fields (Figure 1d).

To shed light on the atomic mechanisms which take place under voltage actuation, compositional characterization of the top sample surface through XPS was carried out (Figure 2). As shown in Figure 2a, the XPS spectrum of the pristine sample is consistent with a rather pure Co_3O_4 phase with traces of CoO, while, upon treatment at –10 V for 60 min, metallic Co or a Co-rich phase is present at least at the sample surface. Hence,

negative biases promote reduction from Co_3O_4 to CoO and from CoO to ferromagnetic Co (Figure 2b), in agreement with the magnetometry results. It should be mentioned that CoO may partially come from natural oxidation from Co since the XPS is performed *ex-situ* and, thus, the sample is exposed to air. In contrast to negative biases, positive voltages allow for the recovery of the Co_3O_4 phase, evidencing that Co tends to re-oxidize (Figure 2c). This demonstrates the high reversibility of the process, which not only takes place magnetically but also compositionally, and further indicates that voltage-driven redox processes could be a plausible scenario. Figure 2d (corresponding to an applied voltage of –200 V for 30 min) confirms that the amount of generated Co scales with the applied negative voltage in concordance with the magnetic results.
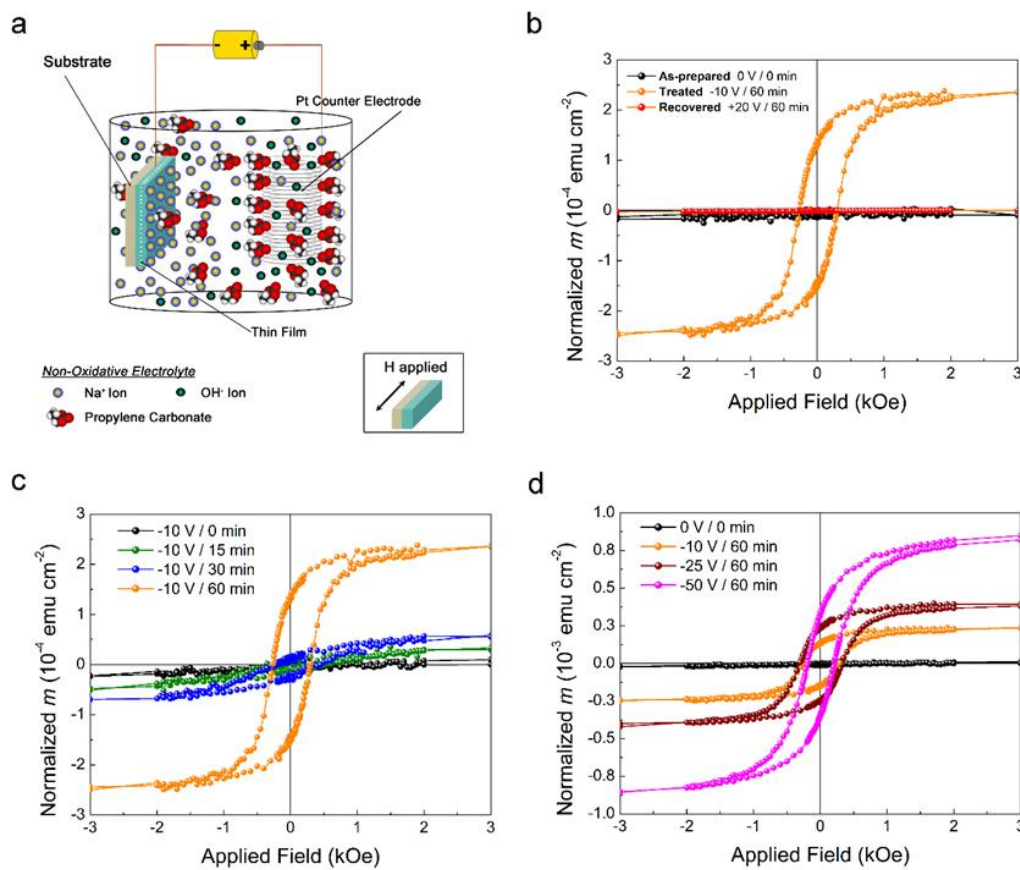
Figure 1 | Voltage actuation and magnetic characterization by VSM. a, Custom-made electrolytic cell used for the *in-situ* voltage-applied VSM measurements. **b**, normalized moment (*m*) versus applied field VSM measurements of a pristine sample, after being treated at –10 V for 60 min and after recovery having applied +20 V for 60 min. **c**, VSM measurements corresponding to a sample subjected to –10 V for 0, 15 min, 30 min and 60 min. **d**, VSM measurements corresponding to a sample subjected to decreasing negative voltages of 0 V, –10 V, –25 V and –50 V, applied during 60 min.

From a compositional viewpoint, it is clear that this ON-OFF ferromagnetism can be electrically-modulated by voltage-driven ion migration. However, further information on

morphological and structural aspects is essential to determine the mechanisms which govern this atomic transport. Actually, Co_3O_4 is prone to exhibit vacancies[32] and, in case of bulk Co_3O_4, Co migration is vacancy-mediated (i.e., via Co^{3+} vacancies)[33,34].
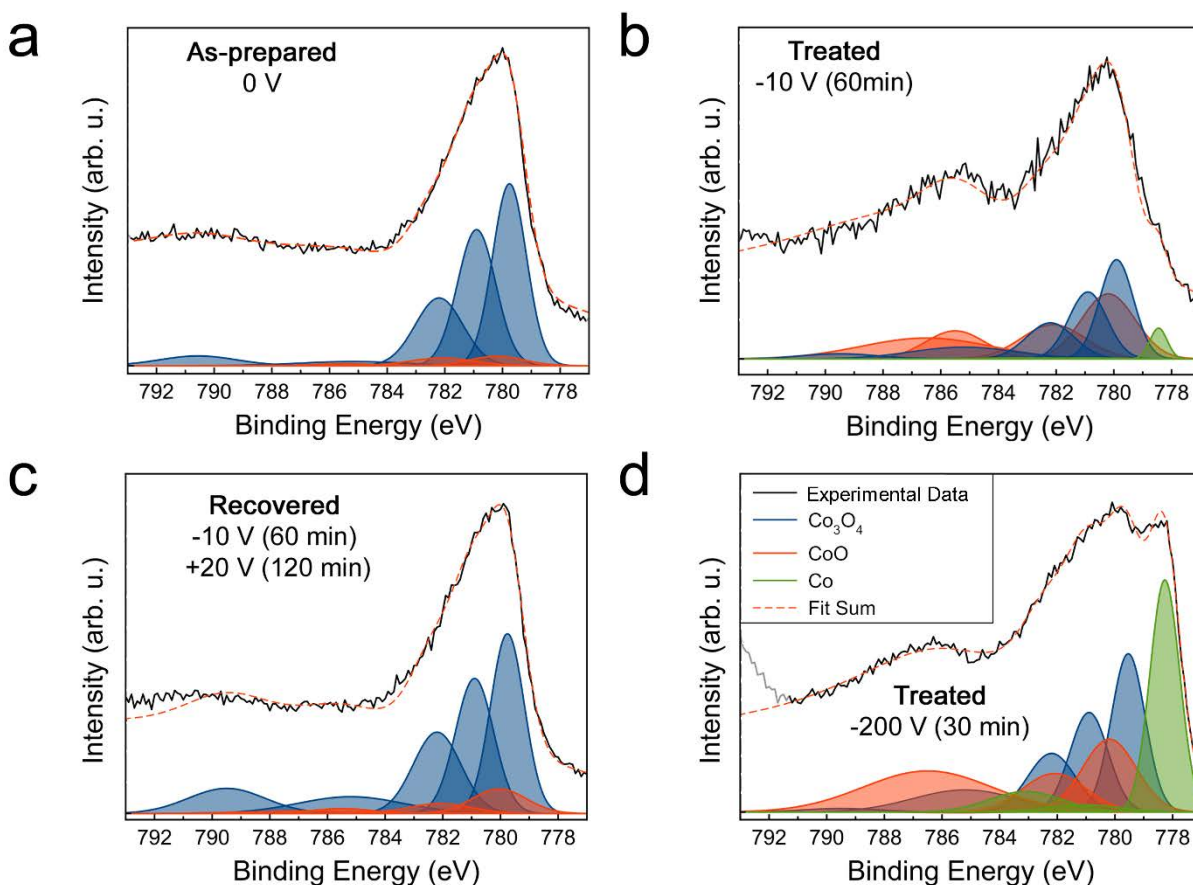
Figure 2 | Compositional characterization by XPS. XPS core level Co2p spectrum of **a** the as-prepared sample, **b** the same sample upon –10 V for 60 min, **c** the sample in **b** after applying +20 V for 120 min and **d** another sample after being treated at –200 V for 30 min. The spectra are deconvoluted taking into account Co_3O_4, CoO and Co contributions.

For a more detailed structural characterization, three samples were investigated: an as-deposited film, a film treated at –200 V for 30 min (where the effects of voltage are maximized) and a sample treated at –50 V for 30 min and subsequently fully recovered (i.e., brought back to the paramagnetic state) by applying +100 V for 60 min. Full recovery from the sample treated at –200 V would require positive voltages higher than the ones available in our setup, hence the recovery was investigated in a sample treated at –50 V.

Remarkably, scanning electron microscopy (Figure S3) and θ/2θ X-ray diffraction (Figure S4 and Table S1) indicate that the ion migration mechanism is, at least partially, grain boundary-mediated (see Supplementary Information).
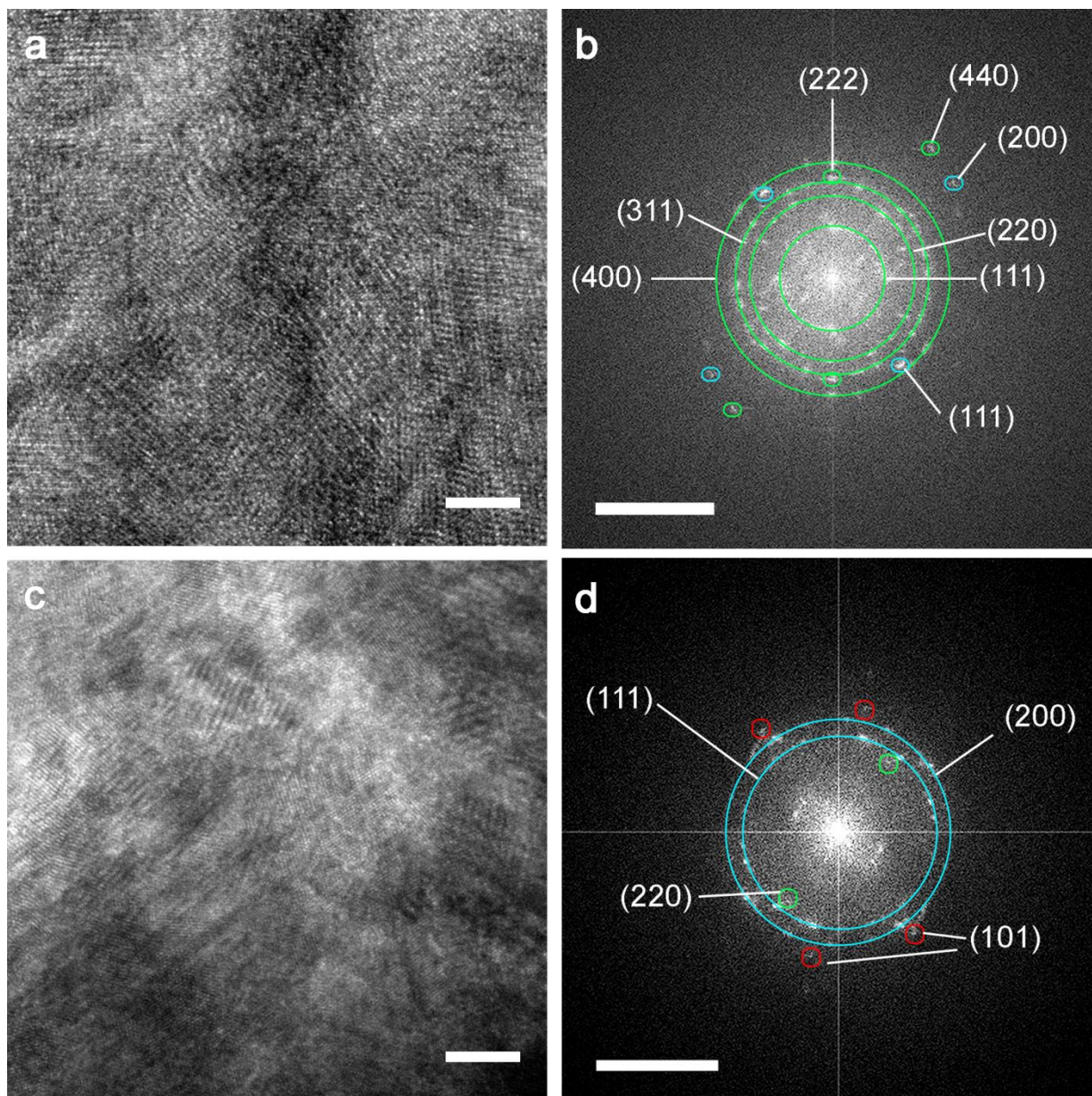
Figure 3 | Structural characterization by HRTEM of the top regions of the films. a, **b** HRTEM image and the corresponding fast Fourier transform of an untreated sample, respectively. **c**, **d**, HRTEM image and the corresponding fast Fourier transform of a sample treated at −200 V for 30 min, respectively. The scale bars in a and c correspond to 5 nm while those in b and d correspond to 5 nm^{-1}. The main diffraction spots have been labelled and indexed (see Table S2 and S3). In green, blue and red, reflections corresponding to Co_3O_4 (JCPDF 42-1467), CoO (JCPDF 43-1004) and HCP-Co (JCPDF 05-0727) are indicated.

To further investigate the structure of the samples, cross-section lamellae of the pristine and treated samples were prepared (Figure S5). The cross sections reveal the fully dense appearance of the films and confirm their average thickness of around 100 nm. High resolution transmission electron microscopy (HRTEM) was carried at a region close to the as-deposited sample surface, as indicated by the green square in Figure S5a (see Figure 3a). The corresponding fast Fourier transform (FFT) (Figure 3b) shows diffraction signal arising mainly from Co_3O_4 and a small contribution from CoO (Fm3m) (Table S2). Conversely, the sample treated at –200 V for 30 min shows, besides Co_3O_4 and CoO, clear spots from hexagonal close-packed (HCP) Co, in agreement with the XPS characterization (green square in Figure S5b, Figure 3c,d and Table S3). This confirms that, for negative applied voltages, O migrates from Co_3O_4 and leaves behind metallic Co areas. Similar results were also obtained from regions closer to the SiO_2 interface (see Figure S6, which correspond to the red squares in Figure S5), evidencing that, at such voltages, the process not only reduces the surface but affects the whole Co_3O_4 film (Tables S4–S7). In Figure S7, a HCP-Co nanocrystallite is identified and highlighted in red. The nanocrystallinity of the generated HCP-Co is consistent with the absence of clear reflections in the θ/2θ XRD pattern of the treated sample (red curve in Figure S4). Finally, HRTEM further confirms that, upon positive biasing, the initial state is recovered (Figure S8).

To investigate the Co-O distribution, energy-filtered transmission electron microscopy imaging of the as-deposited, treated and recovered samples was performed. In the as-deposited sample (Figure 4a), a rather homogeneous distribution of Co and O can be observed. In contrast, the presence of Co-rich and O-rich areas is clearly detected after negative biasing using –200 V (Figure 4b,c). Figure 4b also reveals that O has a tendency to diffuse towards the SiO_2 interface, while Co-rich regions tend to be more abundant close to the film's air-exposed surface. This is probably related to the way voltage is applied to the system (Figure S1). Interestingly, O-rich channels are also observed (Figure 4c). These channels could act as diffusion paths and allow for a large incorporation of O, to compensate for the formation of metallic Co areas. Upon recovery, Co and O redistribute and the sample becomes compositionally homogeneous again (Figure S9).

To locally quantify the Co-O distribution, Co and O electron energy loss spectroscopy mappings were conducted. As shown in Figure 5a–c, both Co and O are homogeneously distributed in the as-grown sample, with Co and O atomic percentages corresponding rather well to those of stoichiometric Co_3O_4 (i.e., 42.9 and 57.1 at.% of Co and O, respectively). In contrast to the as-grown sample, the EELS mappings of the sample biased

at −200 V reveal the presence of Co-rich and O-rich areas, with compositional variations ranging from almost pure Co to O-rich regions with $Co_{20}O_{80}$ (at.%) (Figure 5e,f,h,i). These results indicate that formation of HCP-Co is accompanied with an increase of the O content in Co_3O_4 (i.e., formation of cationic vacancies in the structure of Co_3O_4). Actually, it is known that Co_3O_4 can accommodate more oxygen than the stoichiometric composition in its structure[35], particularly under certain conditions of temperature and oxygen partial pressure[36]. Here, such an effect is electric-field-induced. Similar results have been reported in electrolyte-gated VO_2, where oxygen concentrates forming chains of edge-sharing VO_6 octahedra[16]. Analogous chains of dimeric-sharing CoO_6 octahedra have been also reported in CoO_x nanoparticles[37]. Remarkably, a reduction of the interplanar distances has been reported in O-rich Co_3O_4 fibers[37]. The coexistence of stoichiometric with off-stoichiometric $Co_{3-x}O_{4+x}$ regions could be correlated with the asymmetry in the XRD peaks of the negatively biased sample (Figure S4).

To rule out spurious effects arising from Na^+ from the electrolyte or Si^{4+} from the substrate, EDX spectroscopy and EELS spectra were acquired on the sample treated at −200 V for 30 min. Neither Na nor Si were detected (Figure S10, S11 and S12). The mechanism herein reported is thus different from previous works on lithiation of $ZnFe_2O_4$, $CuFe_2O_4$ and α-Fe_2O_3 aiming at partially tuning their magnetization by electrochemical treatment in 1 M $LiPF_6$ in ethylene carbonate and dimethyl carbonate solutions[27,38]. Finally, Co and O EELS mappings were also performed for the fully recovered sample and, as expected, a homogeneous composition throughout the film close to stoichiometric Co_3O_4 was obtained (Figure S13). Thus, the structural characterization clearly demonstrates that, in contrast to conventional magneto-ionic systems where there is a source/reservoir of oxygen to trigger the redox processes,[15-18] in the here-prepared Co_3O_4 films the magnetic switch is accomplished by a reversible atomic scale reconfiguration of the O and Co ions within the film itself.

Variable energy (VE) and coincidence Doppler broadening (cDB) positron annihilation spectroscopy (PAS)[39,40] as well as positron annihilation lifetime spectroscopy (PALS) experiments were performed (see Methods and Supplementary Information) in an attempt to shed further light on the presence of negatively charged open volume defects (i.e., cationic Co vacancies, Co-O vacancy complexes and grain boundaries) with depth-resolved resolution.

VE-PAS experiments (Figure S14) evidence a relative increase of the low electron momentum fraction, S (directly proportional to the size and concentration of defects[41], see Supplementary Information), after treatment using negative voltages, while S concomitantly decreases again after positive biasing. This is in agreement with the increase of open volume defects for negatively biased samples, supporting the presence of channels for ionic O transport. Since VE-PAS cannot clearly distinguish between defects size and defect concentration, additional PALS and cDB-PAS investigations were performed.
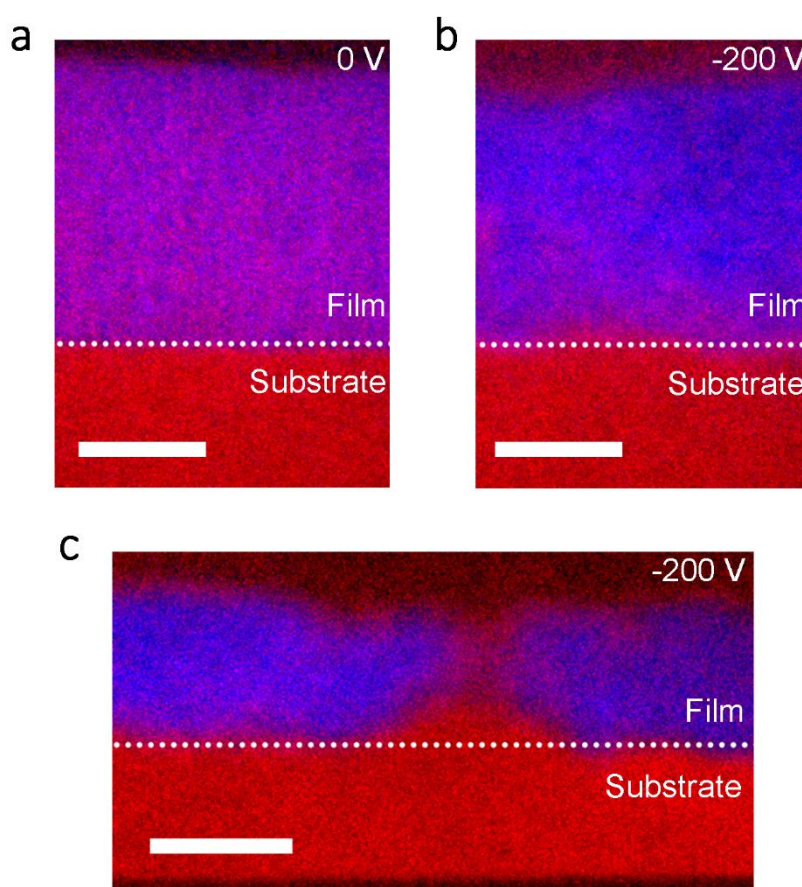
Figure 4 | Depth-resolved structural and compositional characterization by EFTEM. a, **b**, **c**, EFTEM image corresponding to (a) the as-grown sample and (b,c) two different regions of a negatively biased sample at –200 V for 30 min. The scale bars correspond to 50 nm in a and b, and to 100 nm in c. Blue spots correspond to Co and red spots to O.

The PALS spectra after background correction were deconvoluted using the non-linearly least-squared-based package PALSfit fitting software[42,43] into three discrete lifetime components, which directly evidence three different defect types (sizes) [see Figure 6a–b and S15a]. The resulting intensities reflect the concentration of each defect type (size) [Figure 6c and S15b]. In general, positron lifetime scales with defects size (i.e., the larger

the open volume, the longer it takes for positrons to be annihilated)[40,43,44]. The shortest lifetime component (τ_1<0.30 ns) represents vacancy clusters inside the grains, whereas the intermediate (0.35<τ_2<0.70 ns) and the longest (1.5<τ_3<4.0 ns) lifetime components indicate grain boundaries and larger voids (1–3 nm in diameter) contributions, respectively. The lifetime of small vacancy clusters (τ_1) is around 0.21 ns in the as-grown sample. This lifetime strongly increases (up to $\tau_1 \approx$0.29 ns) in the sample treated at –200 V (indicating an increase of the average vacancy size), and then decreases down to about 0.23–0.25 ns in the recovered sample. The lifetime component τ_2, representing grain boundary contributions, behaves similarly, which is in accordance with a Co and O ionic migration mechanism. Namely, during negative biasing, ionic motion is promoted at the grain boundaries and large open volume defects are left behind, so that disordered grain boundaries increase in size (in agreement with Figure S3c); positive biasing reverses the ionic migration and defects states are partially refilled. The contribution from the τ_3 component within the films is below 1% (see Supplementary Information), thus it can be neglected.

In order to translate the obtained positron lifetime values to realistic defects sizes, additional cDB-PAS measurements were also conducted (Figure 6d) and compared with theoretical calculations by means of the so-called atomic superposition (ATSUP) method[45,46] (Figure 6e) [see Methods and Supplementary Information]. Electron momentum distributions, acquired at E_p=3 keV and normalized to a Co defect-free reference spectrum, are presented in Figure 6d for the as-prepared, treated and recovered samples, where annihilation events come from the film region only (see Figure S16). The low momentum part of the spectra, p_L<8×10^{-3} m_0c, is simply another representation of S (E_p=3 keV) from Figure S14. The high electron momentum part of the ratio plots, p_L>8×10^{-3} m_0c, shows a minimum at $p_L \approx$16×10^{-3} m_0c for all the samples, which is in qualitative agreement with the calculated curves from Figure 6e. The high momentum part is a fingerprint of the defect site atomic surrounding and, interestingly, it does not consist of pure HCP-Co phase but, instead, is in agreement with the calculations for mixed vacancies involving different amounts of O and Co atoms (Figure 6e). This does not exclude Co segregation, since positrons preferentially annihilate at the oxide phase (due to their higher affinity to oxides).
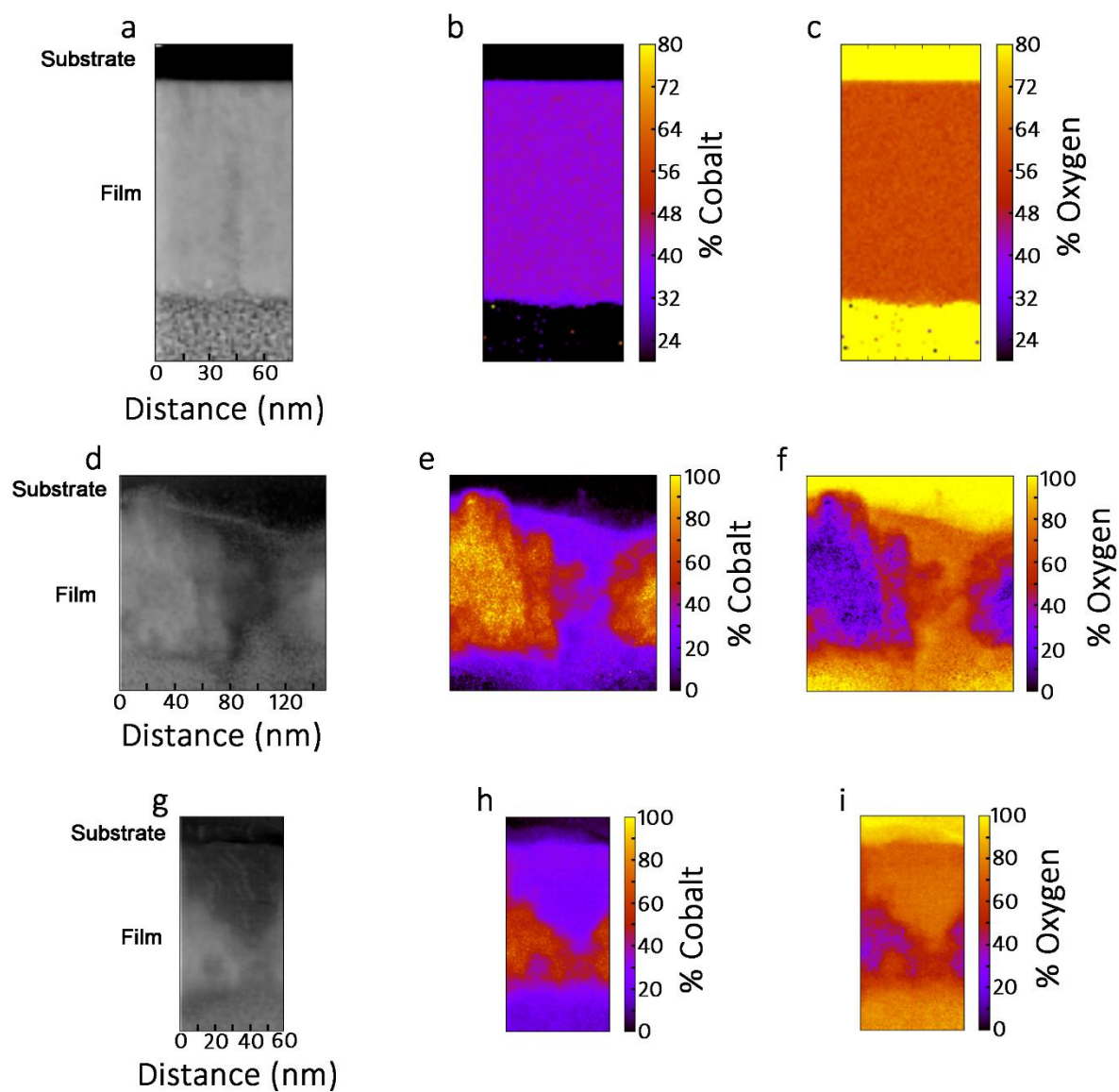
Figure 5 | Structural and compositional characterization by high-angle annular dark-field scanning transmission electron microscopy HAADF-STEM and EELS. a–c, **d–f** and **g–i**, HAADF, Co and O EELS mappings of the pristine sample, and two different regions of a sample negatively biased at −200 V for 30 min, respectively.
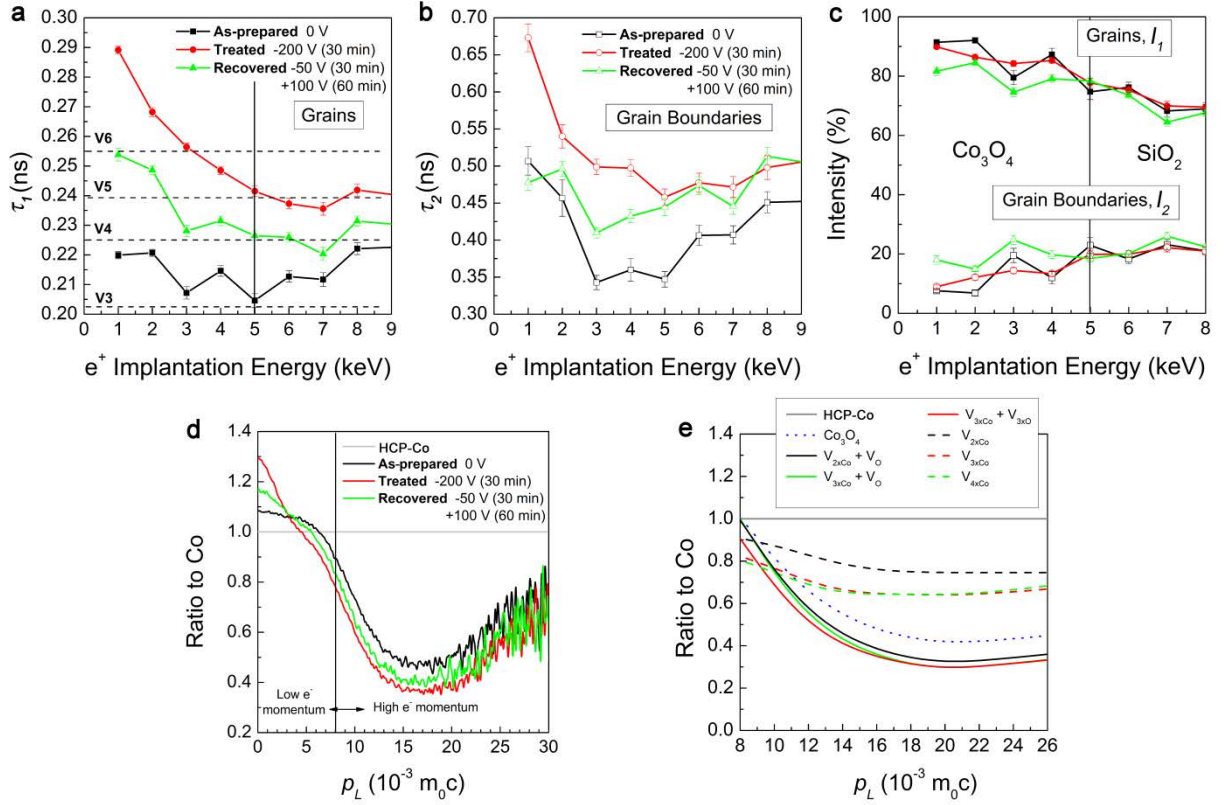
Figure 6 | Positron annihilation spectroscopy characterization: a-c, Positron annihilation lifetime spectroscopy (PALS) analysis, where contributions of the annihilation signal from grains (**a**) and grain boundaries (**b**) is shown for as-grown (black), treated (red), and recovered (green) samples. The black vertical lines show an approximate position of the interface between the Co_3O_4 film and the SiO_2 buffer layer. The straight lines in (**a**) mark the lifetime of the vacancy complexes of different sizes: from trimers (V3) to clusters of 6 vacancies (V6). **c**, the absolute intensity of the lifetime components. **d**, Coincidence Doppler broadening ratio plots (normalization by a defect free Co reference) measured at E_p = 3 keV, with a corresponding atomic superposition (ATSUP) simulation (**e**).

Table S8 shows the calculated positron lifetime values for different types of vacancy defects in HCP-Co and Co_3O_4. The results indicate that existence of small vacancy clusters, probably in the form of cobalt vacancy dimers (two vacancies), V_{2xCo}, or trimers (three vacancies), V_{3xCo}, coupled with an oxygen monovacancy (single vacancy), V_O (where a lifetime higher than 0.2 ns is obtained). These configurations, compatible with our experiment, are indicated in bold in Table S8 (further details can be found in the Supplementary Information).

In conclusion, voltage-driven O and Co redistribution has been demonstrated in 100 nm-thick Co_3O_4 films through electrolyte-gating, allowing for the controlled generation and suppression of ferromagnetism. A negative voltage reduces Co_3O_4 to Co (ferromagnetism:

ON), whereas the process is reversed by applying a positive bias, aimed at oxidizing Co back to Co_3O_4 (paramagnetism: OFF). These gate-induced O and Co migrations are driven by mixed vacancy clusters as evidenced by positron annihilation spectroscopy. Ionic transport seems to be promoted at grain boundaries and is further assisted by the formation of diffusion channels that incorporate large amounts of O. Part of the generated ferromagnetism is not transient but stable, although it can be easily erased by applying adequate positive voltage values. The process is self-sustained in the sense that no external source/sink of oxygen is required. Our approach also circumvents the need of thermally-assisted ionic migration, i.e., voltage-driven oxygen motion takes place at room temperature. Furthermore, our procedure could in principle be extended to room temperature oxide-based antiferromagnets (e.g., NiO), allowing for an extra degree of freedom taking advantage of exchange bias effects, thus opening new avenues in spintronic devices.

Methods

Sample preparation

Co_3O_4 films were grown on thermally-oxidized Si wafers (i.e. SiO_2 (100 nm)/ <100> Si (1 mm)) by plasma-enhanced atomic layer deposition (PE-ALD) using bis(cyclopentadienyl)cobalt ($CoCp_2$, STREM, min. 98%) as Co precursor and O_2 plasma as oxygen source[29]. The depositions were performed in a home-built ALD reactor with a base pressure of 10^{-6} mbar[29,30]. The container with the solid $CoCp_2$ precursor and the tube to the reactor were heated to 80°C and 100°C, respectively, to prevent deposition of the precursor in the tubes or valves. The Co_3O_4 layers were produced by alternate pulsing of $CoCp_2$ and O_2 plasma at a deposition temperature of 200°C. Argon was used as a carrier gas for the Co precursor. The ALD cycle consisted of 5 s $CoCp_2$ exposure, 5 s of pumping, 5 s O_2 plasma exposure and 5 s of pumping. During the exposures, the pressure in the ALD chamber was in the 10^{-3} mbar range. The growth rate was 0.5 Å/cycle, and a total of 2000 ALD cycles were applied to obtain 100 nm thick Co_3O_4 films.

Structural and compositional measurements

SEM images were acquired using secondary electrons in a FEI Magellan 400L microscope operated at 20 kV. TEM, STEM/EDX and EELS were performed on a TECNAI F20 HRTEM/STEM microscope operated at 200 kV. Cross sectional lamellae from the as-grown, treated (−200 V for 30 min) and recovered (−50 V for 30 min / +100 V for 1 h) samples were prepared by focused ion beam (FIB) and placed onto a Cu TEM grid.

θ/2θ X-ray diffraction patterns of the different samples were recorded on a Philips X'Pert Powder diffractometer with a Pixel[1D] detector in the 17°–40° 2θ range using Cu K_α radiation with intensity (Cu $K_{\alpha 2}$)/intensity (Cu $K_{\alpha 1}$)=0.5. The structural parameters of Co_3O_4, such as crystallite size (i.e., average coherently diffracting domain) or lattice parameter were evaluated by fitting the XRD patterns in the 18°-20° 2θ range using the MAUD Rietveld refinement program[47].

VE-PAS[39,40] was used to investigate depth-resolved open volume defects at the Slow-Positron System of Rossendorf (SPONSOR) beamline, which provides mono-energetic but variable energy positron beam. Further details on this type of experiments, as well as on PALS and theoretical calculations using the ATSUP method are given in the Supplementary Information.

Magnetic characterization

Magnetic measurements were carried out at room temperature in a vibrating sample magnetometer from Micro Sense (LOT-Quantum Design), with a maximum applied

magnetic field of 2 T. Figure 1a illustrates the experimental setup used for the *in-situ* magnetoelectric measurements. The sample was mounted in a home-made electrolytic cell filled with anhydrous propylene carbonate with Na^+ solvated species (i.e., non-oxidative media), and the magnetic properties were measured along the film plane after applying different voltages, using an external Agilent B2902A power supply, between the sample and the counter-electrode in a similar fashion of that presented in references 13 and 31. The Na^+ solvated species in the electrolyte are aimed at reacting with any traces of water. The longitudinal magnetic signal was normalized to the area of the sample immersed in the electrolyte.

References

1. Dieny, B. et al. Spin-transfer effect and its use in spintronic components. *Int. J. Nanotechnol.* **7**, 591–614 (2010).

2. Hu, J.-M., Li, Z., Chen, L.-Q. & Nan, C.-W. High-density magnetoresistive random access memory operating at ultralow voltage at room temperature. *Nat. Commun.* **2**, 553 (2011).

3. Shiota, Y. et al. Induction of coherent magnetization switching in a few atomic layers of FeCo using voltage pulses. *Nat. Mater.* **11**, 39–43 (2012).

4. Bader, S. D. & Parkin, S. S. P. Spintronics. *Rev. Condens. Matter Phys.* **1,** 71–88 (2010).

5. Catalan, G. & Scott, J. F. Physics and applications of bismuth ferrite. *Adv. Mater.* **21,** 2463–2485 (2009).

6. Eerenstein, W., Mathur, N. D. & Scott J. F. Multiferroic and magnetoelectric materials. *Nature* **442,** 759–765 (2006).

7. Wang, Y., Hu, J., Lin, Y. & Nan C.-W. Multiferroic magnetoelectric composite nanostructures. *NPG Asia Mater.* **2**, 61–68 (2010).

8. Liu, M. et al. Giant electric field tuning of magnetic properties in multiferroic ferrite/ferroelectric heterostructures. *Adv. Funct. Mater.* **19**, 1826–1831 (2009).

9. Wei, Y. et al. Four-state memory based on a giant and non-volatile converse magnetoelectric effect in FeAl/PIN-PMN-PT structure. *Sci. Rep.* **6**, 30002 (2016).

10. Weisheit, M et al. Electric field-induced modification of magnetism in thin-film ferromagnets. *Science* **315**, 349–351 (2007).

11. Ovchinnikov, I. V. & Wang, K. L. Theory of electric-field-controlled surface ferromagnetic transition in metals. *Phys. Rev. B* **79**, 020402(R) (2009).

12. Cherifi, R. O. et al. Electric-field control of magnetic order above room temperature. *Nature Mater.* **13**, 345–351 (2014).

13. Quintana, A. et al. Voltage-induced coercivity reduction in nanoporous alloy films: a boost toward energy-efficient magnetic actuation. *Adv. Funct. Mater.* **27**, 1701904 (2017).

14. Duan, C.-G. et al. Surface magnetoelectric effect in ferromagnetic metal films. *Phys. Rev. Lett.* **101**, 137201 (2008).

15. Bi, C. et al. Reversible control of Co magnetism by voltage-induced oxidation. *Phys. Rev. Lett.* **113**, 267202 (2014).

16. Song, C., Cui, B., Li, F., Zhou, X. & Pan, F. Recent progress in voltage control of magnetism: Materials, mechanisms, and performance. *Prog. Mater. Sci.* **87**, 33–82 (2017).

17. Bauer, U. et al. Magneto-ionic control of interfacial magnetism. *Nat. Mater.* **14**, 174–181 (2015).

18. Gilbert, D. A. et al. Structural and magnetic depth profiles of magneto-ionic heterostructures beyond the interface limit. *Nat. Commun.* **7**, 12264 (2016).

19. Gilbert, D.A. et al. Controllable positive exchange bias via redox-driven oxygen migration. *Nat. Commun.* **7**, 11050 (2016).

20. Zhang, L. et al. The mechanism of electrolyte gating on high-T_c cuprates: the role of oxygen migration and electrostatics. *ACS Nano* **11**, 9950–9956 (2017).

21. Lu, N. et al. Electric-field control of tri-state phase transformation with a selective dual-ion switch. *Nature* **546**, 124–128 (2017).

22. G. Dubuis et al. Oxygen displacement in cuprates under ionic liquid field-effect gating. *Sci. Rep.* **6**, 32378 (2016).

23. Jeong, J. et al. Suppression of metal-insulator transition in VO_2 by electric field–induced oxygen vacancy formation. *Science* **339**, 1402–1405 (2013).

24. Jeong, J. et al. Giant reversible, facet-dependent, structural changes in a correlated-electron insulator induced by ionic liquid gating. *Proc. Natl. Acad. Sci. U.S.A.* **112**, 1013–1018 (2015).

25. Kim, H. K. D. et al. Magnetoelectric Control of Superparamagnetism. *Nano lett.* **13**, 884–888 (2013).

26. Molinari, A., Hahn, H. and Kruk, R. Voltage-controlled On/Off switching of ferromagnetism in manganite supercapacitors, *Adv. Mater.* **30**, 1703908, (2017).

27. Dasgupta, S. et al. Toward on-and-off magnetism: reversible electrochemistry to control magnetic phase transitions in spinel ferrites. *Adv. Funct. Mater.* **26**, 7507–7515 (2016).

28. Zhang, Q. et al. Atomic-resolution imaging of electrically induced oxygen vacancy migration and phase transformation in $SrCoO_{2.5-\sigma}$. *Nat. Commun.* **8**, 104 (2017).

29. Dendooven, J., Deduytsche, D., Musschoot, J., Vanmeirhaeghe, R. L. & Detavernier, D. Conformality of Al_2O_3 and AlN deposited by plasma-enhanced atomic layer deposition. *J. Electrochem. Soc.* **157**, G111–G116 (2010).

30. Xie, Q. et al. Atomic layer deposition of TiO_2 from tetrakis-dimethyl-amido titanium or Ti isopropoxide precursors and H_2O. *J. Appl. Phys.* **102**, 083521 (2007).

31. Quintana, A. et al. Tunable magnetism in nanoporous CuNi alloys by reversible voltage-driven element-selective redox processes. *Small* In press, 1704396 (2018). DOI: 10.1002/smll.201704396.

32. Casas-Cabanas, M. Defect chemistry and catalytic activity of nanosized Co_3O_4 et al. *Chem. Mater.* **21**, 1939–1947 (2009).

33. Gawali, S. R. et al. Role of cobalt cations in short range antiferromagnetic Co_3O_4 nanoparticles: a thermal treatment approach to affecting phonon and magnetic properties. *Sci. Rep.* **8**, 249 (2018).

34. Chen, X. et al. Nanoscale Magnetization reversal caused by electric field-induced ion migration and redistribution in cobalt ferrite thin films. *ACS Nano* **9**, 4210–4218 (2015).

35. George, G. & Anandhan, S. Structural characterization of nano-crystalline Co_3O_4 ultra-fine

36. fibers obtained by sol–gel electrospinning. *J. Sol-Gel Sci. Technol.* **67**, 256–266 (2013).

37. Zasada, F., Piskorz, W., Sojka, Z. Cobalt Spinel at Various Redox Conditions: DFT+U Investigations into the Structure and Surface Thermodynamics of the (100) Facet, *J. Mater. Chem. C* **119**, 19180–19191 (2015).

38. Chen, Z. *et al*. Amorphous Cobalt Oxide Nanoparticles as Active Water-Oxidation Catalysts. *ChemCatChem.* **9**, 3641–3645 (2017).

39. Dasgupta, S. *et al*. Intercalation-Driven Reversible Control of Magnetism in Bulk Ferromagnets. *Adv. Mater.* **26**, 4639–4640 (2014).

40. Anwand, W., Brauer, G., Butterling, M., Kissener, H. R. & Wagner A. Design and construction of a slow positron beam for solid and surface investigations. *Defect Diffus. Forum.* **331**, 25–40 (2012).

41. Krause-Rehberg, R. & Leipner, H. Positron Annihilation in Semiconductors, Solid-State Sciences. (Springer, Berlin, 1999).

42. Khan, E. H., Weber, M. H., McCluskey, M. D. Formation of Isolated Zn Vacancies in ZnO Single Crystals by Absorption of Ultraviolet Radiation: A Combined Study Using Positron Annihilation, Photoluminescence, and Mass Spectroscopy, *Phys. Rev. Lett.* **111**, 017401 (2013).

43. Wagner, A., Anwand, W., Attallah, A. G., Dornberg, G., Elsayed, M., Enke, D., Hussein, A. E. M., Krause-Rehberg, R., Liedke, M. O., Potzger, K, Trinh, T. T. Positron annihilation lifetime spectroscopy at a superconducting electron accelerator. *J. Phys.: Conf. Ser.* **791**, 012004 (2017).

44. Olsen, J. V., Kirkegaard, P., Pedersen, N. J., Eldrup, M. PALSfit: A new program for the evaluation of positron lifetime spectra. *Phys. Status Solidi C* **4**, 4004–4006 (2007).

45. Tuomisto, F., Makkonen, I. Defect identification in semiconductors with positron annihilation: Experiment and theory. *Rev. Mod. Phys.* **85**, 1583–1631 (2013).

46. Puska, M. J., Nieminen, R. M. Defect spectroscopy with positrons: a general calculational method. *J. Phys. F Met. Phys.* **13**, 333–346 (1983).

47. Seitsonen, A. P., Puska, M. J., Nieminen, R. M. Real-space electronic-structure calculations: Combination of the finite-difference and conjugate-gradient methods. *Phys. Rev. B.* **51**, 14057–14061 (1995).

48. Lutterotti, L. & Scardi, P. Simultaneous structure and size–strain refinement by the Rietveld method. *J. Appl. Crys.* **23**, 246–252 (1990).

Supporting Information

Voltage-controlled ON-OFF ferromagnetism at room temperature in a single metal oxide film

A)   Experimental setup
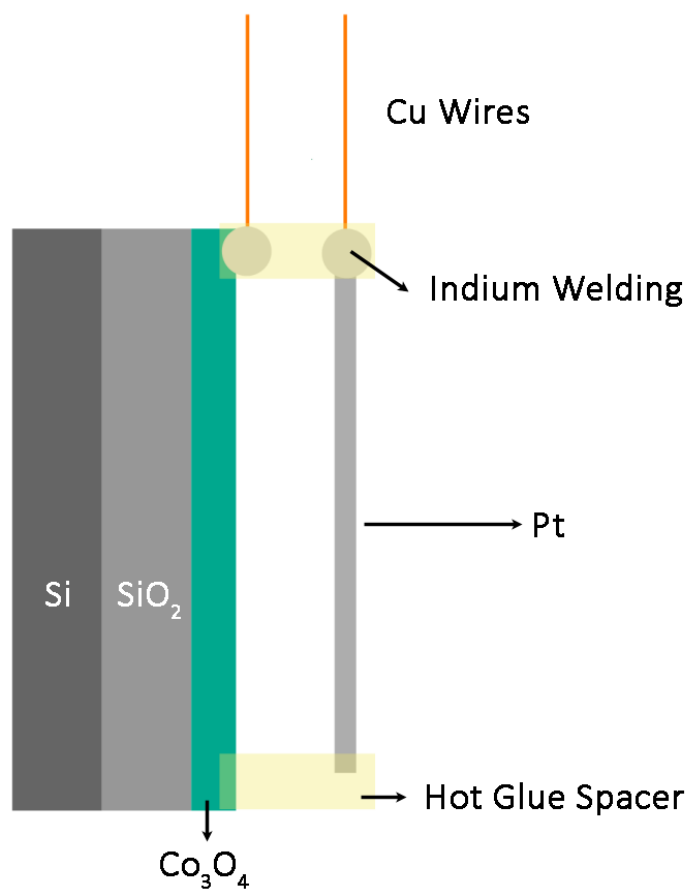
Figure S1: Scheme of the wires connection to the Co_3O_4 film. Cu wires were attached to the sample using indium. The welding is performed at the Co_3O_4 surface. Insulating hot glue spacers were used to avoid short-circuits during VSM measurements.

B)   Further magnetoelectric measurements

a

b

Figure S2 | Magnetic characterization of the system when relaxing at 0 V after having applied –200 V during 30 min. a, VSM hysteresis loops recorded (1) just after removing the voltage and (2) after 325 min. **b**, Time dependence of the magnetization at 3000 Oe, where the corresponding stages in **a** are highlighted by circles.

C) Further structural/compositional characterization

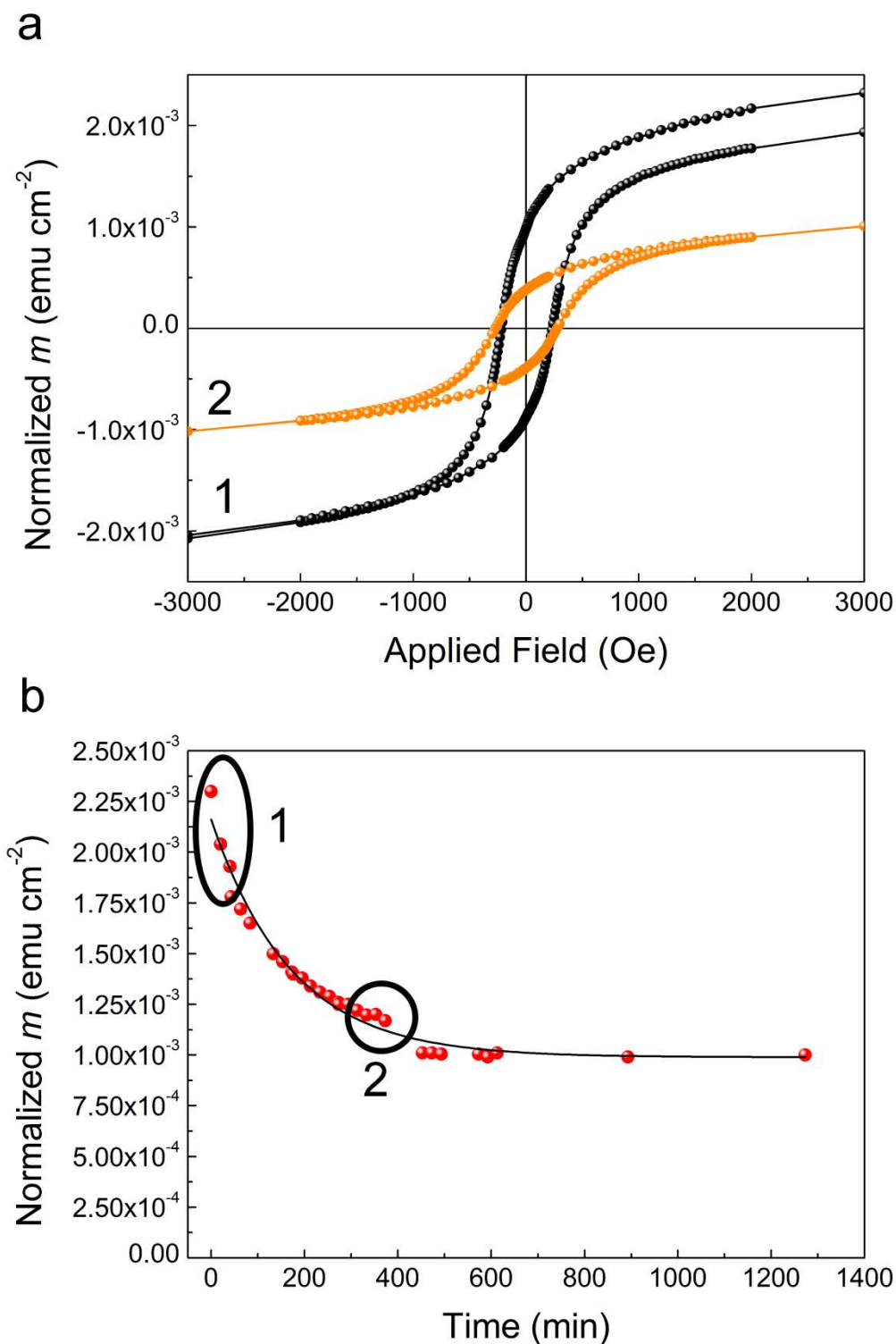Scanning electron microscopy imaging using secondary electrons reveals that the surface of the pristine film consists of polyhedral-shaped grains with well-defined grain boundaries (Figure S3a). After subjecting the sample to –200 V for 30 min, the grain boundaries appear to grow in detriment of the grain size. The average grain area for the as-prepared sample is 557 ± 17 nm^2, whereas that corresponding to the treated sample (–200 V for 30 min) is 527 ± 16 nm^2 (Figure S3b,d). Conversely, after recovery, the grain size increases at the expense of grain boundaries, reaching an average grain area of 613 ± 15 nm^2 (Figure S3f). This suggests that the underlying mechanism for atomic migration is, at least partially, grain boundary-mediated since atomic diffusion is usually enhanced at the grain boundaries[1].

As shown in Figure S4, the $\theta/2\theta$ XRD pattern of the as-prepared sample is consistent with a Co_3O_4 phase (space group Fd3m) textured along the (111) crystallographic direction. After negatively biasing the sample at –200 V for 30 min, the (111) and (222) Co_3O_4 peaks slightly broaden and, in particular, the (111) peak becomes clearly asymmetric at the high 2θ angle side, indicating that a secondary highly nanostructured Co_3O_4 phase with decreased lattice parameter might have been formed during the voltage treatment. Upon recovery, the asymmetry tends to vanish and the XRD peaks become narrower again, resembling those of the pristine sample. In order to provide further structural information, the $\theta/2\theta$ XRD patterns were analysed by Rietveld refinement using the MAUD software[2] to extract structural information on the lattice parameter and the crystallite size (i.e., average coherently diffracting domain) of the Co_3O_4 phase for the pristine sample, upon treatment and after recovery (Table S1). In order to take into account the aforementioned asymmetry, two Co_3O_4 phases with dissimilar lattice parameters were considered in the fitting procedure for the treated sample (see inset in Figure S4). While a single Co_3O_4 phase was essentially sufficient to appropriately refine the patterns corresponding to the pristine and recovered samples, a 25 vol.% of a highly nanostructured Co_3O_4 phase with decreased lattice parameter (7.964 Å; compared to 8.090 Å in the as-made sample) was required to properly fit the pattern of the treated sample. This phase is consistent with an oxygen-rich Co_3O_4 phase[3]. As can be seen in Table S1, a negative voltage of –200 V causes a slight decrease of crystallite size, from 28 nm (as-prepared sample) to 26 nm. Interestingly, the crystallite size recovers and even grows a bit with respect to the pristine sample after recovery, attaining a value of 29 nm. Interestingly, this effect correlates well with the SEM observations (Figure S3), where very similar average grain diameters are obtained from the average areas of the particles

assuming they have roughly spherical shapes. This evidences the high reversibility of the process and suggests that oxygen migration to reduce and re-oxidize Co is, at least partially, grain boundary-mediated.
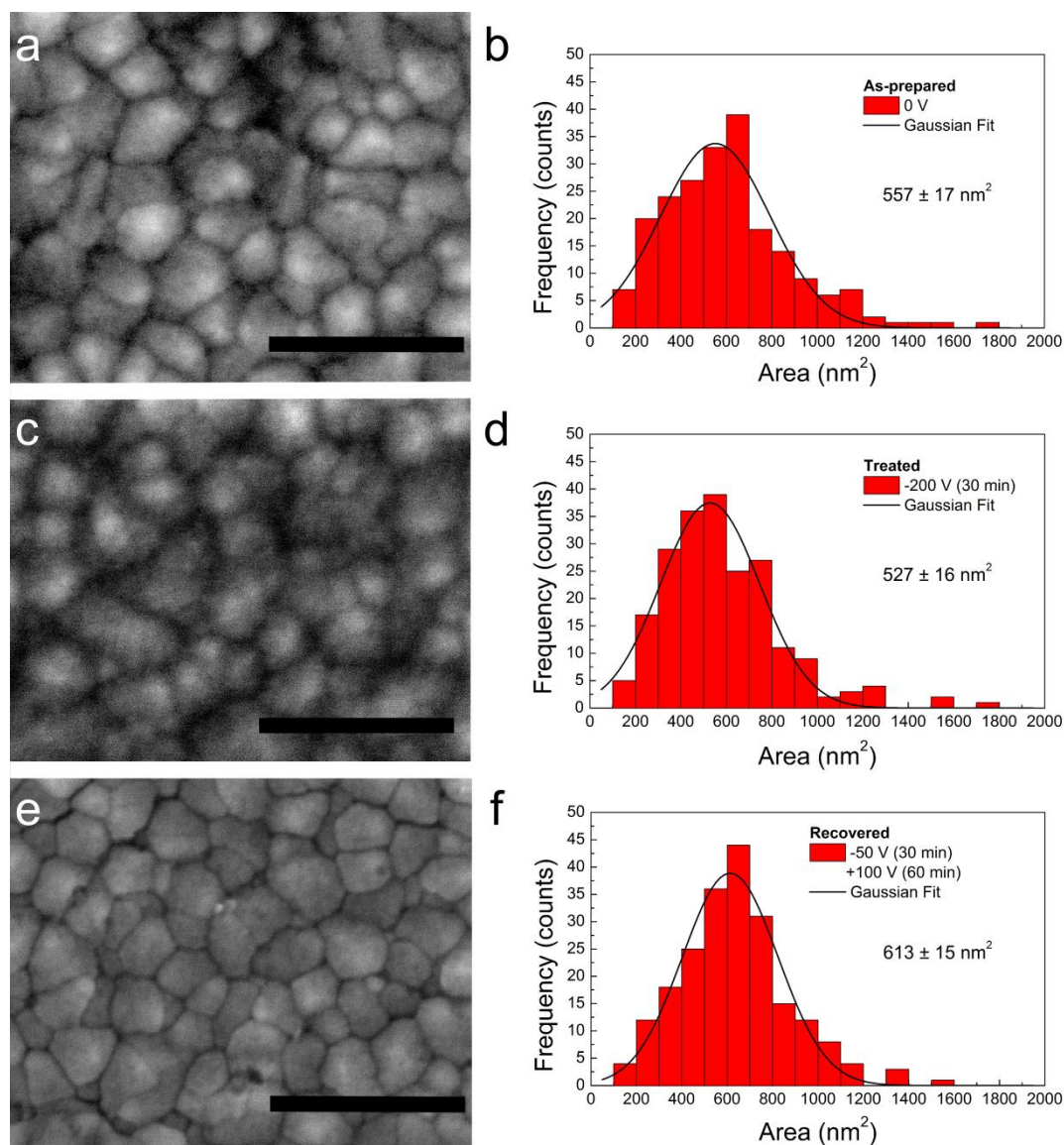
Figure S3 | Morphological characterization of the sample surface by SEM using secondary electrons. a, **c**, **e** SEM images and **b**, **d**, **f** particle size distributions of the as-prepared sample, a sample treated at –200 V for 30 min and a sample first treated at –50 V for 30 min and then recovered by applying +100 V for 60 min, respectively. The scale bar in a, c, and e is 100 nm. Note that the indicated error refers to the standard deviation error ($s_e = s_{sd}/N^{1/2}$, where s_{sd} is the standard deviation and N is the number of observations).
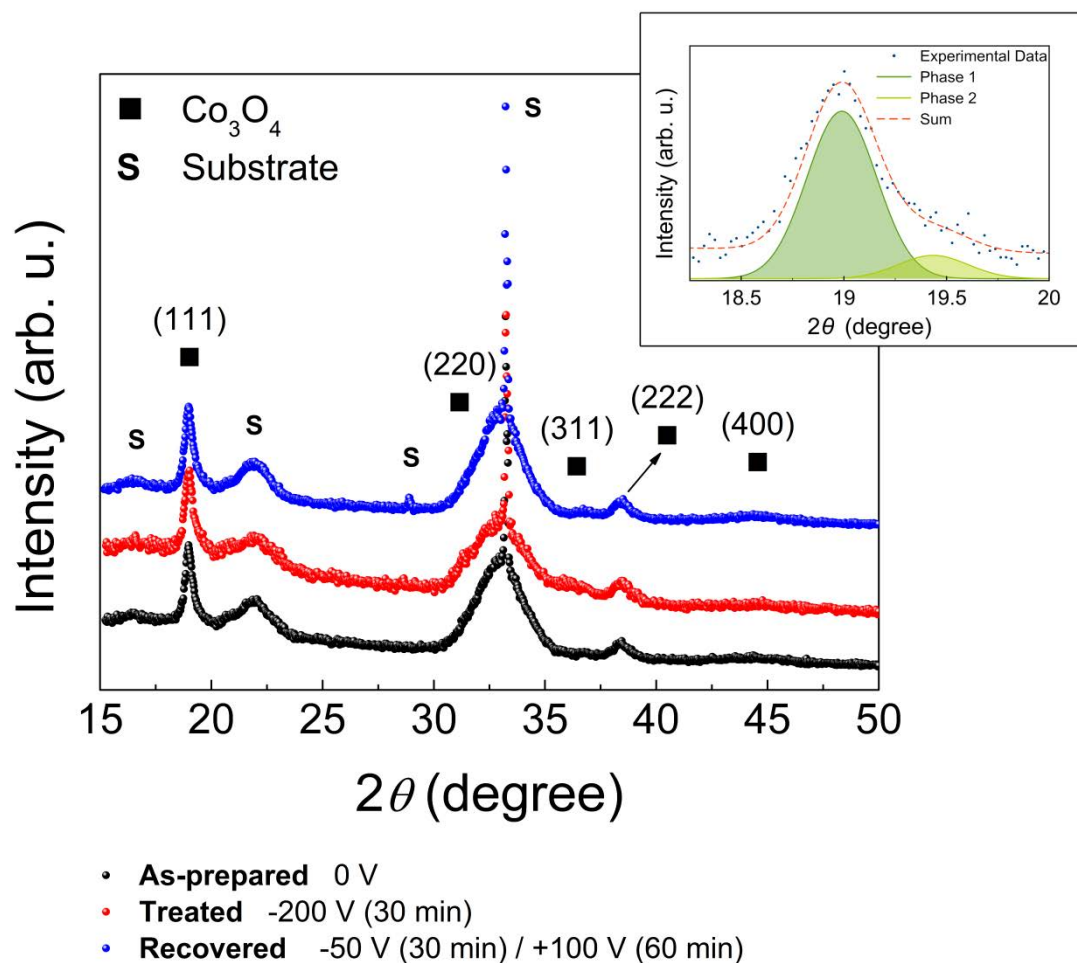
Figure S4 | Structural characterization by θ/2θ XRD. θ/2θ XRD patterns of the as-prepared sample (black), a sample treated at –200 V for 30 min (red) and a sample first treated at –50 V for 30 min and recovered afterwards by applying +100 V for 60 min (blue). The peaks corresponding to Co_3O_4 have been labelled and indexed and those arising from the substrate (Si (200) / amorphous SiO_2) have been indicated. The upper inset shows the Rietveld refinement of the XRD pattern of the sample treated at –200 V for 30 min, in the 18.2º-20º 2q range, assuming two contributions (two Co_3O_4 phases with different cell parameter).
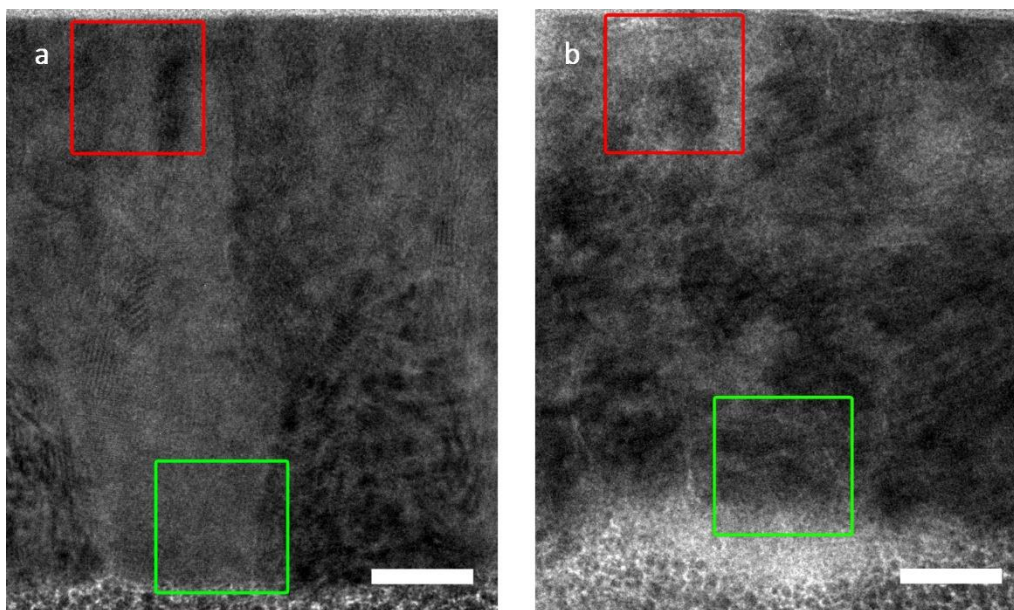
Figure S5 | Structural characterization by TEM. TEM images of the cross-section of **a** the pristine sample and **b** the sample subjected to –200 V for 30 min. The scale bars correspond to 20 nm. The red squares indicate the regions imaged by high-resolution TEM shown in Figure 3 of the manuscript, while the green squares correspond to Figure S6. Note that the Si/SiO_2 substrate would be above the imaged areas.
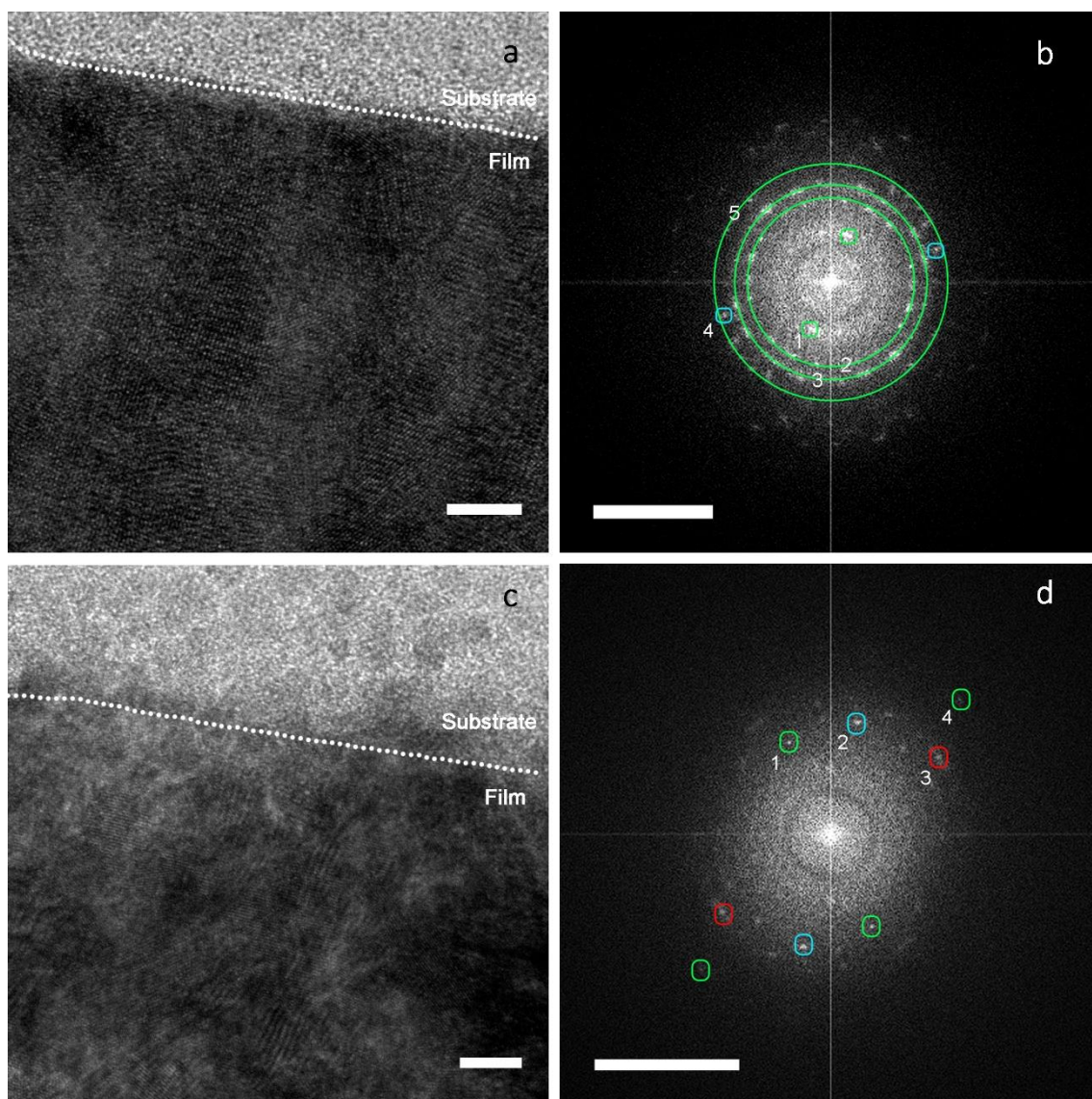
Figure S6 | Structural HRTEM characterization of the as-deposited film and a film treated at −200 V for 30 min, always from a region close to the SiO$_2$ interface. a, **b**, HRTEM image together with the corresponding fast Fourier transform of an untreated sample. **c**, **d**, HRTEM image together with the corresponding fast Fourier transform of a sample treated at −200 V for 30 min. The scale bars in a and c correspond to 5 nm whole those in b and d correspond to 5 nm^{-1}. The main diffraction spots have been labelled and indexed (Table S4 and S5). In green, blue and red are the rings/spots corresponding to Co$_3$O$_4$, CoO and HCP-Co, respectively.
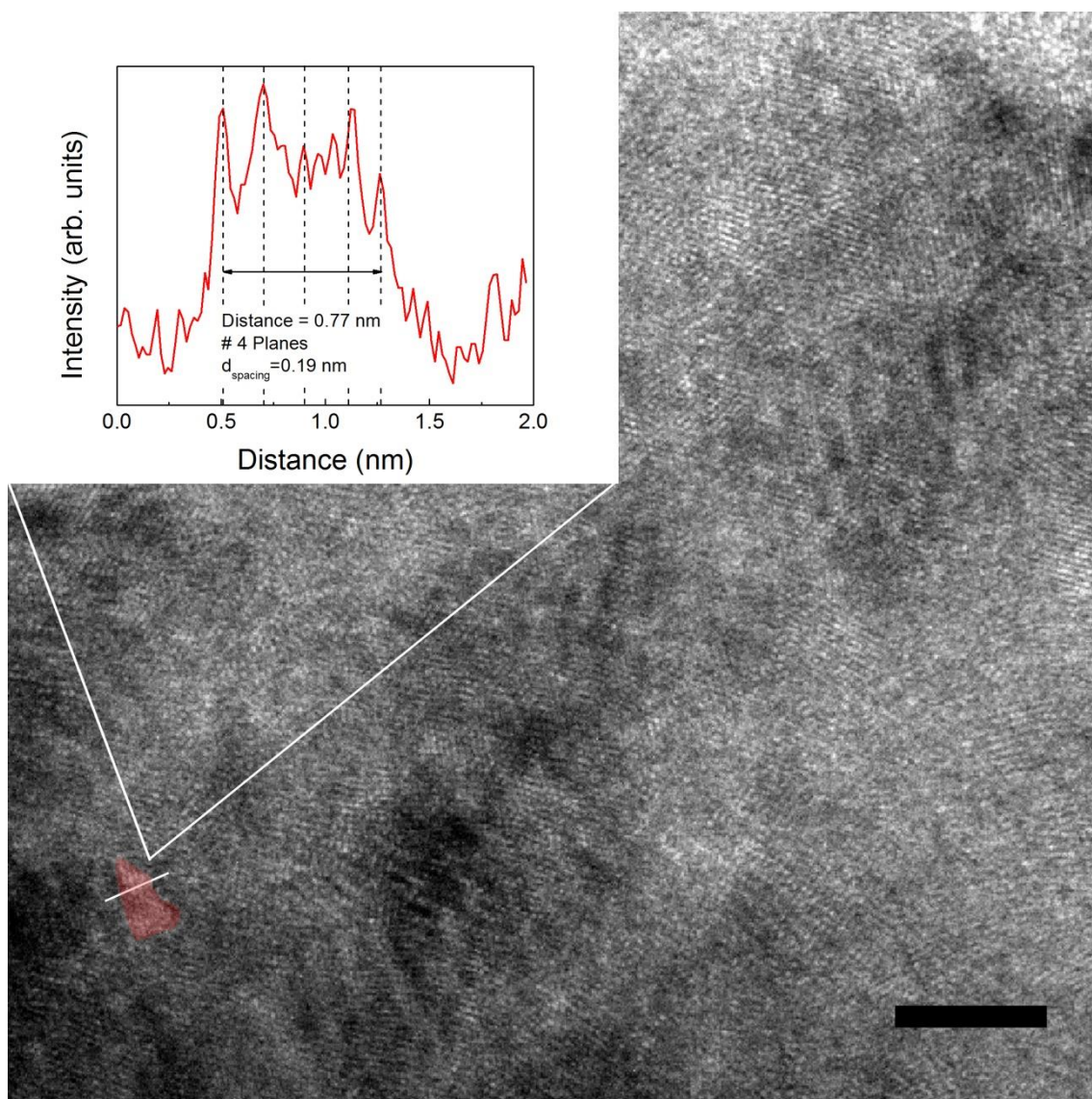
Figure S7 | Structural characterization by HRTEM of the sample treated with negative voltage. HRTEM image of an area located at the middle region of a film treated at −200 V for 30 min where a hexagonal close-packed cobalt (HCP-Co) nanocrystallite is highlighted. In the inset, an average interplanar distance of 0.19 nm, which corresponds to (101) HCP-Co, is obtained for the planes of this Co crystallite. The scale bar corresponds to 5 nm.
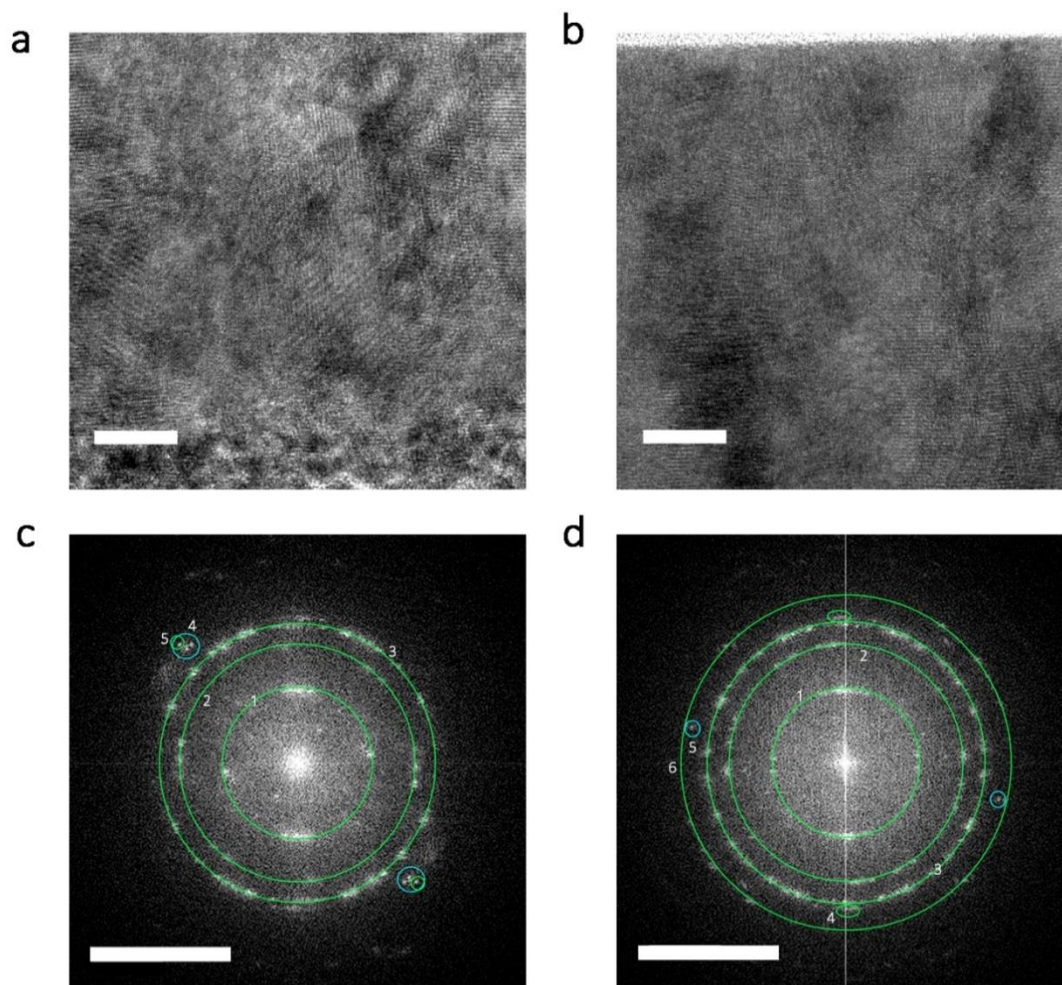
Figure S8 | Structural characterization HRTEM of the sample first treated at −50 V for 30 min and then recovered applying +100 V for 60 min. a, c, HRTEM image and the corresponding fast Fourier transform of the recovered sample from a region close to the surface, respectively. **b**, **d**, HRTEM image and the corresponding fast Fourier transform of the recovered sample close to the SiO_2 interface, respectively. The scale bars in a and b correspond to 10 nm and those in c and d to 5 nm^{-1}. The main diffraction spots have been labelled and indexed (Tables S6 and S7).
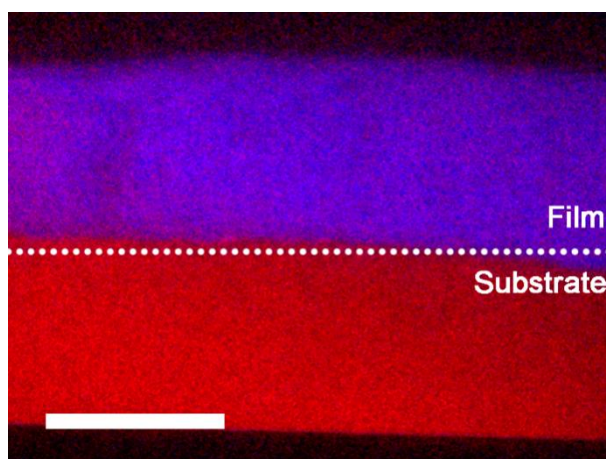
Figure S9 | Compositional characterization by EFTEM. EFTEM image corresponding to the recovered sample (negatively biased sample at –50 V for 30 min and subsequently positively biased at +100 V for 60 min). The scale bar corresponds to 100 nm.

To rule out spurious effects arising from Na$^+$ from the electrolyte or Si from the substrate, EDX spectroscopy and EELS spectra were acquired on the sample treated at –200 V for 30 min. Figure S10 and S11 indicate that neither Na nor Si are present in the O-rich regions (the ones corresponding to Figure 5d–f), ruling out Na$^+$ or Si^{4+} ion intercalation as the origin of this electrically-modulated ON-OFF ferromagnetism. Actually, the EDX analysis (Figure S12) reveals that the Na content in the treated sample is less than 1% (close to the detection limit). Such a small percentage could simply arise from surface contamination and can be also understood bearing in mind that the concentration of Na$^+$ in the propylene carbonate solution is only a few ppm, as assessed by inductively coupled plasma mass spectrometry (ICPMS).
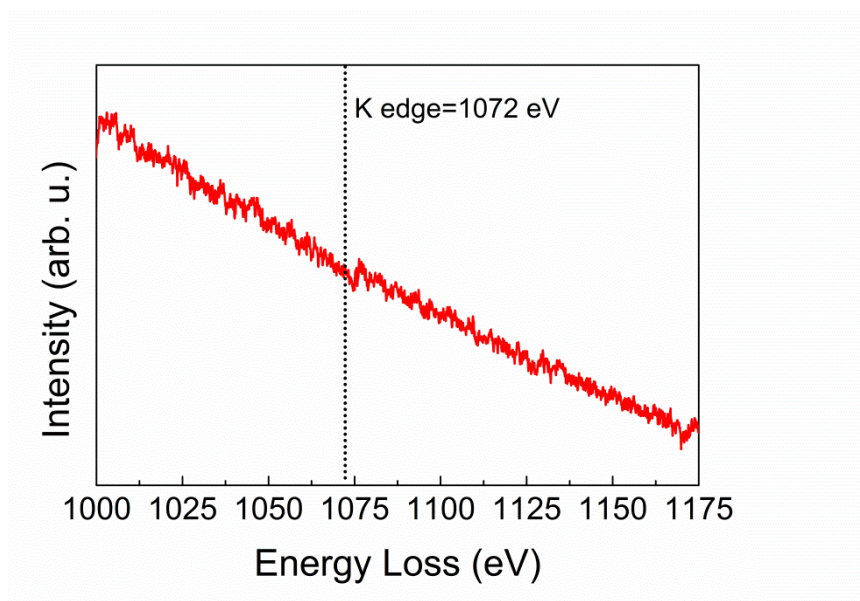
Figure S10 | Compositional analysis of an O-rich diffusion path by EELS. EELS spectrum at the Na K edge of an O-rich diffusion path of the cross-section of a sample negatively biased at −200 V for 30 min.
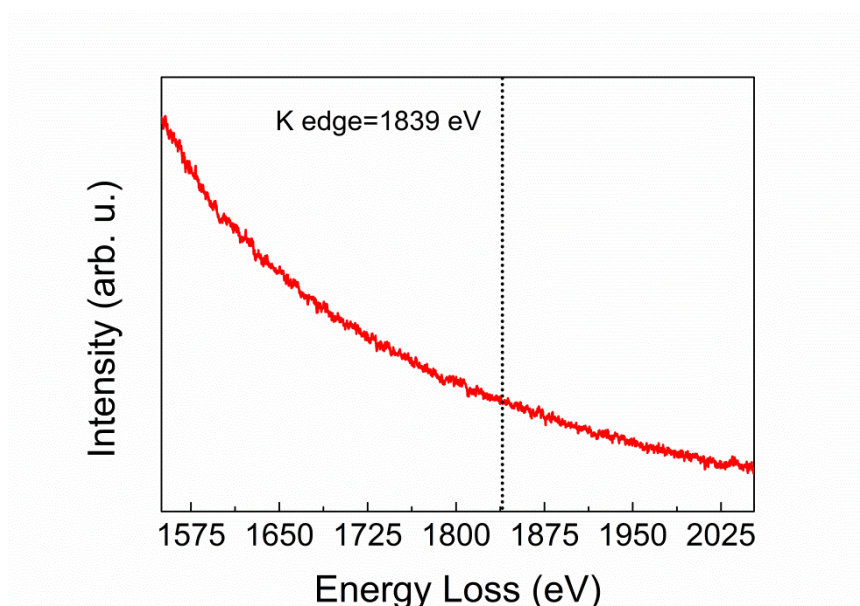
Figure S11 | Compositional analysis of an O-rich diffusion path by EELS. EELS spectrum at the Si K edge of an O-rich diffusion path of the cross-section of a sample negatively biased at −200 V for 30 min.
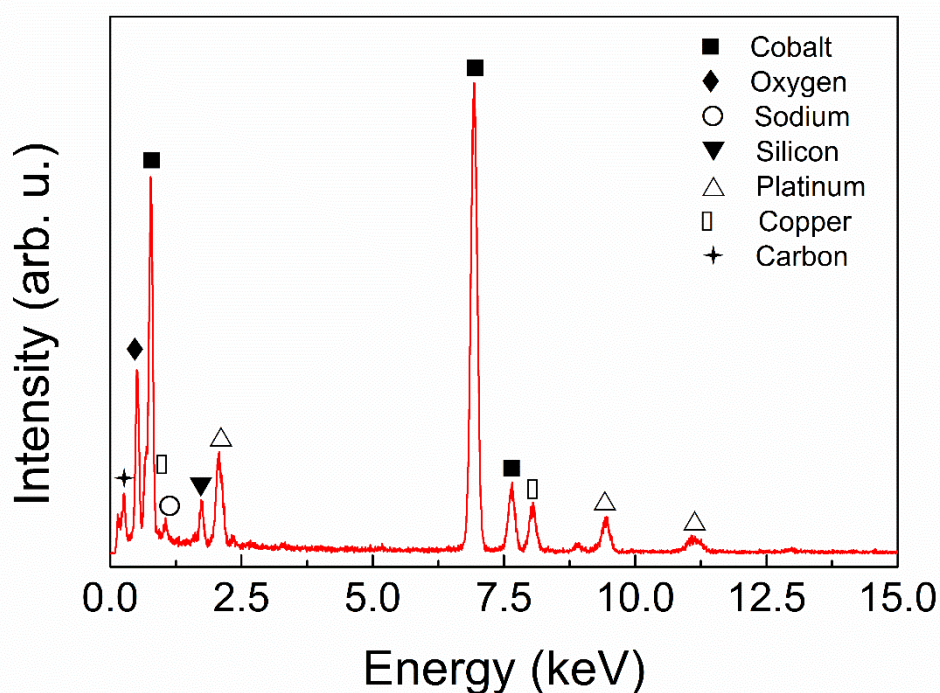
Figure S12 | Compositional analysis of an O-rich diffusion path by EDX. EDX spectrum obtained from the cross-section of a sample negatively biased at −200 V for 30 min. Note that Cu is detected from the TEM grid, whereas Pt was used as a coating thin layer during the lamellae FIB preparation.

Figure S13: Compositional characterization by HAADF STEM and EELS after recovery. a, b, c HAADF, Co and O EELS mappings of the recovered sample (negatively biased sample at −50 V for 30 min and positively biased at +100 V for 60 min).

129

Table S1 | Structural parameters from the Rietveld refinement of the θ/2θ XRD patterns. Lattice cell parameter (a) and crystallite size (<D>) of the as-prepared sample, the sample treated at –200 V for 30 min and the one recovered at –50 V for 30 min and at +100 V for 60 min samples obtained by Rietveld refinement of the XRD patterns in the 18-20° 2θ range. These values correspond to the main (111) Co_3O_4 phase.

	As-prepared	Treated	Recovered
a (Å)	8.09 ± 0.08	8.10 ± 0.06	8.092 ± 0.002
<D> (nm)	28 ± 1	26 ± 2	29 ± 1

Table S2 | Structural characterization by HRTEM of the as-deposited film, from a region of the cross section close to the air-exposed film's surface. Interplanar distances from the fast Fourier transform (Figure 3b) of the HRTEM image of the pristine sample presented in Figure 3a together with the corresponding indexation.

# Ring/Spot	*d* (Å)	Plane	Phase
1	4.690	(111)	Co_3O_4
2	2.861	(220)	Co_3O_4
3	2.465	(311)	Co_3O_4
4	2.367	(222)	Co_3O_4
5	2.165	(111)	CoO
6	2.048	(400)	Co_3O_4
7	1.545	(220)	CoO
8	1.460	(440)	Co_3O_4

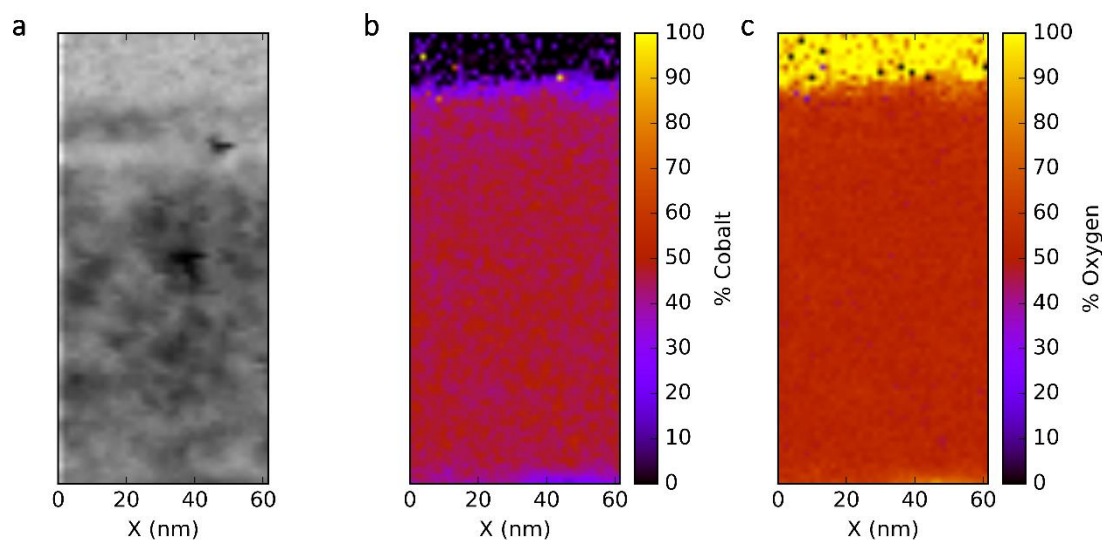**Table S3 | Structural characterization by HRTEM of the sample treated at negative voltage, from an upper region from the cross-section, close to the air-exposed surface.** Interplanar distances from the fast Fourier transform (Figure 3d) of the HRTEM image of the sample treated at –200 V for 30 min presented in Figure 3c together with the corresponding indexation.

# Ring/Spot	*d* (Å)	Plane	Phase
1	2.828	(220)	Co_3O_4
2	2.506	(111)	CoO
3	2.149	(200)	CoO
4	1.911	(101)	HCP-Co

Table S4 | Structural characterization by HRTEM of the as-deposited film close to the SiO_2 interface. Interplanar distances from the fast Fourier transform of the high-resolution transmission electron microscopy image of the pristine sample presented in Figure S6a together with the corresponding indexation.

# Ring/Spot	d (Å)	Plane	Phase
1	4.739	(111)	Co_3O_4
2	2.888	(220)	Co_3O_4
3	2.472	(311)	Co_3O_4
4	2.149	(111)	CoO
5	2.078	(400)	Co_3O_4

Table S5 | Structural characterization by HRTEM of a sample treated with a negative voltage, from a region close to the SiO_2 interface. Interplanar distances from the fast Fourier transform of the high-resolution transmission electron microscopy image of the sample treated at –200 V for 30 min presented in Figure S6c together with the corresponding indexation.

# Ring/Spot	d (Å)	Plane	Phase
1	2.849	(220)	Co_3O_4
2	2.485	(111)	CoO
3	1.912	(101)	HCP-Co
4	1.540	(511)	Co_3O_4

Table S6 | Structural characterization by HRTEM of the recovered sample (upper region, close to the air-exposed surface). Interplanar distances from the fast Fourier transform of the high-resolution transmission electron microscopy image of the recovered sample close to the surface presented in Figure S8a together with the corresponding indexation.

# Ring/Spot	d (Å)	Plane	Phase
1	4.657	(111)	Co_3O_4
2	2.886	(220)	Co_3O_4
3	2.493	(311)	Co_3O_4
4	2.153	(200)	CoO
5	2.057	(400)	Co_3O_4

Table S7 | Structural characterization by HRTEM of the recovered sample (region close to the SiO$_2$ interface). Interplanar distances from the fast Fourier transform of the high-resolution transmission electron microscopy image of the recovered sample close to the SiO$_2$ interface presented in Figure S8b together with the corresponding indexation.

# Ring/Spot	d (Å)	Plane	Phase
1	4.657	(111)	Co$_3$O$_4$
2	2.886	(220)	Co$_3$O$_4$
3	2.493	(311)	Co$_3$O$_4$
4	2.361	(222)	Co$_3$O$_4$
5	2.153	(200)	CoO
6	2.057	(400)	Co$_3$O$_4$

D)   Further analysis by PALS/VE-PAS techniques

During **Variable Energy Positron Annihilation Spectroscopy** experiments (carried out to attain a deeper understanding on the effects of voltage on the structure of the Co_3O_4 films and the mechanism for ion migration), positrons are emitted from an intense [22]Na source and subsequently accelerated to discrete energy values in the range of 0.05 – 35 keV. Such positron implantation energy allows penetrating down to about 2 μm for Co. Doppler broadened spectra representing positron annihilation distribution for each positron implantation energy were acquired using single High-Purity germanium detector (HPGe) with energy resolution of 1.09 ± 0.01 keV at 511 keV. Slow positron annihilation spectroscopy is in general realized by implantation of kinetically accelerated positrons to a sample and detection of the 511 keV gamma photons originating from the electron-positron annihilation. A change in the electron momentum distribution is represented by a Doppler shift of the annihilation gamma spectrum. The low momentum part of the spectrum is characterized by the so-called *S*-parameter (shape parameter)[4], which is defined as a number of annihilation events in the very middle of the spectrum, in the energy window of about 511 ± 0.930 keV normalized to the total number of events. A mono-energetic positron beam with variable energy allows depth profiling across the film thickness, where a positron mean implantation depth is proportional to positron acceleration energy, E_p. In order for such analysis to be feasible, a large enough statistics needs to be acquired. Here, for each value of E_p, a spectrum consisting of minimum 1.5×10^5 total counts was measured.

Typically, in a VE-PAS experiment, the parameter *S* (Figure S14) (defined as positron annihilation with low momentum valence electrons), is proportional to the vacancy density and their size. This parameter can be determined as a function of the positron incident energy, rendering a depth-resolved characterization of structural defects.[4,5,6] As can be seen Figure S14, for all samples, the *S* parameter first decreases with the incident energy and then increases again until levelling off, reaching first the SiO_2 buffer layer and later the Si substrate. The *S* parameter value at the sub-surface region (lower positron energies, E_p < 1 keV), usually reflects positronium formation and positron surface states with surface electrons[5]. At higher energies (larger depths) *S* is proportional to the concentration and size of existing vacancies. Remarkably, when a negative voltage is applied, *S* increases for all depths, suggesting that the density or size of vacancies in Co_3O_4 increases with voltage. In addition, the position of the *S* minimum is shifted slightly towards higher energies for the negatively biased samples. This would correlate well with

(i) the increase of the material density (possibly because of the Co-rich phase segregation), which reduces the penetration depth of positrons for the energy range corresponding to a sub-surface region [see Figure S14] or with (ii) large concentration of inhomogenously distributed defect complexes strongly trapping positrons.
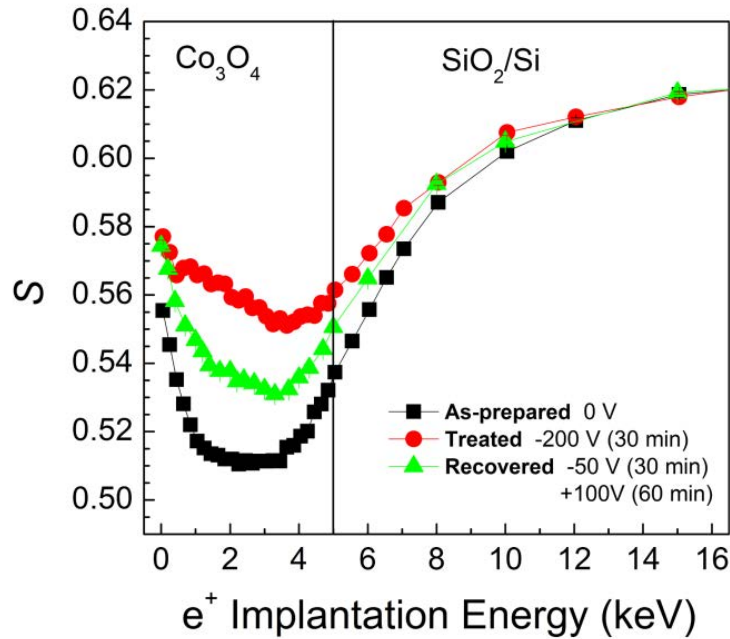

Figure S14 | Low electron momentum fraction, S, as a function of positron implantation energy, E_p, for the as-deposited sample, after treating it at -200 V, and after recovering applying -50 V and +100 V.

Since VE-PAS results cannot clearly distinguish between defects size and defect concentration, additional positron annihilation lifetime spectroscopy (PALS) (Figure 6a–c) and Coincidence Doppler broadening (cDB)-PAS (see Figure 6d) investigations were performed, both supported with theoretical calculations by means of the so-called atomic superposition (ATSUP) method[7,8] (Figure 6e). The cDB of the annihilation line at fixed energy (E_p = 3 keV) using two HPGe detectors with energy resolution of 780 ± 20 eV at 511 keV was conducted on the Co_3O_4 films. The method allows detailed insight into atomic surrounding of a defect site by comparing the electron momentum distribution of the test sample with a defect-free reference material, i.e., Co. The positron lifetime experiments were performed at the mono-energetic positron spectroscopy (MePS) beamline, which is the end station of the radiation source ELBE (Electron Linac for beams with high Brilliance and low Emittance) at HZDR (Germany)[9] using a digital lifetime $CrBr_3$ scintillator detector

with a homemade software employing a SPDevices ADQ14DC-2X with 14 bit vertical resolution and 2 GS/s horizontal resolution, optimized for room-temperature measurements and with a time resolution function down to about 0.205 ns. The resolution function required for spectrum analysis uses two Gaussian functions with distinct intensities depending on the positron implantation energy, E_p, and appropriate relative shifts. All spectra contained at least 5×10^6 counts.

The **positron lifetime** spectra were analysed as a sum of time-dependent exponential decays $N(t) = \Sigma_i\ I_i/\tau_i \cdot exp(-t/\tau_i)$ convoluted with the Gaussian's functions describing the spectrometer timing resolution using the non-linearly least-squared based package PALSfit fitting software[4,6,10]. The yttria-stabilized zirconia (YSZ) reference sample with well-defined single component positron lifetime, $\tau \approx 0.181$ ns, was utilized as a correction spectrum to account for unwanted background by means of subtracting additional (not related to the sample) positron lifetime components during the fitting procedure: $\approx 0.40 -$ 0.90 ns (< 4 %) and < 55 ns (< 0.5 %) depending on E_p. The spectra after background correction were deconvoluted into three discrete lifetime components, which directly evidence three different defect types (sizes) [see Figure 6a–b and S15a]. The resulting intensities reflect a concentration of each defect type (size) [Figure 6c and S15b]. Since the intensity of the τ_3 component within the films is below 1%, the concentration of large voids in the Co_3O_4 film is extremely low and can be neglected, even after the voltage treatments. In the case of SiO_2, due to its amorphous nature, such voids exist intrinsically and $\tau_3 \approx 1.5$ ns is a typical value for SiO_2 (Figure S15a). Hence, the increase of intensity at $E_p \approx 5$ keV (Figure S15b) indicates the film/buffer interface while the subsequent drop reflects increased annihilation within the Si substrate. Detailed discussion on the τ_1 and τ_2 components is given in the main manuscript.

The **coincidence Doppler broadening measurements** of the annihilation peak at given E_p are a perfect probe for investigations of the defect site atomic surrounding. Chemical elements have unique shapes of the cDB spectra. Typically, thermalized positrons have negligible momentum compared to electrons, thus the momentum of annihilating electron-positron pair represents mostly the electron momentum. Hence, the measured Doppler shift in the energy of the annihilation-photons yields the momentum distribution of electrons that have annihilated positrons[6]. Here energy of both annihilation photons is measured in coincidence, which suppresses the background signal in comparison to standard one detector approaches, i.e., VE-PAS. The difference in energies of the two annihilation photons is $E_1 - E_2 = 2 \cdot \Delta E = c \cdot p_L$, where c is the speed of light and p_L is the

longitudinal component of the electron momentum to the direction of emitted annihilation photon.
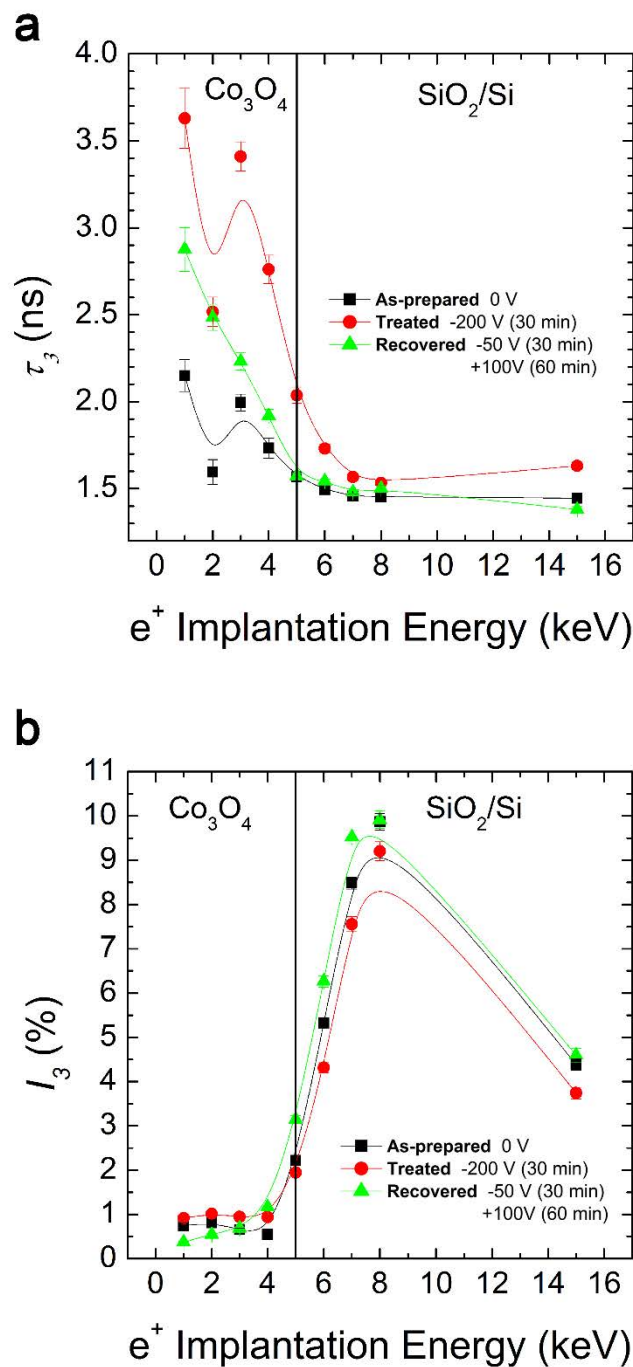
Figure S15 | Longest positron lifetime component, τ_3, and its intensity, I_3, as a function of positron implantation energy, E_p. Positron lifetime components longer than 600-700ps correspond to large open volume defects, e.g., voids and pores. Since the intensity of that component within the films is below 1 % their concentration is extremely low. In the case of SiO_2 due to its amorphous nature such voids exist intrinsically and $\tau_3 \approx 1.5$ ns is a typical value for SiO_2. The increase of intensity at $E_p \approx 5$ keV shows an onset on film/buffer interface and subsequent drop reflects increased annihilation with the Si substrate.

136

To clarify the evolution of the defect structure as a function of voltage treatment, **atomic superposition (ATSUP) modelling** was conducted (see Figure 6e) and compared with cDB experimental ratio plots (Figure 6d) and positron lifetime analysis (Figs. 6a–c). The so-called standard scheme[7,8] has been used, which does not account, however, for atomic relaxations in the vicinity of a defect (which is sometimes necessary to obtain more ideal agreement between theory and experiment). In general, the most standard scheme of ATSUP cannot precisely describe positron annihilation with low momentum valence electrons, $p_L < 8 \times 10^{-3} \ m_0c$. However, it can fully predict trends once vacancy states are introduced for the high electron momentum region, $p_L > 8 \times 10^{-3} \ m_0c$. The obtained calculated ratio plots for a spinel Co_3O_4 structure (Figure 6e) exhibit similar minimum at the high momentum part of the spectrum as the experimental data (Figure 6d), which is however slightly shifted by $p_L \approx 20 \times 10^{-3} \ m_0c$ and the calculated ratio values vary less as a function of the vacancy complex size when compared to the experiment. This is most likely due to limitations of the simulation code, since atomic relaxations around defects and annihilation at grain boundaries were not accounted for. From the modelling, the following parameters have been calculated and summarized in Table S8: (i) vacancy size (vacancies within a complex), (ii) vacancy type, and (iii) positron lifetimes. The HCP-Co and spinel Co_3O_4 structures have been simulated – defect free materials as well as with vacancy states, e.g., monovacancy, dimers, trimers, up to complexes of 6 vacancies both on Co and O sites.

The shortest lifetime component (τ_1) cannot be explained either by a vacancy complex situated at only Co or O sites (i.e., non-mixed vacancies) because the calculated positron lifetime values in these cases are below 0.2 ns. A vacancy complex related to HCP-Co, on the other hand, is excluded due to its completely different electronic structure (see Figure 6d), where no clear minimum was found (as for Co_3O_4) but rather a straight horizontal line. Therefore, the calculations predict existence of small vacancy clusters, probably in the form of cobalt vacancy dimers (two vacancies), V_{2xCo}, or trimers (three vacancies), V_{3xCo}, coupled with an oxygen monovacancy (single vacancy), V_O (where a lifetime higher than 0.2 ns is obtained). These configurations, compatible with our experiment, are indicated in bold in Table S8. Thus, the defects structure in the as-deposited films can be described as dominated (75–93% of the overall open volume; see Figure 6c) by small vacancy clusters (3-4 vacancies, V3-V4). The presence of defects in the as-deposited Co_3O_4 films is likely to be important for the voltage-induced structural changes (and the concomitant magnetoelectric effects) as it promotes an otherwise limited atomic mobility.
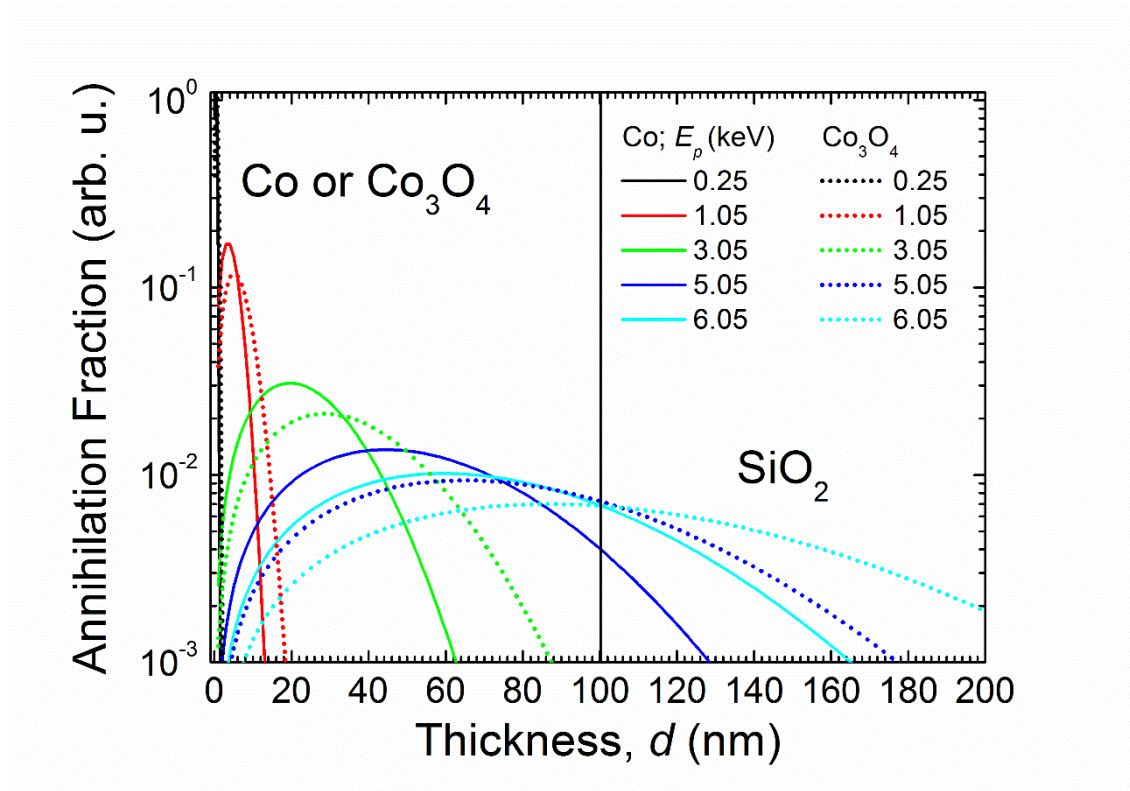
Figure S16 | The so-called Makhov distribution of positron annihilation with a maximum of 1. Since positrons are very light particles they scatter more in case of larger implantation energies, $E_p > 5$ keV. The maxima represent largest probability for positron annihilation and in systems with high enough defect concentration (reduced or suppressed positron diffusion) are a good measure for positioning of layers and interfaces. Comparison between Co ($\rho_{Co} = 8.9$ g·cm^{-3}) and Co$_3$O$_4$ ($\rho_{CoO} = 6.11$ g·cm^{-3}) is given. For $E_p = 6.05$ keV, due to larger density of Co compared to Co$_3$O$_4$, positrons would predominantly annihilate about 40 nm apart from the interface to SiO$_2$. This simple modelling gives only a rough estimation of positron annihilation distribution across the film thickness and cannot be directly applied for phase separated systems.

In the case of the treated sample, τ_1 strongly increases, especially close to the surface area, which can be understood as a vacancy complex involving more than 6 connected defects (V6), likely $V_{3xCo} + V_{3xO}$ (Table S8), and is the consequence of ionic migration. After application of the positive bias, O transfer in the interior of the grains is reversed and defect clusters decrease in size [vacancy complexes composing of 4-5 defects are emerging (V4, V5)]. This suggests that the size of vacancies in the recovered sample decreases, approaching the values of the as-deposited sample.

Table S8 | ATSUP analysis. Calculated positron lifetime for different vacancy configuration in HCP-Co and a Co_3O_4 spinel structure. The positron lifetime for mixed vacancy cluster states fit well to the experimental values from Figure 6d. The types of defects configurations compatible with the experiments are highlighted in bold.

Material	No. of vacancies within a complex	Vacancy type	Positron lifetime (ns)
HCP-Co	0	--	0.0971
	1	V_{Co} (monovacancy)	0.1685
	2	V_{2xCo} (dimer)	0.1873
	3	V_{3xCo} (trimer)	0.2123
	4	V_{4xCo}	0.2240
Co_3O_4 - Co vacancy clusters	0	--	0.1188
	1	V_{Co} (monovacancy)	0.1646
	2	V_{2xCo} (dimer)	0.1757
	3	V_{3xCo} (trimer)	0.1785
	4	V_{4xCo}	0.1795
Co_3O_4 - O vacancy clusters	1	V_O (monovacancy)	0.1201
	2	V_{2xO} (dimer)	0.1255
	3	V_{3xO} (trimer)	0.1347
Co_3O_4 - mixed vacancy clusters	2	$V_{Co} + V_O$	0.1816
	3	$V_{Co} + V_{2xO}$	0.1952
	3	$V_{2xCo} + V_O$	**0.2030**
	4	$V_{3xCo} + V_O$	**0.2251**
	5	$V_{3xCo} + V_{2xO}$	**0.2394**
	6	$V_{3xCo} + V_{3xO}$	**0.2526**

References

1. Garcia-Barriocanal, J. et al. Colossal ionic conductivity at interfaces of epitaxial ZrO_2:Y_2O_3|$SrTiO_3$ Heterostructures. *Science* **321**, 676–680 (2008).

2. Lutterotti, L. & Scardi, P. Simultaneous structure and size–strain refinement by the Rietveld method. *J. Appl. Crys.* **23**, 246–252 (1990).

3. George, G. & Anandhan, S. Structural characterization of nano-crystalline Co_3O_4 ultra-fine fibers obtained by sol–gel electrospinning. *J. Sol-Gel Sci. Technol.* **67**, 256–266 (2013).

4. Krause-Rehberg, R. & Leipner, H. Positron Annihilation in Semiconductors, Solid-State Sciences. (Springer, Berlin, 1999).

5. Khan, E. H., Weber, M. H., McCluskey, M. D. Formation of Isolated Zn Vacancies in ZnO Single Crystals by Absorption of Ultraviolet Radiation: A Combined Study Using Positron Annihilation, Photoluminescence, and Mass Spectroscopy, *Phys. Rev. Lett.* **111**, 017401 (2013).

6. Tuomisto, F., Makkonen, I. Defect identification in semiconductors with positron annihilation: Experiment and theory. *Rev. Mod. Phys.* **85**, 1583–1631 (2013).

7. Puska, M. J., Nieminen, R. M. Defect spectroscopy with positrons: a general calculational method. *J. Phys. F Met. Phys.* **13**, 333–346 (1983).

8. Seitsonen, A. P., Puska, M. J., Nieminen, R. M. Real-space electronic-structure calculations: Combination of the finite-difference and conjugate-gradient methods. *Phys. Rev. B.* **51**, 14057–14061 (1995).

9. Wagner, A., Anwand, W., Attallah, A. G., Dornberg, G., Elsayed, M., Enke, D., Hussein, A. E. M., Krause-Rehberg, R., Liedke, M. O., Potzger, K., Trinh, T. T. Positron annihilation lifetime spectroscopy at a superconducting electron accelerator. *J. Phys.: Conf. Ser.* **791**, 012004 (2017).

10. Olsen, J. V., Kirkegaard, P., Pedersen, N. J., Eldrup, M. PALSfit: A new program for the evaluation of positron lifetime spectra. *Phys. Status Solidi C* **4**, 4004–4006 (2007).

04

General Discussion

4. General discussion of the results

Magnetic actuation in devices is conventionally controlled by electric currents, used to either generate magnetic field through electromagnetic induction or to induce magnetization reversal via spin torque effect (i.e., injecting spin polarized currents). To minimize energy losses by heat dissipation due to Joule effect in current-based magnetic systems, electric field modulation of magnetism is undergoing intense research since it has been predicted that magnetoelectric actuation could boost energy-efficiency in widespread applications, such as magnetic recording, spintronics or, in general, any kind of magnetically-actuated device.

So far, different routes to tackle voltage control of magnetism have been considered: by means of the intrinsic magnetoelectric coupling in single phase multiferroics, by taking advantage of strain-mediated magnetoelectric coupling in extrinsic ferromagnetic/ferroelectric heterostructures, by modifying the electronic band configuration through the injection of electrostatic charges in ferromagnetic/dielectric interfaces (in ultrathin films) or by redox processes. Even though these magnetoelectric effects are of very dissimilar origin, all of them are of interfacial nature. That is why most of the experimental works address the electric control of magnetism by exploiting the large surface to volume ratio of ultrathin films.

With the aim to bring this aspect to a further step, we tackled magnetoelectric effects in nanoporous materials with maximized surface to volume ratios, tailored pore architecture and ultrathin pore walls. This constitutes a novel approach since although nanoporous materials have been widely used in recent years in several areas like heterogeneous catalysis, energy storage or gas sensing, their use in magnetism has been rather overlooked.

The nanoporous materials were prepared by micelle assisted electrodeposition, a deposition technique which had been largely employed in alloy systems containing noble metals, but much less used in non-noble transition metal (in particular, magnetic) alloys. This allowed us to **demonstrate that micelle assisted electrodeposition is a successful approach to synthesize nanoporous noble metal free alloys, such as Cu-Ni, with tailored pore architecture and ultrathin pore walls. This new synthetic approach and the properties of these materials have been patented at National and European levels (EP17170317.6; 1707453.5 (UK); 201700590 (ES)) and constitutes one of the novel aspects of this Thesis.**

To electrically-actuate the samples, we have employed an electrolyte gating approach, in which the formation of an EDL is exploited to generate ultra-high electric fields (of the order of tens-hundreds of MV/cm). Moreover, this is the most efficient way to apply voltage in such large surface areas since the electrolyte can penetrate the interior of the nanopores and make the inner surfaces of the pore walls magnetoelectrically active. Furthermore, current leakage in nanoscale dielectric layers, which is a common failure in solid state magnetoelectric measurements, is avoided by the use of liquid electrolytes. Despite proving that ALD is a suitable technique to conformally coat nanoporous configurations, our preliminary works show that current leakage occurs in porous materials tested in solid-state configuration, thus electrolyte-gating was chosen as the preferred method to perform our magnetoelectric studies, to ensure a suitable electric field actuation via the formation of the EDL.

With the aim to take advantage of different magnetoelectric effects, two main electrolytes have been employed: an aprotic organic solvent (propylene carbonate) and an oxidative aqueous media (NaOH).

Electrolyte-gating in <u>non-oxidative media</u> allowed us to demonstrate that nanoporosity boosts charge-mediated effects in Cu-Ni alloys, confirming that configurations with maximized surface to volume ratio exhibit enhanced magnetoelectric effects.

Specifically, we successfully achieved a 32% reduction in the coercive field of a nanoporous Cu-Ni film. *Ab initio* simulations are consistent with a charge-mediated magnetoelectric effect mechanism and suggest that voltage induces changes in the magnetic anisotropy energy of the Cu-Ni alloy due to the accumulation of electrostatic charges. This coercivity reduction is of paramount importance to enhance the energy efficiency during magnetic actuation, since it implies that lower applied magnetic fields (i.e., electric currents) are needed to reverse magnetization, thus resulting in lower Joule heating effects.

By applying electric fields in <u>oxidative media</u>, the magnetic moment, rather than the coercivity, has been modulated. Nanoporosity not only enhances redox effects but allows for their propagation through the entire sample thickness.

The element-selectiveness in the electrochemical oxidation (positive applied voltage) of a Cu-Ni alloy allowed us to tune the magnetic moment up to an increase of 33 %. Since the oxidative process mainly occurs in the Cu counterpart, the alloy ends up being enriched in Ni, thus yielding a larger magnetic moment. Opposite effects are observed by application

144

of negative voltages (i.e., the redox-mediated magnetoelectric effect is reversible and allows precise control of the magnetic properties of the investigated alloy). Additionally, this result rules out the possibility that redox processes could be the origin of the magnetoelectric effects observed in the electrolyte-gated Cu-Ni using a non-oxidative medium (since redox mainly promotes changes in saturation magnetization, rather than coercivity).

Hence, we have presented two different approaches to tune coercivity and magnetic moment by voltage. The first strategy relies on a charge-mediated magnetoelectric effect, whereas the second route is based on redox processes. This two first works were carried out in a home-made cell setup which allowed us to apply voltages through liquid media while performing *in-situ* MOKE measurements. MOKE is a local and surface sensitive technique and does provide a quantitative determination of the magnetic moment. Therefore, in order to account for magnetization changes while performing magnetoelectric measurements, a similar experimental configuration was implemented in our VSM setup.

Besides nanoporous alloys, we have also induced interesting magnetoelectric effects in relatively thick (not ultrathin) Co_3O_4 films. A magneto-ionic approach has been successfully employed to tune magnetism in a robust, reversible and non-volatile manner at room temperature in a single oxide layer. Previous works from the literature dealing with magneto-ionic effects have typically required of heat assistance, which increases the energy consumption, and have relied on oxygen reservoirs (e.g., Al_2O_3, HfO_2 or Gd_2O_3 layers), which act as donors or acceptors of oxygen (depending on the voltage polarity), hence modifying the magnetic properties of the neighboring ferromagnetic film. Despite these promising results, to the best of our knowledge, no previous works had tackled the room temperature modification of magnetic properties via magneto-ionics. Here, taking advantage of structural defects, magneto-ionics has been successfully demonstrated at room temperature in a dense polycrystalline 100 nm-thick paramagnetic Co_3O_4 film in which magnetoelectric measurements have been performed by electrolyte gating. Upon negative bias application (just above a certain threshold potential), a weak ferromagnetic signal appeared suggesting that at least Co_3O_4 partly reduces to metallic Co. The induced ferromagnetic signal increases with time and it is boosted by voltage. A detailed structural characterization reveals that this effect under negative biases is consistent with an internal redistribution of both anionic and cationic species, thus generating Co-enriched areas (responsible for the observed ferromagnetism) and O-enriched counterparts.

Remarkably, the obtained results were achieved in a single-phase system and no external oxygen sources such as Al_2O_3, GdO_x or HfO_x are needed. Moreover, all ionic motion has been achieved at room temperature which is necessary to bring this effect to practical applications. Magneto-ionics on Co_3O_4 is shown to not only modify the coercivity or the magnetization of magnetic materials (as in the case of Cu-Ni), but to create a real "magnetic switch", where magnetism can be set ON (or OFF) by application of suitable external voltages.

In summary, in this Thesis we have investigated previously unexplored approaches to induce drastic magnetoelectric effects in different types of materials. Depending on the type of magnetic material and electrolyte we have taken advantage of (i) pure charge accumulation effects, (ii) redox or (iii) magneto-ionics to achieve the target magnetoelectric effects. In all cases, we have studied materials which consist of films whose thickness goes beyond the ultra-thin limit (< 1-2 nm), which was a limitation in most previous studies on magnetoelectrics. This is important since thicker films may enable novel approaches to design magnetically actuated devices with enhanced performance, as well as triggering new fundamental studies to better understand the emerging field of magnetoelectric phenomena in matter.

05

Conclusions

5. Conclusions

From a broad viewpoint, this Thesis constitutes one of the first systematic investigations on the effects of externally applied voltage on the magnetic properties of nanoporous alloys. Indeed, nanoporosity has been shown to be successful to enhance charge-mediated magnetoelectric effects (with respect to dense layers) in CuNi alloy films. This is mainly ascribed to the large surface-to-volume ratio of these nanoporous films, together with the uniform pore architecture and the ultra-narrow pore walls. The voltage actuation was carried out by electrolyte-gating using a non-oxidative medium.

In this context, and due to the interface nature of all magnetoelectric effects, the high-surface area of these nanoporous CuNi alloys has been also exploited to induce element-selective redox processes when using an aqueous electrolyte. This allowed us to tailor the magnetic moment of these nanoporous CuNi alloys since the oxidation mainly occurs on the Cu counterpart of the CuNi solid solution, resulting in a Ni-enriched alloy.

Finally, concerning the nanoporous CuNi alloy films, we have been able to conformally coat them with alumina, establishing the basis to perform solid state voltage actuation using condenser-like configurations.

Furthermore, we have also investigated the magnetoelectric response of a dense Co_3O_4 thin film (initially paramagnetic) via electrolyte-gating in non-oxidative media. Voltage-controlled ON-OFF ferromagnetism has been demonstrated and magneto-ionics (i.e., voltage-induced ionic transport) has been established as the main magnetoelectric mechanism for this system.

The following bullet points schematically summarize the main conclusions that can be drawn from this Thesis:

- Ni and Cu–Ni nanoporous metallic films, with highly tunable pore architectures and ultra-thin pore walls, have been successfully synthesized by micelle assisted electrodeposition.

- Nanoporosity (nanoscale pore size with ultrathin pore walls) is shown to boost charge-mediated magnetoelectric effects in CuNi. Specifically, the coercivity can be drastically reduced after applying positive voltages and this effect is ascribed to voltage-induced changes in the magnetic anisotropy due to surface electrostatic charge accumulation.

- The high-surface area of these nanoporous CuNi alloys has been also exploited to induce element-selective redox processes and, to thus, tailor the magnetic moment by voltage actuation using an aqueous alkaline electrolyte.

- Atomic layer deposition has been proven to be a successful technique to conformally coat the nanoporous of the CuNi films, thus establishing the basis to carry out voltage actuation in solid state configurations in the future.

- Voltage-controlled ON-OFF ferromagnetism in a 100 nm dense paramagnetic Co_3O_4 layer has been demonstrated. This effect is mainly due to magneto-ionics, which dominates over any other magnetoelectric effect. The onset of ferromagnetism is attributed to a voltage-induced internal O and Co redistribution, driven by the formation of mixed vacancy clusters, as evidenced by positron annihilation spectroscopy. Ionic transport becomes particularly promoted at grain boundaries and is further assisted by the formation of diffusion channels that incorporate large amounts of O. Remarkably, this approach is carried out at room temperature, circumventing the need of thermally-assisted ionic migration, and does not require external oxygen sources (as opposed to other works in the literature that use HfO_2 or Al_2O_3 as oxygen buffer layers).

Future Perspectives

6. Future perspectives

Based on the novelty and significance of this Thesis, several future research lines emanate from the obtained results:

- Design of novel electrolyte solutions for CuNi electrodeposition in order to tune pore topology and pore wall thickness and, therefore, the surface-to-volume ratio. This could be accomplished by adding other block-copolymers to the electrolyte (e.g. KLE) or using ionic liquid-in-water (IL/W) microemulsions. The dependence of magnetoelectric effects in CuNi alloys as a function of material nanoporosity could be studied.

- CuNi alloys exhibit rather soft magnetic properties. Thus, with the aim to tackle magnetoelectric effects in hard magnetic materials, nanoporous FePt, CoPt, FePd and CoPd can be electrodeposited. Similar voltage protocols to those applied to CuNi could be performed with the aim to investigate their magnetoelectric response.

- In analogy to the work carried out on Co_3O_4, antiferromagnetic oxides with Néel temperatures above room temperature, such as NiO, could be investigated to take advantage, in addition to magneto-ionics, of the extra degree of freedom that exchange bias (arising from the ferromagnetic-antiferromagnetic interactions) could provide.

- Since structural defects, such as vacancies or grain boundaries, play a crucial role in the magneto-ionic behavior of Co_3O_4, the defect density and defect type could be optimized to enhance ionic motion at room temperature. This point is crucial to implement this approach in real technological applications.

- The use of solid dielectrics instead of liquid electrolytes would be appealing for the development of real spintronic devices. For this purpose, optimization of the microstructure and insulting properties of the oxide layers prepared by atomic layer deposition (e.g., HfO_2 or Al_2O_3) would be needed.

Curriculum Vitae

Curriculum Vitae   Alberto Quintana Puebla

Contact Information

Adress __ Autonomus University of Barcelona, Physics department. Building C, C3/202. E08193 Cerdanyola del Vallès, Barcelona, Spain.
e-mail __ qpalberto@gmail.com
LinkedIn __ www.linkedin.com/in/alberto-quintana-puebla
ORCID __ https://orcid.org/0000-0002-9813-735X

Studies

2018 __ *PhD in Materials Science*
PhD Thesis: Enhanced magnetoelectric effects in electrolyte-gated nanoporous metallic alloy and dense metal oxide films
(Group of Smart Nanoengineered Materials, Nanomechanics and Nanomagnetism Autonomus University of Barcelona)

2014 __ *Master in Materials Science and Nanotechnology*
Master Thesis: Synthesis, characterization and mechanical properties of micro/nanostructures of molybde7.504+num oxides
(Autonomus University of Barcelona)

2013 __ *Bachelor's in Physics*
Bachelor Thesis: Mechanical properties and characterization of electrodeposited MoO_x films and micro/nanostructures
(Autonomus University of Barcelona)

Work Experience

2014-2016 __ *Research Technician Assistant*
Project: Synthesis and resistive switching properties of nanoporous single-crystal ZnO nanowires.
(Group of Smart Nanoengineered Materials, Nanomechanics and Nanomagnetism, Autonomus University of Barcelona)

2013-2014 __ *Internship Scientist*
Project: Synthesis of Core-shell Transition Metal Oxide – ZnO nanoparticles for electroluminescent devices
(Group of Smart Nanoengineered Materials, Nanomechanics and Nanomagnetism, Autonomus University of Barcelona)

2012-2013 __ *Internship Scientist*
Project: Development of ZnO based Flexible Hybrid LEDS (Hy-LEDS).
(CETEMMSA Technological Centre)

Languages

Spanish and Catalan – Mother Tongues
English – Level of Advanced
German – Initiation

Stays Abroad

1 Month in the *University of California Davis* under the supervision of **Prof. Kai Liu**.

Attendance to Courses

1. **Workshop in Powder X-Ray Diffraction** (October 2016)
   X-Ray Diffraction Facility. Universitat Autònoma de Barcelona (UAB).

2. **Training School in Electrodeposition** (April 2016)
   European Cooperation in Science and Technology (COST ACTION MP1407).
   Brno, Czech Republic.

3. **Workshop on Transmission Electron Microscopy** (November 2014)
   Microscopy Facility. Universitat Autònoma de Barcelona (UAB)

4. **Workshop on Scanning Electron Microscopy** (April 2014)
   Microscopy Facility. Universitat Autònoma de Barcelona (UAB)

Publications

1. **A. Quintana**, E. Menéndez, M. O. Liedke, M. Butterling, A. Wagner, V. Sireus, P. Torruella, S. Estradé, F. Peiró, J. Dendooven, C. Detavernier, P. Murray, D. A. Gilbert, K. Liu, E. Pellicer, J. Nogués and J. Sort. "*Voltage-controlled ON-OFF ferromagnetism at room temperature in a single metal oxide film*" **Submitted to Science**.

2. S. Robbennolt, **A. Quintana**, E. Pellicer and J. Sort. "*Large magnetoelectric effects in sputtered (nanoparticulate) and electrochemically dealloyed (nanoporous) Fe-Cu films, mediated by electric-field-driven nanoscale phase transformations*" **Submitted to Nanoscale**.

3. I. Fina, **A. Quintana**, X. Marti, F. Sánchez, M. Foerster, L. Aballe, J. Sort, and J. Fontcuberta. "*Reversible and magnetically unassisted voltage-driven switching of the magnetization in FeRh/PMN-PT*" **submitted to Applied Physics Letters.**

4. J. Zhang, **A. Quintana**, E. Menéndez, M. Coll, E. Pellicer and J. Sort. "*Electrodeposited Ni-Based Magnetic Mesoporous Films as Smart Surfaces for Atomic Layer Deposition: An "All-Chemical" Deposition Approach toward 3D Nanoengineered Composite Layers*" **ACS Appl. Mater. Interfaces** 2018, 10, 14877–14885. (IF: **7.504**)

5. S. Robbennolt, J. Fornell, **A. Quintana**, H. Zhang, E. Menéndez, E. Pellicer and J. Sort. "*Structural and Magnetic Properties of Fe_xCu_{1-x} Sputtered Thin Films Electrochemically Treated To Create Nanoporosity for High-Surface-Area Magnetic Components*". **ACS Appl. Nano Mater.** 2018, 1, 1675–1682. (IF: -)

6. **A. Quintana**, E. Menéndez, E. Isarain-Chávez, J. Fornell, P. Solsona, F. Fauth, M. D. Baró, J. Nogués, E. Pellicer and J. Sort. "*Tunable magnetism in nanoporous CuNi alloys by reversible voltage-driven element-selective redox processes*". **Small** 2018, 1704396. (IF: **8.64**)

7. J. Fan, E. Menéndez, M. Guerrero, **A. Quintana**, E. Weschke, E. Pellicer, J. Sort "Unraveling the origin of magnetism in mesoporous Cu-doped SnO_2 magnetic semiconductors". **Nanomaterials** 2017, 7, 348. (IF: **3.553**)

8. **A. Quintana**, A. Altube, E. García-Lecina, S. Suriñach, M. D. Baró, J. Sort, E. Pellicer, M. Guerrero *"A Facile Co-Precipitation Synthesis of Heterostructured ZrO2/ZnO Nanoparticles as Efficient Photocatalysts for Wastewater Treatment"* **J. Mater. Sci.** 2017, 52, 13779 13789 (IF: **2.599**)

9. **A. Quintana**, A. Gómez, M. D. Baró, S. Suriñach, E. Pellicer, J. Sort *"Self-Templating Faceted and Spongy Single-Crystal ZnO Nanorods: Resistive Switching and Enhanced Piezoresponse"* **Mater. Des.** 2017, 133, 54-61. (IF: **4.364**)

10. **A. Quintana**, J. Zhang, E. Isarain-Chavez, E. Menéndez, R. Cuadrado, R. Robles, M. D. Baró, M. Guerrero, S. Pané, B. J. Nelson, C. M. Müller, P. Ordejón, J. Nogués, E. Pellicer, J. Sort *"Voltage-Induced Coercivity Reduction in Nanoporous Alloy Films: A Boost Toward Energy-Efficient Magnetic Actuation"* **Adv. Funct. Mater.** 2017, 27, 1701904. (IF: **12.12**)

11. I. Fina, **A. Quintana**, J. Padilla-Pantoja, X. Martí, F. Macià, F. Sánchez, M. Foester, L. Aballe, J. Fontcuberta, J. Sort. *"Electric-Field-Adjustable Time-Dependent Magnetoelectric Response in Martensitic FeRh Alloy"* **ACS Appl. Mater. Interfaces** 2017, 9, 15577–15582 (IF: **7.504**)

12. **A. Quintana**, A. Varea, M. Guerrero, S. Suriñach, M.D. Baró, J. Sort and E. Pellicer, *"Structurally and Mechanically Tunable Molybdenum Oxide Films and Patterned Nanostructures by Electrodeposition"* **Electrochim. Acta**, 2015, 173, 705-714. (IF: **4.798**)

Patents

J. Sort, E. Pellicer, A. Quintana, E. Isaraín-Chavez, J. Nogués "A method for tuning the magnetic coercivity of nanoporous film, a device and uses thereof" **UK 1707453.5 | EP17170317.6 | 201730721**

Congress

1. **A. Quintana***, E. Menéndez, E. Isarain-Chávez, J. Fornell, P. Solsona, F. Fauth, M. D. Baró, J. Nogués, E. Pellicer and J. Sort. "Reversible voltage-driven element-selective redox tuning of magnetism in nanoporous CuNi alloy". International Workshop on Magneto-Electric Actuation, Magneto-ionics and Related Phenomena in High-Surface Area Materials (**IW-MAG'18**). Barcelona, Spain.

2. M. O. Liedke*, M. Butterling, **A. Quintana**, E. Menéndez, J. Ehrler, R. Bali, E. Hirschmann, V. Sireus, J. Nogués, J. Sort, A. Wagner. *"Vacancy mediated magnetic phase transitions"* 18th International Conference on Positron Annihilation (**ICPA 18**) Orlando, United States of America.

3. **A. Quintana**, C. Navarro-Senent, J. Fornell, E. Menéndez, R. Cuadrado, R. Robles, D. Baró, P. Ordejón, J. Nogués, E. Pellicer, J. Sort*. *"Enhanced energy efficiency in voltage-actuated magnetic nanoporous alloy films and patterned structures"* International Conference on Innovative Applied Energy (**IAPE'19**). Oxford, United Kingdom.

4. S. Robbennolt*, **A. Quintana**, J. Fornell, E. Menéndez, H. Zhang, E. Pellicer, J. Sort. *"Magnetic and magnetoelectric properties of Fe-Cu thin films made nanoporous by electrochemical dealloying"*

5. C. Navarro-Senent,* J. Fornell, E. Isarain-Chávez, **A. Quintana**, J. Nogués, E. Pellicer, J. Sort. *"Magneto-electric properties of nanoporous Co-Pt dots synthesized by micelle-*

assisted electrodeposition on lithographed substrates." 32nd International Conference on Surface Modification Technologies (**SMT32**). San Sebastian, Spain.

6. V. Sireus,* **A. Quintana**, E. Menéndez, S. Suriñach, M. D. Baró and J. Sort. *"Voltage-controlled magnetism in $Fe_{60}Al_{40}$ (at. %) / (100) PMN-PT multiferroic heterostructures"*. 3rd Scientific Meeting of BNC-b Students (**BNC-b**). Bellaterra, Spain.

7. S. Robbennolt*, J. Fornell, **A. Quintana**, E. Menéndez, H. Zhang, V. Sireus, A. Gordó, E. Pellicer, J. Sort "*Structural and Magnetic Properties of Fe-based, Nanoporous Thin Films*" European Advanced Materials Congress (**EAMC 2017**). Stockholm, Sweden.

8. I. Fina*, **A. Quintana**, F. Sánchez, J. Sort, X. Marti, J. Fontcuberta "*Electrically driven magnetic memory effect in Antiferromagnetic-Ferromagnetic mixed phase system*" European Materials Research Society Spring Meeting (**E-MRS 2017**). Strasbourg, France.

9. H. Zhang, S. Robbennolt*, **A. Quintana**, A. Gordó, E. Menéndez, J. Fornell, E. Pellicer, J. Sort, "Structural and magnetic properties of ribbons and thin films of FexCu1-x electrochemically treated to create 3D nanoporosity" IEEE International Magnetics Conference (**INTERMAG 2017**). Dublin, Ireland.

10. **A. Quintana***, J. Zhang, A. Varea, S. Pané, E. Pellicer, J. Sort "*Highly-tunable magnetic properties in novel $Cu_{1-x}Ni_x$ architectures: from fully dense films to patterned pillars and micro-/nanoporous structures*" 61st Annual Conference on Magnetism and Magnetic Materials (**MMM 2016**). New Orleans, United States of America.

11. **A. Quintana***, A. Gómez, M. D. Baró, S. Suriñach, E. Pellicer, J. Sort "*Piezoresponse and resistive switching in self-templating hierarchically porous single crystal ZnO nanowires*" 23rd International Symposium on Metastable, Amorphous and Nanostructured Materials (**ISMANAM 2016**). Nara, Japan.

12. **A. Quintana***, A. Varea, M. Guerrero, S. Suriñach, M. D.Baró, J. Sort, E. Pellicer "*Electrodeposited molybdenum oxide films and patterned submicrometer motifs: structure and mechanical properties*" International Conference on Processing and Manufacturing of Advanced Materials (**Thermec 2016**). Graz, Austria.

13. E. Martinez* and **A. Quintana**, "*Sol-Gel Materials as electron transport layers in Hyleds*", XVII International Sol-Gel Conferences (**SG2013**). Madrid, Spain.

14. E. Martinez* and **A. Quintana**, "Flexible Hybrid Light Emitting Diodes" 6th International Symposium on Flexible Organic Electronics (ISFOE13). Thessaloniki, Greece.

Experiments in Large Scale Facilities

1. **Helmholtz-Zentrum Berlin (HZB) at the BESSY II** (4 - 10 June 2018).
   Beamline: UE46_PGM-1 / High-Field Diffractometer (XAS – XMCD)
   Proposal Ref and Title: 16204243 - Unraveling the origin of magnetoelectric effects in nanoporous CoPt films **(Scientific Coordinator)**

2. **Alba Synchrotron** (14-15 March 2017)
   Beamline: MSPD – BL04 (XRD)
   Proposal Ref and Title: 2016091903 - Unraveling the origin of magnetoelectric effects in nanoporous CuNi by synchrotron XRD **(Scientific Coordinator)**

3. **Helmholtz-Zentrum Berlin (HZB) at the BESSY II** (6-12 February 2017).
   Beamline: UE46_PGM-1 / High-Field Diffractometer (XAS – XMCD)
   Proposal Ref and Title: 16204243 - Unraveling the origin of ferromagnetism in mesoporous Cu-doped SnO2 diluted magnetic semiconductors **(Scientific Coordinator: Enric Menéndez)**

Teaching Experience

1. **Bachelor in Nanotechnology.**
   Autonomus University of Barcelona (2015-2016)
   Subject: Electron Microscopy Lab and Materials Characterization Techniques.
2. **Experience in supervising undergraduate students**.
   Autonomus University of Barcelona (2015-2017)

Technical Skills

Sol-Gel, Electrodeposition, Thermal evaporation, Spin-coating, Sputtering, X-ray diffraction, Scanning electron microscopy, Transmission electron microscopy, Optical microscopy, Mechanical Profilometry, UV-Vis Spectroscopy, Contact Angle, Nanoindentation, X-ray fluorescence, X-ray Photoelectron Spectroscopy, Vibration Sample Magnetometer, Magneto-optic Kerr Effect Microscope, Magneto-electric Measurements, X-Ray Absorption, X-ray Magnetic Circular Dichroism.